Universität Hamburg
DER FORSCHUNG | DER LEHRE | DER BILDUNG

Development of Bio-Based Composites made with Chemically Modified Cellulose Nanofibrils for 3D Printing Purposes

Entwicklung von Biobasierten Verbundwerkstoffen aus Chemisch Modifizierten Cellulose-Nanofibrillen für den 3D-Druck

DISSERTATION

For the doctoral degree award in the Department of Biology at the
Faculty of Mathematics, Informatics, and Natural Sciences at the
University of Hamburg.

Written by:

Feras DALLOUL

Date of disputation:

11.07.2024

Reviewers: Prof. Dr. Bodo Saake
University of Hamburg, Germany

Pr. Dr. Henrikki Liimatainen
University of Oulu, Finland

List of Published publications and manuscripts.

The thesis contains individual chapters consisting of submitted, under revision and published papers in peer-reviewed journals. To ensure consistency, the sections of these papers have been renumbered. The published papers are included in the Appendix 1 and 2. Figures not shown in the manuscript, which is currently being revised, are shown in Appendix 3.

-1-

Feras Dalloul, Jakob Benedikt Mietner and Julien R. G. Navarro
Production and 3D Printing of a Nanocellulose-Based Composite Filament Composed of Polymer-Modified Cellulose Nanofibrils and High-Density Polyethylene (HDPE) for the Fabrication of 3D Complex Shapes
Fibers, 2022, 10, 91

-2-

Feras Dalloul, J. Benedikt Mietner, and Julien R. G. Navarro
Three-Dimensional Printing of a Tough Polymer Composite Gel Ink Reinforced with Chemically Modified Cellulose Nanofibrils Showing Self-Healing Behavior
ACS Appl. Polym. Mater. 2023, 5, 5, 3256–3269

The experimental work in these two published papers was solely conducted by me. My supervisor, Dr. Julien R.G. Navarro, and Dr. J. Benedikt Mietner provided guidance, support, data analysis, and contributed to the writing and publication of the research in research journals.

Signature of candidate
Feras DALLOUL

Signature of the supervisor
Dr. Julien R.G Navarro

Julien R.G. Navarro

Manuscript under revision:

-3-

Feras Dalloul, J. Benedikt Mietner, Dhanya Raveendran, Fabio Hubel, Dennis M. J. Möck, Jörn Appelt and Julien R. G. Navarro

Development of a bio-based composite for 3D printing from diphenylalanine peptide (Fmoc-FF) nanowires with unmodified or polymer-grafted cellulose nanofibrils: from an unprintable material to a strong and reliable printable gel

Eidesstattliche Versicherung - Declaration on oath

Hiermit erkläre ich an Eides statt, dass ich die vorliegende Dissertationsschrift selbst verfasst und keine anderen als die angegebenen Quellen und Hilfsmittel benutzt habe.

I hereby declare, on oath, that I have written the present dissertation on my own and have not used other than the acknowledged resources and aids.

Hamburg, den Unterschrift

24.01.2024

Acknowledgements

I want to express my sincere gratitude towards the people who have contributed greatly to the achievement of this Ph.D. thesis. Firstly, I would like to express my gratitude to Prof Dr. Bodo Saake, the director of our laboratory, whose career and publications have been a great source of inspiration to me. I am grateful for the opportunity to be hosted at the Institute of Wood Science. I would like to express my gratitude to my thesis supervisor, Dr. Julien R.G. Navarro, for his expert guidance, constant support and invaluable advice throughout this great journey. Certainly, his enthusiasm and passion for research have been a great source of inspiration for me and stimulated my curiosity and dedication to the field.

I would also like to thank Dr. J. Benedikt Mietner, who has considerably contributed to this thesis with his expertise in technical information and constructive comments. His willingness to help and his guidance have greatly contributed to the shaping of my ideas.

Special gratitude to *Fachagentur Nachwachsende Rohstoffe* (FNR) for their financial support which allowed this research to be carried out.

I would like to thank my colleagues in the laboratory, Xuehe Jiang, Enguerrand Barba and Dhanya Raveendran for their enthusiasm and support which helped create a stimulating and collaborative environment. I am grateful to my other colleagues at the institute, such as Maï Bergmann, Frederik Schüler, and Yue Chen, for their kind and friendly support. It was something I will remember for a very long time to come.

And finally, but not least, I would like to express my gratitude to my parents, my sister Dima, and my brother Fadi, who is watching me from above. I would especially thank Sacha Roudine, Marine Artaud and Lucien Bouviez, whose tireless encouragement, despite the distance, helped me to overcome the challenges of the PhD. A special thanks is owed to Alexandra Arp, who provided continuous moral and kind care.

Contents

Abbreviation lists

The abbreviations are grouped by topic below for better clarity:

- Chemical compounds:

    - CDI: 1,1'-Carbonyldiimidazole
    - CNF: Cellulose nanofibrils
    - Cu: Copper
    - DEGEEA: Di(ethylene Glycol) Ethyl Ether Acrylate
    - DMSO: Dimethyl sulfoxide
    - eBiB: Ethyl α-bromoisobutyrate
    - Fmoc: 9-fluorenylmethoxycarbonyl
    - Fmoc-AEEA: 2-(N-Fmoc-2-aminoethoxy)ethyl acrylate
    - Fmoc-FF: Fmoc-diphenylalanine
    - HDPE: High-Density Polyethylene
    - LDPE: Low-Density Polyethylene
    - Me_6TREN: Tris[2-(dimethylamino)ethyl]amine
    - SA: Stearyl acrylate
    - $scCO_2$: Supercritical carbon dioxide
    - UPy: Ureidopyrimidinone

- Cellulose nanofibrils based compounds:

    - CNF-MI: Cellulose nanofibrils-based Macroinitiator
    - CNF-g-Fmoc: Fmoc grafted cellulose nanofibrils
    - CNF-g-SA: Stearyl acrylate grafted cellulose nanofibrils
    - CNF-g-UPy: UPy grafted cellulose nanofibrils

- Characterization techniques:

    - ATR-FTIR: Attenuated Total Reflection Fourier Transfer Infrared Spectroscopy
    - CLSM: Confocal Laser Scanning Microscopy
    - CP-MAS NMR: Cross-Polarization Magic-Angle-Spinning NMR
    - DSC: Differential Scanning Calorimetry
    - HRMAS: High-Resolution Magic Angle Spinning
    - NMR: Nuclear Magnetic Resonance
    - UV-Vis: Ultraviolet-visible spectroscopy

- Parameters:
    - G': Storage modulus
    - G'': Loss modulus

  - M_n: Number average molecular weight
  - M_w: Weight average molecular weight
  - Tg: Glass Transition Temperature
  - δ: Chemical shift in NMR spectroscopy
  - ϕ: Volume ratio
  - wt.%: percentage by weight
  - τ: Shear stress
  - $\dot{\gamma}$: Shear rate
  - γ: Shear strain
  - η: viscosity
- Other:
  - AM: Additive Manufacturing
  - FDM: Fused Deposition Modeling
  - LWMG: Low-Weight-Molecular Gelator
  - SET-LRP: Single Electron Transfer Living Radical Polymerisation
  - SI-SET-LRP: Surface-Initiated Single Electron Transfer Living Radical Polymerisation

List of illustrations

Lists of figures:

List of schemes:

List of tables:

Conference contributions

2023

Feras Dalloul

3D gel printing of a tough polymer composite gel ink reinforced with chemically modified cellulose nanofibrils showing self-healing behavior.

Poster presentation

8th European Polysaccharide Network of Excellence (EPNOE) International Polysaccharide Conference, September 2023, Graz, Austria.

Abstract:

Cellulose nanofibrils (CNF) have been widely used as additives to improve the mechanical and functional properties of a large panel of materials, from lightweight composites to eco-friendly packaging solutions. Although their use as fillers in bio-based composites has been intensely investigated, the CNF's potential as reinforcing agents in the field of 3D printing has been less explored and deserves further development. A composite material is considered as the combination of two or more components, each of which has distinct physical and chemical properties. By combining those elements, a new material with improved properties (stronger, lighter, greener...) is produced.

In this thesis, wood CNF was successfully extracted from elemental chlorine-free (ECF) bleached softwood Kraft pulp through mechanical disintegration by milling and microfluidization at high pressure (Microfluidizer®). The tendency of 'surface unmodified' CNFs to aggregate due to the inter-fibrillar interactions between adjacent chains is a major limitation to their use in numerous applications. To overcome this drawback, those inter-fibrillar interactions can be reduced, or even suppressed, via a surface modification process. The introduction of new chemical groups or polymer grafting on their surface also improved the stability of the CNF suspension in numerous solvents (polar & apolar). The presented research approach utilises a two-step surface modification of CNF. Firstly, an initiator group is introduced to obtain a CNF-based macroinitiator (CNF-MI) through an esterification reaction. Secondly, monomers are grafted onto the CNF surface through a well-known polymerisation process known as surface-initiated single electron transfer living polymerisation (SI-SET-LRP).

The reaction of esterification on the hydroxyl groups present on the surface of CNF with 2-bromomethylpropionic acid in the presence of 1,1'-carbonyldiimidazole (CDI) was found to be a highly efficient approach for producing CNF-MI.

The composite obtained from the combination of thermoplastics and unmodified CNF would ultimately result in poor interfacial compatibility, leading to significant aggregation of CNF in the host matrix. This is explained by the fact that most common thermoplastics (PP, PE, ABS) are non-polar and that CNF has an inherent hydrophilic character due to the large number of hydroxyl groups on its surface. It is necessary to reduce the hydrophilic character of the CNF

to overcome this issue and increase its compatibility with the non-polar host matrix. Therefore, in this case, stearyl acrylate, a monomer consisting of a long linear 18 carbons chain was grafted onto the CNF via SI-SET-LRP to obtain a hydrophobic grade CNF, referred to here as stearyl acrylate-grafted CNF (CNF-g-SA). High-density polyethylene (HDPE), a thermoplastic commonly found in household items, has been hardly used in 3D printing applications due to warping and deformation issues while being processing. The addition of CNF-g-SA was expected to address this issue and improve its suitability. A composite made of CNF-g-SA/HDPE with a content of 10 wt.% CNF-g-SA was produced and a comparison with the initial starting material resulted in an increase in the material stiffness (Young's modulus, from 1094 MPa to 888 MPa). CNF-g-SA/HDPE was used for 3D printing tests and various challenging objects were 3D printed. While printing, the warping issue was significantly reduced and the 3D-printed composite showed excellent shape fidelity.

In a separate approach, the possibility of creating a self-healing gel composite based on CNF was investigated. CNF was modified through an SI-SET-LRP process, using a homemade synthesized ureidopyrimidinone monomer (UPy). The resulting modified CNF is referred to as UPy-grafted cellulose nanofibrils (CNF-g-UPy). In the meantime, a random copolymer composed of UPy and diethylene glycol ethyl ether acrylate (DEGEEA) was also synthesized and will later on serve as a host matrix. The presence of the UPy unit on the random copolymer and the CNF will create a strong physical cross-linking network. The CNF-g-UPy/UPy-DEGEEA composite was obtained by adding CNF-g-UPy to the random copolymer DEGEEA. The rheological characterization was performed to evaluate the mechanical properties of the composite and examine the gel's stress behaviour. The objective was to determine whether the composite is suitable for 3D gel printing. A 3.7-fold increase in G' (storage modulus) and a 2.8-fold increase in G'' (loss modulus) were observed in comparison to the rheological properties of the starting material, demonstrating the strengthening potential (physical cross-linking) of the modified CNF. The composite was successfully used for 3D gel-printing. Two half-arrows were printed with high resolution and fused after being heated at 60 °C for 10 seconds. The experiment demonstrated the self-healing capacity of the gel, as there was no structural change observed after the self-healing process.

In final part of my research work was aimed at the production of a high-resolution 3D printable gel using a low molecular weight gelator (LWMG). Fmoc-FF, a self-supporting peptide, was selected as LWMG for this study. However, its 3D unprintability is hampered by its lack of elasticity. To increase the Fmoc-FF 3D printability, unmodified CNF and 9-fluorenylmethoxycarbonyl (Fmoc) grafted cellulose nanofibrils (CNF-g-Fmoc) were incorporated into the Fmoc-FF gel (as matrix), yielding two sets of composites (CNF/Fmoc-FF and CNF-g-Fmoc/Fmoc-FF). CNF-g-Fmoc was prepared using SI-SET-LRP with 2-(N-Fmoc-2-aminoethoxy)ethyl acrylate (Fmoc-AEEA), an in-house synthesized monomer. The amount of Fmoc-AEEA was measured using UV-Vis and found to be 20 wt.% of the total structure. The synthetical parameters for the hybrid gel production were here investigated, such as the composition (ratio modified CNF & Fmoc-FF) and concentration of the solvents (ratio DMSO-H_2O). It was found that a higher water content was associated with an improvement in mechanical properties. The printing tests were conducted on grids made of both composites, and both provided satisfactory resolution. Some complex 3D objects such as wheels, stars and bridges were 3D printed with a high shape fidelity. The 3D-printed gel object was finally dried using a supercritical CO_2 drying procedure, which yielded satisfactory results with good shape retention.

This study has demonstrated that the surface modification of the CNF through the grafting of numerous polymers is an effective approach for improving the mechanical and structural properties of bio-based composites, making them also suitable for 3D printing applications. The surface chemical modification method (SI-SET-LRP) was effective and consistent, enabling the adjustment of CNF properties to achieve greater compatibility. Incorporating CNF into various composites has led to increased strength, flexibility, and compatibility with a range of print materials. This work provides an opportunity for further exploration and optimization of bio-based functional 3D printable materials, thus promoting innovation in 3D printing applications.

Zusammenfassung:

Cellulose-Nanofibrillen (CNF) werden in großem Umfang als Zusatzstoffe zur Verbesserung der mechanischen und funktionellen Eigenschaften einer Vielzahl von Materialien eingesetzt, von leichten Verbundwerkstoffen bis hin zu umweltfreundlichen Verpackungslösungen. Obwohl ihre Verwendung als Füllstoffe in biobasierten Verbundwerkstoffen intensiv erforscht wurde, ist das Potenzial der CNF als Verstärkungsmittel im Bereich des 3D-Drucks weniger erforscht worden und verdient weitere Entwicklung. Ein Verbundwerkstoff ist eine Kombination aus zwei oder mehr Komponenten, von denen jede unterschiedliche physikalische und chemische Eigenschaften aufweist. Durch die Kombination dieser Elemente wird ein neues Material mit verbesserten Eigenschaften (stärker, leichter, umweltfreundlicher usw.) hergestellt.

In dieser Arbeit wurde erfolgreich CNF aus elementar chlorfrei gebleichtem Weichholz-Kraftzellstoff durch mechanische Zerkleinerung durch Mahlen und Mikrofluidisierung bei hohem Druck (Microfluidizer®) extrahiert. Die Tendenz der "oberflächenunmodifizierten" CNFs, aufgrund der interfibrillären Wechselwirkungen zwischen benachbarten Ketten zu aggregieren, ist eine wesentliche Einschränkung für ihre Verwendung in zahlreichen Anwendungen. Um diesen Nachteil zu überwinden, können diese interfibrillären Wechselwirkungen durch einen Oberflächenmodifizierungsprozess verringert oder sogar unterdrückt werden. Die Einführung neuer chemischer Gruppen oder das Aufpfropfen von Polymeren auf ihre Oberfläche verbessert auch die Stabilität der CNF-Suspension in zahlreichen (polaren und apolaren) Lösungsmitteln. Der vorgestellte Forschungsansatz nutzt eine zweistufige Oberflächenmodifikation von CNF. Zunächst wird eine Initiatorgruppe eingeführt, um durch eine Veresterungsreaktion einen Makroinitiator auf CNF-Basis (CNF-MI) zu erhalten. Zweitens werden Monomere auf die CNF-Oberfläche durch einen bekannten Polymerisationsprozess aufgepfropft, der als oberflächeninitiierte lebende Einzelelektronentransferpolymerisation (SI-SET-LRP) bekannt ist.

Die Reaktion der Veresterung der auf der Oberfläche der CNF vorhandenen Hydroxylgruppen mit 2-Brommethylpropionsäure in Gegenwart von 1,1'-Carbonyldiimidazol (CDI) erwies sich als hocheffizienter Ansatz zur Herstellung von CNF-MI.

Der aus der Kombination von thermoplastischen Kunststoffen und unmodifizierten CNF gewonnene Verbundwerkstoff würde letztlich zu einer schlechten Grenzflächenkompatibilität führen, was eine erhebliche Aggregation der CNF in der Wirtsmatrix zur Folge hätte. Dies ist darauf zurückzuführen, dass die meisten gängigen Thermoplaste (PP, PE, ABS) unpolar sind und dass CNF aufgrund der großen Anzahl von Hydroxylgruppen auf ihrer Oberfläche einen inhärent hydrophilen Charakter haben. Um dieses Problem zu überwinden und die Kompatibilität mit der unpolaren Wirtsmatrix zu erhöhen, muss der hydrophile Charakter der CNF verringert werden. Daher wurde in diesem Fall Stearylacrylat, ein Monomer mit einer langen linearen 18-Kohlenstoff-Kette, über SI-SET-LRP auf die CNF aufgepfropft, um eine hydrophobe CNF zu erhalten, die hier als Stearylacrylat-gepfropfte CNF (CNF-g-SA) bezeichnet wird. Polyethylen hoher Dichte (HDPE), ein thermoplastischer Kunststoff, der häufig in Haushaltsgegenständen zu finden ist, wurde aufgrund von Verformungsproblemen bei der Verarbeitung bisher kaum für 3D-Druckanwendungen verwendet. Durch die Zugabe von CNF-g-SA sollte dieses Problem gelöst und die Eignung des Materials verbessert werden. Ein Verbundwerkstoff aus CNF-g-SA/HDPE mit einem Gehalt von 10 Gew.-% CNF-g-SA wurde hergestellt, und ein Vergleich mit dem ursprünglichen Ausgangsmaterial ergab eine Erhöhung der Materialsteifigkeit (E-Modul, von 1094 MPa auf 888 MPa). CNF-g-SA/HDPE wurde für 3D-Druckversuche verwendet und verschiedene anspruchsvolle Objekte wurden 3D-gedruckt. Während des Drucks wurde das Problem der Verformung deutlich reduziert und der 3D-gedruckte Verbundstoff zeigte eine ausgezeichnete Formtreue.

In einem separaten Ansatz wurde die Möglichkeit der Herstellung eines selbstheilenden Gel-Verbundwerkstoffs auf der Basis von CNF untersucht. CNF wurde durch ein SI-SET-LRP-Verfahren modifiziert, wobei ein selbst synthetisiertes Ureidopyrimidinon-Monomer (UPy) verwendet wurde. Die resultierende modifizierte CNF wird als UPy-gepfropfte Cellulose-Nanofibrillen (CNF-g-UPy) bezeichnet. In der Zwischenzeit wurde auch ein statistisches Copolymer aus UPy und Diethylenglykolethyletheracrylat (DEGEEA) synthetisiert, das später als Wirtsmatrix dienen wird. Das Vorhandensein der UPy-Einheit auf dem Random-Copolymer und der CNF wird ein starkes physikalisches Vernetzungsnetzwerk schaffen. Der CNF-g-UPy/UPy-DEGEEA-Verbundstoff wurde durch Zugabe von CNF-g-UPy zum statistischen Copolymer DEGEEA hergestellt. Die rheologische Charakterisierung wurde durchgeführt, um die mechanischen Eigenschaften des Komposits zu bewerten und das

Spannungsverhalten des Gels zu untersuchen. Ziel war es, festzustellen, ob das Komposit für den 3D-Geldruck geeignet ist. Im Vergleich zu den rheologischen Eigenschaften des Ausgangsmaterials wurde eine 3,7-fache Erhöhung von G' (Speichermodul) und eine 2,8-fache Erhöhung von G" (Verlustmodul) festgestellt, was das Verstärkungspotenzial (physikalische Vernetzung) der modifizierten CNF belegt. Das Komposit wurde erfolgreich für den 3D-Geldruck verwendet. Zwei Halbpfeile wurden mit hoher Auflösung gedruckt und verschmolzen, nachdem sie 10 Sekunden lang bei 60 °C erhitzt worden waren. Das Experiment zeigte die Selbstheilungskapazität des Gels, da nach dem Selbstheilungsprozess keine strukturelle Veränderung beobachtet wurde.

Im letzten Teil meiner Forschungsarbeit ging es um die Herstellung eines hochauflösenden, druckbaren 3D-Gels unter Verwendung eines niedermolekularen Gelators (LWMG). Fmoc-FF, ein selbsttragendes Peptid, wurde als LWMG für diese Studie ausgewählt. Seine 3D-Undruckbarkeit wird jedoch durch seine mangelnde Elastizität beeinträchtigt. Um die 3D-Druckbarkeit von Fmoc-FF zu erhöhen, wurden unmodifizierte CNF und 9-Fluorenylmethoxycarbonyl (Fmoc)-gepfropfte Cellulose-Nanofibrillen (CNF-g-Fmoc) in das Fmoc-FF-Gel (als Matrix) eingearbeitet, was zu zwei Gruppen von Verbundwerkstoffen führte (CNF/Fmoc-FF und CNF-g-Fmoc/Fmoc-FF). CNF-g-Fmoc wurde unter Verwendung von SI-SET-LRP mit 2-(N-Fmoc-2-Aminoethoxy)ethylacrylat (Fmoc-AEEA), einem intern synthetisierten Monomer, hergestellt. Der Anteil von Fmoc-AEEA wurde mittels UV-Vis gemessen und betrug 20 Gew.-% der Gesamtstruktur. Die synthetischen Parameter für die Herstellung des Hybridgels wurden hier untersucht, wie z. B. die Zusammensetzung (Verhältnis modifizierte CNF & Fmoc-FF) und die Konzentration der Lösungsmittel (Verhältnis DMSO-H_2O). Es zeigte sich, dass ein höherer Wassergehalt mit einer Verbesserung der mechanischen Eigenschaften verbunden war. Die Drucktests wurden mit Gittern aus beiden Verbundstoffen durchgeführt, und beide lieferten eine zufriedenstellende Auflösung. Einige komplexe 3D-Objekte wie Räder, Sterne und Brücken wurden mit einer hohen Formtreue gedruckt. Das 3D-gedruckte Gelobjekt wurde schließlich mit einem überkritischen CO_2-Trocknungsverfahren getrocknet, das zufriedenstellende Ergebnisse mit guter Formstabilität lieferte.

Diese Studie hat gezeigt, dass die Oberflächenmodifizierung der CNF durch das Aufpfropfen zahlreicher Polymere ein wirksamer Ansatz zur Verbesserung der mechanischen und strukturellen Eigenschaften von biobasierten Verbundwerkstoffen ist, so dass sie sich auch für 3D-Druckanwendungen eignen. Die Methode der chemischen Oberflächenmodifikation (SI-SET-LRP) war effektiv und konsistent und ermöglichte die Anpassung der CNF-Eigenschaften, um eine größere Kompatibilität zu erreichen. Die Einbindung von CNF in verschiedene Verbundwerkstoffe hat zu einer erhöhten Festigkeit, Flexibilität und Kompatibilität mit einer Reihe von Druckmaterialien geführt. Diese Arbeit bietet die Möglichkeit zur weiteren Erforschung und Optimierung biobasierter funktioneller 3D-druckbarer Materialien und fördert so Innovationen bei 3D-Druckanwendungen.

1 Introduction

1.1 Cellulose

Cellulose is one of the world's most abundant biopolymers, as it can be found mainly in trees and plants such as cotton, hemp and bamboo. It can also be extracted from bio-organisms including bacteria and algae[1–3]. Although cellulose produced from cotton and certain bacteria is highly pure, the cellulose found in plants and the cell walls of wood is associated with other biopolymers, such as lignin and hemicelluloses, which are responsible for maintaining the plant's cell stability[4]. As shown in Figure 1, these plant components aggregate and entangle cellulose into a highly organised hierarchical structure forming small, tightly packed elementary fibrils[5].

Wood contains between 30 % and 45 % cellulose, depending on the species, and cellulose fibers must be isolated and separated from the other main components before use. The process involves the treatment of lignocellulosic biomass for the selective removal of hemicelluloses and lignin. Depending on the raw material, the process can be carried out by either alkali or acid-chlorite treatment. Once the cellulosic matrix materials have been completely isolated, the cellulose fibres are then defibrillated through a mechanical disintegration process. The manmade cellulose fibers produced in 2021 amounted to 7.2 million tonnes and their use is constantly increasing[6]. It’s used widely in different industries, particularly in textiles, and in the production of paper and cardboard. The typical length of wood fibres is about 2 mm and the width varies from 20-50 µm.

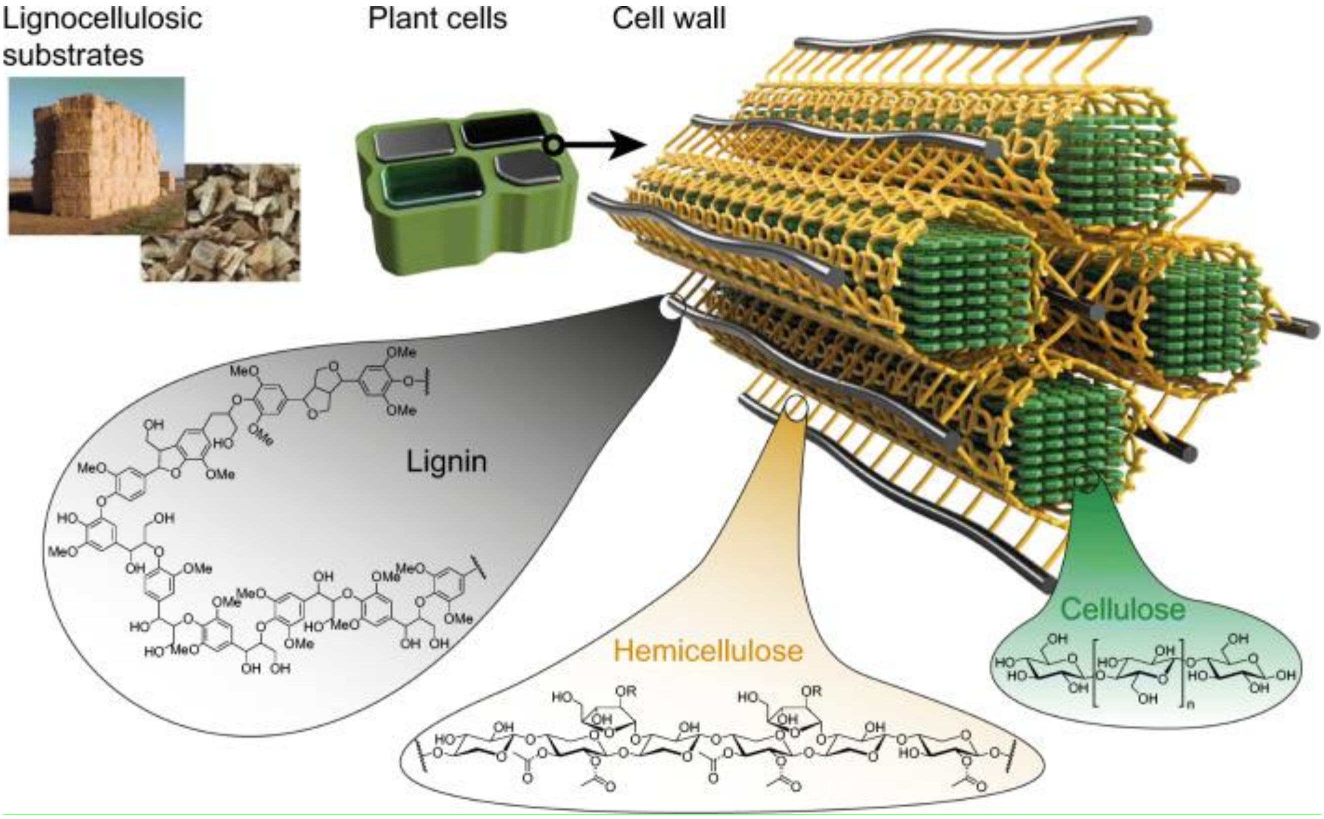

Figure 1: Lignocellulosic plant cell wall components and structure. Authorised reproduction of figure from S. Brethauer *et al.*[7]

1.1.1 Hierarchical structure of cellulose

The hierarchical structure, from the wood tree to the cellulose chain, is illustrated in the Figure 2a. Cellulose is a high molecular weight linear homopolymer, composed of D-Glucose repeating units linked together through a β-1,4-glucosidic bond. With respect to its neighbours, each glucose molecule is rotated by 180 degrees[8]. On the molecular scale, the basic structural unit, e.g. the building block, consists of two anhydroglucose units (AGU) with one primary hydroxyl group located on the carbon 6 position and two secondary groups on the carbon 2 and 3 positions (Figure 2b). The presence of those hydroxyl groups, with the oxygen atoms embedded in the pyranose rings, promotes a specific arrangement by means of intra- and inter-chain interactions via hydrogen bonding (Figure 2c). The intra-chain interactions increase the axial stiffness, while the inter-chain interactions bind the chains together into two-dimensional sheets. The parallel stacking, facilitated by a combination of van der Waals and hydrogen bonding, forms the elementary fibrils, which then also self-assemble, through the same inter- and intra-interaction, into microfibrils.

Those interactions are responsible for the entanglement of cellulosic fibers and the strengthening of the structure of plant cell walls. Those hydroxyl groups also play an important role in the physical properties of cellulose, such as hydrophilicity. Moreover, those hydroxyl groups provide a reactive site, an anchoring point for the grafting of many molecules onto the nanocellulose surface (polymers for example)[9]. Each cellulose backbone possesses a reducing end, which is the equilibrium of an open aliphatic aldehyde/hemiacetal, with one non-reducing tail (closed ring structure with a pendant hydroxyl group). The degree of polymerisation (DP) of the repeating unit can vary from 2,000 to 16,000. The DP depends on the cellulose source and the isolation treatment[10–12]. The accurate length measurement of the nanofibrils poses a challenge due to their curved morphology and their aggregation behaviour. Several theoretical models based on the fibril cross sections were used to estimate the number of packed cellulose chains necessary for the formation of the elementary fibrils. Studies indicated that the elementary cellulose fibril (ECF) contains variable numbers of microfibril chains according to the source of that cellulose. As an example, Fernandes *et al.*[13] demonstrated that cellulose microfibrils in spruce wood followed a 24-chain ECF model, and Ding *et al.*[14] revealed that cellulose fibrils in maize cell walls conformed more to a 36-chain model ECF model. However, the accurate number of cellulosic chains necessary to form a fibril is still under debate. Cellulose chains are either uniformly or non-uniformly arranged within these fibrils. This results in two distinct domains, a highly ordered crystalline region and a disordered domain, the amorphous part. The degree of crystallinity is highly dependent on the source of the cellulose and ranges from 40 to 70%[15]. The crystalline structure of cellulose consists of four different polymorphs (I, II, III, IV) with each its unique structural arrangements and properties[16–18].

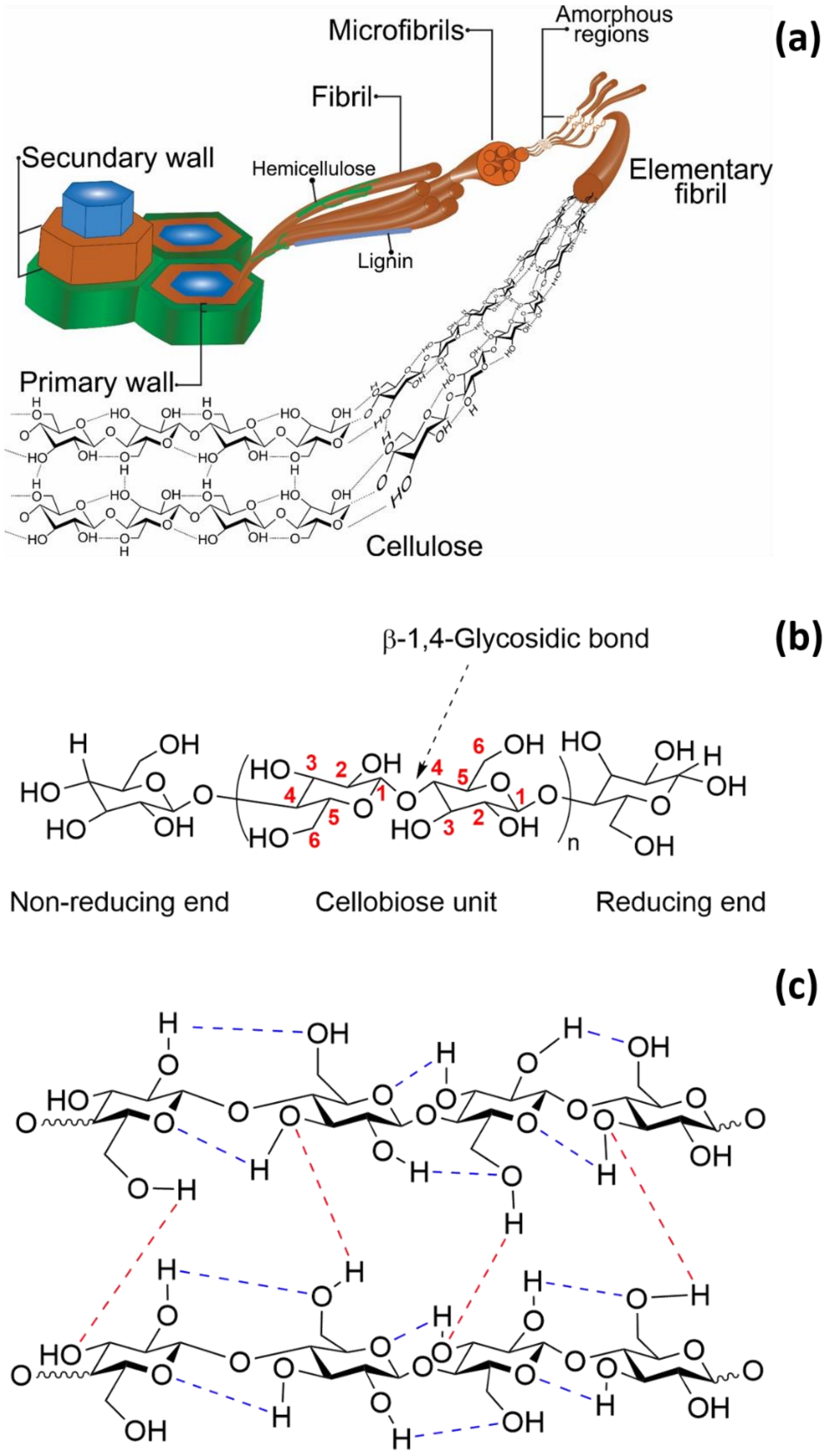

Figure 2: Hierarchical structure of cellulose extracted from plants wood. Authorised reproduction of figure from Rojas *et al.*[19] (a); Chemical structure of the cellulose chains which shows the cellobiose unit, numbered carbons, and reducing and non-reducing ends (b); Cellulose chains inter- and intramolecular interactions (c).

1.1.2 Nanocellulose: isolation, mechanical properties.

The cellulose used in this research is obtained from elemental chlorine-free (ECF) bleached softwood Kraft pulp, therefore the focus will be on chemical pulping as it's the most relevant process. The most widely used process (90 % of all the cellulose pulp produced worldwide) is the 'Kraft' process which was developed by the German chemist Carl F. Dahl[20] in 1879. The first step is the treatment of the woodchips by immersion in a strong alkaline solution, typically consisting of sodium hydroxide (NaOH) and sodium sulphide (Na_2S). The elevated temperatures and pressures during the cooking process serve two purposes: to break down the lignin and to facilitate the extraction of the cellulose. The cooking process dissolves about 90 % of the lignin and hemicellulose present in wood, while the remaining 10 % of lignin is primarily responsible for the brown colour of kraft pulp. A necessary step is then the bleaching process, in which the 10 % of residual lignin is removed from the pulp in the most selective way possible without breaking down the cellulose. Traditionally, this procedure has been done using elemental chlorine and chloride dioxide, but it is now being replaced by more environmentally friendly elemental chlorine-free (ECF) or totally chlorine-free (TCF) bleaching processes[21].

Cellulose is available in a variety of hierarchical forms with defined sizes, morphologies, aspect ratios and crystallinities. These include cellulose fibres (CF), microcrystalline cellulose (MCC), microfibrillated cellulose (MFC) or cellulose nanofibrils (CNF), and cellulose nanocrystals (CNC). A Scanning Electron Microscopy (SEM) image of each was that cellulose particle is displayed in Figure 3. *The thesis exclusively concentrates on CNF utilization and, therefore, only this section is described in detail.*

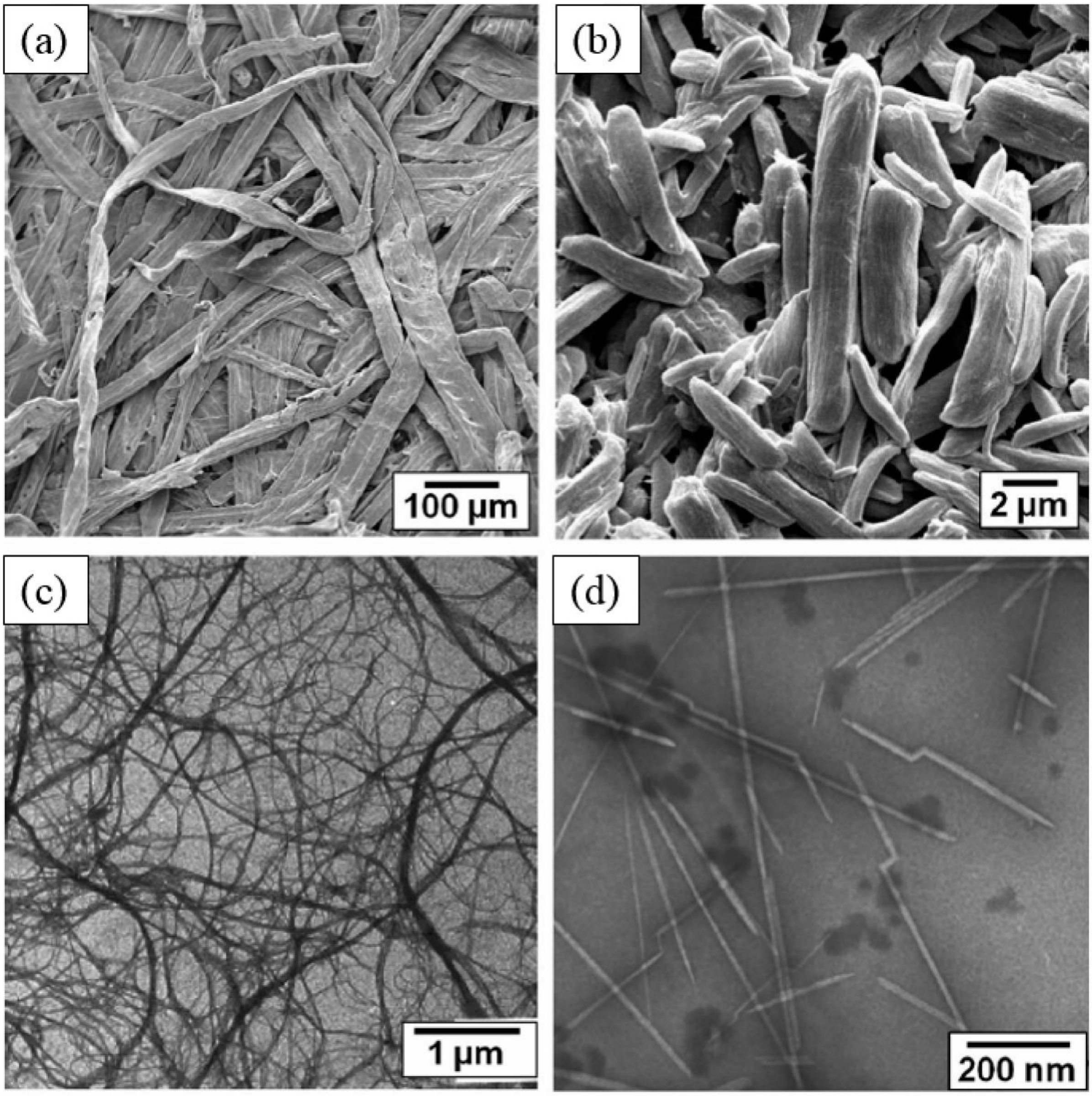

Figure 3: SEM images of different types of cellulose particles: cellulose fibers (CF) (a); microcrystalline cellulose (MCC) (b); cellulose nanofibrils (CNF) (c) and tunicate cellulose nanocrystals (CNC) (d). Authorised reproduction of figure from Kisuk *et al.*[22].

The crystalline portions of CNF are responsible for the high Young's modulus, with values reported in the range of 130 GPa[23]. Nanocellulose is amongst the least dense biopolymers[24] with an average density of 1.60 $g\cdot cm^{-3}$. Its high specific surface area, renewability and biodegradability are highly attractive properties that render it suitable for materials reinforcement in a wide range of applications, including composite engineering[25,26].

1.1.3 Cellulose nanofibrils (CNF)

CNF comprise crystalline and amorphous portions and are obtained in suspension with a dimension of a single fibril of 5 to 60 nm in width and a length of 700 nm to a few µm[27]. The process of extraction was initially described in 1970 by Turbak et al. and Herrick et al.[28], they were able to produce a 2 wt.% suspension, with an obtained diameter of less than 100 nm, from wood pulp using a mill at 10,000 rpm and passing it through a homogeniser at 550 bar. Various methods such as microfluidisation, refining, homogenisation, cryocrushing or high-intensity ultrasound have since been used to effectively isolate CNF. These processes rely on the use of high shear rates to defibrillate the macrofibrils, inducing cleavage of the inter-fibrillar interaction along the longitudinal axis, and leading to the extraction of cellulose fibrils with a relatively higher aspect ratio[15]. Nevertheless, the high-shear mechanical disintegration methods are highly energy-consuming[29]. Several pre-treatment proposals have been made before mechanical processing that can reduce energy consumption to less than 1 MWh/tonne, thus providing an interesting approach for upscaling[30]. Some of the pre-treatment approaches include biological, chemical (TEMPO-mediated oxidation, carboxymethylation, phosphorylation) and mechanical (refining, homogenisation, ultrasound)[31–33]. The biological process employs endoglucanases, an enzyme that selectively breaks the glycosidic bonds in the amorphous region. An example of enzymatic pre-treatment of lignocellulosic feedstock is displayed in Figure 4. The use of enzymatic pre-treatment enhances the effectiveness of subsequent mechanical treatments, leading to the production of nanocellulose with reduced energy consumption[34]. Another mechanical pre-treatment has also been proposed, based on the dry grinding of cellulose pulp using the shear cutting method, which results in efficient disintegration into cellulose nanofibrils (CNFs), thus achieving a significant reduction in overall energy consumption[35].

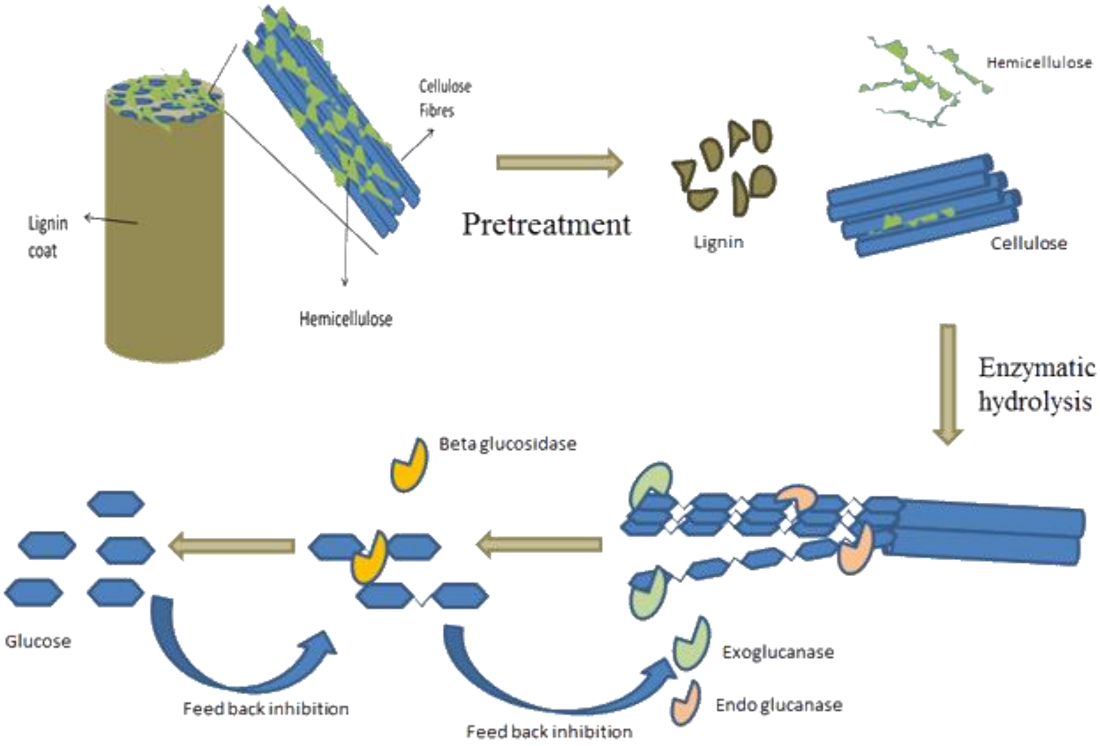

Figure 4: Enzymatic pre-treatment of lignocellulosic feedstocks for the production of CNF. Figure reproduced from Celignis[36].

The composite materials obtained with cellulose nanofibrils (CNF) have numerous applications in the medical[37], automobile[38] and packaging sectors[39]. When used as an additive, CNF could act as a reinforcing agent to increase strength and stiffness, while the surrounding material ensures an even load distribution.

1.1.4 Surface Modification of CNF

CNFs have the potential to be used as fillers in a wide range of materials, but their surface modifications are often required to ensure proper compatibility with the host matrix material. Various surface treatments, e.g. chemical modification, have been already reported to modify the structural and surface properties of the CNF. The purpose of these would be to improve their adhesion and to achieve better compatibility with the interfaces[40]. The precise tailoring of cellulose properties, especially through thermal and surface modification, has already made it possible to manufacture composites with specific performance requirements[41,42]. The surface properties of the nanocellulose can be modified since a relatively high amount of reactive hydroxyl groups are present on their surfaces. Thermal treatment, drying or hornification are highly effective modifications for enhancing the hydrophobicity, crystallinity, and dimensional stability of wood fibrils[43,44]. The surface modification, e.g. chemical treatment, can also be used to introduce new functional groups, some examples are shown in Figure 5.

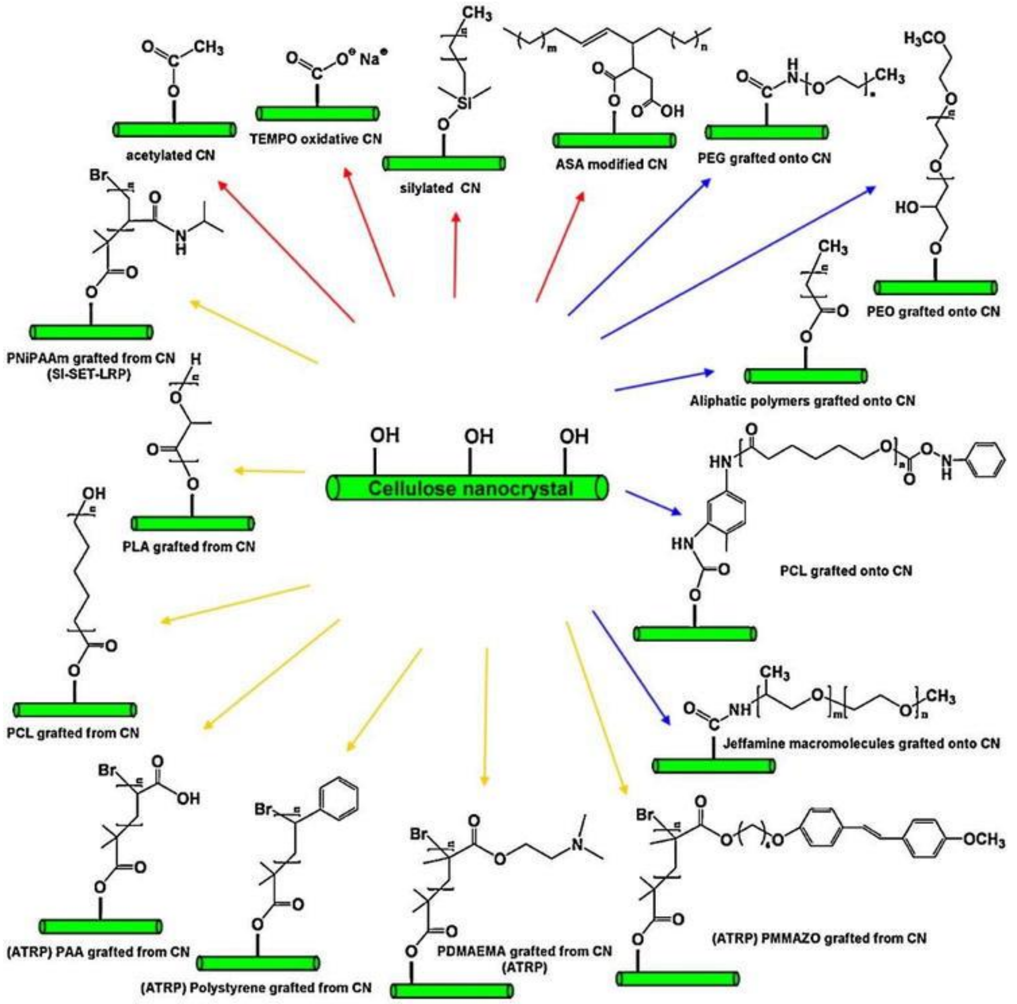

Figure 5. Common studied chemical modifications of cellulose nanocrystals (CNCs); [PEG: poly(ethylene glycol); PEO: poly(ethylene oxide); PLA: poly(lactic acid); PAA: poly(acrylic acid); PNiPAAm: poly(N-isopropylacrylamide); and PDMAEMA: poly(N,N-dimethylaminoethyl methacrylate)]. Authorised reproduction of figure from Lin *et al.*[45]

The main methods are outlined below:

- Mercerization, one of the oldest pioneered processes developed by John Mercer in 1844, involves immersing cellulosic fibers, particularly cotton, in a highly concentrated solution of sodium hydroxide[46]. This process leads to the breaking of about 25 % of hydrogen bonds and ultimately improving properties. Mercerization was reported to improve dye affinity and reduce shrinkage, which makes the mercerized cellulose a highly valuable material in the textile industry[47].

- The addition of coupling agents is a commonly used method in industry. Coupling agents are used in small quantities to bond fillers and matrixes. Maleic Anhydride Grafted Polyethylene (MAPE) is one of the commonly employed additives for compatibility increase between cellulose and a thermoplastic matrix[48].
- The oxidation of cellulose fibrils involves the introduction of oxygen-containing functional groups (aldehydes or acids). One common chemical modification technique is the 2,2,6,6-tetramethylpiperidine-1-oxyl (TEMPO) mediated oxidation of cellulose. This approach selectively targets the primary hydroxyl groups converting them to carboxylates (C6 position), thereby negatively charging the cellulose surface. The radical produced acts as a catalyst in the presence of a co-oxidant, typically sodium hypochlorite (NaClO). This modification improves the hydrophilicity and reactivity, which enhances compatibility[49].
- The modification can also be achieved by grafting components or polymers onto the surface of the cellulose fibrils. The three primary approaches for grafting are illustrated in Scheme 1. *Grafting-to* entails covalently linking pre-formed chains of polymer onto the surface. This requires the polymer and cellulose to both contain reactive functional groups. The surface-initiated polymerisation (SIP), or *grafting-from*, involves immobilizing a reactive group onto the surface of cellulose, which triggers the polymerisation of a monomer. *Grafting-through* refers to the anchoring of a polymerisable functional group to the cellulose backbone, subsequently copolymerised with another monomer in the presence of an initiator in the medium[50].

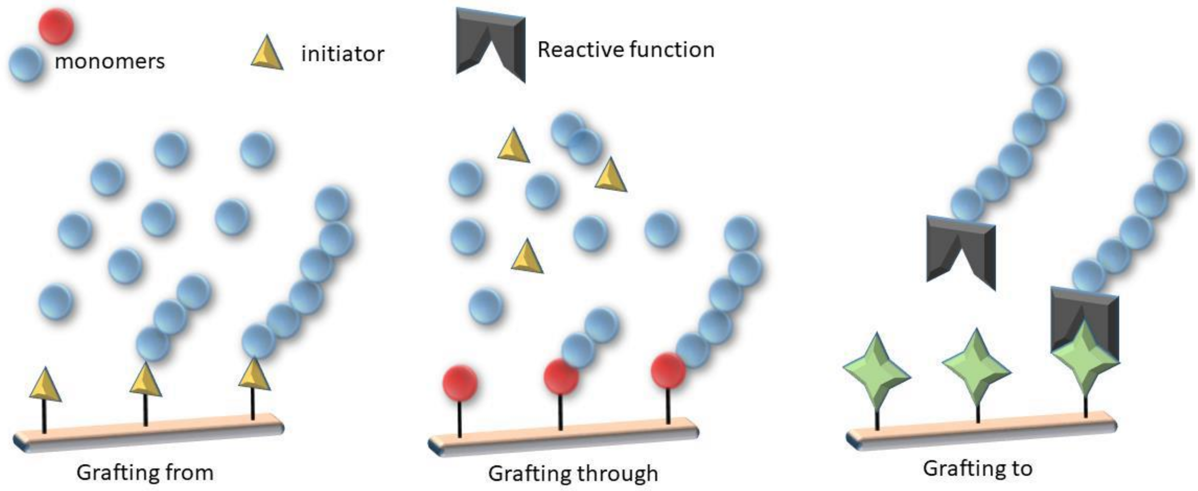

Scheme 1: Schematic illustration of surface modification approaches: grafting to, grafting from, and grafting through.

In this research, the technique used for the chemical surface modification of CNF is known as Surface Initiated Single Electron Transfer Living Radical Polymerisation (SI-SET-LRP) and is classed as *grafting-through* type modification.

1.1.5 Polymerization process: Single Electron Transfer Living Radical Polymerisation (SET-LRP)

Introduced by Virgil Percec in 2002[51], Single Electron Transfer Living Radical Polymerisation (SET-LRP) emerged as a polyvalent, ultra-fast and reliable synthetic polymerisation method. The process allows to have a high molecular mass control, with a low polydispersity index and a high level of end-group functionality/fidelity. It has shown greater efficiency due to its relative 'simplicity' as it can be carried out under mild conditions, without the need for rigorous deoxygenation when compared with other existing living polymerisation techniques[52,53]. Among the advantages of this technique, the catalyst (copper wire) can be easily removed from the medium and recycled. A general scheme of the SET-LRP reaction is shown in Figure 6a, illustrating the types of polymers that can be obtained from this reaction. There is a wide range of monomers that can be used, including acrylates, methacrylates and acrylamides, many of which are commercially available (Figure 6b).

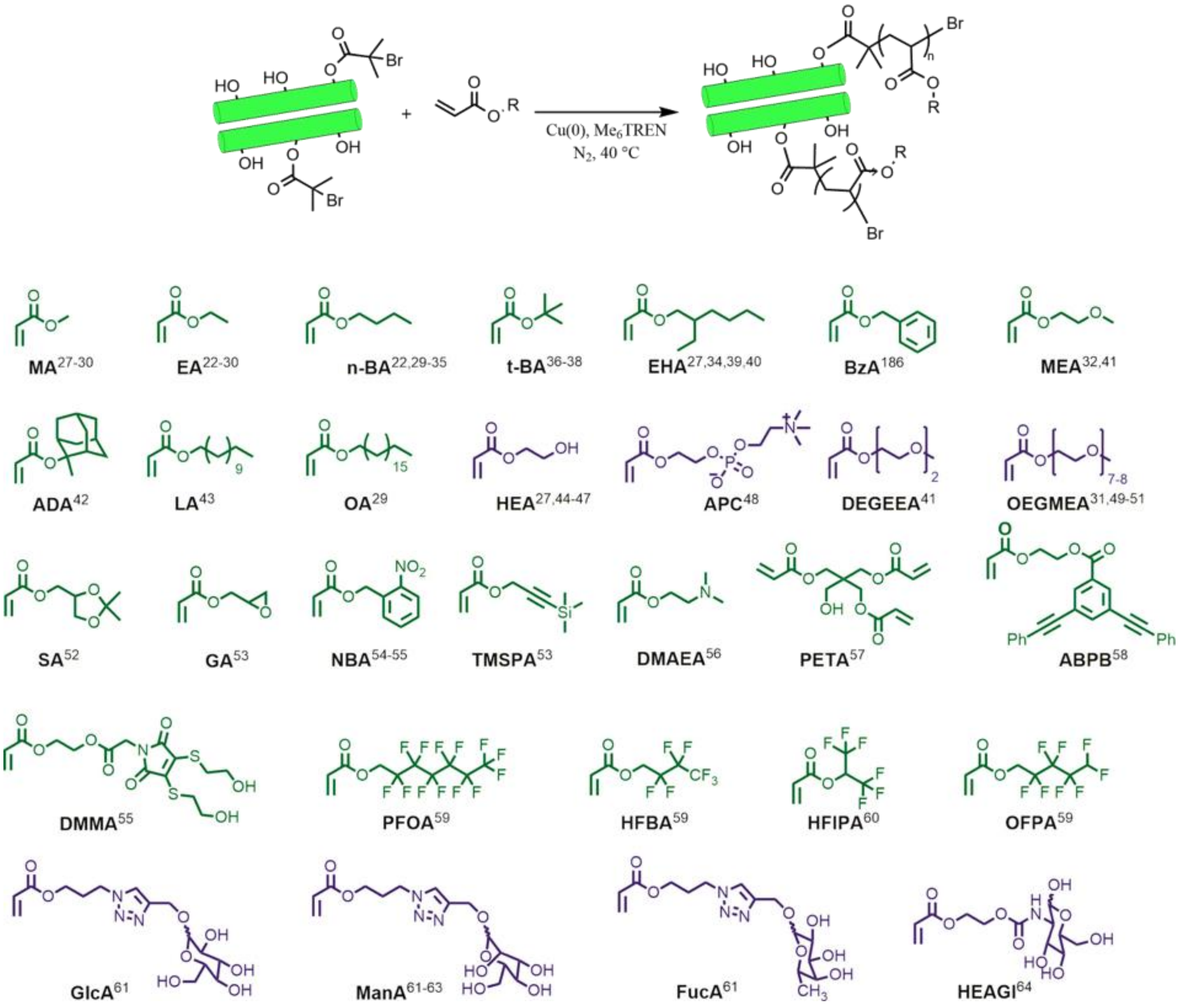

Figure 6: Scheme of a standard reaction for the synthesis of a copolymer using SET-LRP (a); Some of the acrylates employed in SET-LRP (blue, hydrophilic and water soluble; green, hydrophobic and water-insoluble) (b). Authorised reproduction of figure from Lligadas *et al.*[54].

In addition, several types of polymer composition can be obtained via the synthesis of homopolymers, and copolymers such as alternate, random and block polymers. Accordingly, the SET-LRP mechanism relies on several key factors that constrain the reaction conditions, such as solvent, monomers, and nature of complexing ligand[55]. Alsubaie *et al.*[56] have reported the synthesis of a hexablock polymer synthesis, as shown in Figure 7. The block copolymers produced in this study demonstrate the range of possible copolymers which can be produced.

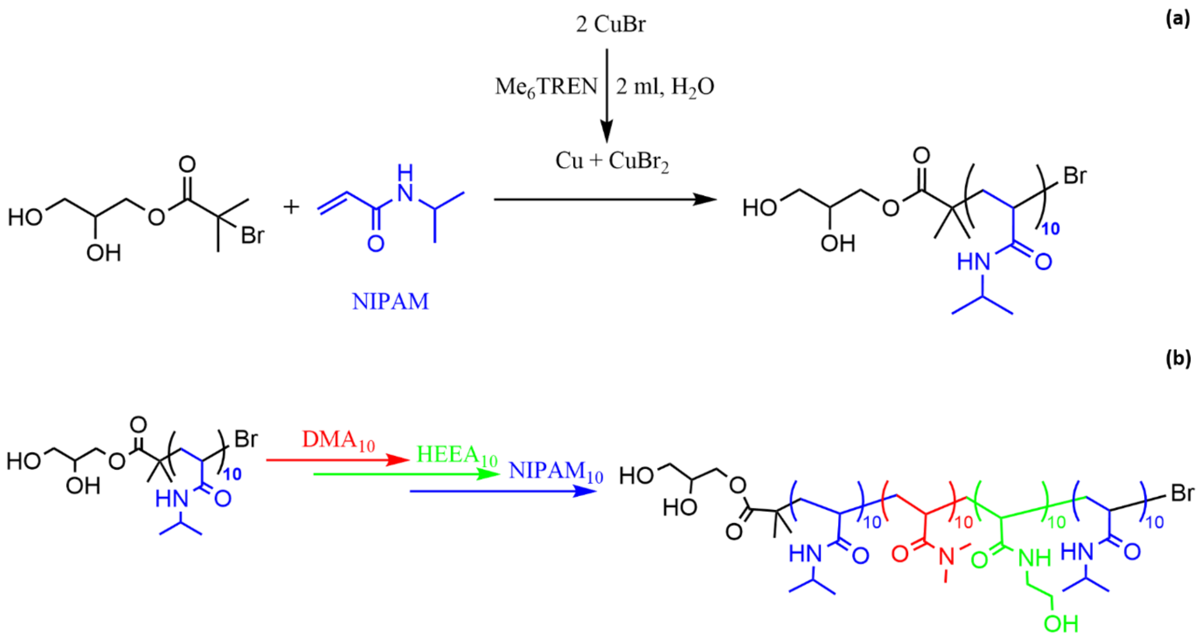

Figure 7: Synthesis of P(NIPAM)$_{10}$ polymer (a); Synthesis of P(NIPAM)$_{10}$-b-(DMA)$_{10}$-b-(HEAA)$_{10}$-b-(NIPAM)$_{10}$-b-(HEAA)$_{10}$-b-(DMA)$_{10}$ by iterative SET-LRP in H_2O (b). Abbreviations: N-Isopropylacrylamide (NIPAM), 2- Hydroxyethyl acrylamide (HEAA), N,N-Dimethyl acrylamide (DMA), N,N-Diethylacrylamide (DEA) and 4- acryloylmorpholine (NAM). This figure is an authorised reproduction from Alsubaie *et al*.[56].

The SET-LRP is based on four main steps:

- activation of polymer or monomer chains by copper (Cu) in its uncharged state Cu(0);
- propagation, spontaneous disproportionation of Cu(I) to Cu(II);
- deactivation of propagating radicals.

Initially, the Cu(0), as an electron donor, triggers the bond cleavage of the halogenated organic compound R-X (X= Cl, Br, or I), resulting in a radical $R^{\cdot}$, the halide anion X^- and the Cu(I) complex stabilised with a nitrogen ligand (L)[57]. This step is summarised in equation (1).

$$R - X + Cu(0)/L \rightarrow R^{\cdot} + Cu(I)X/L \tag{1}$$

The bond cleavage can occur either in a one-step, concerted process or through the formation of a radical anion intermediate, which subsequently undergoes dissociation, depending on the structure of the initiator and halogen. These processes can be classified as either outer-sphere electron transfer (OSET) or inner-sphere electron transfer (ISET), which differ according to the coordination sphere in which the electron transfer takes place. In SET-LRP, OSET is considered the most plausible pathway, as no evidence was found for the formation of bridging species (R-X-Cu(0)) during electron transfer, which would occur in the ISET mechanism[58].

In the propagating phase, the radical $R^{\cdot}$ proceeds to react with monomer (M) to generate propagating radicals (P_n), as shown in (2). The previously generated Cu(I)X/L complex undergoes spontaneous disproportionation to Cu(0) and CuX_2/L according to (3), which is favoured by polar solvents and nitrogen-containing ligands[59]. This step is crucial in the SET-LRP process, as it controls the amount of activating and deactivating copper species that regulate the activation/deactivation balance of the polymerisation. The copper complex CuX_2/L has the role of deactivator in the polymerisation, since it reverts the propagating species $P_n^{\cdot}$ to dormant species, as shown in (4). The key principle of SET-LRP is the control of Cu(0) and Cu(II) species levels through a combination of steps that regulate the balance between activation and deactivation during polymerisation[60]. A schematic summary of the catalytic cycle mechanism involved in polymerisation is shown in Scheme 2.

$$R^{\cdot} + nM \rightarrow P_n^{\cdot} \qquad (2)$$

$$2\ Cu(I)X/L \rightleftharpoons Cu(0) + Cu(II)X_2/L + L \qquad (3)$$

$$P_n^{\cdot} + Cu(II)X2/L \ \rightarrow P_n - X + Cu(I)X/L \qquad (4)$$

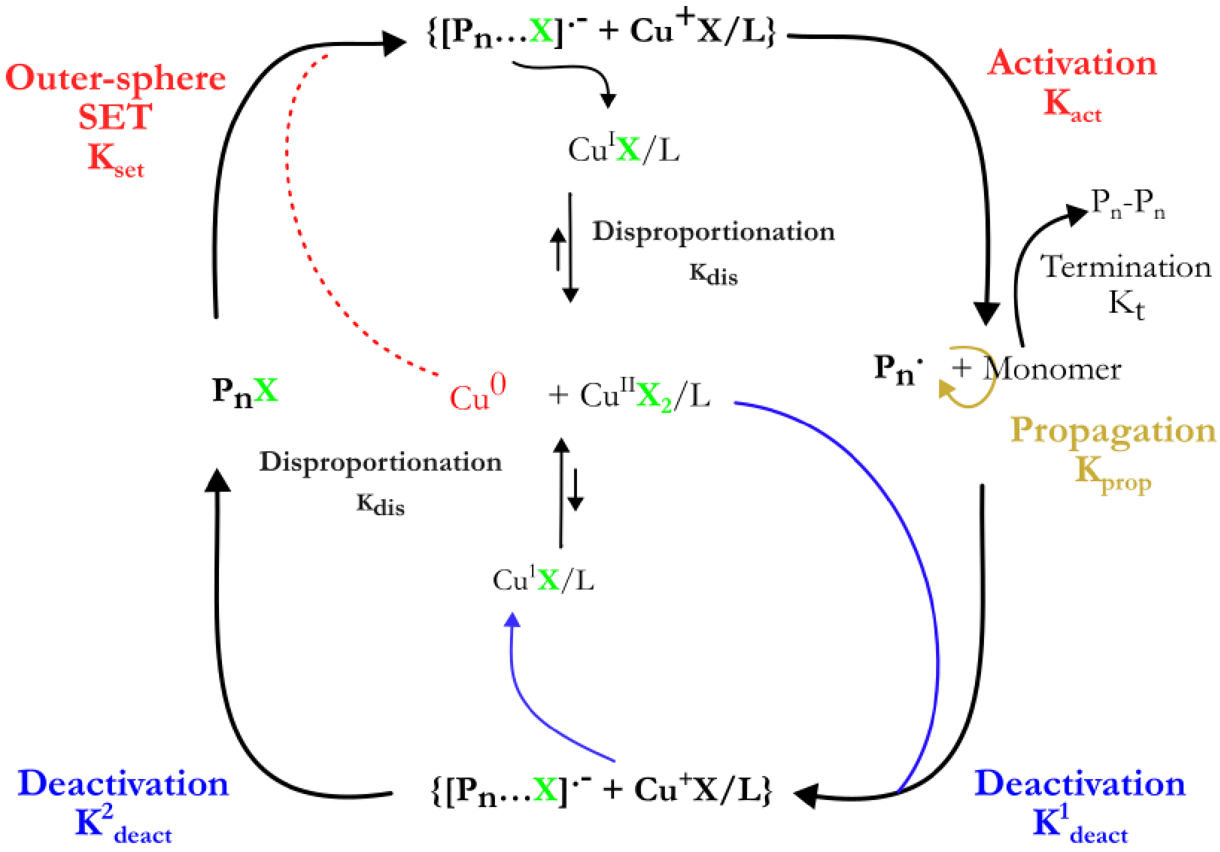

Scheme 2: The catalytic process of the SET-LRP mechanism. Adapted from Guliashvili and Persec[61].

The successful disproportionation of CuX/L is crucial for generating activating and deactivating species. If this is not achieved, there will be insufficient deactivating species to balance out the reaction and the polymerisation will no longer be controlled[62,63]. The system would, therefore, generate an increasing amount of deactivating species via irreversible bimolecular termination, resulting in the loss of end-of-chain functionalization and inactivation. This phenomenon has a direct impact on the molecular weight and polydispersity index of the resultant polymer.

The coordination profiles of each form of copper differ according to the polarity and solvation of the solvent. For instance, the disproportionality constant is relatively high in water, methanol, ethanol and acetone[64]. Whereas in organic solvents where the Cu(I) form is more stable, these constants decrease systematically with the solvent dielectric constant (ε). In general, dimethylsulfoxide (DMSO) is usually chosen as the polar solvent for this reaction. This selection is justified by the high polarity of DMSO, the ease of electron transfer, the excellent solubility of organic molecules and the coordination/stabilisation properties of Cu(II) species[65]. Binary mixtures of water and organic solvents have also been reported to be effective in expanding the range of usable solvents[66].

The presence of certain nitrogen compounds has been shown in the literature to promote disproportionation by their ability to form more stable complexes with CuX_2 compared to CuX. As a result, their application has emerged as an effective option for performing reactions in organic media, thus expanding the range of solvents that can be used[67,68].

The most common form of copper catalyst used in SET-LRP polymerisations is in wire form, most likely owing to the numerous advantages compared to powder form (ease of reaction rate control, simplified handling and removal). However, spontaneous oxidation of Cu in the air forms a thin layer of Cu_2O which, although capable of mediating activation, occurs at a slower rate than Cu(0), thereby causing an induction period at the beginning of polymerisation. To overcome this delay, the copper wire has to be pre-treated with concentrated acids such as hydrochloric acid to dissolve the oxide layer. The research by Nguyen *et al.* showed that Cu(0) subjected to acid activation achieved comparable kinetic rate constant (kP) values to inactivated Cu(0) while eliminating the induction period and allowing precise polymerisation[69].

Several studies have been carried out to modify the surface of materials to confer specific characteristics, given the proven effectiveness of this approach in the production of artificial polymers[70–73]. Another example of the employment of SET-LRP was reported by Deng et al.[74] with the aim to graft thermosensitive polymers onto graphene oxide (GO) in order to broaden its potential applications to include thermally responsive thermoelectric devices and microfluidic switches. Their approach comprised of the covalent binding of an initiator onto the GO surface sheets, followed by an in situ grafting of poly[poly(ethylene glycol) ethyl ether methacrylate] (PPEGEEMA) via SET-LRP (Figure 8). The GO sheets retained their dissociated layers and showed significantly improved dispersibility. They also exhibited reversible self-assembly and thermoresponsive behaviour at 34 °C.

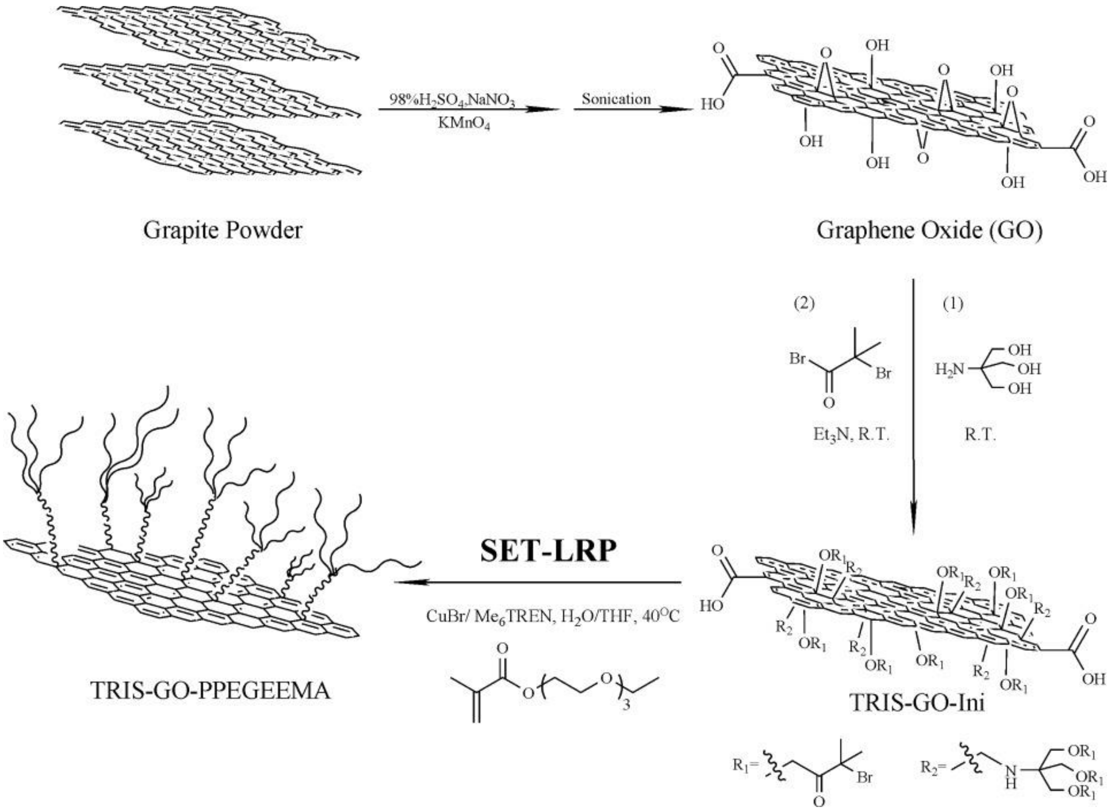

Figure 8: Surface chemical modification approach for in situ grafting of PPEGEEMA polymer chains via SET-LRP from surface modified graphene oxide sheets. Authorised reproduction of figure from Deng et al.[74]

The use of SET-LRP has also been reported in the field of polymer membrane-based separations. The work carried out by Ramesh *et al.* features a novel approach (shown in Figure 9) for improving the selectivity of polymer brush membranes in organic solvent nanofiltration[75]. A significant increase in stiffness and selectivity was achieved by using two crosslinkers: aliphatic itaconic acid and aromatic trimesic acid. This was achieved by graft polymerisation of aminoethyl methacrylate using single electron transfer living radical polymerisation (SET-LRP). The obtained membranes demonstrated superior separation performance for both hydrophilic (methanol-toluene) and hydrophobic (toluene-TIPB) organic solvent mixtures. Nanofiltration of organic solvents, possibly replacing energy-intensive distillation methods currently in use, could be a promising approach to advancing this field.

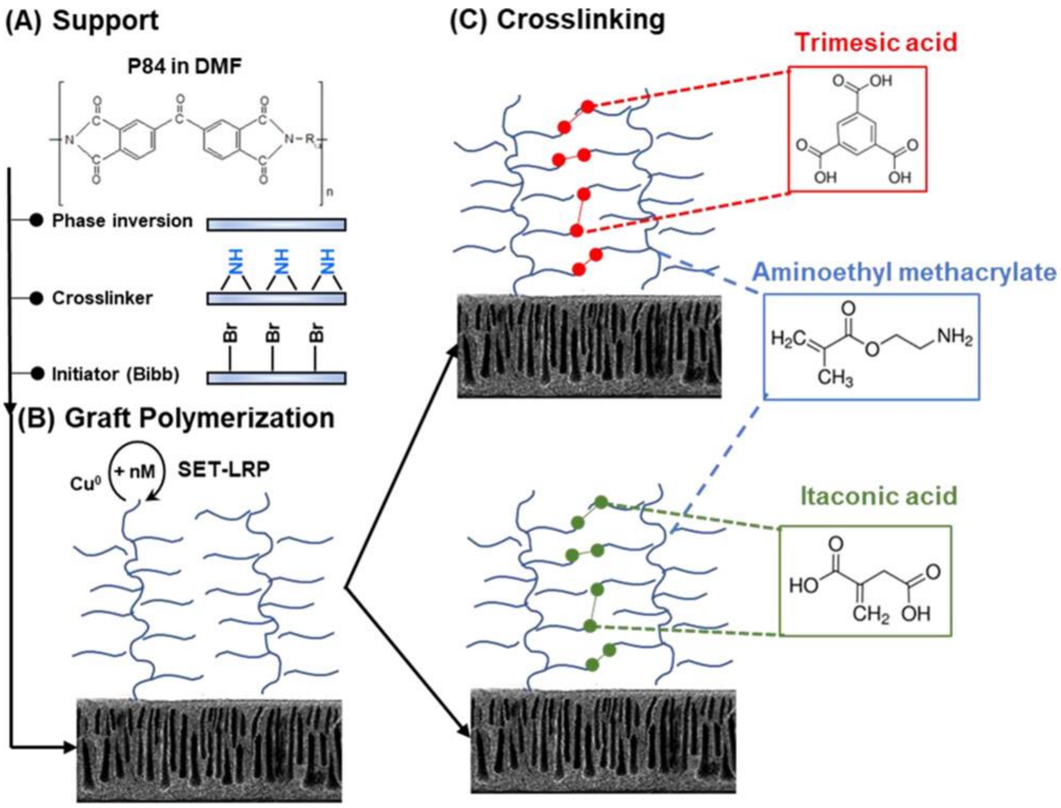

Figure 9: Schematic for synthesis of cross-linked brushes: (A) Creation of cross-linked polyimide support from P84 and initiator attachment; (B) Aminoethyl methacrylate (AEMA) modification via graft polymerization; (C) Cross-linking using trimesic acid (TA) and itaconic acid (IA). Authorised reproduction of figure from Ramesh *et al.*[75].

1.2 3D printing

The manufacturing industry in Germany, as in any other industrialized country seeking to expand its industrial production, is a key sector in its contribution to total economic output. The development and large-scale production of a new product to answer a specific need must go through a stage of manufacturing. Injection moulding (IM) and 3D printing (also known as Additive Manufacturing (AM)) are two of the main techniques at the heart of modern manufacturing. IM is a widely used process in the industrial sector. The molten material is injected into a pre-designed mould cavity, where it cools and solidifies to form the desired shape. In contrast, 3D printing represents more recent and innovative technology which attracted a rapidly growing interest in academia and public interest during the last decade[76,77]. It involves the layer-by-layer material deposit in a specific design to produce the desired object. A summarised comparison of each approach's pros and cons is presented in Table 1[78].

Table 1 Comparison between injection moulding and additive manufacturing: advantages and disadvantages

	Injection moulding (IM)	**3D printing (or AM)**
Complexity and Customization	More suitable to produce large-scale consistent, intricate components. Expenses related to tooling restrict modifications to design and bespoke adjustments	A high degree of customisation and well-suited for prototyping and low-volume production of complex designs
Speed and Volume	Fast and more effective for large production	Slow especially for large volumes
Materials	Reduced choice	Wider choice
Surface finish and quality	Smoother, polished surfaces with higher precision	Rough, and possible visible layer lines affecting strength; needs additional step of polishing

1.2.1 Fused deposition modeling (FDM)

3D printing covers a range of techniques, each involving distinct methodologies and materials. The main techniques involve Fused Deposition Modeling (FDM), whereby the plastic is melted and extruded in a specific pattern. Another method, Selective Laser Sintering (SLS), involves using a laser to combine powdered material, whereas Stereolithography (SLA) uses laser curing of resin[79]. *The focus will be placed on FDM and gel-printing (also known as bioprinting or Direct Ink Writing) in this project*.

The FDM involves printing using a thermoplastic filament as the starting material through a heated nozzle and deposited, layer by layer, onto a heated bed along a predetermined path. The setup of FDM is shown in Figure 10. Using modelling software such as Trinkercad or Fusion360, the first step is to build an object through a computer model. This enables the design in a virtual 3D space and defines the shape and size, and generates an STL file. To be used by the 3D printer, the code needs to be converted using a slicer software program, which splits it into commands with horizontal layers and allows the setting of different printing parameters for each material and print, such as layer height, print speed, temperature, and infill. The resulting file, known as a G-code, is ready to use on a 3D printer.

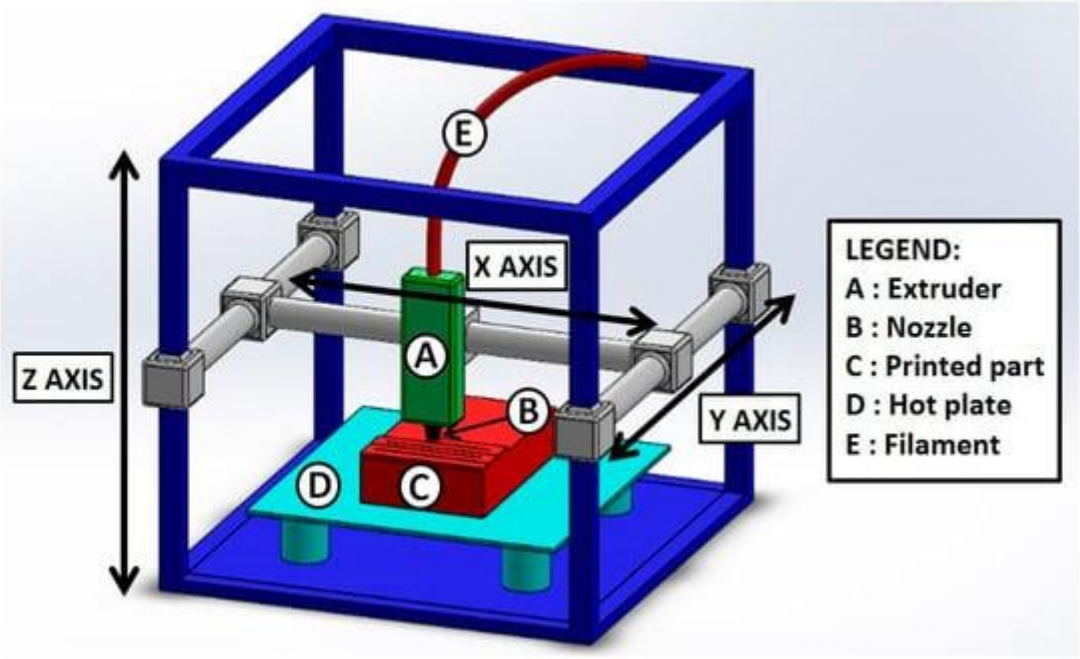

Figure 10: Schematic representation of a typical fused deposition modeling (FDM) setup illustrated by Mazzanti *et al.*[80].

There are many starting materials which can be used, which mostly are thermoplastics, i.e., capable of being deformed at a certain temperature. The most commonly used materials include those listed below:

- **Polylactic Acid (PLA):** most common printing material. Easy to print, low warping, biodegradable, odourless and printable at relatively low temperatures. However, it can be brittle.
- **Acrylonitrile Butadiene Styrene (ABS):** durable and heat resistant. But while 3D printing, may emit fumes, requiring a specific setup for safety reasons.
- **Thermoplastic Polyurethane (TPU):** Elastic and flexible. Special settings are required, which complicates the printing process.

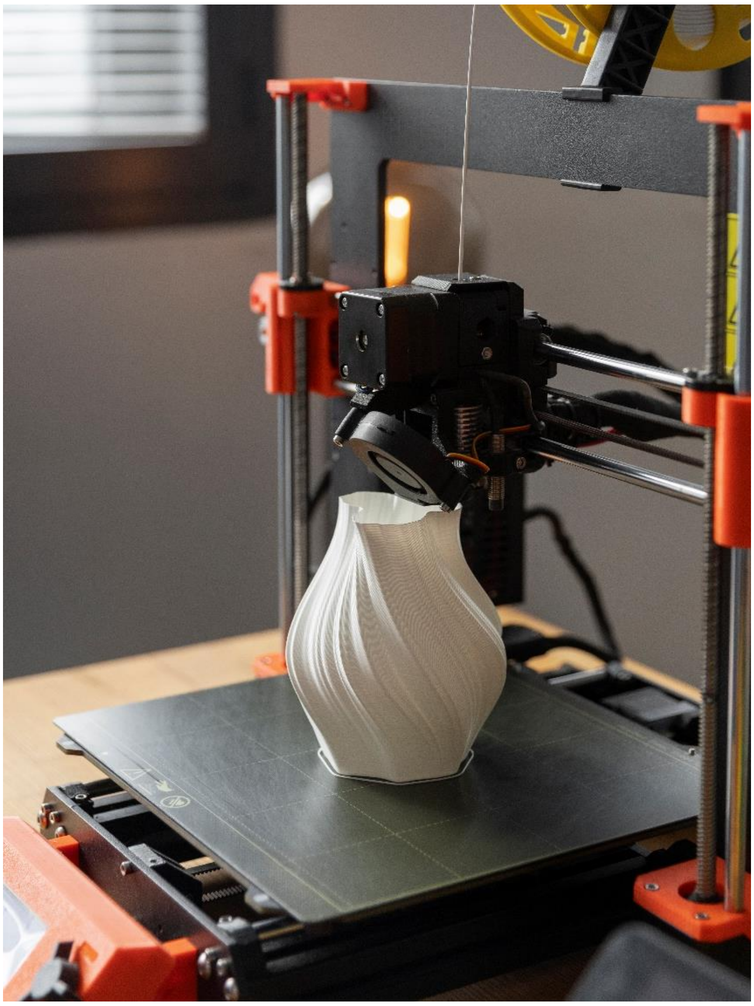

Figure 11: Photo of an object that has been 3D printed using FDM.

1.2.2 Semi-crystalline polymer (HDPE) as 3D printing feedstock

In response to environmental challenges, scientists worldwide seek out solutions to tackle the problem of plastic pollution and recyclability. Global demand has resulted in approximately 390 million tonnes of plastic produced by 2021. The major plastics used include polystyrene (PS), low-density polyethylene (LDPE), high-density polyethylene (HDPE) and polyethylene terephthalate (PET). The HDPE's chemical structure consists of long chains of ethylene monomer units with a high degree of crystallinity, creating a densely packed and linear macromolecular assembly. Some of its properties are high tensile strength, chemical resistance, and resistance to environmental conditions, which makes it suitable for packaging applications[81,82]. However, the inadequate waste management worldwide leads to approximately nine billion tonnes of plastic ending in the environment annually, of which 22 % is HDPE waste even though it being relatively recyclable[83]. Yet, their use in 3D printing still raises challenges, such as shrinkage, voiding, warpage, and poor adhesion to build plates due to their semi-crystalline properties, which complicates their large-scale deployment[84]. The manufacturers state that there is no reliable printing method when advertising HDPE 3D printing filament[85]. Consequently, researchers have been working on developing composites from these materials to enhance their performance and efficiency[86–88]. Mora *et al.* reported that the incorporation of carbon nanotubes (CNT) in the HDPE formulation provides considerable improvements in the printing process while also increasing the final mechanical properties[89]. It can be noted that the mechanical properties of the composite can be improved by adding a reinforcing agent for the reduction of undesired and unwanted effects (shrinkage, warpage). These modifications lead to better object printability and shape fidelity as already reported elsewhere[90,91].

1.2.3 Extrusion methods used for polymers

The extrusion of polymers is a fundamental process in material engineering allowing the production of composites, obtained through the melting of thermoplastic polymers, with the addition of additives. Having selected the compatible elements to be blended to obtain the desired product, it is essential to select the appropriate process to ensure a correct homogenisation[92]. More specifically, in the case of polymers, this refers to materials made from thermoplastic polymer, which is a type of polymer that can undergo reversible physical changes with temperature variations. These materials have distinctive temperature phases: glass transition temperature (T_g), melting temperature (T_m) and degradation temperature. The T_g is the temperature at which the thermoplastic material changes from a rigid, brittle state to a more flexible, rubber-like state. The T_m is the temperature at which the polymer undergoes a phase change from a solid to a molten, viscous state. Finally, the degradation temperature is the temperature at which the polymer begins to chemically degrade, resulting in an irreversible loss of structural and mechanical properties. The extrusion process involves the rise of the temperature of the materials above the T_m (and below the degradation temperature) and using a screw mechanism for thorough mixing, resulting in a composite with a homogeneous composition[93].

The success of achieving a successful compound/composite depends mainly on the characteristics of the individual components (working temperature range) and their mutual compatibility. When this is the case, the resulting product should be homogeneous in appearance, with no visible defects or aggregates. Both components, the thermoplastic matrix and the filler should not degrade at the extrusion working temperature. The composite's mechanical properties can be different depending on the filler's size, shape, dispersion, interaction/adhesion with the matrix and the inherent properties of the matrix[94–96]. Since the application of extruding in our case is to produce a novel composite filament for 3D printing, the material was extruded onto a conveyor belt which is set at a certain speed. The resulting material is a form of filaments with a precise diameter.

1.2.4 3D gel-printing

Additive manufacturing (AM) technology used in the field of tissue engineering and regenerative medicine is a valuable tool for producing unique tissue/organ-like structures for transplantation[97]. 3D printing of gel-based structures is commonly referred to as 3D bioprinting, Direct Ink Writing (DIW) or 3D gel-printing. Bioprinting is a term defined when 3D printing involves the use of living cells, bioactive molecules, biomaterials, cellular aggregates or hybrid cell-material to produce complex biologically engineered devices[98]. Extrusion-based gel-printing is a commonly used method that works similarly to FDM, but instead of using molten materials, the gel material is extruded under a constant strain. Different types of extrusion-based systems exist, and are illustrated in Scheme 3 and are listed below:

- **Pneumatic**. The gel is displaced by the action of increasing air pressure flowing through the syringe.
- **Piston-driven**. The gel is pushed out by a mechanically driven piston.
- **Screw-driven systems.** A higher shear system for pushing the gel is usually used for thicker gels.

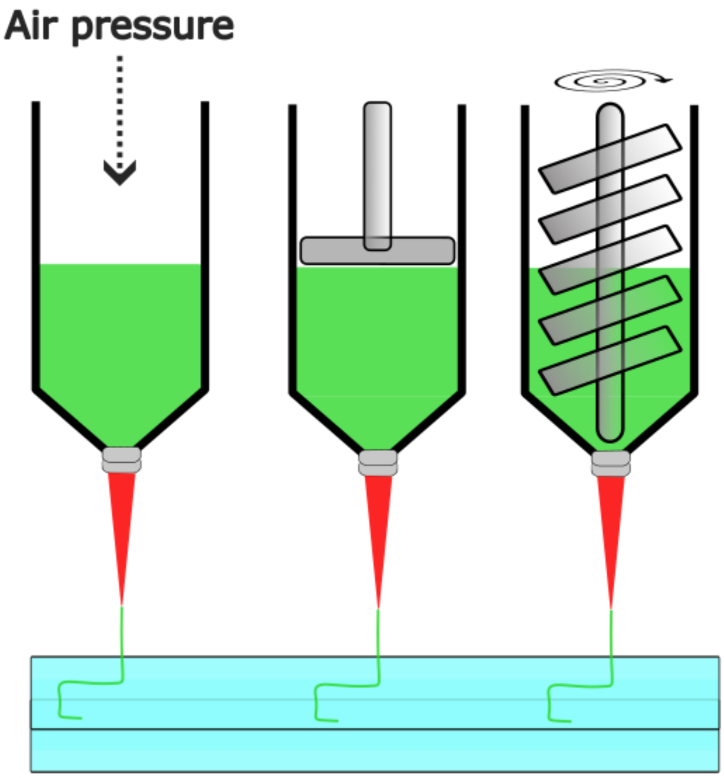

Scheme 3: Schematic representation of the extrusion printing techniques; pneumatic (on the left), piston (in the middle) and extrusion (on the right).

For accurate deposition of a variety of inks (a term referring to the gels suited for printing), it is important that these gels can be easily and evenly extruded to produce uniform layers and therefore objects. Printers often contain additional features such as multiple print heads, cooling and heating systems, and light sources to control cross-linking, i.e. gelation[99]. In some instances, if the ink is excessively viscous, an additional dilution and mixing step is required to ensure uniform and accurate extrusion. Xu *et al.* reported the preparation of a biodegradable hydrogel that is highly elastic and can be activated by visible light. This hydrogel has great potential for simplifying cell printing. It demonstrated its compatibility with native tissue properties, its ability to promote cell growth, and its support of complex patterns[100].

The degree of conformity between the printed pattern and the 3D model is referred to as shape fidelity. This is largely dependent on the selected ink, its concentration and the formation of stable shapes after printing, as well as the parameters of the printer such as the printing speed and the nozzle size[101,102]. Hydrogels like alginate, agarose, collagen, and other biopolymers are commonly chosen as inks for their similarity to the native tissue structure and, therefore, their biological compatibility. Conversely, their mechanical properties are typically weaker[103,104]. The employment of synthetic materials, including polyethylene glycol (PEG), has therefore attracted considerable interest[105]. However, despite their versatile mechanical properties, some might not be biocompatible. The incorporation of bioactive substances into composites and their modification with functional groups to improve cross-linking during extrusion can provide an alternative.

Frequently employed in the manufacture of biological components, the need for cell survival during the printing process necessitates specific properties[106]. Blaeser *et al*. report on a microvalve-based bioprinting system capable of producing high-resolution, multi-material 3D structures and highlight the importance of controlled shear stress in maintaining a balance between resolution and stem cell integrity[107]. The method allowed the precise control of shear stress at the nozzle site through a simple fluid dynamic model. The key factors influencing shear stress and cell outcome were also identified (print pressure, hydrogel viscosity, nozzle size). Given these factors, there is a clear gap in terms of further research in this area, and it has not yet been implemented on a large scale. The development of suitable inks that meet the demands for high fidelity, good mechanical properties and biocompatibility is therefore a priority. An example of high-definition printing achieved with gels of Kevlar nanofibres is shown in the Figure 12, together with excellent structure retention after drying[108].

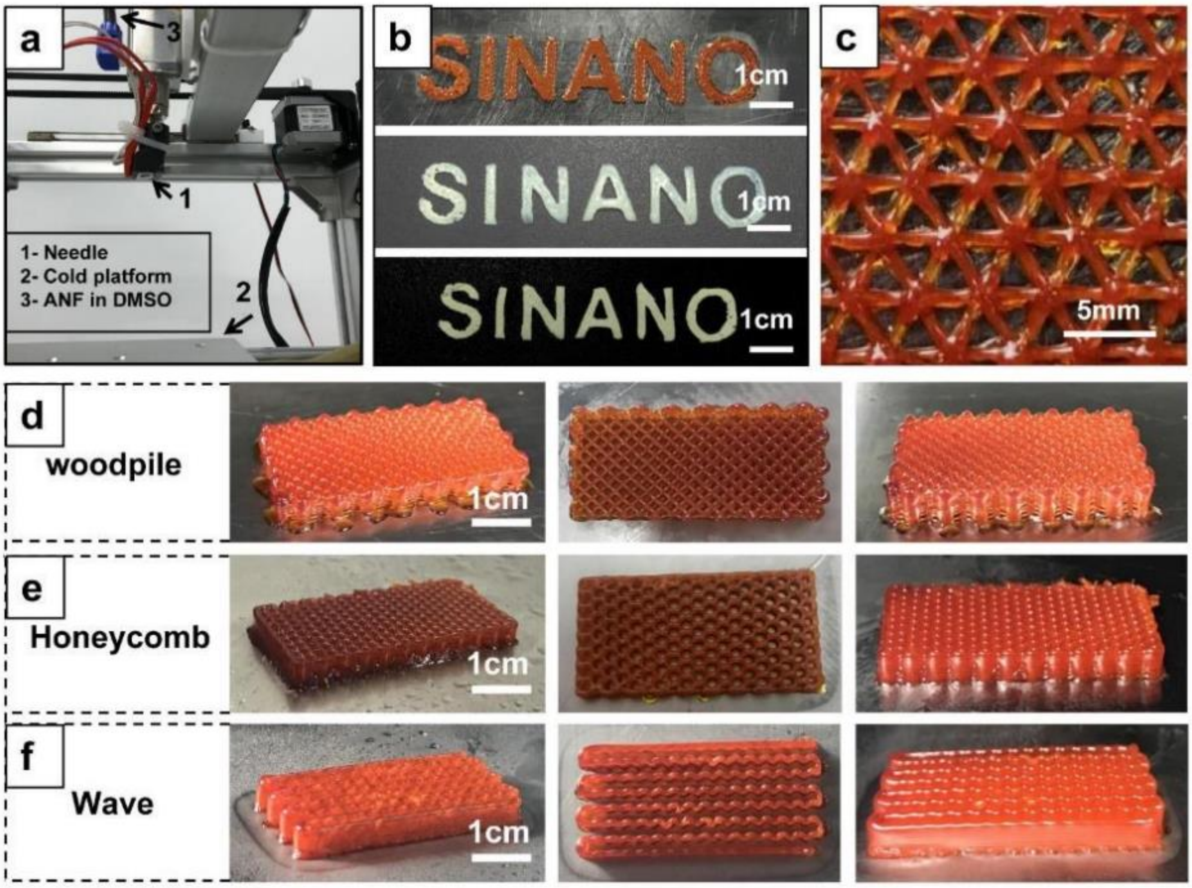

Figure 12: 3D gel-printing of Kevlar nanofibers gels. Setup for 3D printing (a); 3D printed Kevlar cryogel letters (top) and corresponding hydrogels after solvent exchange with water (middle) and aerogels after supercritical CO2 drying (bottom); The 3D printed Kevlar cryogel has a cellular structure with patterns of triangles (c), wood piles (d), honeycombs (e) and waves (f). Authorised reproduction of a figure from Cheng et al.[108].

Injectability is the ability of a material to be reliably extruded without its liquid and solid components separating[109]. It is commonly encountered in tissue engineering for non-invasive delivery of drugs or molecules[110]. Bioprinting must be smoothly blended with cells after preparation, not agglomerate and sediment in the syringe, and be pushed through a nozzle without compromising cell viability. After being deposited, they must quickly cure to support layers, maintain porosity, and resist gravitational collapse[111,112]. These mechanical aspects distinguish printable from injectable materials. The rheological measurements are generally performed to measure mechanical properties and to assess printability.

1.3 Gels

According to the IUPAC (International Union of Pure and Applied Chemistry) definition, gels are three-dimensional, non-liquid colloidal or polymeric networks expanded throughout their volume by a fluid[113]. Gels can also be described as a soft, colloidal, semi-solid material that consists of a solid cross-linked network tapping a liquid. They exhibit solid-like properties on the analytical timescale due to capillary forces and surface tension restricting bulk flow, while allowing molecular-scale fluid mobility within the structure[114]. The nature of the swelling fluid determines the name of the material: for instance, in a hydrogel, the swelling agent is water, organogel is solvents or oils, and aerogel refers to the network once all the swelling agents have been removed[115]. Hydrogels have long been of interest to researchers owing to their properties, which are both unique and their similarity to physiological mediums (extracellular medium). Hydrogels were investigated as early as the early 20th century, and their application has expanded rapidly to include personal care products, ophthalmology, drug delivery, biosensors, tissue engineering and regenerative medicine[116–118]. Hydrogels can be categorised into two groups, natural, which are derived from biosubstances like collagen; alginate, or synthetic, such as polyacrylamide or polyethylene glycol. Careful consideration must be given to the polymer/solvent mix chosen as it will affect key properties such as strength, swelling and response to stimuli[119,120]. Hydrogels are grouped into two categories based on the cross-linking process involved in their preparation: physical cross-linking and chemical cross-linking. The chemical crosslinked hydrogels involve covalent bond (irreversible or reversible) formation between components, which can be through radical polymerisation, condensation and click chemistry[121,122]. The physical crosslinking, in contrast, is based on a supramolecular structure that results from aggregation and interaction of individual components through non-covalent forces such as van der Waals forces, ionic interactions or hydrogen bonding[123,124]. Chemically crosslinked materials exhibit mechanical robustness, while physically crosslinked materials are more sensitive to medium conditions, allowing the design of responsive materials (pH, solvent properties, electrical conductivities and temperature)[125,126].

1.3.1 Rheology

Rheology is the scientific study that focuses on the deformation and flow behaviour of materials, including solids and liquids, in response to applied forces or stresses[127]. The overall behaviour is the result of resistance to flow due to internal friction between molecules and particles set in motion, and it is described as viscosity. It's essential for product development in the food, pharmaceutical and petroleum industries, providing crucial insight into the interaction between ingredients, flow, and shape, as well as valuable information about the physical underlying structure[128].

A rheometer or viscometer is generally used to perform these measurements. Viscosity measurements made with a viscometer are relative and depend on the instrument used (e.g. flow cups or ball viscometers)[129]. It is performed by rotational testing, commonly with speed control, and is reported as flow or viscosity curves. For absolute viscosities, independent of the type of measurement, it is necessary to use a rheometer with specific standards and geometries, such as cone-plate, concentric cylinder or plate-plate, as shown in Scheme 4a. It is also capable of testing a broader spectrum of rheological parameters beyond viscosity.

Modern rheometers are versatile instruments that can perform shear and torsion tests using continuous rotation and rotary oscillation, as illustrated in Scheme 4a. Rotational testing can be performed in one of two modes:

- shear rate control to simulate flow-dependent processes
- shear stress control to simulate force-dependent applications

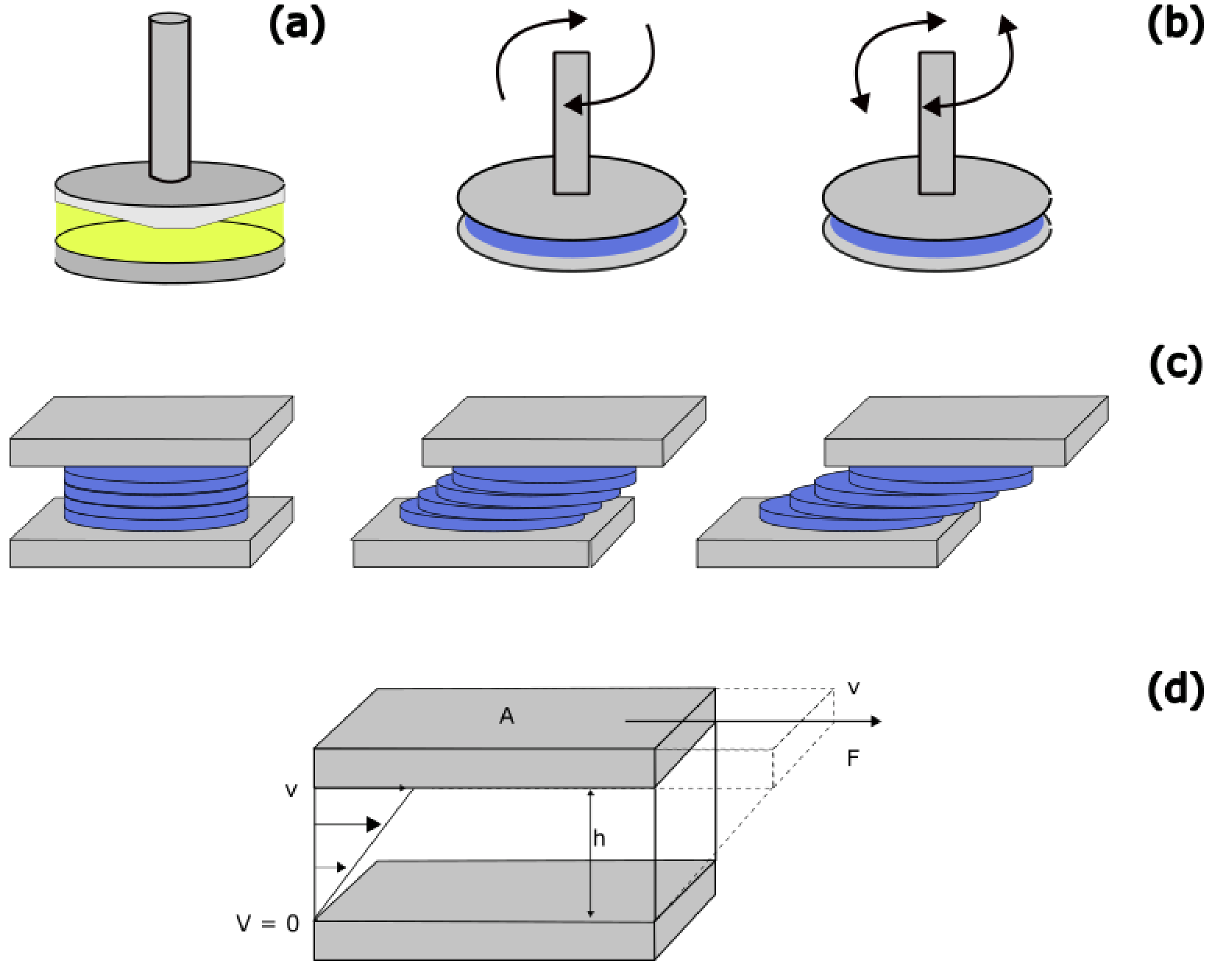

Scheme 4: a comprehensive visualization rheometer design and operation; (a) Schematic diagram of rheometer cone and plate, cone rotating while lower plate stationary; (b) Operating mechanism for rotational tests with continuous rotation (left) or rotational oscillation (right); (c) Illustration of the two-plate model used for shear tests; (d) Schematic representation of the two-plate model with key parameters for shear stress and rate calculations. These include the shear area (A), the gap width (h), the shear force (F) and the velocity (v).

The two-plate model is often used by scientists to assess strain and gel flow. In this setup, the sample is positioned between two plates. The lower one remains fixed to a support, while the upper one moves parallelly (Scheme 4c,d). The setup performs the measurement of viscosity, which is dependent on the shear applied to the gel. There are two types of shears, which are described as:

- **Shear stress τ (in Pa):** describe shear exerted on an object by an applied force (F, in N) parallel to its surface, per unit area (A, in m^2).

$$\tau = \frac{F}{A} \tag{5}$$

- **Shear rate ($\dot{\gamma}$, in s^{-1}):** describes the velocity gradient (v, in m·s^{-1}), within a material by the rate at which adjacent layers of a material move against each other, separated by a gap between the plates (h, in m).

$$\dot{\gamma} = \frac{v}{h} \tag{6}$$

Viscosity, more precisely dynamic viscosity, represented by the symbol η, is determined by dividing shear stress by shear rate following Newton's law (equation (7)). Kinetic viscosity on the other hand expresses the resistance to deformation under shear stress relative to fluid density.

$$\eta = \frac{\tau}{\dot{\gamma}} \tag{7}$$

Gases, liquids, oils, and polymer melts differ in their consistency and composition. Based on their behaviour to shear, they are classified into two main categories: Newtonian and non-Newtonian. The former obeys Newton's law (7), which states that there is a linear relationship between shear stress and viscosity. The latter, in contrast, do not exhibit a linear relationship and their properties vary as a function of the force applied under different conditions (temperature, e.g.).

Therefore, a flow curve is defined for each material and its characteristics, which is shown in Figure 13. Fluids fall into several classes, the most common are represented below:

- **Ideal flow behaviour.** Newtonian flow as described above. Some examples are water, mineral oil, silicone oil, vegetable oil and solvents.
- **Shear thinning.** Pseudoplastic, is seen in materials such as coatings and polymers, where viscosity decreases with higher shear rates. This phenomenon is directly linked to the internal structures.
- **Shear thickening.** The material's viscosity increases with higher shear rates. Common examples are ceramic suspensions, starch dispersion and dental fillings.
- **Thixotropic.** Under constant shear, the viscosity decreases over time. At high shear, the weak bonds rupture permitting an easier flow.

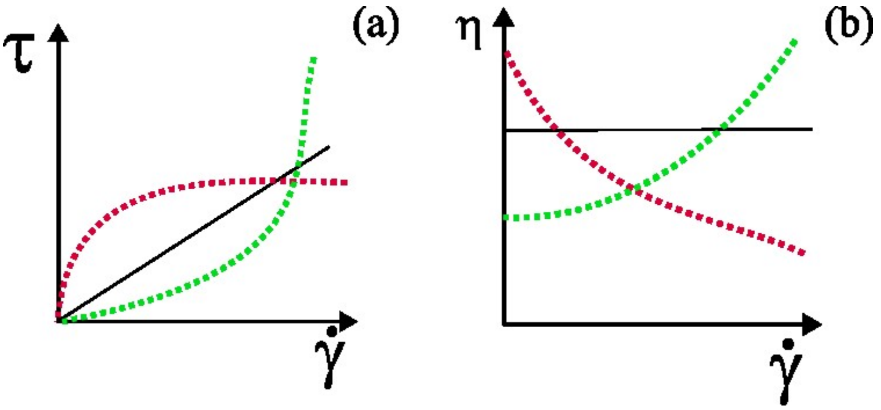

Figure 13: Flow curves (a) and viscosity curves (b) for Newtonian materials (black), shear-thinning (red), and shear-thickening (green) flow behaviour.

At low shear rates, the polymers have limited deformation due to their high viscosity, which is known as the Newtonian plateau, from which the zero-shear rate viscosity (η^0) is determined.

Materials frequently display a combination of viscous and elastic traits, known as viscoelastic behaviour[130]. The elastic portions dominate under conditions with higher deformation rates or colder temperatures. In contexts where significant elastic effects result from viscoelastic interaction, measuring viscosity alone may not be sufficient.

The study still employs the two-plate model, but collects different data (Scheme 5); however, measurements rely on other dimensions, allowing the obtention of new data, for example:

- **Shear strain γ:** refers to the ratio of deformation relative to the original dimensions, measured perpendicular to a given line. The deflection path is s (in m), and the shear gap h (in m).

$$\gamma = \frac{s}{h} \tag{8}$$

- **Shear modulus *G* (in Pa):** defined as the ratio of shear stress (force per unit area) to shear strain (edge displacement). This is a measure of the stiffness of a material and its ability to withstand the shear strain.

$$G = \frac{\tau}{\gamma} \tag{9}$$

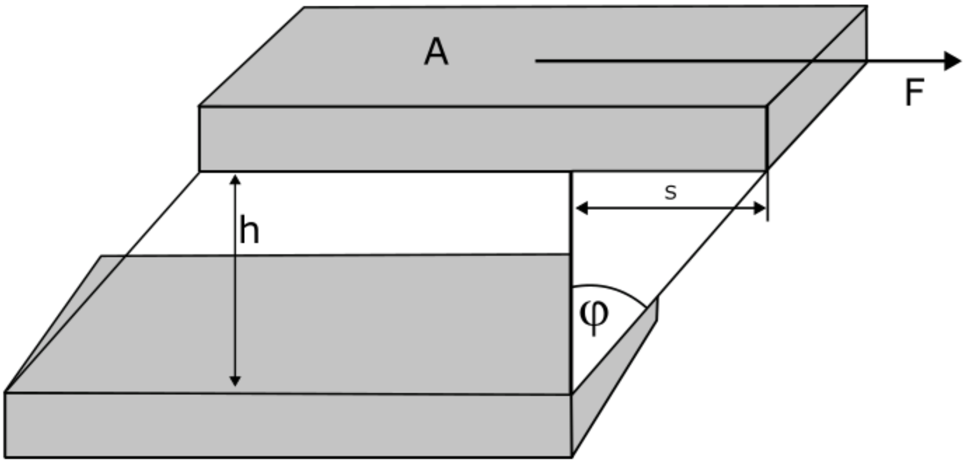

Scheme 5: Schematic representation of the two-plate model with shear area A, gap width h, shear force F, deflection path s, and deflection angle φ.

The two-plate model continues to be suitable for the understanding of oscillatory tests. As previously mentioned, the upper plate acts as the moving component and moves in parallel to the immobile plate. However here, the mobile plate moves back and forth, as shown in Scheme 4b at a constant speed, and thus, the process operates at a constant oscillating frequency. The amplitude of deflection of the upper plate is measured as shear strain or deformation γ. The measurement is then taken from the stationary plate to determine the amount of force that is required to keep it static, referred to as the shear stress τ. The data is collected from both disks and plotted against time as shown in Figure 14. Both sinusoidal curves, shear strain and shear stress, oscillate at the same frequency.

In most samples, the sine curves exhibit a time lag, called the phase shift δ, which varies between 0 ° and 90 °. Materials can be categorised based on the phase shift value:

- If $\delta = 0$ °, ideally elastic deformation behaviour. The material returns to its original shape after all stress is removed, without any permanent deformation.
- If $\delta = 90$ °, ideally viscous deformation behaviour. The material deforms continuously under shear with no resistance.
- If 90 ° $\geq \delta \geq$ 45 °, this means that the material is a liquid at rest.
- If 45 ° $\geq \delta \geq$ 0 °, this indicates a solid or gel-like state, as seen in substances like hand cream at rest.

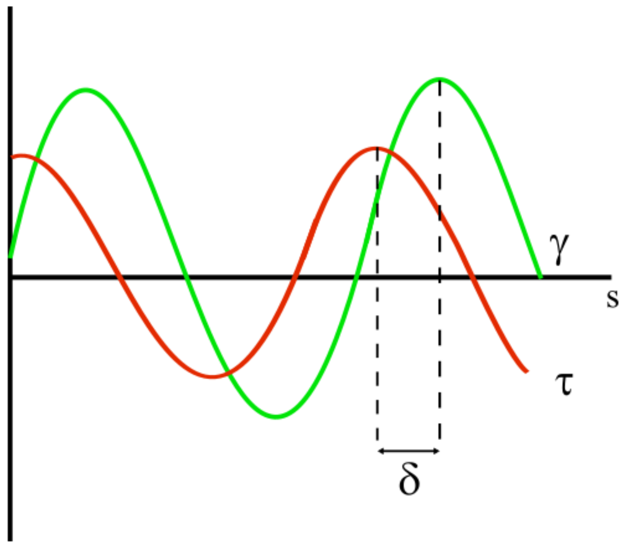

Figure 14: Example of results from an oscillatory test for viscoelastic behaviour, plotted as a sinusoidal function versus time: shear strain γ and shear stress τ. The two curves are offset by the phase shift δ.

The ratio of shear stress (τ) to shear strain (γ) is defined as the complex shear modulus G^*. It is a measure of the overall viscoelastic behaviour of a specimen. Moreover, G^* is composed of two components, which are the storage modulus and the loss modulus, both expressed in pascals (Pa). Its definition in brief:

- G'' corresponds to the liquid-like, viscous behaviour of the visco-elastic sample. This property results from internal friction and is associated with frictional heat generation, i.e., the conversion of deformation energy into heat. This energy is considered lost and not available for motion and is referred to as energy dissipation.
- G' corresponds to the elastic behaviour of the sample, which allows the return to its original shape after deformation. The energy is stored within the stretched material by expanding its inner structure with no degradation. Once the stress is released, the unutilised stored energy becomes the driving force to reshape the material back to its original shape.

When G' is higher than G'', it indicates stronger internal links like chemical bonds, while when higher G'' suggests weaker molecular bonds. This distinction categorizes materials by viscoelastic properties, providing insights into their behaviour under stress.

1.3.2 Rheological assessment of gel printability

Various methods, both qualitative and quantitative, have been explored by researchers to assess the printability of gels[131]. This includes printing multi-layered structures to evaluate encapsulation porosity and employing rheological analysis to quantify extrusion forces, their impact on cell viability, and post-extrusion behaviour. Despite the existence of some standard tests, a challenge lies in the absence of standardized experimental parameters. Some researchers have sought to address this by developing mathematical models considering rheological factors and shape complexity[132]. Two common methods for evaluating a sample's mechanical properties involve unidirectional rotation and low-amplitude oscillation. The following tests are typically conducted on gels to confirm their printability and the corresponding graphs are shown in Figure 15. Here’s a brief description of each:

- **Shear rate sweep**: It studies the flow properties of non-Newtonian materials and simulates the extrusion stress applied to the ink. During the test, the shear rate is progressively increased, generally by several orders of magnitude and the shear stress is recorded. Apparent viscosity is then computed. An ink that undergoes shear thinning (viscosity reduction under applied stress) is essential for extrusion bioprinting.
- **Shear stress sweep:** this is one of the methods used for the determination of yield stress of a non-Newtonian fluid. Yield stress is defined by the shear stress that needs to be applied that can disrupt the chains sufficiently that the material starts to flow and, thus, extruded[133]. This differs from the shear rate sweep in that it focuses on increasing shear stress while monitoring strain and strain rate and subsequently computing viscosity. The increase in shear stress can be adapted to suit the desired application[134]. Understanding the yield stress of a gel-ink is critical in bioprinting as it estimates the extrusion pressure required.
- **Frequency sweeps:** This testing is used to distinguish between viscoelastic liquid and solid-like gel ink behaviour. The process involves maintaining a constant strain value, well within the gel's linear viscoelastic region, as the frequency is gradually ramped up. Gel-like behaviour displays the dominance of G' over G'', while viscoelastic liquids reveal the opposite. The modulus of viscoelastic liquids exhibits an increase with frequency, while gel-like materials are less responsive to changes in frequency.

- **Thixotropy test (changing shear rates):** This evaluation assesses the time-dependent properties, specifically viscosity, through three stages: low, high, and then returning to the original shear rate. The viscosity is monitored continuously, as well as the time required to recover initial viscosity. In gel printing, this trial is critical to evaluate the material's recovery to initial viscosity for stable filament formation and multi-layered patterning.
- **Oscillating stress sweep**. This is another method of measuring the yield stress, but through the measurement of the shear storage modulus (G') and the loss modulus (G''). Viscoelastic behaviour is studied by measuring G' and G'' under increasing oscillatory stress. The first region where the modulus is independent of stress is defined as the linear viscoelastic region (LVR). Next, there occurs a crossover point between G' and G'', where G'' begins to dominate and indicates the oscillatory strain beyond which the material flows, hence the yield point.
- **Rotational temperature sweep.** In the setting of inks with temperature-responsive components, the viscosity is often characterised as a function of increasing (or decreasing) temperature. Such profiles establish the optimum temperature range for extrusion under suitable pressure conditions to ensure shape fidelity.

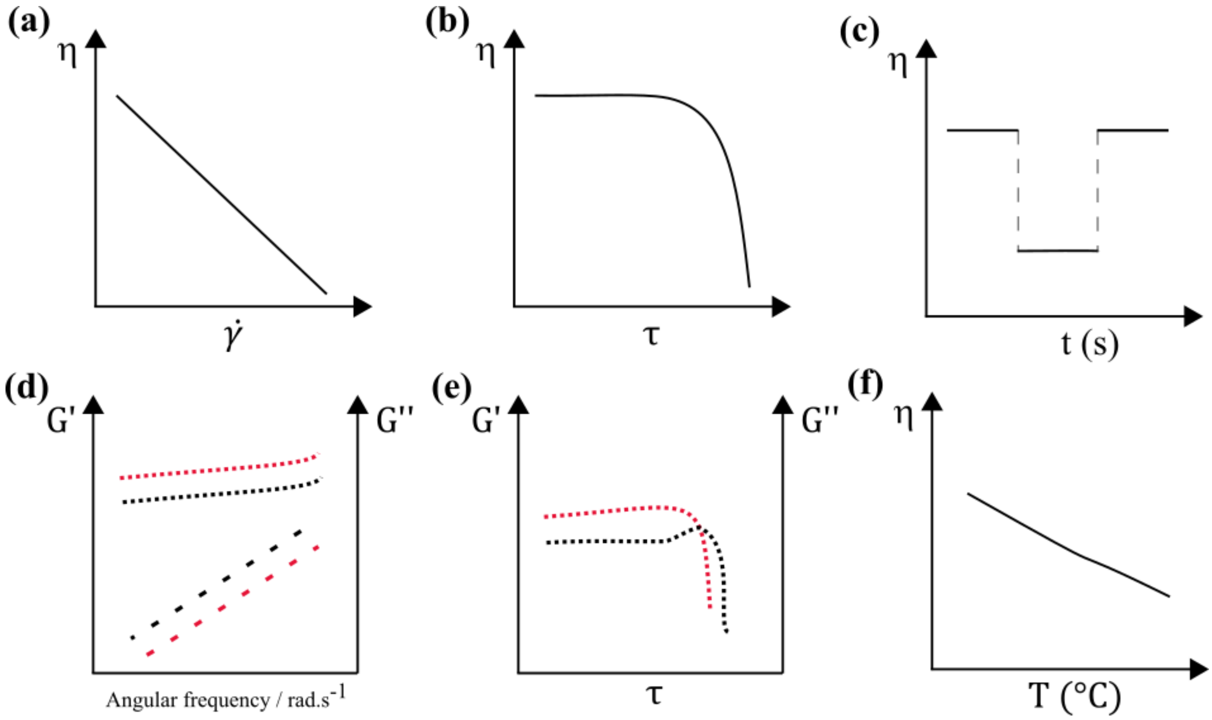

Figure 15: Conventional rheological methods used to characterise gel-inks include*:* (a) shear rate sweep; (b) stress ramp; (c) viscosity thixotropy assessment; (d) frequency scanning of different materials, distinguishing between solid gels (shown by the narrower dotted line) and viscoelastic liquids (shown by the wider dotted line); (e) oscillating stress ramp (amplitude sweep); and (f) rotational temperature sweep.

Once the mechanical properties of a ink have been measured and approved, a series of trial prints are produced to assess suitability. Typically, researchers evaluate fidelity by creating a model with known attributes, such as a grid or spaced layers[135]. This is shown in Scheme 6, which illustrates the gel aspect as well as the gelling degree effect. For optimum results, the ideal ink has a continuous flow through the nozzle that ceases when the pressure is released. For weaker gels, thicker printed fibres tend to result from longer relaxation times of the polymer chains, which can lead to fusing and reduced shape accuracy. If the physical properties of the gel exceed the ideal range for gel ink, the ink becomes more difficult to flow as it exits the nozzle and may gel prematurely, resulting in an unsatisfactory product. The purpose of this is to prevent fusing, sagging and inadvertent pore filling.

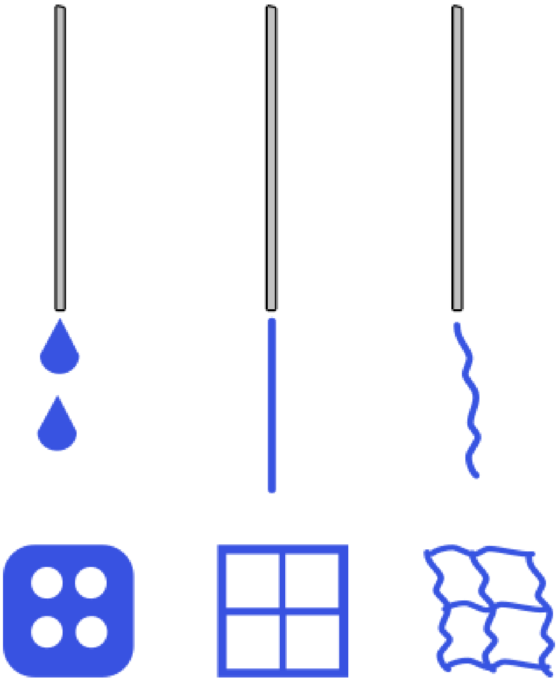

Scheme 6: Schematic representation of the effect of gel-ink's degree of gelation on the printed results. From left to right, under-gelation, ideal gel-ink, over-gelation.

1.3.3 Procedures for gel drying

The structural integrity of a gel may be affected by the liquids in which it is immersed, which can be seen by their swelling in different solvents. This maintenance depends on several factors such as concentration, intrinsic properties, porosity and so on[136]. Aerogels are a class of lightweight, porous materials derived from gels in which gas replaces the liquid component in a process[137,138]. Removing the liquid phase from the gel while preserving the established nanoporous structure, and consequently preventing any shrinkage or rupture of the dried gel, presents a significant challenge in the process. Three main drying techniques are distinguished in Figure 16 :

- Atmospheric drying, the easiest and most accessible method, is generally unsuccessful in maintaining the gel structure and causes massive shrinkage. The quick evaporation of the liquid by capillary action leads to a concentration gradient that disturbs the nanostructures. The shrinkage, osmotic changes and surface tension forces (up to 100-200 MPa) contribute to gel collapse[139–141]. The collapse of the gel is therefore dependent on the cohesive forces of the particles, the composition, the stabilisers and the drying conditions[142].

- Unlike most conventional methods involving heat for evaporation, freeze-drying works by immersing the gel in liquid nitrogen, which instantly freezes the structure, and then sublimates the solvent under high pressure. It allows precise control of the development of the solid structure through the formation of the crystal structure[143,144]. The resulting product is typically classified as a 'cryogel'. Nevertheless, due to the volume expansion of the liquid upon freezing, the gel is subjected to stresses which can cause it to shatter into tiny particles, resulting in a powder which makes it difficult to achieve a whole solid structure[145,146].
- Supercritical drying uses substances such as supercritical fluids, with supercritical CO_2 ($scCO_2$) being the most widely used due to its mild condition. This process preserves the porous structure of the aerogel by exploiting the liquid-gas transition beyond the critical point. It is achieved by heating and pressurizing to the critical point of the solvent, followed by its full replacement in the gel pores with the original solvent, followed by an isothermal de-pressurisation and phase change. This process results in high porosity and excellent structural properties of the gel by removing the surface tension within the pores[147–149]. It does, however, require a considerable amount of processing time, specialised equipment and safety precautions.

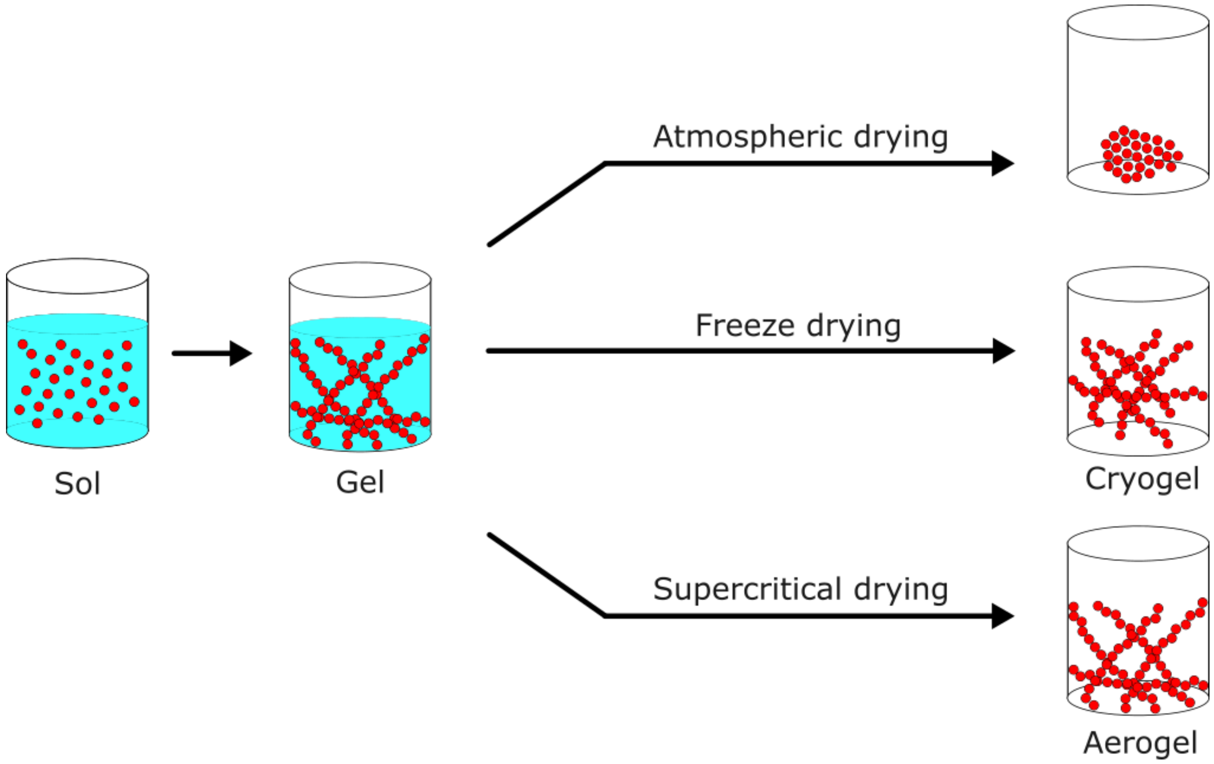

Figure 16: Procedures used to dry gels for gel drying.

The resulting aerogels are rigid, strong and highly porous materials, distinguished by the presence of a three-dimensional network. The material possesses a considerably high porosity due to air-containing pockets occupying the majority of the internal volume. As a result, their density is very low, making them super-light[150,151]. Despite this, their mechanical properties and load-bearing capacity can be remarkable depending on the chemistry, bond strength and solid content concentration. Meador *et al*. have successfully produced aerogels from polyimide cross-linked with aromatic triamine, resulting in materials with a high modulus of elasticity and flexibility that can be rolled and folded back to their original shape. Tensile strengths of 4 to 9 MPa have been achieved, along with a high glass transition temperature which gives them excellent insulating properties[152]. Silica aerogels are particularly renowned for their mesoporous structure which allows gas conduction to be reduced, resulting in excellent thermal insulation[153,154]. Due to their high surface area and controlled pores, aerogels have the potential to act as catalyst supports, enabling efficient catalysis. Furthermore, their potential biocompatibility makes them suitable for applications in biomedicine and sensors[155–157]. An innovative approach has been presented by Wang *et al.* for supramolecular self-assembly of 3D conductive cellulose nanofibrils aerogels[158]. The approach involved the modification of CNF with carboxyl groups and the incorporation of polyaniline. The resultant aerogel was lightweight, flexible, and demonstrated good electrochemical properties. This advance holds great promise for applications in energy storage and highly sensitive sensors.

1.4 Building smart materials from supramolecular network building blocks.

1.4.1 Smart materials

Throughout history, mankind has been inspired by the remarkable adaptability of living creatures. Living organisms can alter their behaviours to improve their survival in different environments. This capacity for adaptation has inspired researchers to develop advanced materials that emulate these characteristics, by making them smarter, safer, functional, and self-sufficient. Smart materials can be defined as materials capable of executing sensing and actuation functions, analogous to those found in living systems when subjected to external stimuli[159]. The earliest reported example of a material exhibiting these properties was in 1971 when significant recoverable strain was observed in a NiTi alloy, and the phenomenon began to attract real attention for engineering applications[160,161].

The stimuli can come from physical sources, such as changes in temperature, exposure to light or the application of electrical, magnetic, or mechanical forces, or else from chemical sources, such as changes in pH or solvent exchange[162,163]. Smart gels rapidly alter their structure, either expanding or contracting when stimulated. This transition causes a switch in their properties, leading them to adopt a different configuration, which may become more or less hydrophilic, depending on the specific stimulus applied and the chemistry employed. The chemistry and distribution of the monomers in the polymer chain make synthetic polymer-based materials ideal for producing these smart materials, as the overall properties can be monitored. An example of this behaviour can be seen in thermosensitive materials such as poly(N-isopropylacrylamide) (PNIPAM), which undergoes a transition in water at around 32 °C. Below this temperature, it swells and remains hydrophilic, while above it becomes hydrophobic and aggregates[41,164].

Smart biomaterials have potential applications across various domains, including targeted drug delivery for improved therapeutic efficacy and reduced side effects[165]; scaffolding for tissue regeneration[166]; biosensors capable of detecting specific biomolecules[167]; and adaptive implants capable of responding to physiological variations[168].

1.4.2 Self-healing

Although smart materials are already remarkable, it would be desirable, from a sustainability point of view, to minimise the deterioration of the material's properties over time, when subjected to stress (generally cracking). The propagation of cracks impacts the integrity of network structures and the mechanical properties of gels limiting their shelf life. Mimicking the regenerative properties found in living organisms, the innovative smart gels with self-healing properties have been developed to restore their functionality and structure after damage[169,170]. Similar examples of these polymers, known as shape memory polymers (SMPs), are made using similar approaches. SMPs can 'remember' their initial shape and retrieve it when a stimulus is applied[171].

Self-healing materials are typically categorized based on their 'healing' conditions, as briefly described below:

- **Extrinsic:** these materials consist of a matrix filled with microcapsules or 3D hollow lattice channels containing "healing agents" (microvessels filled with substances). Upon impact, these microvessels release via damage-induced in situ polymerisation, thereby sealing the fracture[172].
- **Intrinsic:** These self-healing materials incorporate reversible bonds within their structure. In the event of damage, physical or chemical processes enable them to recover their initial configuration[173].
- **Autonomous:** these systems are capable of self-healing automatically without any external stimulus[174].
- **Non-autonomous materials:** these systems necessitates an external stimulus to trigger the 'healing' mechanism[125,175].

In the case of materials that are intrinsically self-healing, the reversible mechanisms by which they 'repair' can be divided into two main categories:

- **Physical**: Having non-covalent interactions within their polymer chains that are reversibly bound. These include hydrophobic interactions, host-guest interactions, and hydrogen bonds[176–178].

- **Chemical**: These, on the other hand, are reconstructed through the reversible covalent bonds. Different types of covalent bonds can be used, most notably boron-oxygen bonds, disulphide bonds, imine bonds, reversible radical reactions, and Diels-Alder reactions[179–181].

Among the physical bonds mentioned above, the hydrogen bonding is widespread and plays an important role in various biological processes, contributing to a variety of natural phenomena such as the formation of the secondary and tertiary structure of proteins and the pairing of DNA bases[182]. For the fracture to heal effectively, the fractured connections need to be reconnected. The chain mobility of a polymer is influenced by several factors including the degree of entanglement, molecular weight, steric hindrance, and degree of cross-linking[183,184]. These properties cause a material to become more crystalline or more amorphous, and chain mobility is characterized by glass temperature (T_g). A low T_g allows accelerated healing under mild conditions, otherwise, it must be increased artificially by external stimuli[185]. In this case, the advantages of gels over solids are that the solvent in the cross-linked network promotes the formation of a mobile phase.

1.4.3 Ureido-pyrimidinone (UPy)

The dimerization properties of ureido-pyrimidinone (UPy) hydrogen bonding were first investigated by Meijer[186]. The molecule has a high dimerisation constant ($K_{dim} = 6 \cdot 10^7$ M^{-1} in chloroform) and is known for its self-complementary physical bonding[187]. The UPy's accessibility and ease of synthesis from cheap and commercially available products make it particularly attractive.

The structure is composed of a pyrimidinone ring linked by a urea bond. The nitrogen-hydrogen-oxygen (N-H-O) unit facilitates the formation of strong, directed hydrogen bonds, four in total, between two UPy units (Scheme 7). These interactions can lead to the formation of complex and stable structures, both intra and intermolecularly.

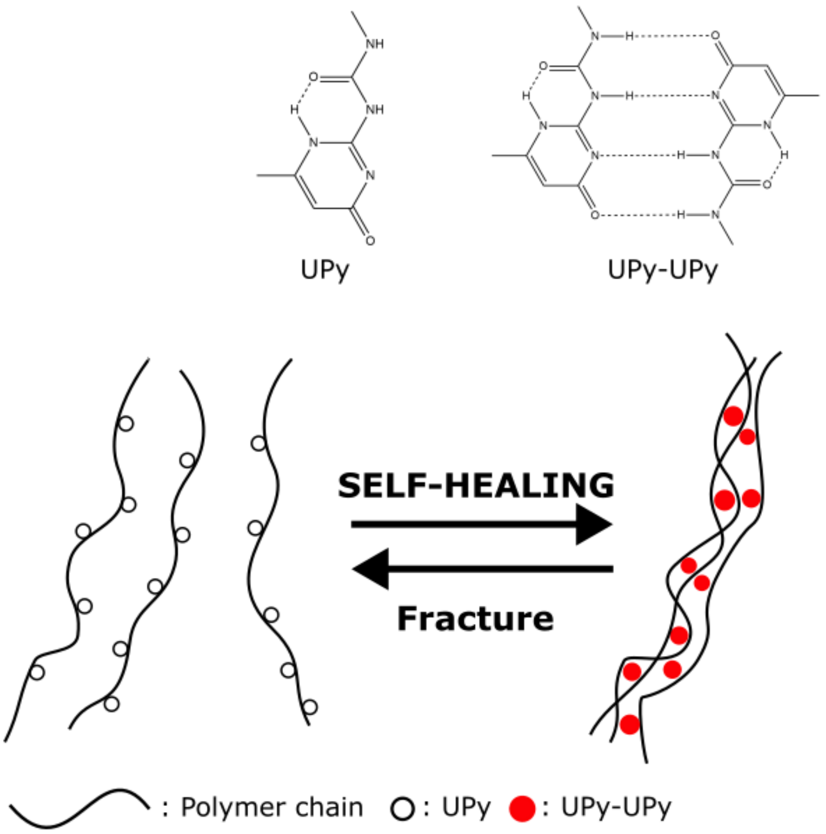

Scheme 7: *Above:* Chemical structure of UPy units and their dimerization; *Below:* Schematic presentation of the self-healing process.

UPy exhibits binding strengths between covalent and non-covalent bonds, with reported dissociation temperatures of around 60 °C[188]. These bonds can be disrupted by external stimuli such as heat, mechanical force and UV light[189]. As a result, materials incorporating these structures can reform after the stimulus removal, rendering them suitable for injection[190]. Many researchers have employed a variety of approaches to achieve self-healing under milder conditions[191–193]. Biyani *et al.*[194] reported novel UV-responsive nanocomposites with improved strength and stiffness using UPy-functionalised cellulose nanocrystals. These materials efficiently heal defects upon UV exposure, even with high filler content.

1.4.4 Fmoc-diphenylalanine (Fmoc-FF)

The peptide-based hydrogels possess both biodegradability and biofunctionality[195] and are derived from biopolymers and peptides found in nature. Silk, elastin and resilin are characterised by their elastic properties and are therefore promising for biomedical applications in hydrogels[196]. These hydrogels organise themselves into fibrillar nanostructures through mutual recognition of their precursors, forming self-supporting networks. The amino acid sequence, concentration and hydrophobic/hydrophilic balance influence their mechanical properties; therefore, careful selection plays a key role in tailoring hydrogel properties[197].

Natural peptides, encoded in DNA, can comprise up to 22 different α-amino acids, with individual side chains or residues significantly contributing to their biological functionality[198]. In biological systems, they serve as scaffolding materials on multiple scales, ranging from self-assembled actin cytoskeletons at the nanoscale to microtubules that act as nanoscopic protein railways for cellular transport[199].

Low-molecular-weight gelators (LMWGs) are compounds with molecular weights ranging from 100 $g \cdot mol^{-1}$ to 10,000 $g \cdot mol^{-1}$ which can self-assemble into fibrillar networks and trap solvents under certain conditions[200]. This is achieved by non-covalent, reversible interactions such as π-stacking, and hydrogen- or van der Waals bonding to form three-dimensional networks between subunits resulting in a gel-like structure. Once arranged in a defined sequence, they take on a specific secondary structure allowing self-assembly into nanostructures, usually in the form of nanofibers. Through physical cross-linking and entanglement, a self-supporting structure can be achieved[201]. However, the mechanical properties are usually influenced by factors such as amino acid selection, concentration, and physicochemical properties (hydrophobicity and hydrophilicity). Fluorenylmethoxycarbonyldiphenylalanine (Fmoc-FF) is an extensively researched LWMGs, owing to its excellent self-assembly, commercial availability and stability at physiological pH[202]. A proposed mechanism for the self-assembly of Fmoc-FF is shown in Figure 17.

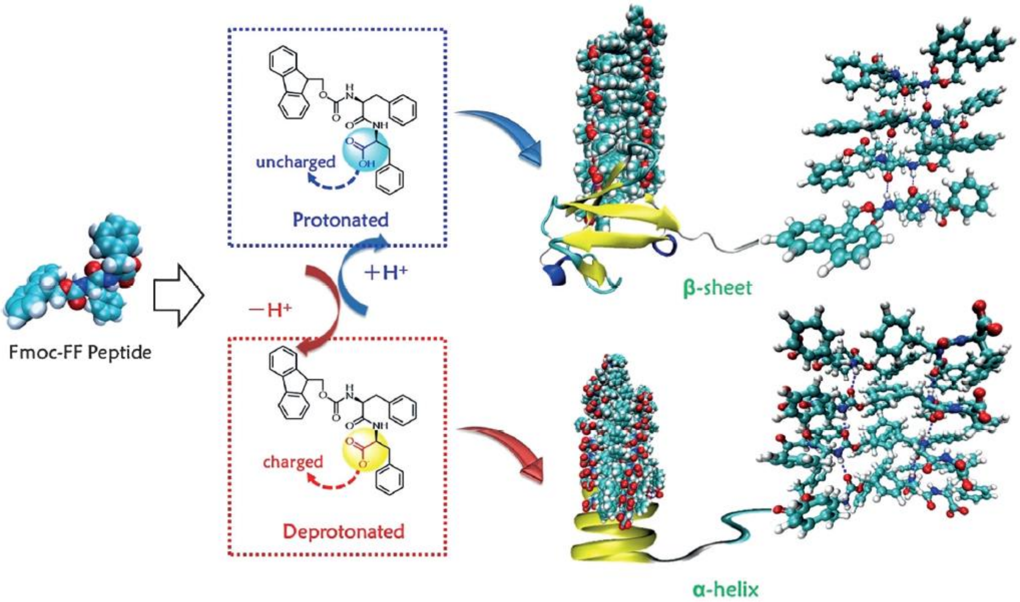

Figure 17: Proposed mechanism for the self-assembly of Fmoc-FF with β-sheet and α-helix secondary structures by Xing et al.[203].

Structurally, this peptide is made up of two phenylalanine (F) amino acids and an Fmoc function, normally required during synthesis as a protective group. All these functions are characterised by the presence of large aromatic moieties, which make the compound hydrophobic. Therefore, Fmoc-FF is quite insoluble in most solvents except DMSO, DMF or in basic aqueous conditions. Gelation occurs under specific conditions and generally by two methods, described briefly here:

- **Solvent switch**: Fmoc-FF is initially dissolved in an appropriate solvent, followed by the addition of a certain amount of water which causes direct gel formation. This self-assembles into a metastable state of spherical clusters which then rearrange into uniform, transparent, fibrous networks.This has been extensively reported previously and has enabled the generation of rigid gels possessing storage moduli as high as 10^4 Pa, even at concentrations as low as 0.01 wt.% of Fmoc-FF[202,204].
- **pH switch**: Fmoc-FF is dissolved in an alkaline aqueous solution (pH = 10.5), then the solution is acidified. As soon as the pH reaches 8.5, the gelation occurs since the acid function is protonated (losing its negative charge). A mechanism of gelation by pH switch was proposed by Tang *et al.*[205] to explain this phenomenon (Figure 18).

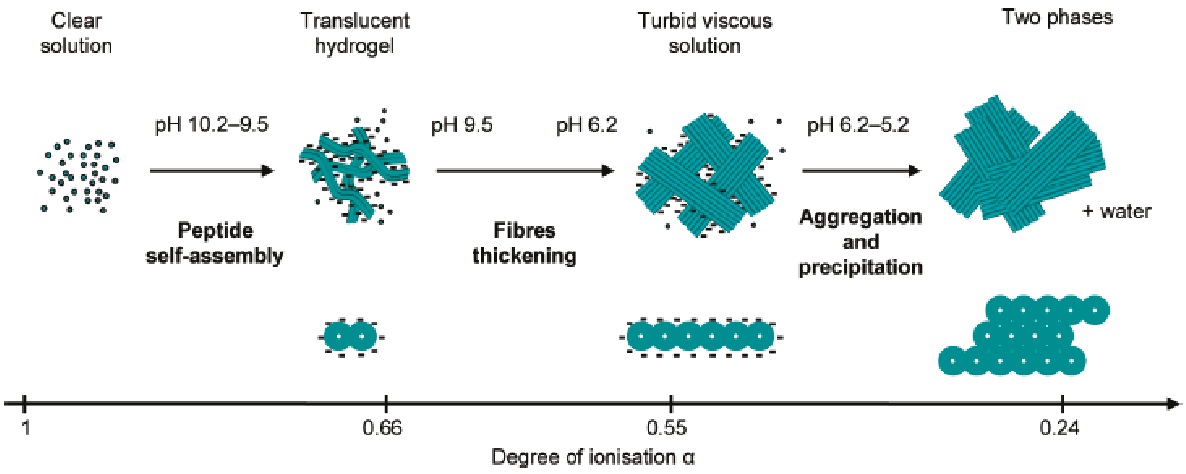

Figure 18: Proposed self-assembly mechanism of Fmoc-FF as a function of the peptide degree of ionization. Authorised reproduction of figure from Tang *et al.*[205].

For both preparation systems, Smith *et al.* have provided a mechanism for gelation based on nanocylinder architecture[206]. The resulting supramolecular fibres are composed of antiparallel β-sheets interlocked by π-stacking interactions and hydrogen bonds. Their closest natural analogues are amyloids, which are associated with neurodegenerative diseases such as Alzheimer's and Parkinson's[207]. Their stability under physiological conditions and ability to support cell growth makes them highly attractive for tissue engineering and drug delivery[208].

However, the preparation of composite gels from Fmoc-FF can increase its versatility for a range of applications, resulting in superior properties such as increased strength, specific shapes, complex structures, stability and enhanced biological activity[209–211]. Nolan and his research team were successful in developing 3D printable Fmoc-FFs gels through solvent switch[200]. This method has been shown more effective than the pH-switch approach in forming spherical domains from densely packed primary fibrils. The primary forces responsible for gelation were identified as solvent-gel and solvent-solvent hydrogen bonds, and it was also found that higher water content results in a greater amount of H-bond formation. Their properties can be tuned, as different preparation methods, amounts of solvent and conditions can be used to produce gels of varying strength[212].

2 Results and discussion

2.1 Preparation and surface chemical modification of cellulose nanofibrils (CNF) for composite engineering

The project employed a chemical modification method that involved three essential steps. The first step involved exchanging the solvent from water to dimethyl sulfoxide (DMSO). Next, the CNFs underwent an esterification reaction to introduce a macro-initiator onto their surface, yielding CNF-MI. A surface-initiated polymerization (SIP) reaction, known as surface-initiated single-electron transfer living radical polymerization (SI-SET-LRP), was then carried out to graft polymers onto the surface. Subsequently, an evaluation was made to assess the success of the modification. Scheme 8 provides a graphical representation of each step in the modification process.

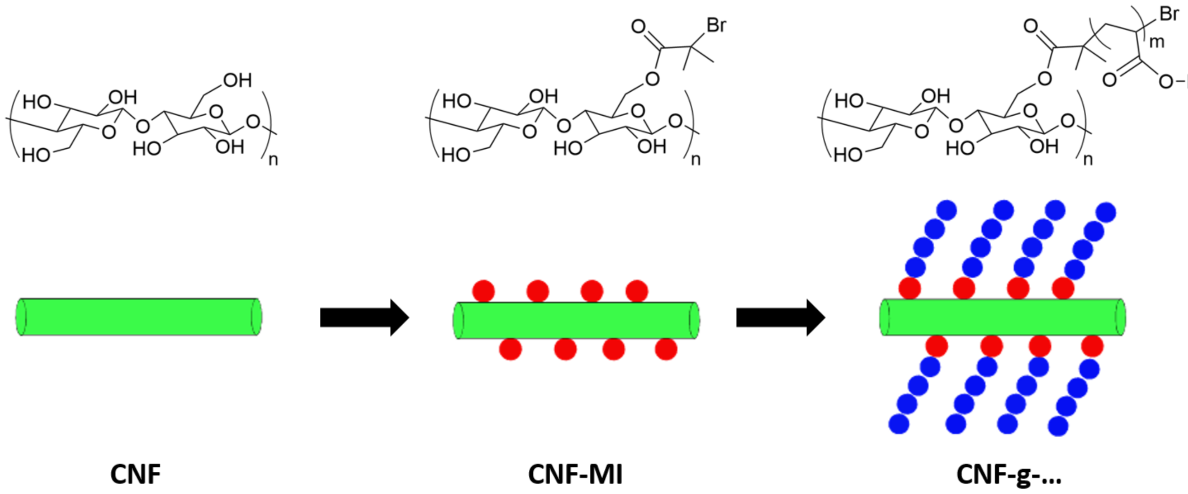

Scheme 8: Schematic representation of the CNF chemical modification procedure

2.1.1 Extraction procedure from extracted from elemental chlorine-free (ECF) bleached softwood Kraft pulp

The production of cellulose nanofibrils was carried out using a microfluidizer using elemental chlorine-free (ECF) bleached softwood Kraft pulp as a starting product. The morphology of the cellulose throughout each phase of the process was observed by Field Emission Scanning Electron Microscopy (FESEM), and the results are shown in Figure 19. Throughout the process, a gradual decrease in the diameter of the cellulose nanofibrils and an increase in homogeneity were observed. The diameter of the final CNF was measured multiple times, with the range of width found to be between 20 to 60 nm.

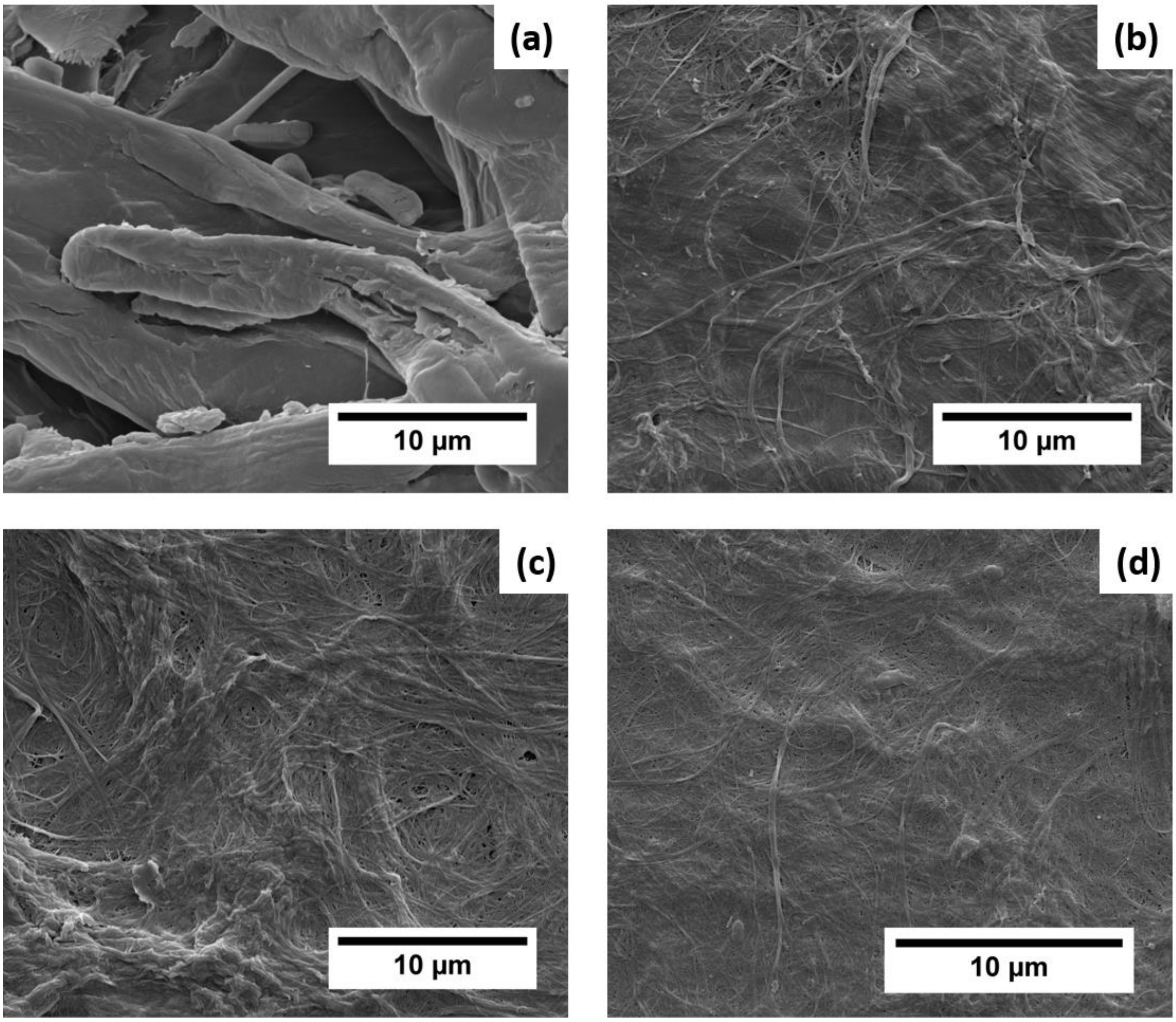

Figure 19: Field emission scanning electron microscopic (FESEM) images; (a) Elemental chlorine-free (ECF) bleached softwood Kraft pulp before milling; (b) fibrils after the milling step; (c) after the first step of microfluidic treatment; (d) after second step of microfluidic treatment.

2.1.2 Solvent exchange procedure

The esterification is a well-established reaction involving the equilibrium reaction between a carboxylic acid and an alcohol, resulting in the formation of the corresponding ester and water as a by-product. The efficient water removal is essential to prevent hydrolysis and increase yield due to the reversible nature of this reaction. To achieve effective chemical surface modification, it is therefore necessary to perform a solvent exchange of CNF from water to

DMSO. This solvent was selected as the primary organic solvent for its high solubility in the organic precursors used the upcoming reactions and its miscibility with water. By means of solvent exchange, no change in morphology or stability was observed when CNF was transferred between solvents. In this method, the initial CNF gel was suspended in water and an equal amount of DMSO was gradually added to it. The resulting mixture was then centrifuged and the supernatants were discarded. Additional DMSO was then added and the process was repeated until there was no trace of water.

2.1.3 Macroinitiator synthesis

Considering the chosen chemical modification of cellulose in this work is based on a *grafting-from* SI-SET-LRP, which involves a radical reaction, the introduction of a halogenated group is necessary. The surface chemical modification occurred on the primary hydroxyl groups through esterification with 2-bromoisobutyric acid promoted by carbonyldiimidazole (CDI) at 55 °C for 16 hours (shown in Scheme 9). This reaction resulted in a CNF-based macroinitiator (CNF-MI) suitable for SET-LRP reaction. The chemical modifications of CNF were evaluated using ATR-FTIR and the result is shown in Figure 20a,b. The characteristic bands of the native nanocellulose were easily identifiable with bands at 3320 cm^{-1} (O-H), 2950 cm^{-1} and 2895 cm^{-1} (C-H), 1430 cm^{-1} (C-H) and 1161 cm^{-1} (C-O-C). The successful synthesis of CNF-MI was achieved and, in comparison with the pristine CNF, an additional absorption band at 1733 cm^{-1}, attributed to the ester groups (C=O), was observed in its spectra.

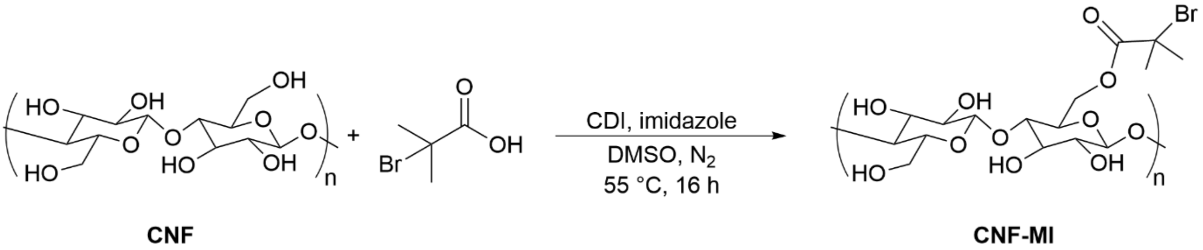

Scheme 9: Synthetic process of the CNF-based macroinitiator (CNF-MI).

The reaction yielded a translucent gel in DMSO which is like unmodified CNF. This procedure was repeated before all the SI-SET-LRP modifications were performed in this project.

2.1.4 Surface initiated single electron transfer living radical polymerization (SI-SET-LRP) with stearyl acrylate monomer (SA)

The surface properties of CNF, which tend to be hydrophilic, need to be modified to match the hydrophobic nature of high-density polyethylene (HDPE). The aim was to decrease the hydrophilic character of the fibrils, thereby limiting their aggregation due to fibril-fibril interactions and in the same way, improving the host matrix compatibility. This would potentially make a promising candidate out of CNF for use as an HDPE composite reinforcing agent. The CNF surface modification through SI-SET-LRP has previously been utilized and described in detail by Navarro *et al.*[213]. The polymerization reaction of stearyl acrylate (SA) monomer was initiated by CNF-MI in the presence of copper wire (Cu) and a tetradentate tertiary amine ligand (Me_6TREN) in a biphasic solvent system of toluene and DMSO, as shown in Scheme 10. Following the polymerisation, the poly-SA-grafted CNF (CNF-g-SA) is obtained as a translucent gel in toluene. In *Appendix 1*, CNF-g-SA is referred to as CNF-PSA, but the name was changed in order to maintain consistency. Upon SI-SET-LRP reaction, the spectrum of CNF-g-SA (Figure 20c) exhibited a significant increase in the number of bands. The major characteristic absorption bands were located at 2916 cm^{-1} and 2848 cm^{-1} (C-H), 1736 cm^{-1} (C=O), 1470 cm^{-1} (C-H), 1159 cm^{-1} (C-O-C) and 721 cm^{-1} for linear alkane functions.

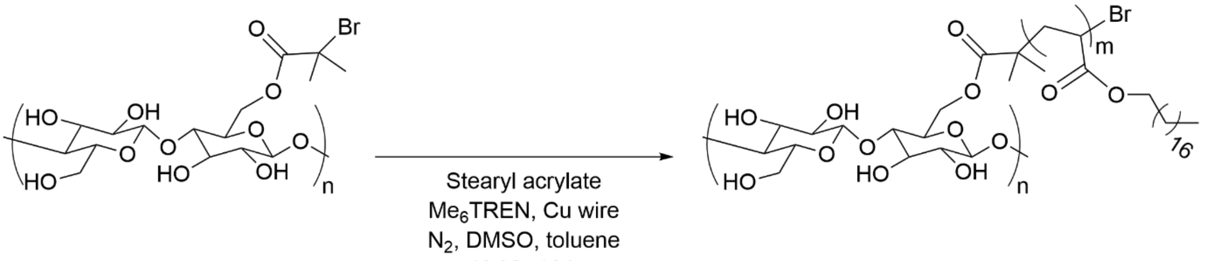

Scheme 10: Synthetic process of polymerization onto CNF-MI with the SA monomer through SI-SET-LRP, yielding CNF-g-SA.

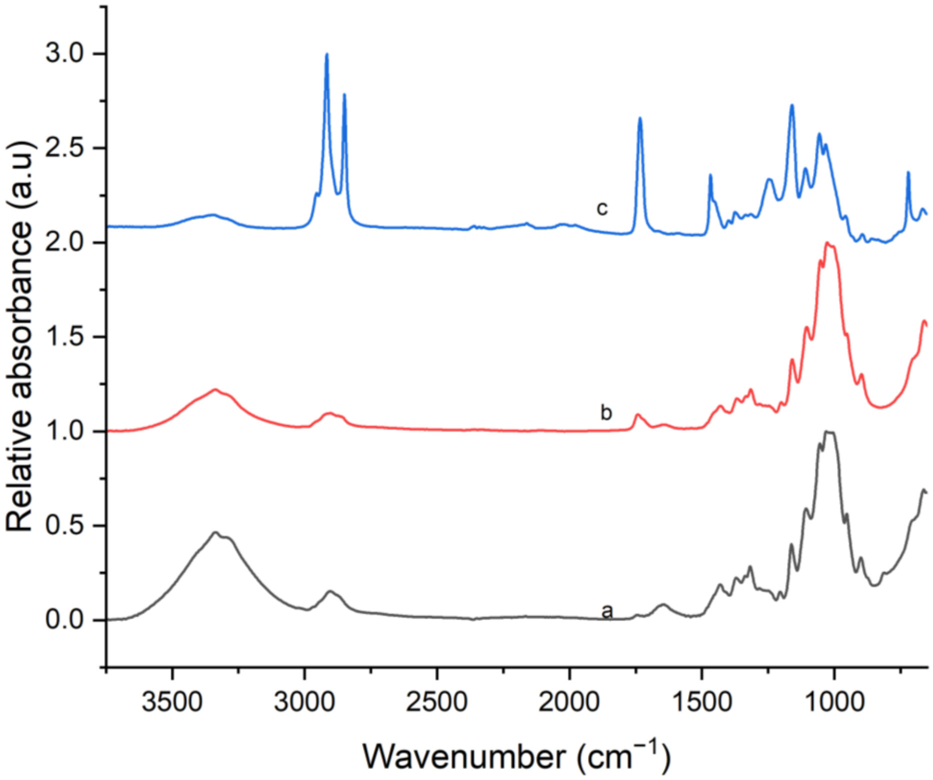

Figure 20: ATR-FTIR spectra of pristine CNF (a); CNF-MI (b); CNF-g-SA (c).

Unmodified CNF and CNF-g-SA were also analyzed using ^{13}C CPMAS NMR. Figure 21 displays the corresponding spectra with their respective bands assignments. The unmodified CNF typical bands shown in red) were found located at 105 ppm for C1, with double contributions for C4 and C6 signals due to crystalline (at 89 ppm and 65 ppm) and amorphous (at 84 ppm and 62 ppm) regions, with the remaining carbon signal, C2, C3, C5, clustered in the 72-75 ppm region. An increase in NMR bands density was observed following the grafting of stearyl acrylate. A signal at 175 ppm, corresponding to the carbonyl bond C12, was seen, while an intense signal between 40-20 ppm has been observed for long alkyl chains that have been grafted onto the CNF (C14 to C20). The presence of esters and abundant methylene groups supports the successful chemical modification of CNF.

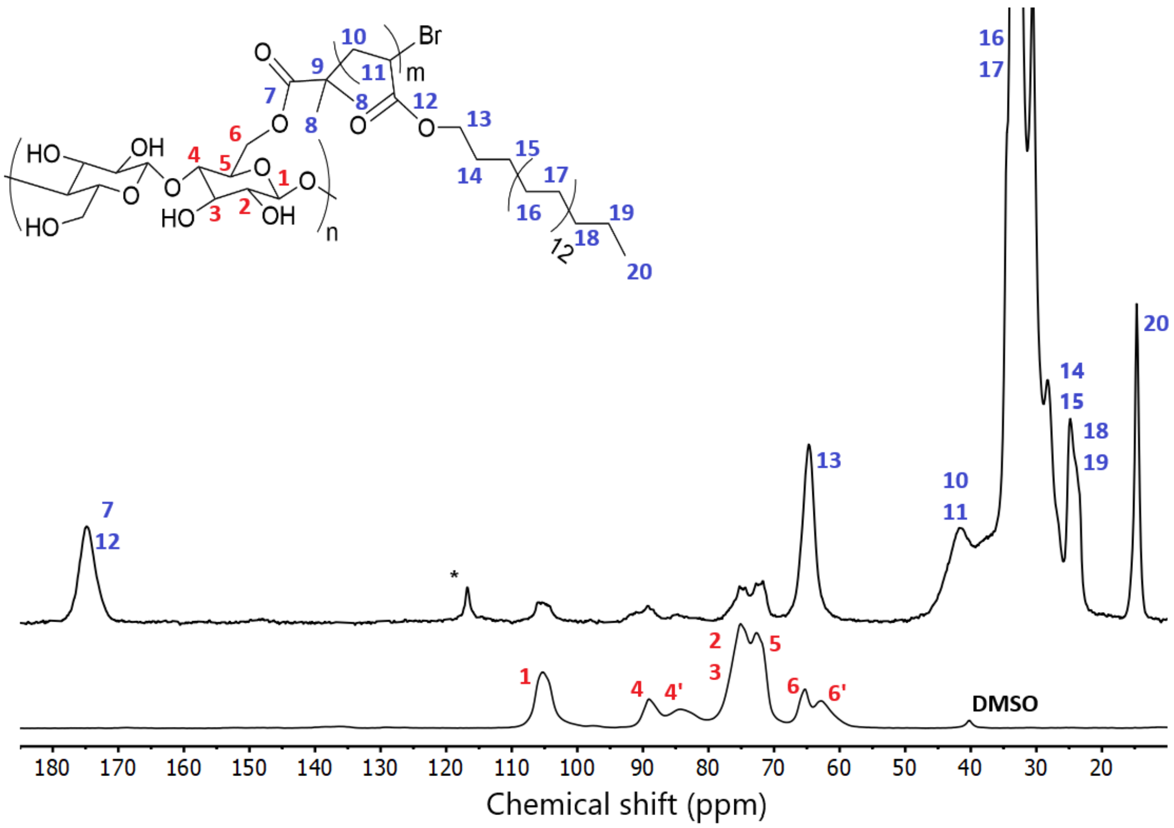

Figure 21: Solid-state ^{13}C NMR spectra of unmodified CNF on the lower part and CNF-g-SA on the upper part.

The numerous carbon atoms incorporated through this process are expected to result in a change in the physical properties and, thus, leads to a significant increase in hydrophobicity. The water contact angle was measured for each sample to verify this assumption. To perform the measurement, concentrated solutions of each sample were applied to flat surfaces and dried in an oven to obtain films of CNF and CNF-g-SA. The water contact angle increased significantly from 36° to 105° after polymerization (Figure 22), demonstrating significant hydrophobicity of CNF-g-SA.

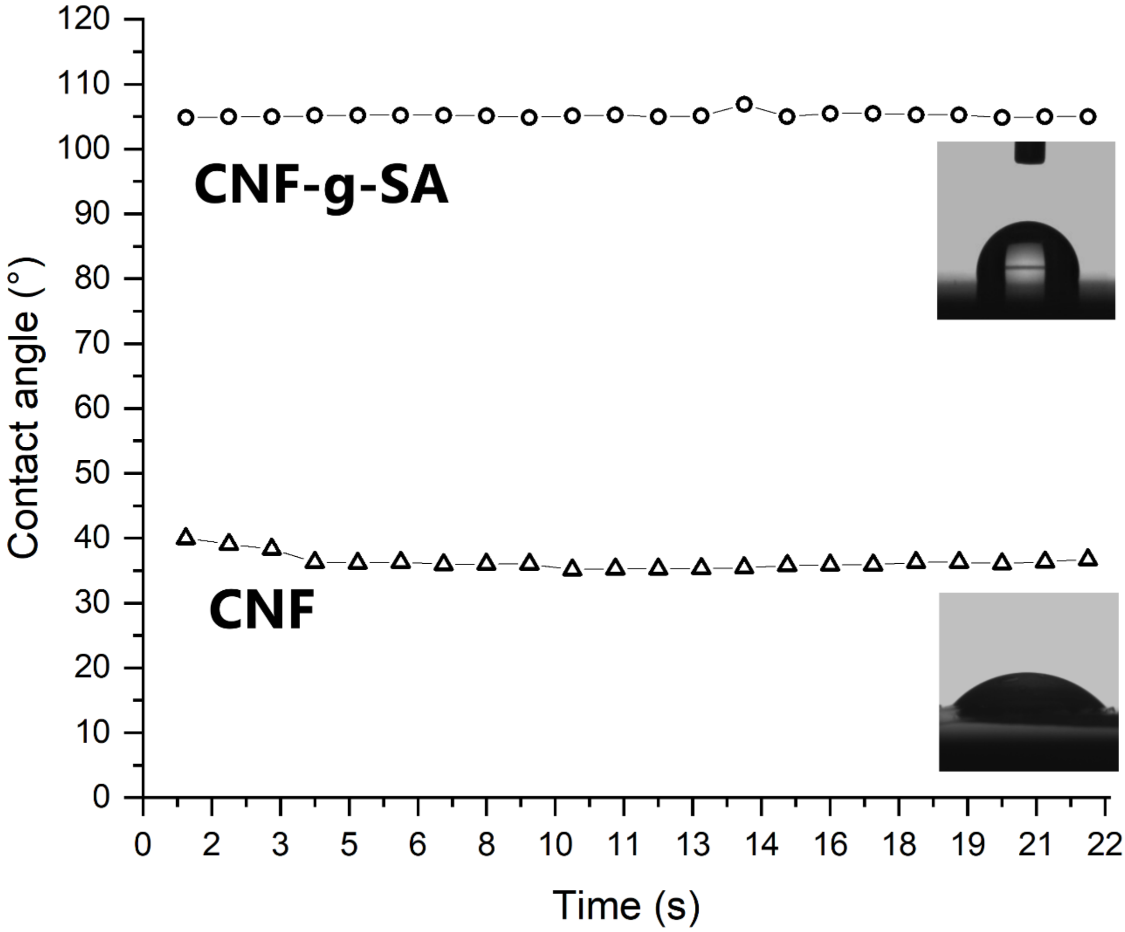

Figure 22: Photographs of the static contact angle measurements of water on unmodified CNF and CNF-g-SA films, and the evolution of the contact angle against time. The CNF-g-SA film has a contact angle of 105°, while unmodified film has a 36° contact angle.

Field emission scanning electron microscopy (FESEM) was used to examine CNF, CNF-MI and CNF-g-SA to verify the nanofibrils morphology after chemical modification. The compounds were dried overnight in an oven at atmospheric conditions. CNF and CNF-MI images (Figure 23A,B) showed a dense network of aggregated fibrils with only minor differences after esterification. Meanwhile, the fibrils are fully embedded in the grafted polymer as shown in the CNF-g-SA images (Figure 23C). All observations are in support of a shift in the properties of the CNF, which is the result of the successful chemical modification.

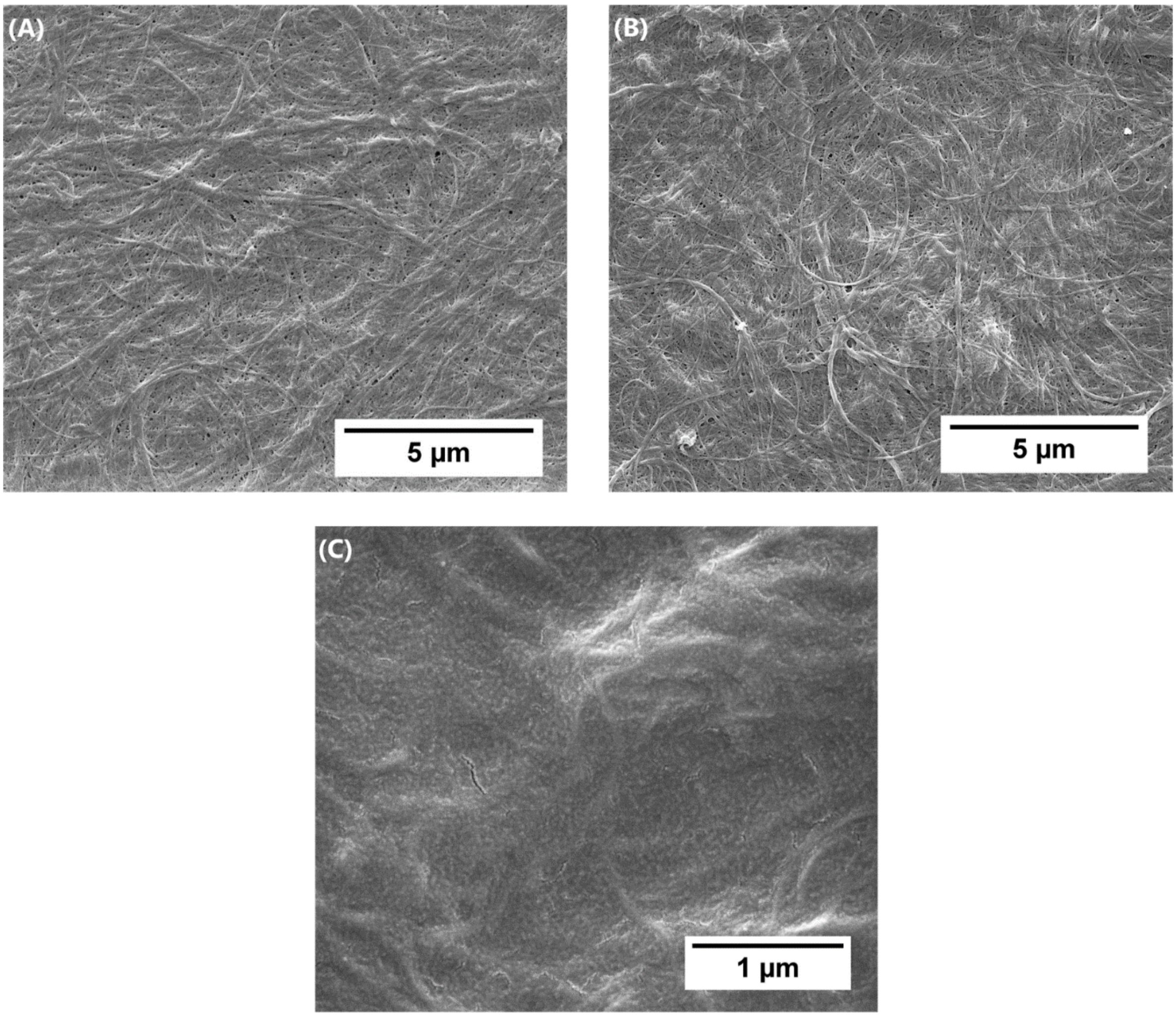

Figure 23: FESEM images of **(**A) CNF; (B) CNF-based macroinitiator; (C) CNF-g-SA.

2.1.5 Determination of the supramolecular organization of CNF, and evaluation of the impact of CNF-graftings (with the different grafting rates)

The qamples of CNF, CNF-MI, and CNF-g-SA underwent further analysis to determine the impact of macroinitiator grafting and SA grafting. As quantifying each modification and isolating the polymer grown on the CNF surface was complicated, this was considered the most appropriate procedure. For each sample, two measurements were performed:

- The first analysis was a ^{13}C multi CPMAS spectrum, providing signals associated with the rigid parts of the sample allowing the characterization of the supramolecular structure (crystallinity index, LFD and LFAD)[214].

- The second analysis, which provided signals from the whole sample and ensured the quantitative nature of the signals from different molecules, was a ^{13}C multi-CPMAS spectrum[215]. A molar grafting ratio can be determined.

A characteristic spectrum of CNF and higher purity, with a low level of contamination by lignins, was observed for this type of sample, as shown in Figure 24a. The presence of a significant amount of hemicelluloses (Figure 24b, orange peaks), approximately 15 % molar, was highlighted by the spectral deconvolution. This is in agreement with previous results on CNF[216].

Following the widely recognized "core and shell" model, the supramolecular organization of CNF was characterized by three parameters: the crystallinity index, the lateral fibril dimension (LFD) and the lateral fibril aggregate dimension (LFAD), as shown in Figure 24b. Potential changes in the CNFs resulting from different grafting techniques can be tracked using these parameters and the results are summarized in Table 2.

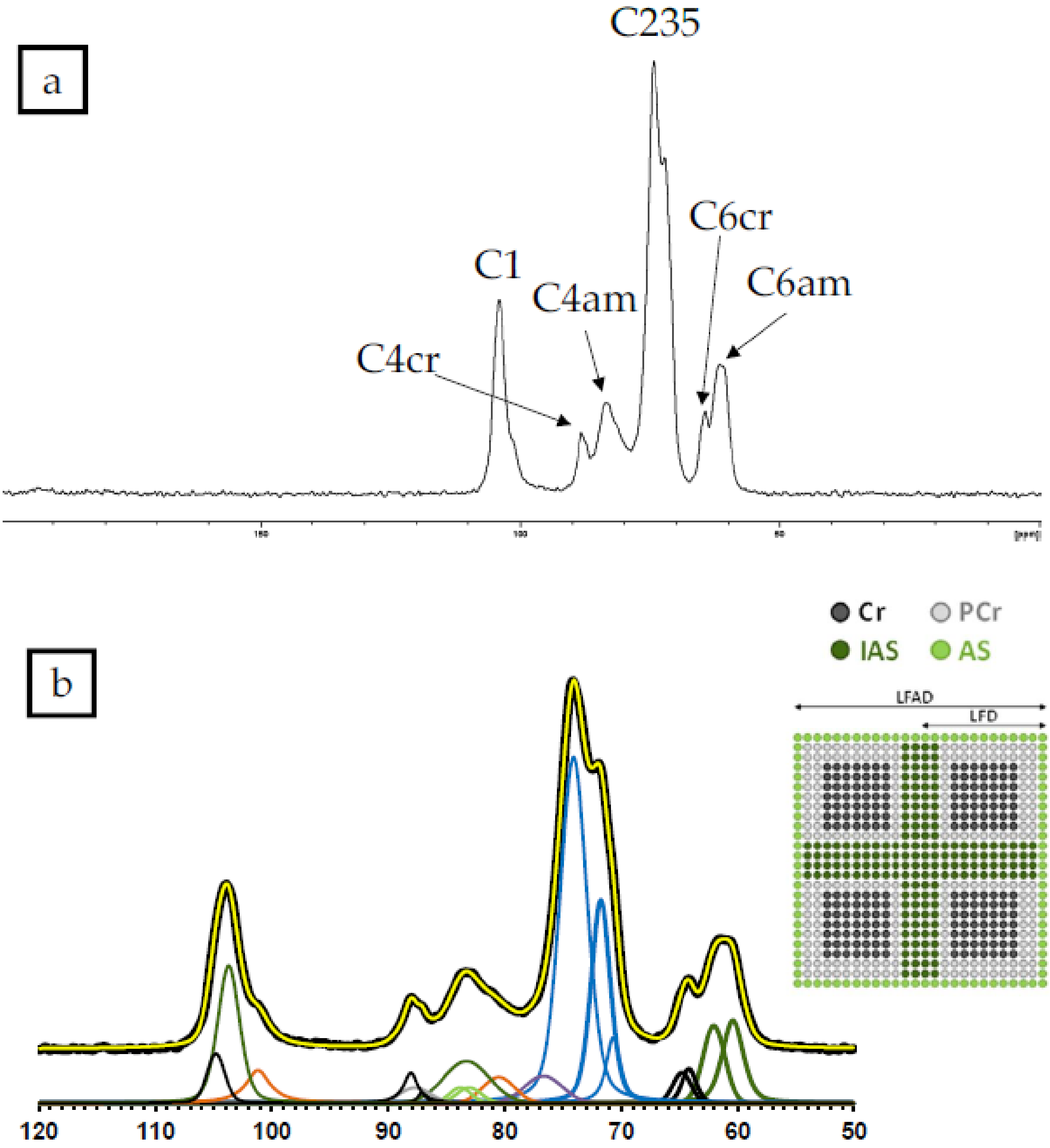

Figure 24: (a) CNF sample's ^{13}C CPMAS spectrum; (b) The 50-120 ppm region has been deconvoluted. The upper black line represents the experimental data, while the yellow line represents the sum of individual peaks resulting from the spectral deconvolution. Two signals from hemicelluloses are indicated in orange. The C-4 region has been deconvoluted with the crystalline forms Cr (Iβ) and Cr (Iα+β) (black), the paracrystalline form (PCr) (grey), the accessible fibril surfaces (AS) (green) and the inaccessible fibril surface (IAS) (dark green).

Table 2: Summary of the resulting characteristics of each of the CNF, the CNF-MI and the CNF-g-SA. * : calculation performed with a signal representing 2 esterified to minimise error.

	CNF	CNF-MI	CNF-g-SA
Crystallinity index (in %)	32	27	54
lateral fibril dimension, LFD (nm)	2.6	2.4	4.3
LFAD	5.2	3.9	4.3
Grafted rate (molar percentage)	N.C.	0.8	486 (187*)

For the CNF-MI sample, there is a slight decrease in crystallinity (from 32 % to 27 %) and a significant increase in crystallinity (54 %) for the CNF-g-SA sample, indicating degradation of amorphous cellulose, consistent with the decrease in the molar fraction of hemicelluloses to 7 % and 9 %, respectively.

The grafting rates were calculated for the three samples of interest. This involved dividing the area under a peak corresponding to carbon 1 of the grafting over all signals corresponding to carbon 4 of the cellulose. Importantly, the peak at ~39.5 ppm, visible almost exclusively in multiCP spectra, corresponds to residual DMSO and is not part of the graft. The grafting rate for CNF-MI was found to be low at 0.8 %, while a rate of 486 % was measured for the CNF-PSA sample. This is often associated with insufficient washing and the presence of residual non-grafted molecules. It was also concluded that the CNF-MI sample possessed a more significant proportion of mobile cellulose than the CNF-g-SA sample.

Since then, CNF-g-SA has been obtained in toluene, which contains a CH_3 group, so the grafting calculation is obsolete as it was performed based on this chemical group. The calculation was performed with a signal representing 2 esterified carbons to minimise the risk of error. The conclusions of the previous report are still valid as the grafting rate thus determined is 187 %.

2.1.6 Surface initiated single electron transfer living radical polymerization (SI-SET-LRP) with ureido-pyrimidinone monomer (UPy)

To create a printable gel with self-healing properties, one possible method is to enhance the non-covalent molecular entities with physical cross-links. The supramolecular material networks incorporating ureido-pyrimidinone (UPy) have been widely used to create self-healing materials[217,218]. The initial step necessary for incorporating this self-dimerisation component into the CNF involved the synthesis of the corresponding monomer with a function capable of undergoing a radical polymerisation reaction. The UPy monomer in question was synthesized by reacting 2-amino-4-hydroxy-6-methylpyrimidine with 6-methylisocytosine (Scheme 11a). The experiment was carried out using DMSO at a temperature of 140 °C to achieve complete solubilization, which was achieved in just 15 minutes. A white solid was precipitated upon cooling to room temperature, washed with an excess of cold distilled water and dried under vacuum. This gave the desired compound a yield of 92 %. The monomer composition of the compound was confirmed through ^{1}H NMR analysis in DMSO-d$_6$ at 60 °C. The peak analysis of the resulting spectrum (*figure shown in Appendix 2*) was consistent with the proposed structure. UPy grafting through SI-SET-LRP becomes possible as it carries an acrylate function. However, the monomer's solubility at room temperature was rather poor, so the polymerisation reaction had to be carried out in DMSO at a higher temperature than the 40 °C as performed with stearyl acrylate. The CNF-MI acquired from esterification can therefore trigger the controlled polymerisation of the UPy monomer, which had to be first solubilised at 120 °C and then cooled to 60 °C (for the minimization of the risk of spontaneous precipitation at lower temperature). SI-SET-LRP was performed similarly to CNF-g-SA (Cu(0) and (Me$_6$TREN)) in DMSO except at 60 °C, as shown in Scheme 11b). The UPy-grafted CNF (CNF-g-UPy) is finally obtained as a translucent gel in DMSO after purification by centrifugation.

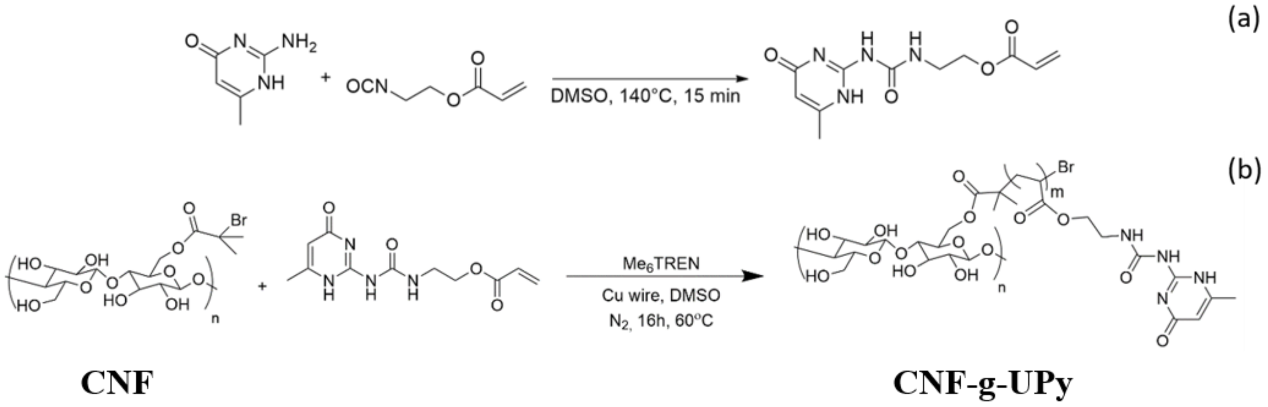

Scheme 11: Synthetic scheme for UPy monomer (a); Graft polymerization of CNF-based macroinitiators (CNF-MI) with UPy monomer via SI-SET-LRP, yielding CNF-g-UPy (b).

The obtained compounds were initially analyzed through FTIR spectroscopy, and the corresponding spectrum is presented in Figure 25. Successful grafting of the UPy monomer was confirmed by the occurrence of absorption bands between 1500-1700 cm^{-1}, with specific signals at 1733 cm^{-1} (C=O), 1657 cm^{-1} (R-CO-NH), and 1576 cm^{-1} (R-NH-C=C), which corresponds to amide and urea signals, while characteristic spectrum for CNF was still observed.

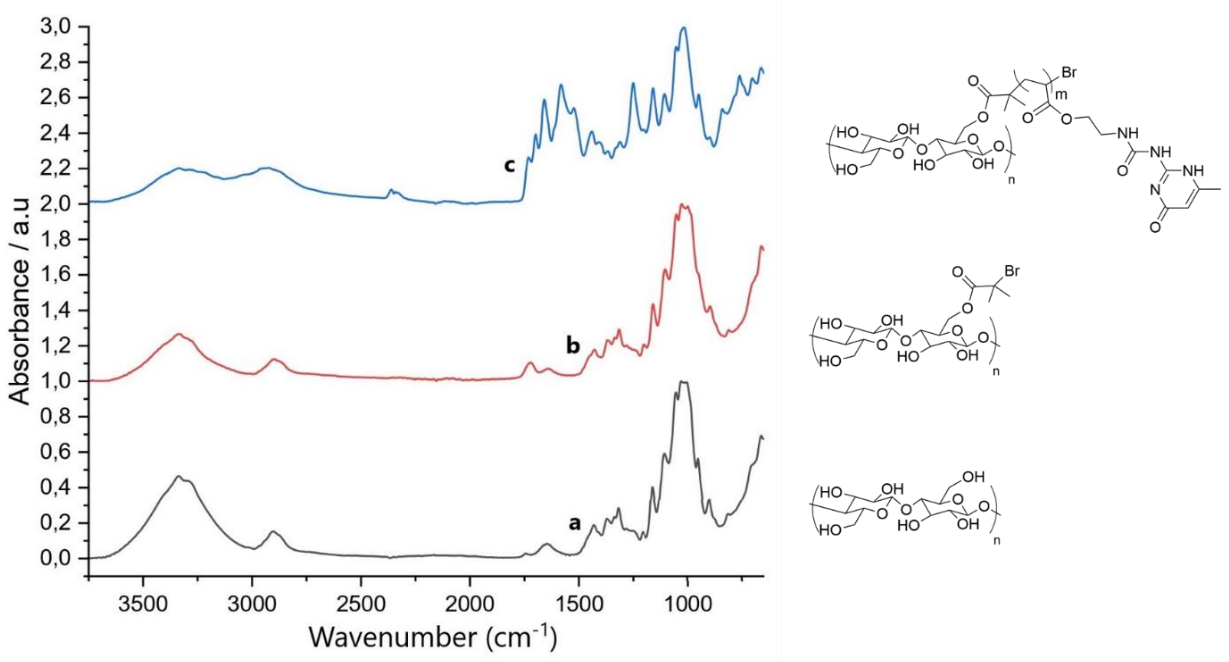

Figure 25: FTIR spectra of pristine (a) CNF; (b) CNF-MI, and (c) CNF-g-UPy.

The chemical modification of CNF was monitored using solid-state CP-MAS ^{13}C NMR. Figure 26 illustrates the spectra of both modified and unmodified CNF, with each peak correctly assigned. An increase in signal density was expected and observed as a result of the increased number of differently shielded carbons. Carbons in proximity to one oxygen molecule or taking part in a double bond were responsible for the signal found at approximately 63 ppm (C13) and 105 ppm (C18), whilst the least shielded group were found between 20-40 ppm. Finally, it can be observed that the region exhibiting heavy shielding at a chemical shift above 140 ppm and below 180 ppm corresponds to carbons adjacent to two or more heteroatoms. The combination of FTIR analysis and solid-state NMR confirmed a successful grafting of the monomer and the obtention of UPy-grafted CNF (CNF-g-UPy).

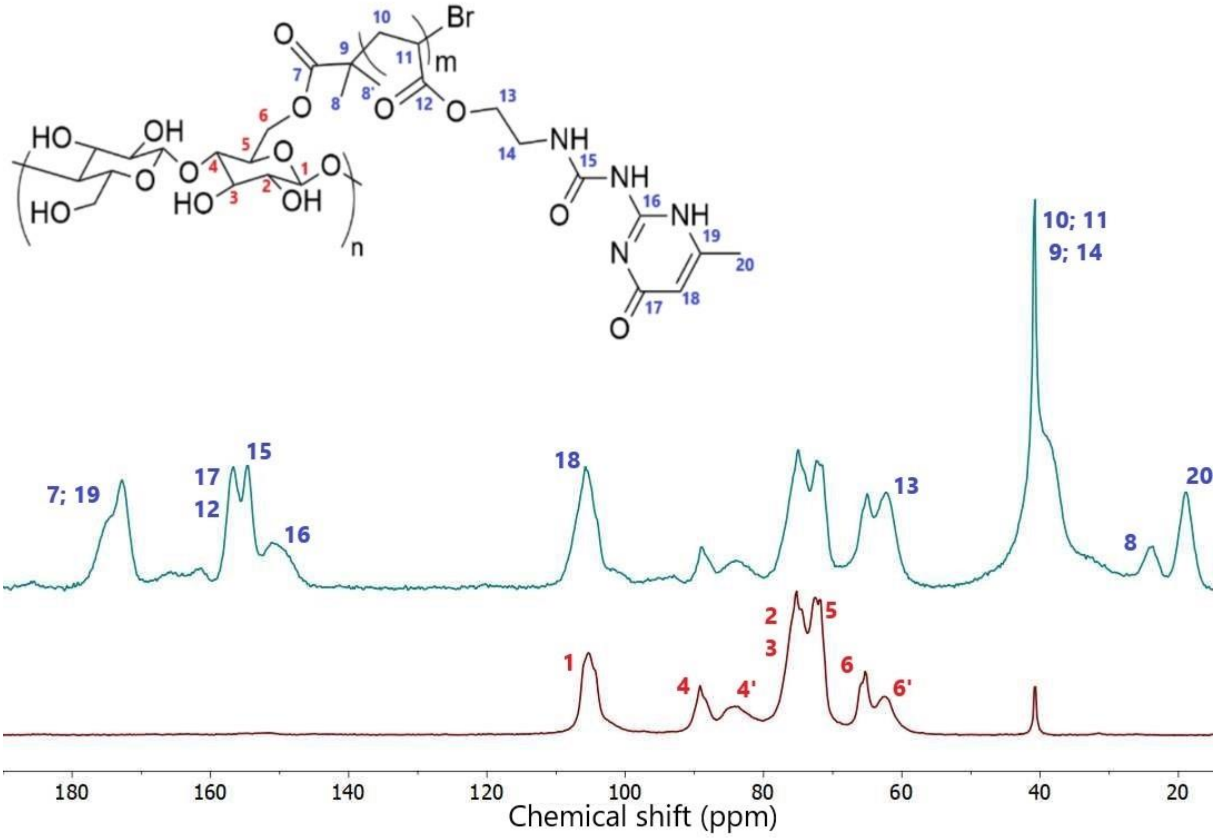

Figure 26: Solid-state CP-MAS ^{13}C NMR spectra of unmodified CNF on the lower part and CNF-g-UPy on the upper part.

2.1.7 Surface Initiated single electron transfer living radical polymerization (SI-SET-LRP) with fluorenylmethyloxycarbonyl (Fmoc)

The versatility, stability, and ease of removal of 9-fluorenylmethyloxycarbonyl (Fmoc) as a protecting group in organic synthesis have proven it to be highly effective. It is widely employed in peptide chemistry, particularly for selective protection of amine functions. In addition, Fmoc is recognized for its ability to increase π-π stacking and hydrophobic interactions, promoting excellent self-assembly[219,220]. The envisaged modification involved the introduction of Fmoc moieties onto the CNF surface via SI-SET-LRP. It is therefore expected that it would affect the overall properties and potentially induce self-assembly through the formation of additional supramolecular bonds. Both these effects are expected to enhance the bond strength of the material, as well as alter its gelation properties. The process of CNF modification is carried out using SI-SET-LRP with a CNF-based macroinitiator (CNF-MI) and an Fmoc group-bearing monomer. The monomer was synthesised in a two-step process, as shown in Figure 27a. Firstly, 2-(2-aminoethoxy)ethanol underwent a reaction with Fmoc-Cl under basic medium conditions. This was followed by a reaction of the 2-(N-Fmoc-2-aminoethoxy)ethanol with acryloyl chloride in a basic medium (Et_3N, triethylamine) and with dichloromethane as solvent. This two-step procedure resulted in 2-(N-Fmoc-2-aminoethoxy)ethyl acrylate (Fmoc-AEEA) monomer, which is now ready for use in SI-SET-LRP, with a yield of 82 %. Nuclear magnetic resonance (NMR) spectrum of the starting molecule (Fmoc-Cl), 2-(N-Fmoc-2-aminoethoxy)ethanol and Fmoc-AEEA are presented in Figure 27c. The structure of the intermediate molecule, 2-[2-(Fmoc-amino)ethoxy]ethanol, was confirmed through the occurrence of the N-H (5.27 ppm), H7 (3.40 ppm), H8/9 (3.55 ppm) and H10 (3.72 ppm) bands. The structure of the Fmoc-AEEA monomer, 2-(N-Fmoc-2-aminoethoxy)ethyl acrylate, was finally identified by the occurrence of absorption bands of H11 (6.08 ppm), H12 (6.34 ppm) and H12' (5.75 ppm), which are correlated with the acrylic function. The Fmoc-AEEA moieties were grafted to CNF in identical conditions as used in previous procedures reported in this dissertation. The reaction was carried out in DMSO as solvent at a temperature of 60 °C for 16 hours (Figure 27b). The higher temperature resulted in a higher amount of grafted polymer compared to 40°C. This was observed by an increase in signal intensity in ATR-FTIR. The Fmoc-AEEA grafted CNF, labelled as CNF-g-Fmoc, was ultimately obtained as a vivid yellow gel with a 2-3 wt.% concentration following purification by centrifugation.

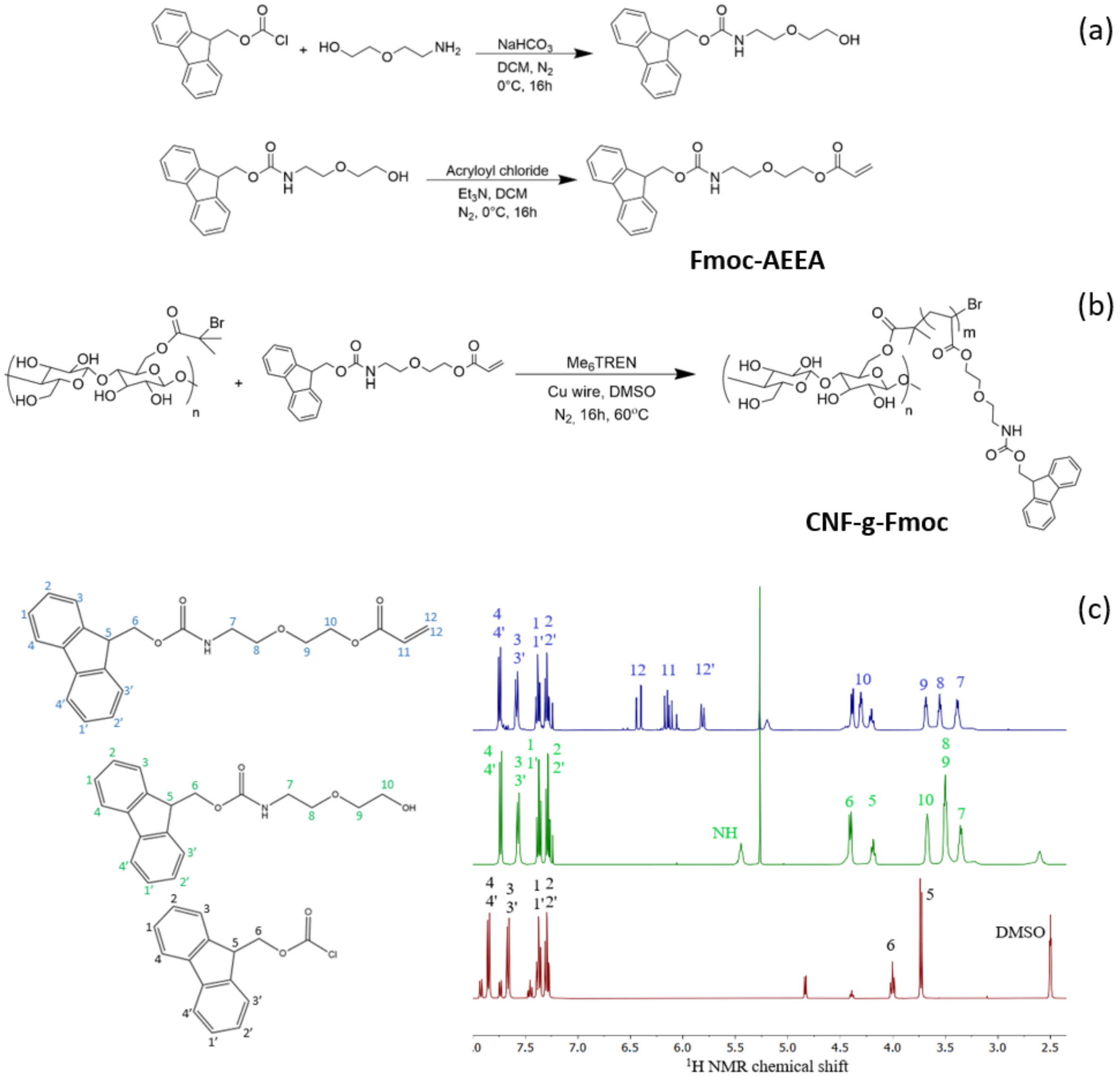

Figure 27: Synthetic scheme for Fmoc-AEEA (a); Graft polymerization of CNF-MI with Fmoc-AEEA via SI-SET-LRP, yielding CNF-g-Fmoc (b); ^{1}H-NMR spectrum of monomer synthesis; red: Fmoc-Cl; green: 2-(N-Fmoc-2-aminoethoxy) ethanol; blue: Fmoc-AEEA (c).

ATR-FRIR was used to characterize the grafting. The resulting spectra (*shown in Appendix 3*) of CNF, CNF-MI, Fmoc-AEEA and CNF-g-Fmoc have been analyzed and the comparisons were made. The characteristic signals of CNF and CNF-MI were consistent with previous macroinitiator synthesis. Bands at 1717 cm^{-1} (C=O), 1141 cm^{-1} (N-H), and 738 cm^{-1} (C=C) can be identified for Fmoc-AEEA monomer. However, for Fmoc-g-CNF, the bands of the monomer blended with the CNF bands, making them more difficult to distinguish. Next, solid-state CP/MAS ^{13}C NMR spectroscopy was conducted on CNF-g-Fmoc to investigate its modification. Expected chemical shifts linked to Fmoc-AEEA fragments were anticipated in the range of 120-145 ppm[221], but these remained undetected. A relatively weak signal at 120 - 135 ppm is discernible, which may correspond to Fmoc-AEEA functions. However, this proved to be insufficient to certify the modification. High-Resolution Magic Angle Spinning (HR-MAS) Nuclear Magnetic Resonance (NMR) was conducted to detect the modification. The compatibility with swollen samples (in gel form per example) while maintaining high resolution and sensitivity is one of the main advantages of this technique in this particular context[222]. In comparison to the deuterated solvent signals, the signal corresponding to CNF was relatively small, as a result of the irreversible aggregation of the cellulose nanofibrils during the drying process (before analysis), leading to less swelling and dispersibility, which is a common characteristic of cellulose materials[223,224]. Figure 28 displays the ^{1}H NMR spectra of HRMAS and CP-MAS ^{13}C NMR spectrum whilst it is difficult to identify the chemical shifts associated with CNF, it is possible to distinguish bands associated with Fmoc-AEEA functional group in the 7 – 8 ppm range, which supports the grafting of Fmoc-AEEA on CNF.

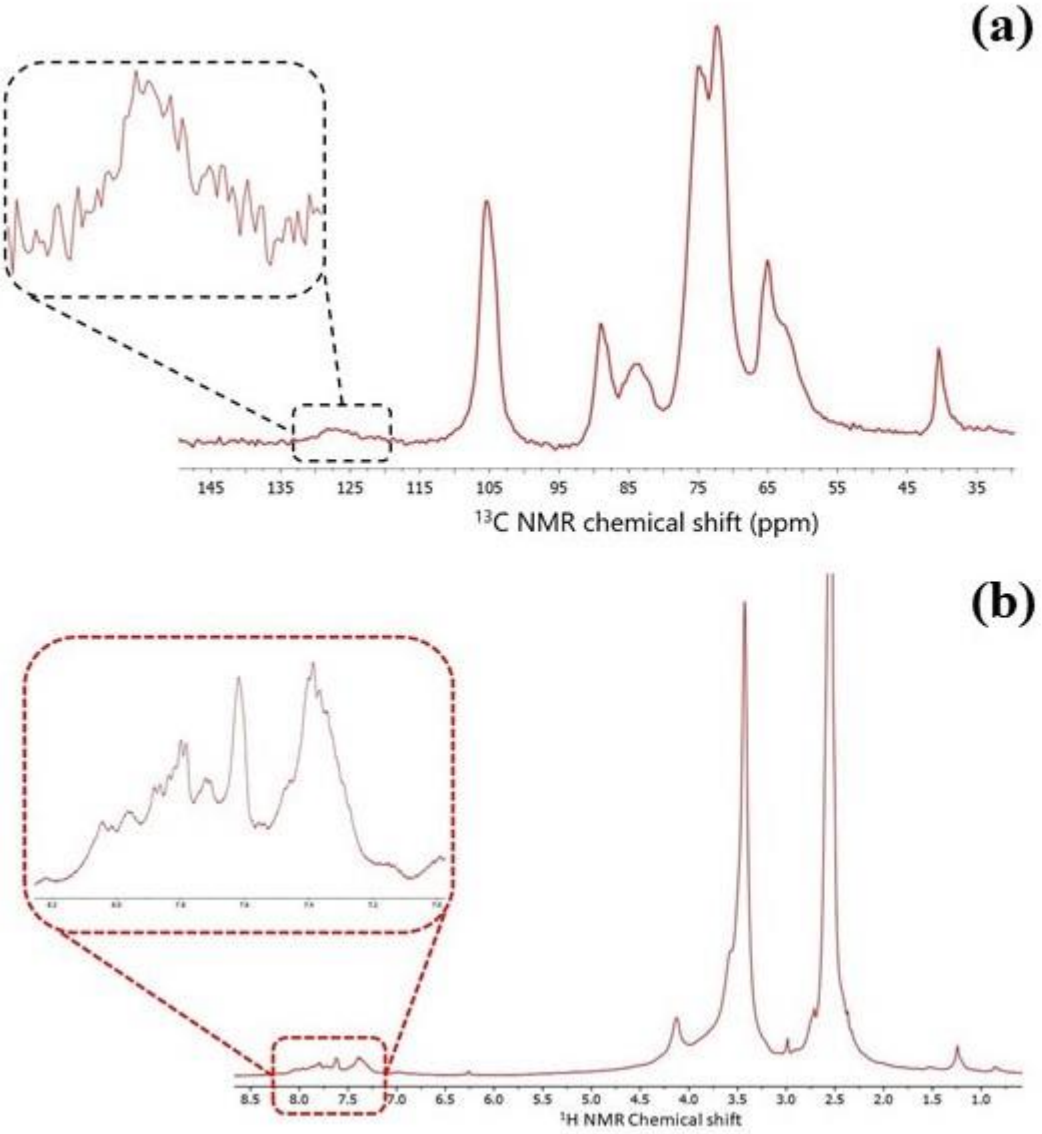

Figure 28: (a) Solid-state CP-MAS ^{13}C NMR spectra CNF-g-Fmoc; (b) ^{1}H HR-MAS NMR spectrum of CNF-g-Fmoc sample in DMSO-d_6.

As it has been reported that Fmoc-Cl has strong absorption bands in the UV-Vis region (210 and 260 nm) [225,226], it is therefore expected that CNF-g-Fmoc would exhibit an absorption band in this region. An initial trial was conducted using UV light, and the "before and after" photographs of the gels are presented in Figure 29a, and the CNF-g-Fmoc can be seen to emit light in the visible region compared to CNF-MI. The absorption spectra of CNF-g-Fmoc and Fmoc-AEEA were recorded using a UV-visible spectrophotometer. Several new absorption bands were detected in the spectrum of CNF-g-Fmoc (280 to 310 cm^{-1}), which were not present in unmodified CNF. This further supports the hypothesis of successful grafting, as these signals originate exclusively from Fmoc-AEEA. For the determination of the Fmoc-AEEA content in the CNF-g-Fmoc sample, different solutions with distinct concentrations of Fmoc-AEEA were measured. Figure 29b shows the plot of absorbance at 284 nm, which is identical for both samples, versus concentration. The results revealed a linear correlation between absorbance and Fmoc-AEEA concentration, which allowed the quantification of the amount of Fmoc-AEEA which was incorporated into CNF-g-Fmoc. A concentrated CNF-g-Fmoc solution with a concentration of 0.2 mg·ml^{-1} resulted in an absorbance of 0.55, indicating a Fmoc-AEEA concentration of 0.04, corresponding to 20 % of the total content of the sample.

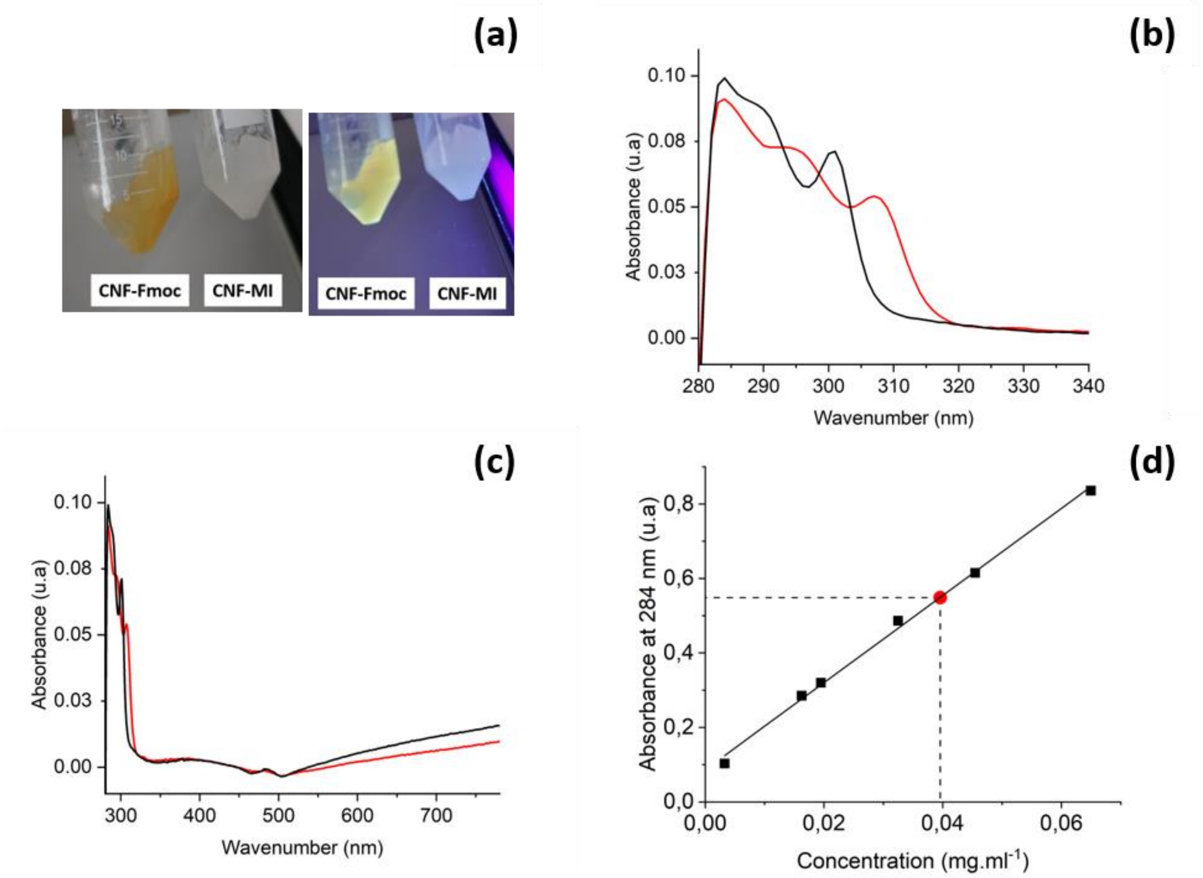

Figure 29: Photograph of CNF-g-Fmoc and CNF-MI before UV exposure and after exposure at 366 nm (a); UV–Vis spectra of Fmoc-AEEA (C = 0.003248 M) in black, and CNF-g-Fmoc (C = 0.2 M) in red, spectrum with wavenumber range from 280-800 cm^{-1} (b); zoomed spectrum with wavenumber range from 280-340 nm^{-1} (c); Calibration curve obtained from Fmoc-AEEA solutions at 284 nm, and determination of the unknown concentration for CNF-g-Fmoc depicted by the red dot (d).

The dry sample underwent characterisation using confocal laser scanning microscopy (CLSM) with a 488 nm excitation wavelength. Figure 30a depicts the results, which confirmed the fluorescent signal of the sample. The images produced included the fluorescence image on the left, the bright field image in the middle, and the combined overlay fluorescence-bright-field image on the right. Furthermore, the overlay of bright field and fluorescence revealed the uniform distribution of fluorescence signals from the modified surface of the fibrils across the CNF surface. Field Emission Scanning Electron Microscopy (FESEM) was used to obtain a thorough understanding of the fibril structure of CNF-g-Fmoc samples and to assess the effects of chemical modification on their morphology (Figure 30b). The addition of Fmoc-AEEA onto cellulose has substantially altered the fibril structure, causing a visible change in the fibril appearance. The structure of CNF, which was previously compact, underwent significant modification, leading to a larger fibrillar structure. The modification of morphology and addition of Fmoc groups results in greater aggregation compared to unmodified cellulose, hence accounting for the observed structures.

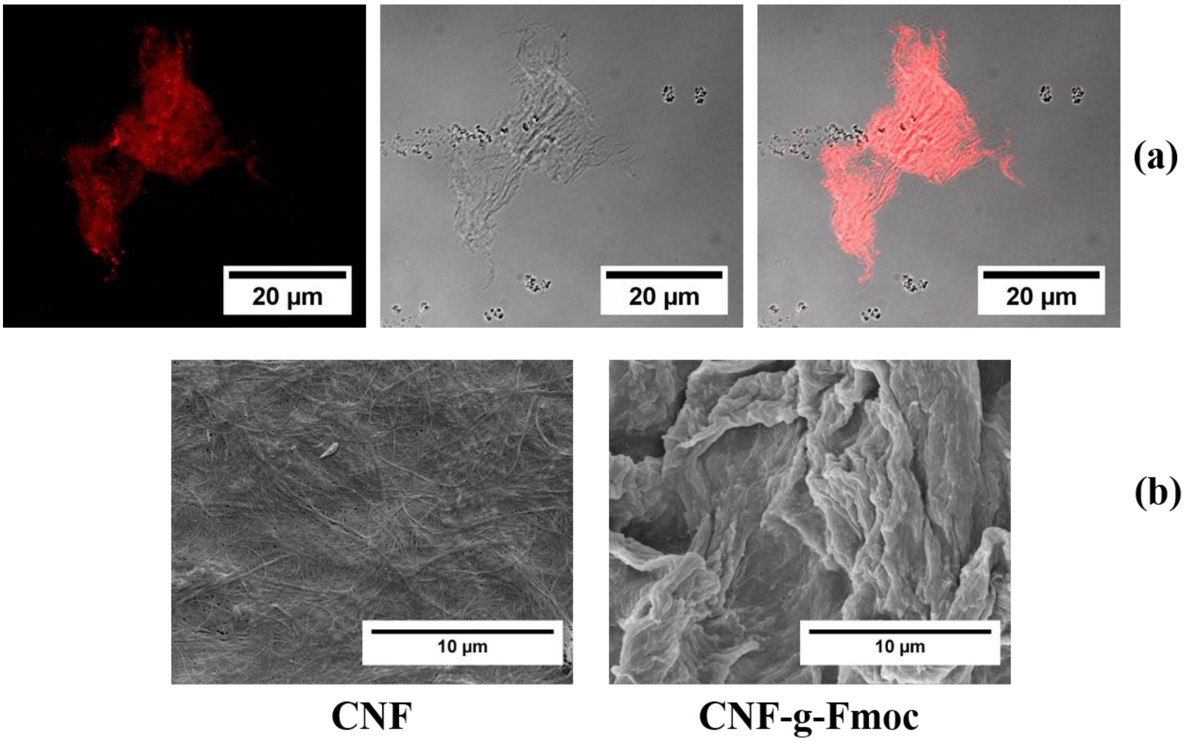

Figure 30: (a) CLSM images (Fluorescence, bright-field, combined overlay) of CNF-g-Fmoc. Excitation wavelength: 488 nm; (b) Field emission scanning electron microscopic (FESEM) images of CNF and CNF-g-Fmoc.

2.2 Composites production, characterization and 3D printing

2.2.1 Stearyl acrylate grafted cellulose nanofibrils reinforced HDPE composite: CNF-g-SA/HDPE

The desired composite material was made from HDPE pellets and dried CNF-g-SA (stearyl acrylate grafted cellulose nanofibrils). The extrusion process was conducted at 150 °C with a twin-screw extruder with a CNF-g-SA content of 10 wt.%. The extruded CNF-g-SA/HDPE nanocomposite underwent ATR-FTIR analysis, and its spectrum is displayed in *Appendix 1*. Characteristic HDPE absorption bands such as 2912 and 2846 cm^{-1} (C-H) and the rocking peak at 719 cm^{-1} (-CH$_2$) were visible and well defined[227]. Adsorption bands were present at 1741 cm^{-1} (C=O) and 1165 cm^{-1} (C-O-C), demonstrating the presence of the ester groups in the extruded filament, ensuring proper incorporation of the CNF-g-SA.

The successful incorporation of CNF-g-SA was expected to result in a reinforcement of the HDPE matrix properties and thus lead to superior mechanical properties bearing composite. The typical stress-strain curves for both native HDPE and HDPE/CNF-g-SA composite can be observed in Figure 31. Additionally, the mechanical properties such as Young's modulus, tensile strength, and strain at the break are presented in Table 3. An improvement in the overall mechanical properties was noted with the addition of CNF-g-SA. The young's modulus reached a maximum of 1094 MPa with a 23 % improvement. However, a slight reduction in tensile strength and a significant decrease in elongation at break was observed. This can be attributed to the increased stiffness caused by the filler's characteristic and a similar effect has been reported elsewhere[228,229]. The fracture of the material is predominantly driven by crack initiation and propagation, consequently, leading to an increase in granulation and agglomeration, and resulting in areas requiring less energy for fracture development[230]. The composite samples exhibited a lack of necking elongation compared to HDPE, supporting this statement.

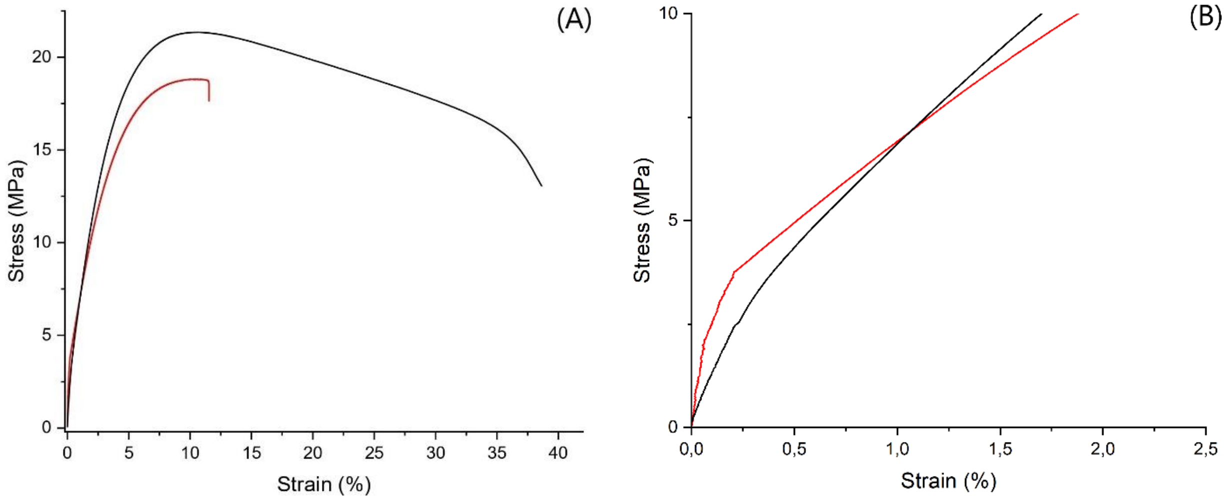

Figure 31: Experimental stress-strain curves of HDPE/CNF-g-SA with neat HDPE; HDPE is represented by the black curve and red for the composite. Stress-strain curve (B) is a zoomed version of (A).

Table 3: Summary of the tensile properties of the HDPE and composites of 10 wt.% of CNF-g-SA/HDPE.

CNF-g-SA content in HDPE / %	Extrusion temperature / °C	Young's Modulus / MPa	Yield strength / MPa	Strain at break / %
0	150	888 ± 135	21.4 ± 0.3	38.6 ± 1.4
10	150	1,094 ± 77	18.8 ± 0.1	11.6 ± 1.3

A cross-section of the composite mechanical test specimen at the fracture point is shown in Figure 32. In general, the surface appears uniformly smooth with few CNF-g-SA aggregates, which indicates a clear absence of cavities or significant clusters of fibrils. The composites of unmodified CNF with the HDPE matrix were also attempted for comparative purposes, however as expected this proved to be unsuccessful, mainly due to the high degree of macroscopic aggregation of the CNF. The poor dispensability of the material was due to its hydrophilic properties, incompatible with HDPE. Consequently, these findings endorse the necessity of chemical modification to transform the initially hydrophilic CNF into a more compatible CNF-g-SA.

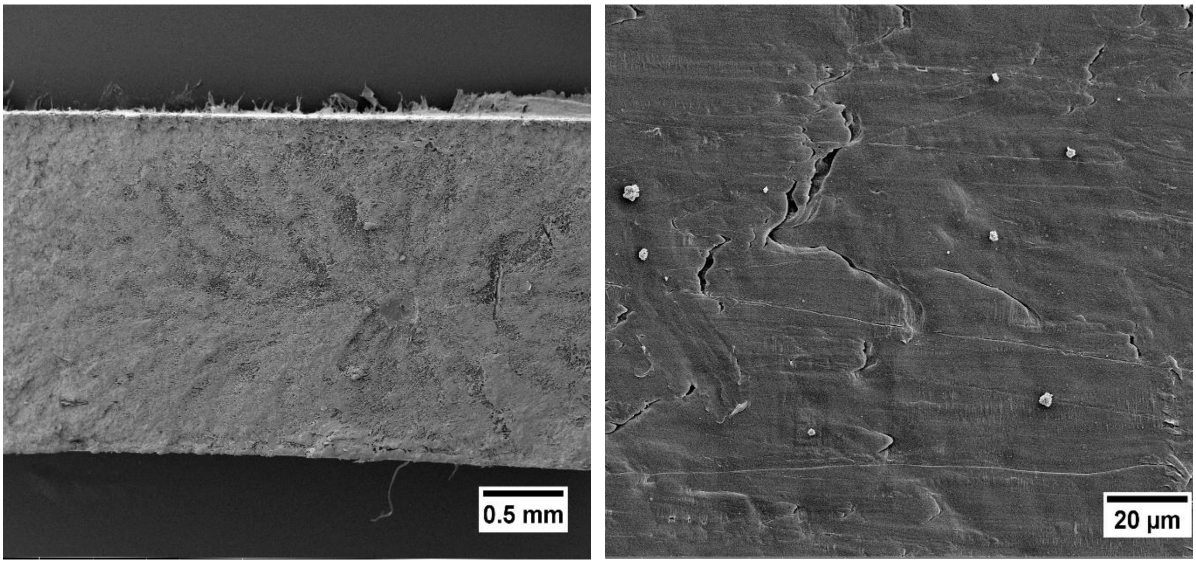

Figure 32: FESEM images showing the cross-section of a broken mechanical test specimen made with CNF-g-SA/HDPE.

To assess CNF-g-SA 3D printability, filaments with a diameter of 1.75 cm were utilized while printing parameters consisted of a nozzle temperature of 215 °C and a bed temperature of 60 °C. To have the best comparability between printed parts with HDPE and CNF-g-SA/HDPE all the other print parameters (extrusion speed, retraction, details found in *Appendix 1*) were kept the same as well. To assess the potential for improving 3D printing accuracy, we selected models that were difficult to print using a semi-crystalline polymer. Two cuboid designs were produced, with dimensions of 60 mm length, 10 mm width, and 3 mm height. One of the designs was full and the other was a hollow model, as shown in Figure 33a,b. It is expected that the hollow model would experience less deformation compared to the solid model. The reason for this is that the solid model contains a higher amount of layers contributing to the overall deformation. 3D printing of this kind of object is usually subject to post-printing deformation issues such as warping and by that coming loose from the printbed, instead of sticking on the printing bed. Therefore, for the quantification of their degree of deformation, the distorted samples have been assumed to belong to an arc of a circle and the radius has been calculated. As the size of the circle increases with reduced distortion in the rectangular block, the radius increases. The various factors influencing print quality were analyzed in this study, which involved the use of an LDPE-based tape as a printbed coating, known to enhance HDPE adhesion and using an enclosure for temperature stabilization[88]. The outcomes are indicated in Figure 33c.

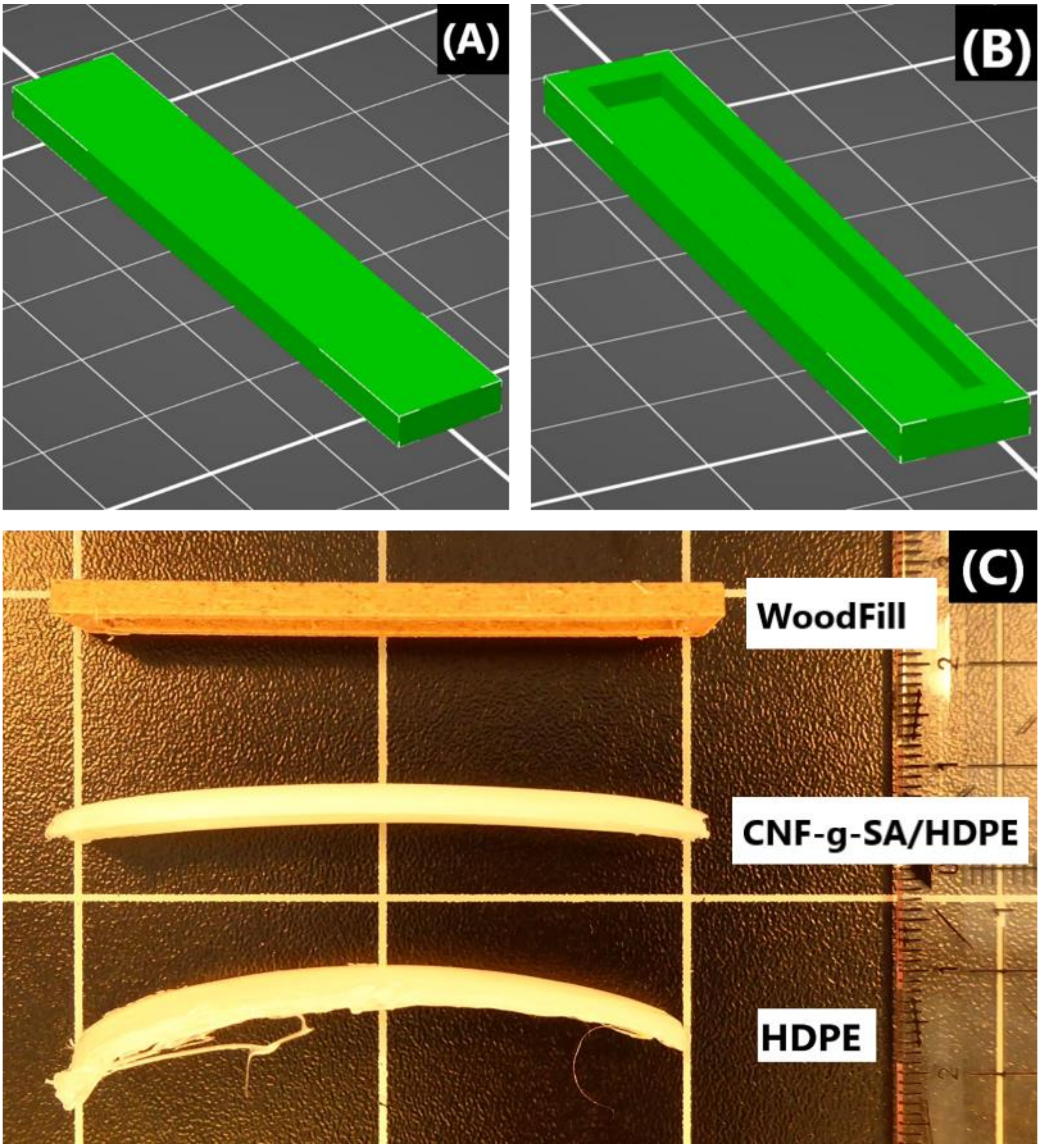

Figure 33: 3D models of full (A) and notched (B); Representative photograph of printed notched models (C).

Without the addition of LDPE tape or using the enclosure (cases 1-2 and 7-8), HDPE and composite failed to produce satisfactory results in both models, highlighting HDPE's inadequate suitability for printing. Conversely, the application of LDPE tape to the printer bed led to enhanced performance. Samples 3 and 4 demonstrated the composite's printing capabilities, whereas HDPE was unable to do so. An increase in radius ranging from 58 % (samples 5-6) to 222 % (samples 11-12) was observed for the one produced using the composite filament compared to the one produced using HDPE, highlighting a reduction in deformation. The models printed with CNF-g-SA reinforced composite filaments exhibited significantly less warping than those printed with HDPE, demonstrating the enhancing and strengthening effects of CNF-g-SA.

Table 4: Summary of warping measurement of HDPE and CNF-g-SA/HDPE composites; samples from 1 to 6 represent the full model, and 7 to 12 the notched model.

Sample	Material used	LDPE tape	Enclosure	Radius (cm)
1	HDPE	No	No	-
2	CNF-g-SA/HDPE	No	No	-
3	HDPE	Yes	No	-
4	CNF-g-SA/HDPE	Yes	No	11.62
5	HDPE	Yes	Yes	7.80
6	CNF-g-SA/HDPE	Yes	Yes	12.30
7	HDPE	No	No	-
8	CNF-g-SA/HDPE	No	No	-
9	HDPE	Yes	No	9.67
10	CNF-g-SA/HDPE	Yes	No	23.57
11	HDPE	Yes	Yes	7.15
12	CNF-g-SA/HDPE	Yes	Yes	23.05

A chess pawn was produced using filaments composed of HDPE, CNF-g-SA/HDPE and WoodFill (PLA-based filament with a woodfiber filler) for comparative purposes. This model can be challenging to produce as some difficulties, such as overhangs, can interfere with the printing process. Figure 34 displays a representative picture of the pawns printed using the same parameters. As anticipated, the pawn printed with the WoodFill filament used as the standard did not pose any difficulties. However, the pawn printed with HDPE filaments was unsuccessful. The upper part of the pawn did not print according to the set structure and collapsed instead. The pawns created using CNF-g-SA/HDPE filaments showed significant improvements in print resolution and overall quality. The lines were smoother, warping was reduced, and layer definition was better, resulting in good dimensional accuracy.

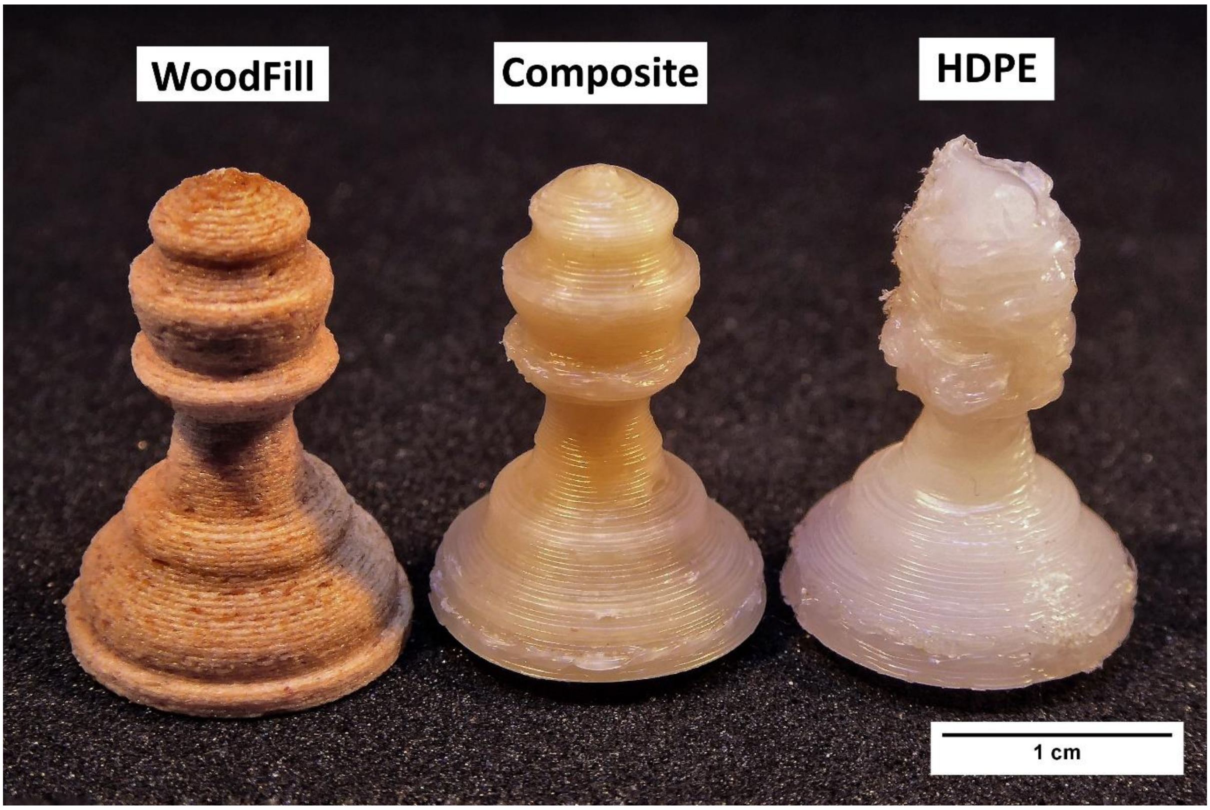

Figure 34: 3D printed models; filament used on the left pawn is Woodfill, HDPE for the middle and CNF-g-SA/HDPE composite for the right one.

2.2.2 UPy-grafted cellulose nanofibrils reinforced composite (CNF-g-UPy/UPy-DEGEEA)

The materials with self-healing properties must fulfil certain specific criteria, including possessing reversible physical bonds and a certain degree of molecular mobility that is capable of being activated (or not, in the case of autonomous self-healing). A polymer based solely on UPy functions was synthesised by SET-LRP, but it proved to be highly crystalline and hence lacked any gel properties. Zhu *et al*.[231] reported a self-healing polymer based on low cross-linking materials which involved the use of hydroxyethyl acrylate (HEA) and poly(ethylene glycol) methacrylate (PEGMA) containing UPy moieties. Consequently, a similar polymer consisting of UPy and di(ethylene glycol) ethyl ether acrylate (DEGEEA) repeating units was prepared. DEGEEA functions possess the ability to increase thermo-responsive properties, improve solubility in dimethylsulfoxide (DMSO), as well as reduce aggregation of the UPy functions, all while maintaining overall hydrogen bonds in the structure[232,233]. The resulting polymer would then be used as the host matrix for the preparation of the desired composite gel. The polymer synthesis was carried out under SET-LRP conditions, similar to CNF-g-UPy synthesis. However, instead of the CNF-MI, the molecular initiator ethyl-2-bromo-2-methylpropionate (eBiB) was utilised with a polymerisation ratio of $[M]_0/[I]_0/[L]_0$ at 100/1/0.2 with one-third of the DEGEEA monomer and the rest of UPy monomer (Figure 35a). As both monomers were added at the beginning of the reaction and possess the same chemical function, a random copolymer made of both monomers was expected to be produced. It was allowed to react for 16 h at 60 °C and was then purified by centrifugation with water and DMSO resulting in a white gel. In addition, the polymer exhibited a reversible thermo-responsive behaviour, with an observed lower critical solution temperature (LCST) of 40°C. Above this temperature, the gel underwent a transition in its physical properties, i.e. phase change from a gel to a liquid state. Upon cooling (at a temperature below the LCST), the polymer returned to its initial properties. The polymer analysis was carried out using ^{1}H NMR and for comparison, the monomer spectrum is also shown in Figure 35b. The signals associated with the UPy monomer were identifiable, such as the peak at 5.78 ppm corresponding to the unshielded C-H in the heterocyclic ring. The absence of the signals at 5.91 and 6.40 ppm, which belong to the acrylate function of the monomer, indicates that the polymerization has been completed. Furthermore, new bands such as 1.05, and 2.26 ppm and an increase in the intensity of the signal at the chemical shifts 3.43 and 4.08 ppm were observed derived from the DEGEEA.

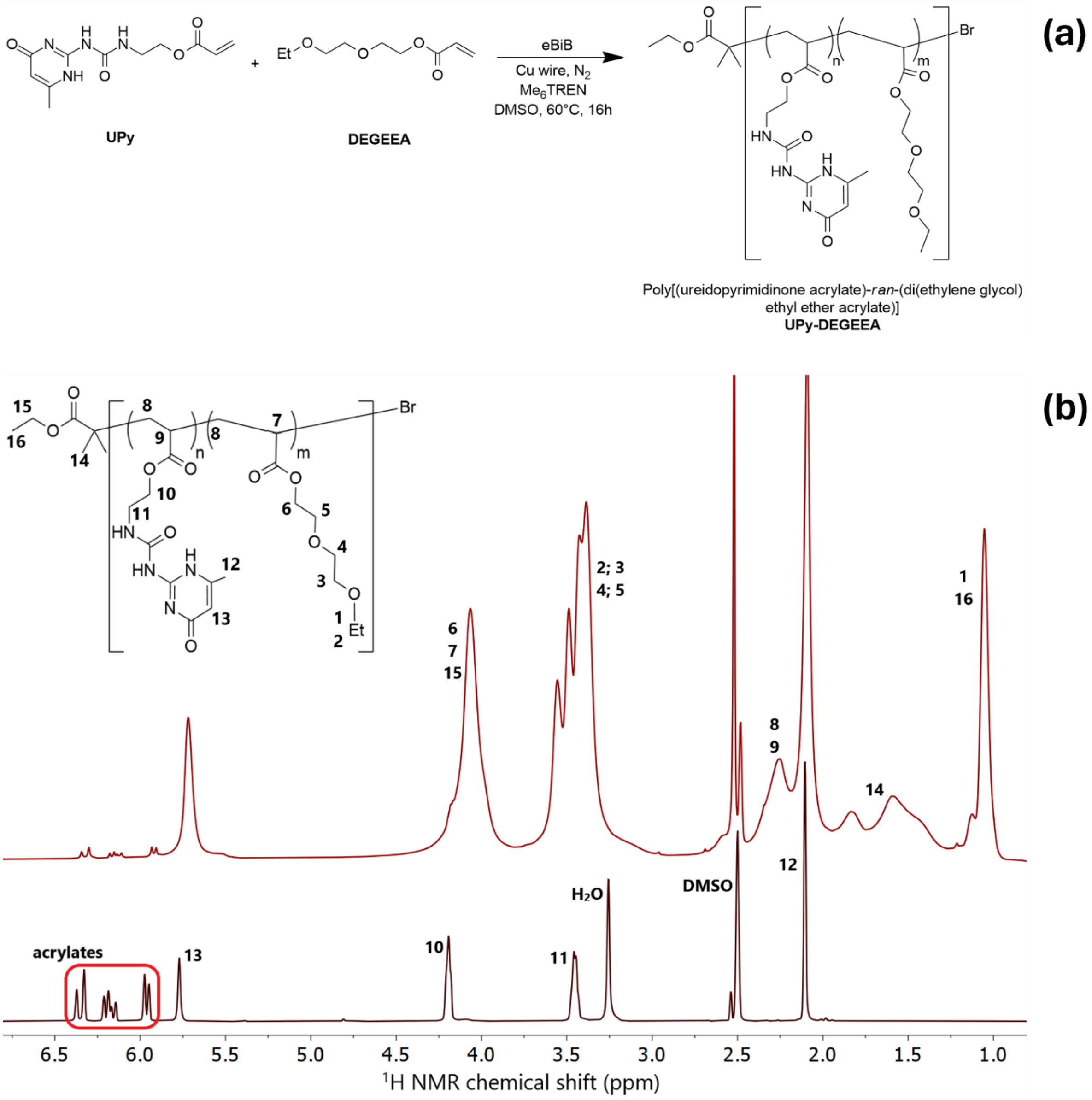

Figure 35: Synthetic scheme of poly[(ureidopyrimidinone acrylate)-*ran*-(di(ethylene glycol)ethyl ether acrylate)], referred as UPy-DEGEEA random polymer with n = 59 and m = 39 (a); ^1H NMR spectrum of the UPy-DEGEEA on the upper part and UPy monomer represented on the lower part (b).

The ratio of each compound in the obtained copolymer poly[(ureidopyrimidinone acrylate)-*ran*-(di(ethylene glycol)ethyl ether acrylate)], referred to as UPy-DEGEEA for more convenience, were determined by integrating signal at chemical shifts corresponding to each monomer. The C13 located at 5.78 ppm was selected as a reference for the UPy monomer. Although the band at 1.05 ppm corresponds to C1 and C16, the signal from the initiator can be disregarded due to its negligible amount, and therefore was selected as the representative for

DEGEEA. The calculated ratio was 59:39 for UPy:DEGEEA, which is in good agreement with the theoretical ratio.

The CNF-g-UPy was incorporated as a reinforcing additive to enhance the polymer's mechanical properties and was expected to result in improved post-printing behaviour of the nanocomposite. The combination would lead to an exponential increase in hydrogen bonding, increasing the degree of cross-linking in the supramolecular network. Scheme 12 displays a schematic illustration of the bonds established between the CNF-g-UPy and the UPy-DEGEEA.

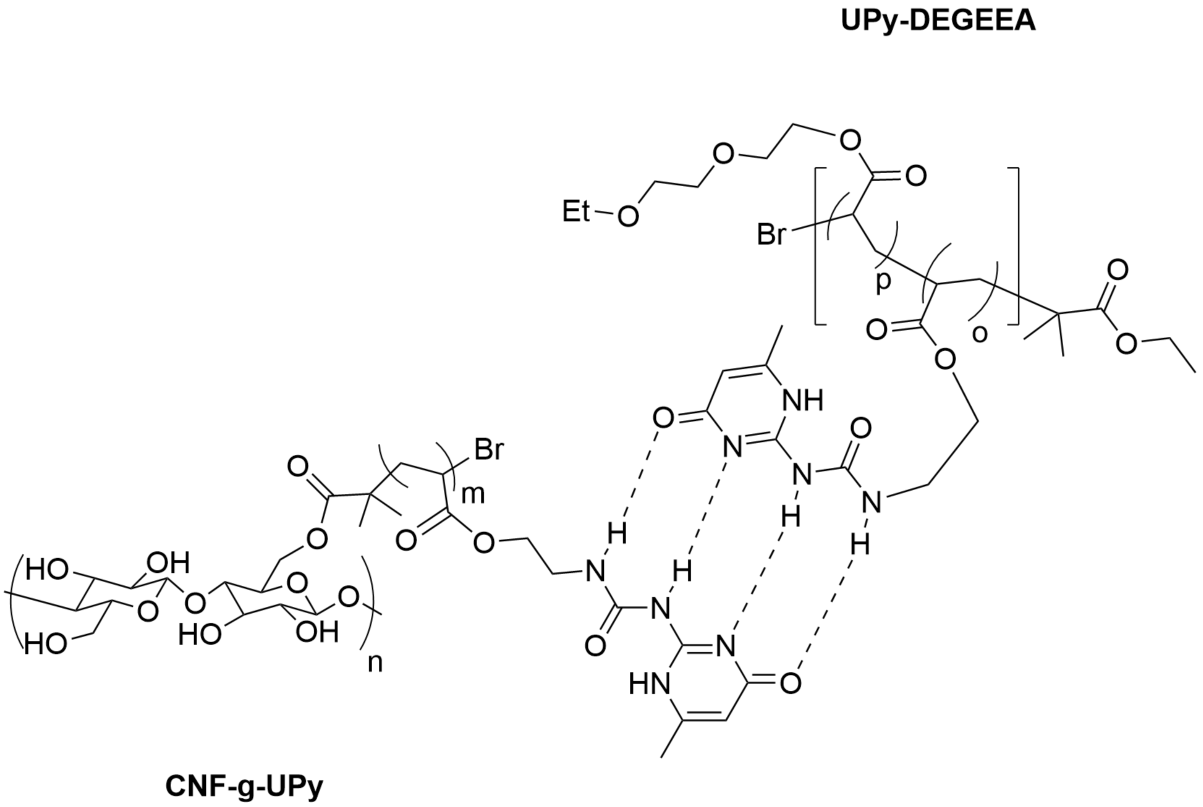

Scheme 12: Schematic illustration representing the types of bonds created between CNF-g-UPy and UPy-DEGEEA

Composite CNF-g-UPy/UPy-DEGEEA gels have been made by combining a 20 wt.% amount CNF-g-UPy. Rheology tests were conducted on the UPy-DEGEEA matrix, as well as CNF-g-UPy and CNF-g-UPy/UPy-DEGEEA composites to evaluate their properties and the results are shown in Figure 36. The composite demonstrated a five-fold increase in viscosity compared to UPy-DEGEEA, proving the reinforcing aspect of CNF-g-UPy and that both components exhibited good compatibility. The thixotropic behaviour was then studied as an extrusion simulation with varying shear rates over different ranges of time. All materials exhibited appropriate printing behaviour, with an immediate recovery to the initial viscosity after the removal of excessive shear rates. The viscoelastic properties were determined for a range of angular frequencies (0.1 to 100 rad·s^{-1}). The storage moduli (G') exhibited higher values than the loss modulus (G'') across the entire frequency range, which is indicative of a gel-like behaviour. The composite exhibited a higher modulus related to both CNF-g-UPy/UPy-DEGEEA, with very little variation over the range of defined angular frequencies. Lastly, an oscillating stress sweep was undertaken to mimic injectability, and upon reaching a critical shear stress level, all gels experienced a loss of viscoelastic properties. The high density of reversible supramolecular bonds in the composite, attributed to the dimerization functions of the UPy, accounted for these observations, as there is a correlation between viscoelastic properties and the number of cross-links[234].

Further rheological analysis was conducted on an unmodified CNF and UPy-DEGEEA polymer composite prepared in the same way as CNF-g-UPy/UPy-DEGEEA (results shown in *Appendix 2*). The storage modulus and loss modulus of CNF-g-UPy/UPy-DEGEEA showed an increase of a 3.7-fold increase in G' and a 2.8-fold increase in G'' measured compared to CNF/UPy-DEGEEA. These outcomes were consistent with the previous results and demonstrated the improved mechanical properties of the composite due to the high level of crosslinking.

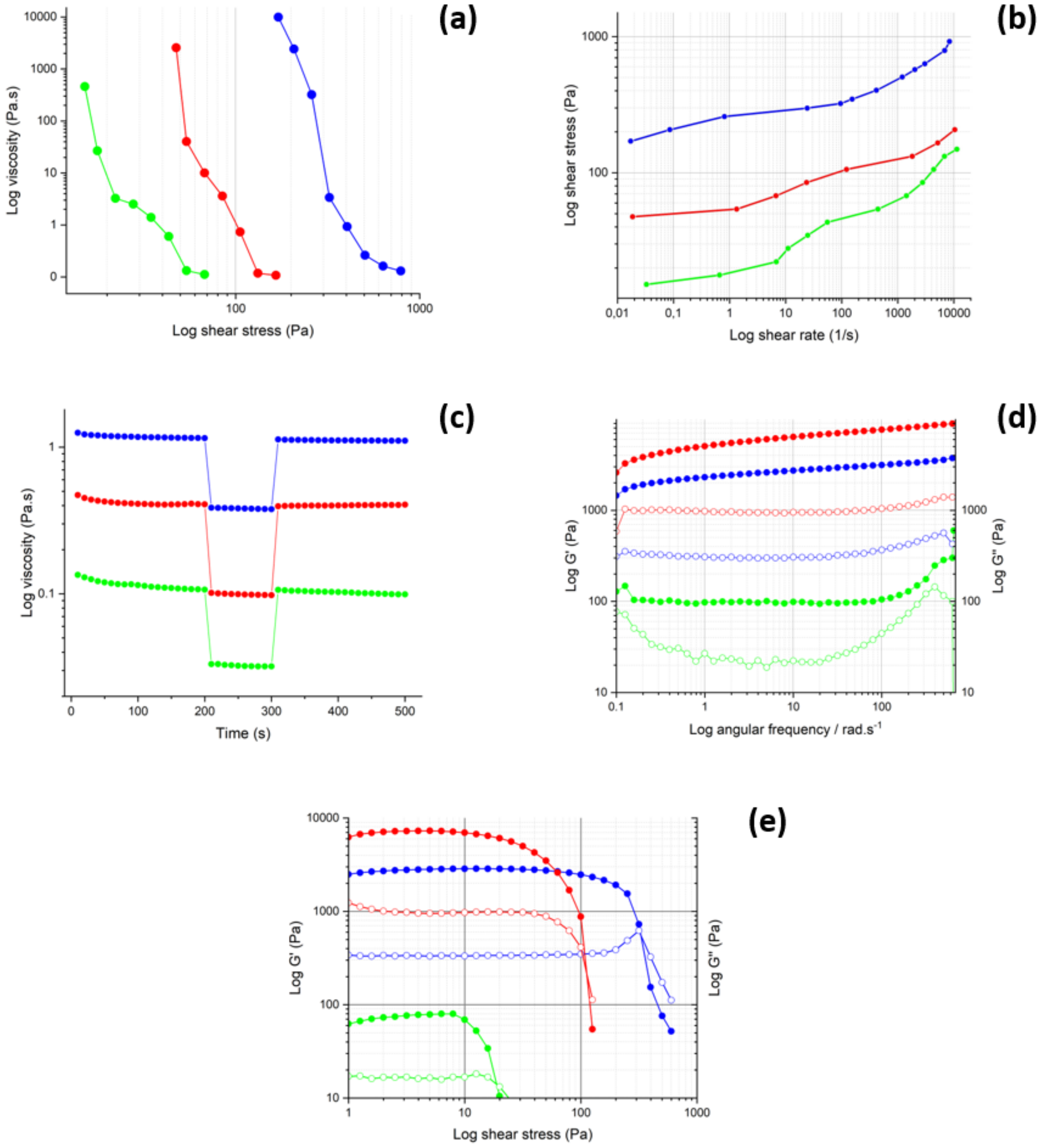

Figure 36: Rheological tests to assess gels printability; (a) Shear stress ramp data; (b) Flow curves (shear stress vs shear rate); (c) Thixotropic test (d) frequency sweep; (e) Oscillating stress sweep; red: CNF-g-UPy/UPy-DEGEEA; blue: CNF-g-UPy; green: UPy-DEGEEA. For viscoelastic properties, G' values are represented with full symbols and G'' with open symbols.

To examine the nanofibril morphology pre- and post-chemical modification, each of the compounds (CNF, CNF-g-UPy, and CNF-g-UPy/UPy-DEGEEA) underwent characterization via field emission scanning electron microscopy (FESEM). An image of unmodified cellulose (Figure 37a) displays a dense network of aggregated fibrils. Figure 37b depicts a clear spacing between the nanocellulose fibers, with spherical shapes present throughout, likely resulting from UPy moiety aggregation. These structures appear to be quite widely scattered and cover most of the visible fibrils. In contrast, considerably fewer distinguishable fibril structures can be observed in Figure 37c of composite CNF-g-UPy/UPy-DEGEEA. This outcome is anticipated due to the ratio of CNF-g-UPy (20 %) in the UPy-DEGEEA polymer.

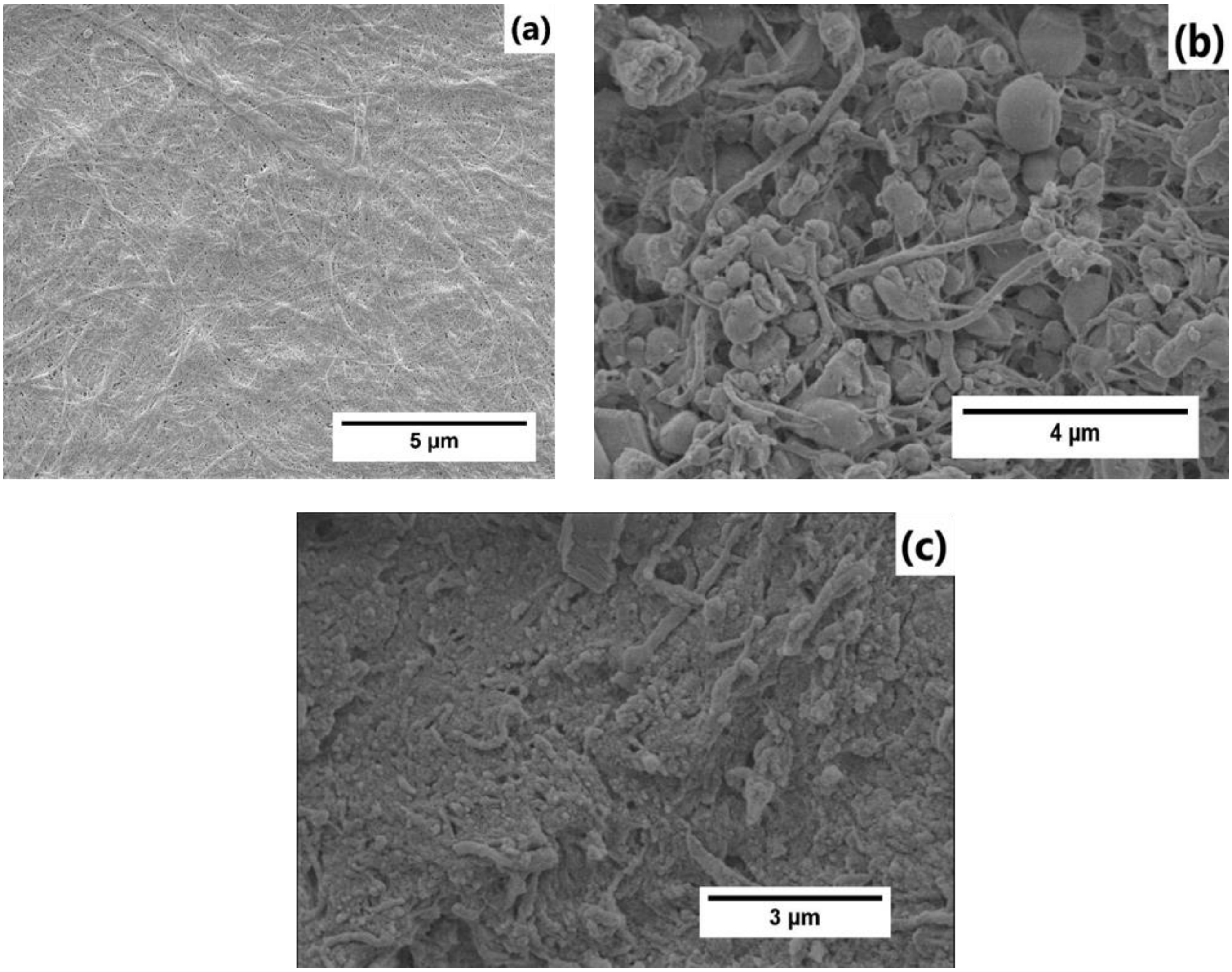

Figure 37: FESEM images of (a) CNF; (b) CNF-g-UPy; (c) CNF-g-UPy/UPy-DEGEEA.

Preliminary studies were carried out to assess the self-healing properties of the copolymer UPy-DEGEEA and the results are shown in Figure 38a. A sample was placed on an aluminium plate, split in two and then re-sealed after heating to 60 °C for approximately 2 minutes. Self-healing was observed, but a complete change in the structural appearance of the gel was observed, probably due to the poor physical properties of the polymer. To investigate the mechanism of self-healing in more detail, two parts of the gels were deposited on a glass plate, cut into two pieces and observed under a microscope. The composite was placed on a heated plate at 60 °C and the photographs taken before and after the experiment are shown in Figure 38b. As a result of the heating process, the two sections have combined and the incision has been reconstructed effectively, consequently showcasing the self-healing characteristics of the material.

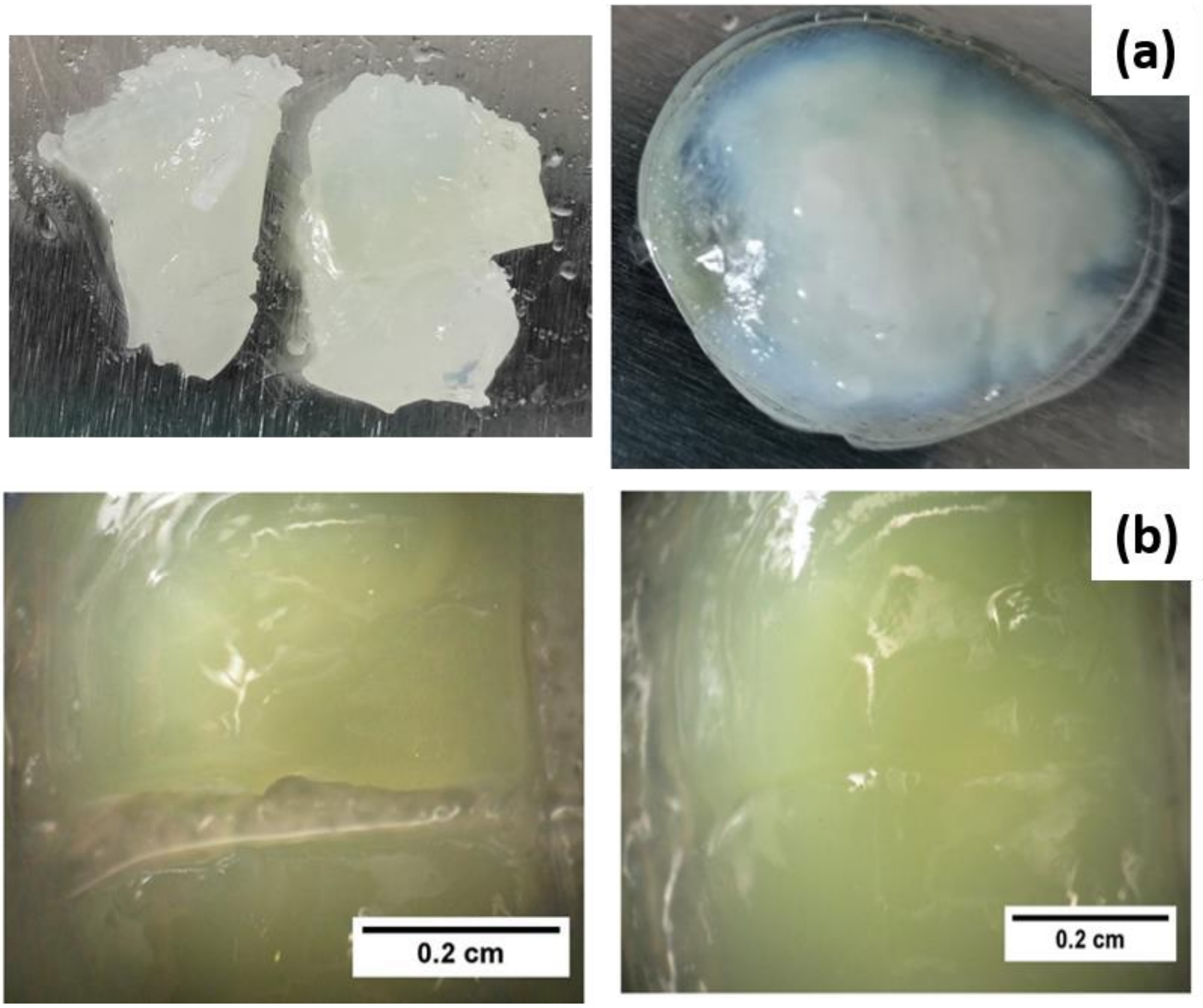

Figure 38: (a) Picture of DEGEEA-UPY sample before heating at 60 °C for 2 minutes before and after the heating; (b) Photograph of CNF-g-UPy/UPy-DEGEEA composite cut before self-healing at room temperature and after heating to 60 °C for 5 minutes.

To have a characterization of the printing quality, two designs have been developed. One of the samples consisted of part of a grid, while the second comprised a pattern with gradually increasing distances between each strand, ranging from 0.5 to 1 mm, to assess the fusion of each strand and the minimum distance between strands. The suitability of the UPy-DEGEEA polymer for printing models was evaluated, but despite attempts to dilute, homogenize and vary the nozzle size, printing was unsuccessful, and no satisfactory resolution was achieved, which is probably due to the physical properties of the polymer. The CNF-g-UPy/UPy-DEGEEA composite was then printed using a 0.59 mm nozzle and the results are shown in Figure 39. The partial lattice was produced with clearly defined strands and no structural collapse was observed. This result can be related to the previously observed improvement in rheological properties. A magnified image of the printed design featuring Rhodamine B-stained CNF-g-UPy/UPy-DEGEEA and notably, no significant strand fusion was observed within the 0.5 mm separated strands. These findings confirmed the printing capability of this composite and its appropriateness for extrusion gel printing.

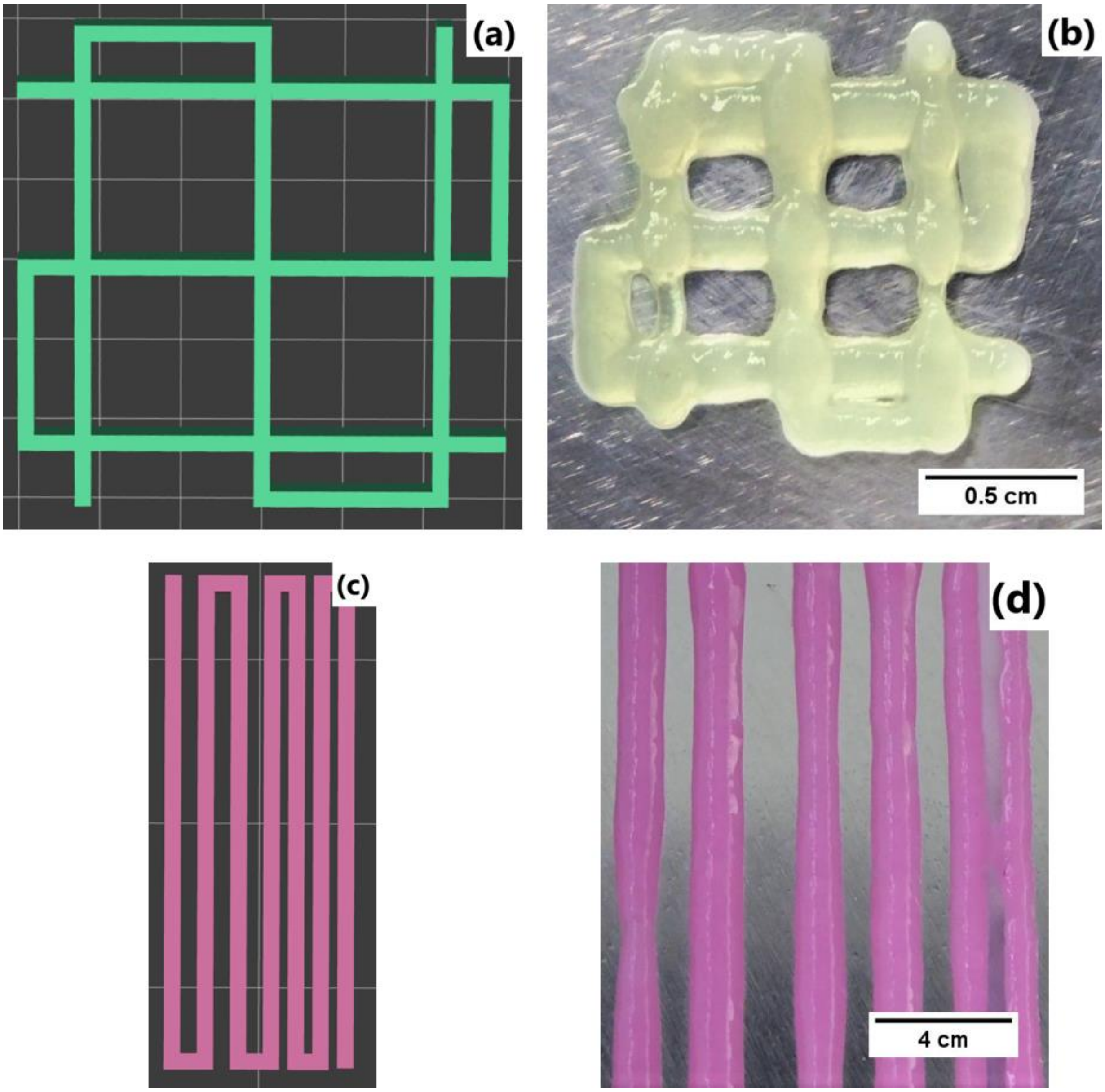

Figure 39: (a) 3D grid model composed of one layer of 15 x 15 mm with orthogonal strands; (b) Picture of the printed model using CNF-g-UPy/UPy-DEGEEA composite; (c) 3D models of a 12 x 30 mm layer, to evaluate minimal distance between the strands and gel-ink shape fidelity; (d) Zoomed picture of the printed model using CNF-g-UPy/UPy-DEGEEA composite.

To achieve a more significant and clearer outcome demonstrating the self-healing properties, two identical half arrows were printed which, after self-healing, would result in a complete arrow. The two models were created, and they were printed using the CNF-g-UPy/UPy-DEGEEA gel (Figure 40). Rhodamine B was used to dye one of the gels for better visibility and assessment of the gel's printing quality and superior impression. Subsequently, the produced gels were flash-frozen for transportation and positioned beside each other in preparation for self-healing (Figure 8c). Subsequently, they were brought together and positioned on a heating plate (60 °C) for two minutes, resulting in the successful self-healing shown in Figure 40. The self-healing process was successful without any degradation of the structure of the arrow. This phenomenon can be attributed to the superior mechanical performance of the composite.

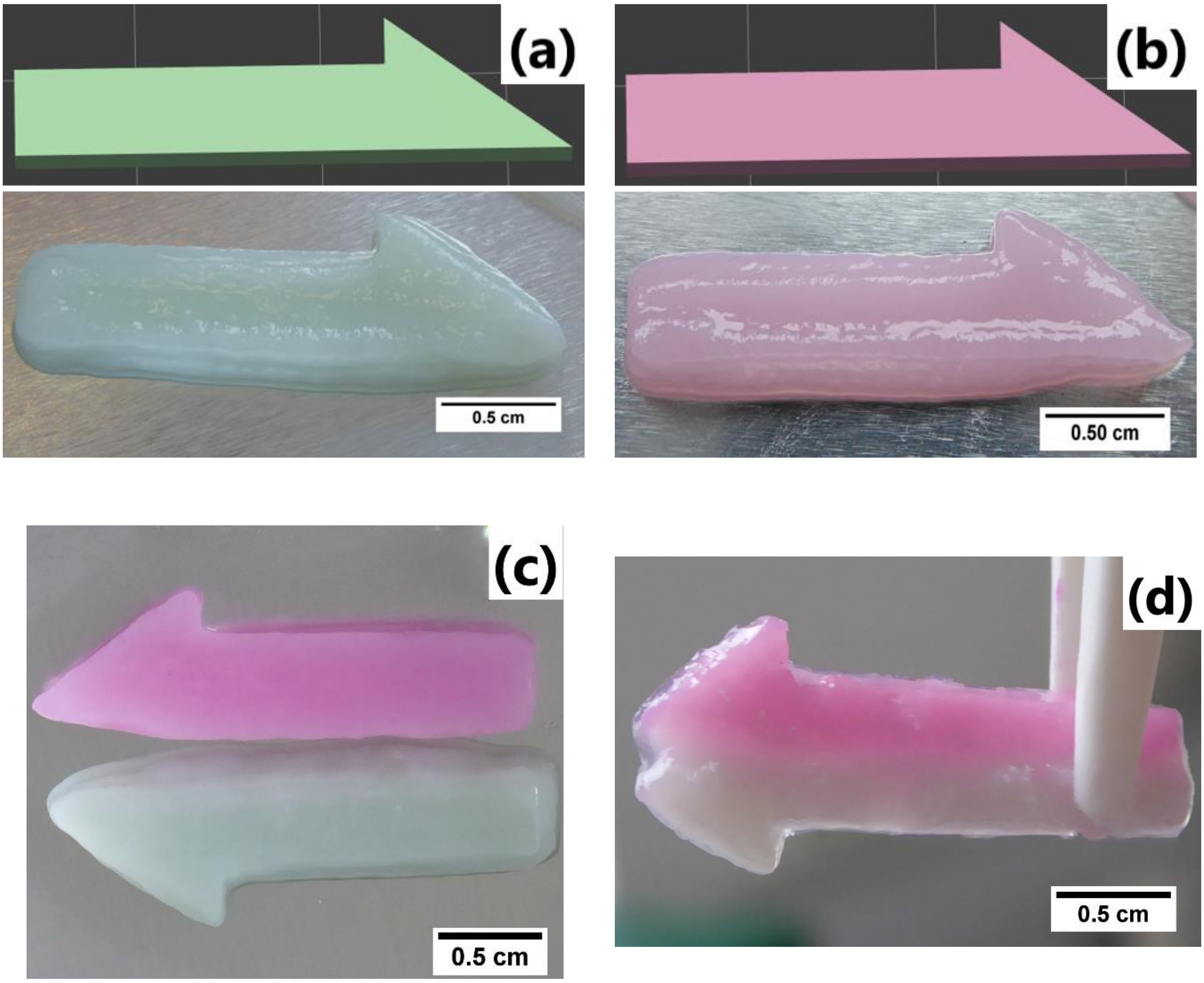

Figure 40: Templates of half-arrows at the top and pictures of the printed templates at the bottom, greenish gel corresponds to the unstained gel, and pink is the Rhodamine B-stained gel (a,b); pictures of the two half-arrows frozen and laid side by side (c); picture of the resulting arrow formed after that joined half-arrows were heated to 60 °C for 2 minutes. After completing the self-healing process, the newly reformed arrow was frozen for better handling with the tweezer (d).

For a closer examination of the self-repairing process, two strands of every composite gel were positioned on a glass plate. The undyed gel was situated above the coloured and viewed through an optical microscope (figure shown in *Appendix 2*). The microscope slide was placed on a heating bed and heated from 25 °C to 60 °C before cooling to 40 °C. The first striking effect was seen in the transparency of the gels upon heating, as they became translucent from their initial opaque appearance. This transition is observed at a temperature of approximately 60 °C and reversed when the temperature is reduced. The decrease in supramolecular interaction, therefore, leads to a greater degree of molecular mobility, which is associated with a change in the material's optical properties and light transmittance[235]. This high mobility also allows for new molecular rearrangement among the whole structure upon recovery to room temperature. This was supported by the opaque reappearance after cooling. The edges of the two bands appeared to be less marked and were accompanied by a decrease in the colour of each gel, indicating a diffusion of the dye (rhodamine B) between the two gels.

2.2.3 Composites based on Fmoc-FF with unmodified and modified cellulose nanofibrils

This study aimed to prepare Fmoc-FF based composite gels. The gelation method used was solvent-induced because of its simplicity and efficiency. The use of Fmoc-FF in printing has been previously documented. However, the print quality achieved was quite unsatisfactory[200]. Scheme 13 displays a schematic illustration of the bonds established between the CNF-g-Fmoc and Fmoc-FF.

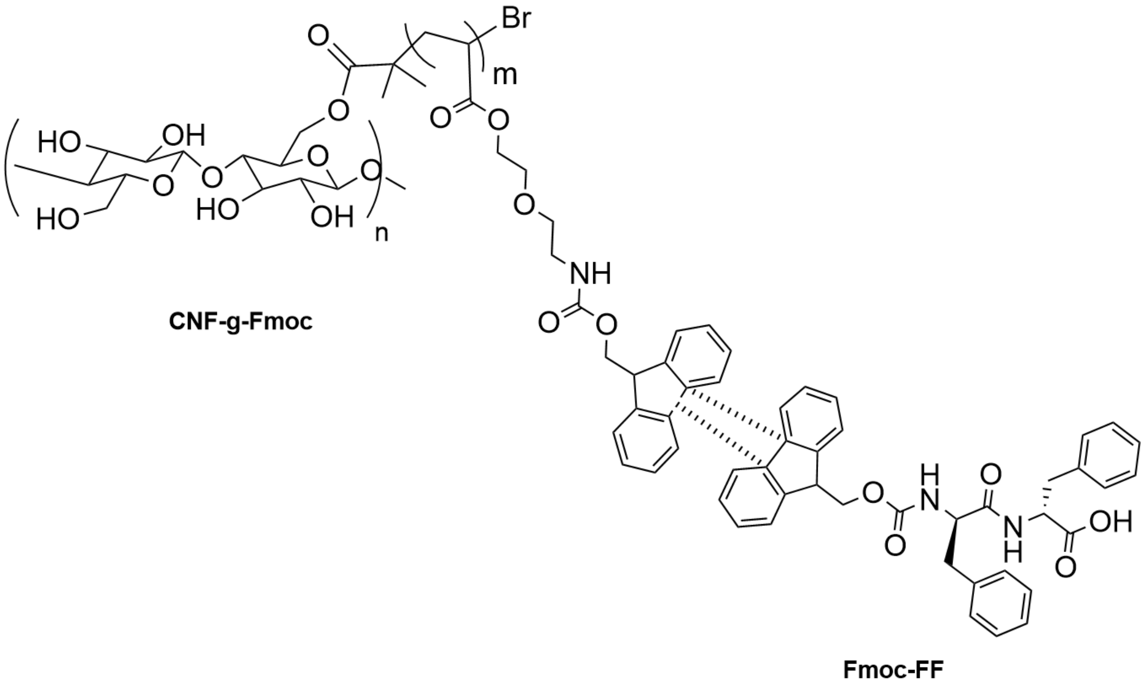

Scheme 13: Schematic illustration representing the types of bonds created between CNF-g-Fmoc and Fmoc-FF. Non-continuous lines represent the π-π bonds.

Therefore, the present research aimed to determine if improved printing quality could be achieved by using CNF as an filler. The solvent DMSO was chosen to dissolve the peptide and water to trigger gelation. Dudukovic *et al.* reported a concentration range within which a Fmoc-FF solution in DMSO formed gels on the addition of water[236,237]. Their research showed a Power-law relationship between the dilution of water and the volume fraction of Fmoc-FF solvent. This method was used to calculate the fractions of solvent needed to produce the desired composite gels, with a concentration of 3.4 wt.% and a DMSO volume ratio of 0.66.

To determine the appropriate gel formulation, e.g. the ratio of the individual components, unmodified CNF was first used due to its accessibility and availability. Different ratios of Fmoc-FF and CNF (75:25, 50:50) were produced with identical final concentration and volume ratios of DMSO. Table 5 presents the characteristics and properties of the prepared gels as well as the mechanical properties. Measurements indicated that the higher peptide content gel exhibited higher viscoelastic properties compared to the lower peptide content gel. Based on this observation, and considering the availability and affordability of Fmoc-FF, as opposed to CNF which requires extraction, a ratio of 75 % Fmoc-FF and 25 % CNF was determined to be the appropriate ratio.

Table 5: Summary of the characteristics of CNF/Fmoc-FF composite gels with different ratios. Young's and loss modulus were measured by rheology.

CNF/Fmoc-FF ratio	concentration wt.%	ϕ_{DMSO}	*G'* /Pa	*G''* /Pa	Pressure applied during 3D-printing /kPa
75:25	2.67	0.66	14,530	2848	31
50:50	2.67	0.66	7,772	1021	15

a) Fmoc-FF and cellulose nanofibrils composite (CNF/Fmoc-FF).

A range of CNF/Fmoc-FF gels were prepared at different dilutions and concentrations and their characteristics and properties, as well as mechanical data, are shown in Table 6. These are sequentially labelled from CNF/Fmoc-$FF_{7.50}$ to CNF/Fmoc-$FF_{3.89}$ in ascending order of dilution in water, with the subscript number to designate the concentration of the composite gel. The mechanical properties of CNF/Fmoc-FF$_{7.50}$, obtained without water addition, were the weakest, exhibiting the lowest values for storage, loss modulus, and yield stress. This can be attributed to the absence of nucleation and consequent gelation of Fmoc-FF, resulting in properties that reflect only those of CNF. With the addition of water, a slight increase in viscoelastic properties was observed, slightly influencing mechanical properties. However, a significant improvement was observed in CNF/Fmoc-FF$_{6.40}$ and CNF/Fmoc-FF$_{6.20}$, which indicated the gel point. This corresponds to the point at which the Fmoc-FF fragments start to nucleate in large clusters, incapable of dissolving and forming a structure based on the lateral π-π stacking of antiparallel ß-sheets[206]. Increasing dilution (starting from CNF/Fmoc-FF$_{5.74}$) allowed the formation of a larger hydrogen bonding network, resulting in a larger reinforced intramolecular 3D network. This automatically lead to a constant improvement in mechanical properties. This observation suggests that the increase in mechanical properties and gelation were primarily influenced by the volume of water within the system rather than its concentration**.**

Table 6: Summary of the characteristics of CNF/Fmoc-FF composite gels; ϕ: volume ratio; * gel unprintable even after 100 kPa applied pressure; ** After 5 minutes of high-speed mixing, required from the obtaining of homogeneous gel.

	Concentration / wt.%	ϕ (DMSO)	*G'* / Pa	*G''* / Pa	Yield stress / Pa	Pressure applied for printing (kPa)
CNF/Fmoc-FF$_{7.50}$	7.50	1	3,172	385	147	15
CNF/Fmoc-FF$_{6.40}$	6.40	0.83	4,066	547	152	17
CNF/Fmoc-FF$_{6.20}$	6.20	0.80	4,491	1,203	587	70
CNF/Fmoc-FF$_{5.74}$	5.74	0.74	105,400	24,130	1259	15**
CNF/Fmoc-FF$_{5.10}$	5.10	0.66	233,800	55,850	2074	18**
CNF/Fmoc-FF$_{3.89}$	3.89	0.50	274,900	70,000	3268	Unprintable*

Rheological measurements have also been carried out. Rheological measurements have also been carried out and the resulting plot is displayed in Figure 41. A shear stress sweep was conducted on the composite gels, all of which exhibited a shear-thinning effect, reflected by a decrease in viscosity with an increase in shear stress. The thixotropic test demonstrated a print-friendly behaviour, as evidenced by the instant recovery of initial viscosity after the removal of the shear rate, which is indicative of the state of equilibrium and the rapid re-forming capacity of the bonds within the gel. As can be seen, CNF/Fmoc-FF$_{3.89}$ exhibited a slight drop in viscosity within the test measurements because the material is closer to a solid than a gel and tends to creep out of the measurement range, giving a misleading drop in viscosity.

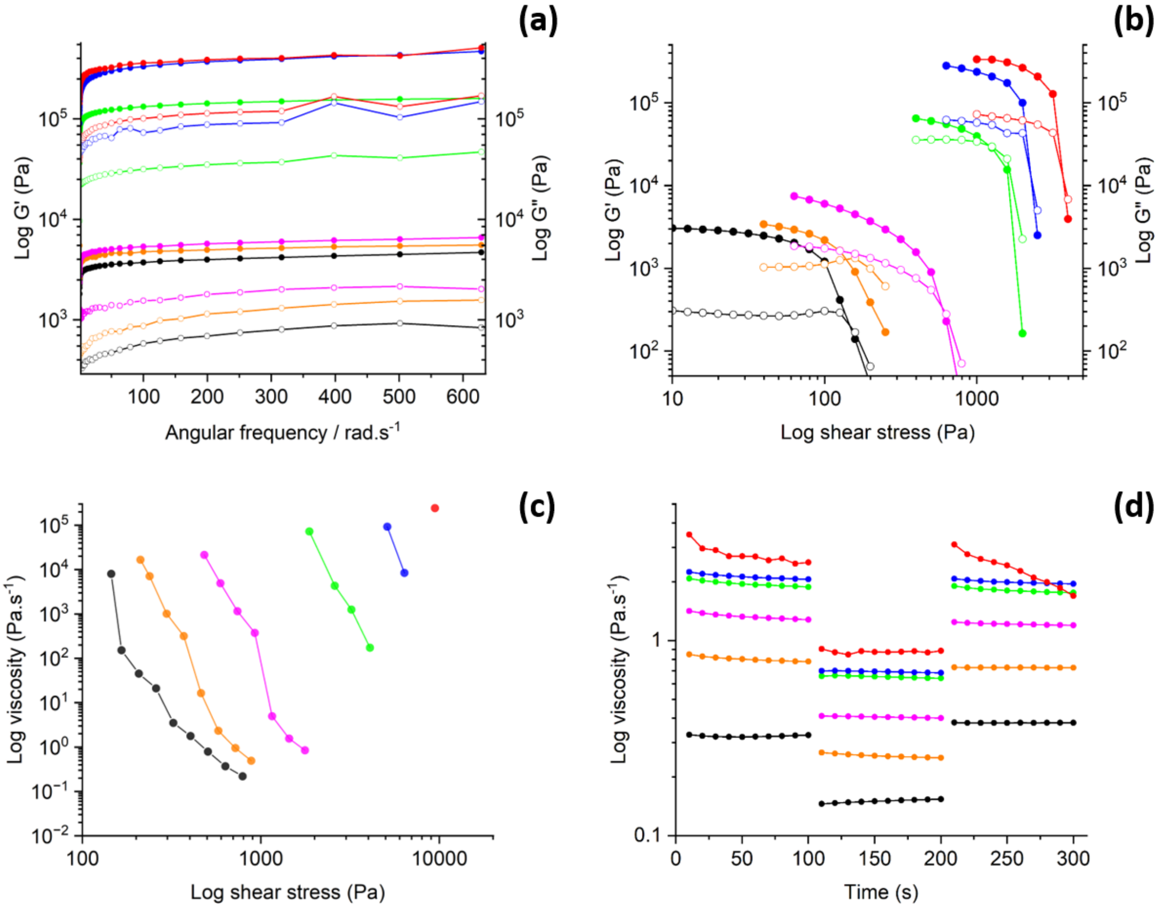

Figure 41: Rheological tests to assess CNF/Fmoc-FF composite gels printability (a) frequency sweep plot; (b) oscillating stress sweep for yield stress measurement; (c) shear stress ramp data; (d) Thixotropic tests with different shear rates; Colours code: CNF/Fmoc-FF$_{7.50}$: black, CNF/Fmoc-FF$_{6.40}$: orange, CNF/Fmoc-FF$_{6.20}$: magenta, CNF/Fmoc-FF$_{5.74}$: green, CNF/Fmoc-FF$_{5.10}$: blue, CNF/Fmoc-FF$_{3.89}$: red.

b) Fmoc-FF and Fmoc-AEEA grafted cellulose nanofibrils composite (CNF-g-Fmoc/Fmoc FF).

Since the addition of CNF to the Fmoc-FF peptide was found to result in enhanced mechanical properties and suitability for 3D gel printing, the question arises as to whether modified Fmoc-grafted cellulose nanofibrils (CNF-g-Fmoc) would have any additional advantage. Following an identical preparation method (same mixing, concentrations and volume ratio of DMSO) as the composite gels prepared with cellulose nanofibrils (CNF/Fmoc-FF), with the exception that CNF was replaced by CNF-g-Fmoc, a new set of composites were obtained and designated CNF-g-Fmoc/Fmoc-FF. The rheological properties were assessed to determine the mechanistic properties and the findings are presented in Table 7. As an initial observation, it is noteworthy that all gels, except CNF/Fmoc-FF$_{3.89}$, obtained with CNF-g-Fmoc as an additive displayed notably poorer mechanical properties when compared to those produced with CNF, which at first glance is rather unexpected. A marked contrast is observed between CNF-g-Fmoc/Fmoc-FF$_{5.74}$ and CNF-g-Fmoc/Fmoc-FF$_{5.10}$, with a rapid increase in mechanical properties, implying that higher water content is required to produce a stiffer structure. Additional interactions, namely π-π-interaction and hydrophobic bonding, lead to a higher aggregation effect and could explain the obtained results. However, at the same concentration and volume DMSO ratio, CNF-g-Fmoc/Fmoc-FF$_{3.89}$ exhibited superior mechanical properties (*G'*, *G''*, and yield strength) compared to its counterpart composite, made with unmodified CNF as an additive. This is an indication that the additional interactions result in a gel that is stronger overall and is closer to a 'solid' than a 'gel'. Figure 42 displays the detailed rheological outcomes obtained through the same procedures used previously. However, CNF-g-Fmoc/Fmoc-FF$_{3.89}$ could not be measured for rotational recovery due to a gradual viscosity decline at a steady shear speed, making it unsuitable for analysis. To compare and visualise the mechanistic results, the *G'* and *G''* of the gels at their maximum dilutions are presented in a bar chart.

Table 7: Summary of the characteristics of composite made using CNF-g-Fmoc; ϕ: volume ratio; * The gel is too thin;

	Concentration wt.%	ϕ_{DMSO}	*G'* /Pa	*G''* /Pa	Yield stress /Pa)	Pressure applied for printing /kPa
CNF-g-Fmoc/Fmoc-FF$_{7.50}$	7.50	1	15	3	0.32	Unprintable*
CNF-g-Fmoc/Fmoc-FF$_{6.40}$	6.40	0.83	31	5	2	Unprintable*
CNF-g-Fmoc/Fmoc-FF$_{6.20}$	6.20	0.80	452	57	20	12
CNF-g-Fmoc/Fmoc-FF$_{5.74}$	5.74	0.74	2537	407	146	43
CNF-g-Fmoc/Fmoc-FF$_{5.10}$	5.10	0.66	95,300	27,460	1,268	25**
CNF-g-Fmoc/Fmoc-FF$_{3.89}$	3.89	0.50	452,400	80,680	7,012	Unprintable*

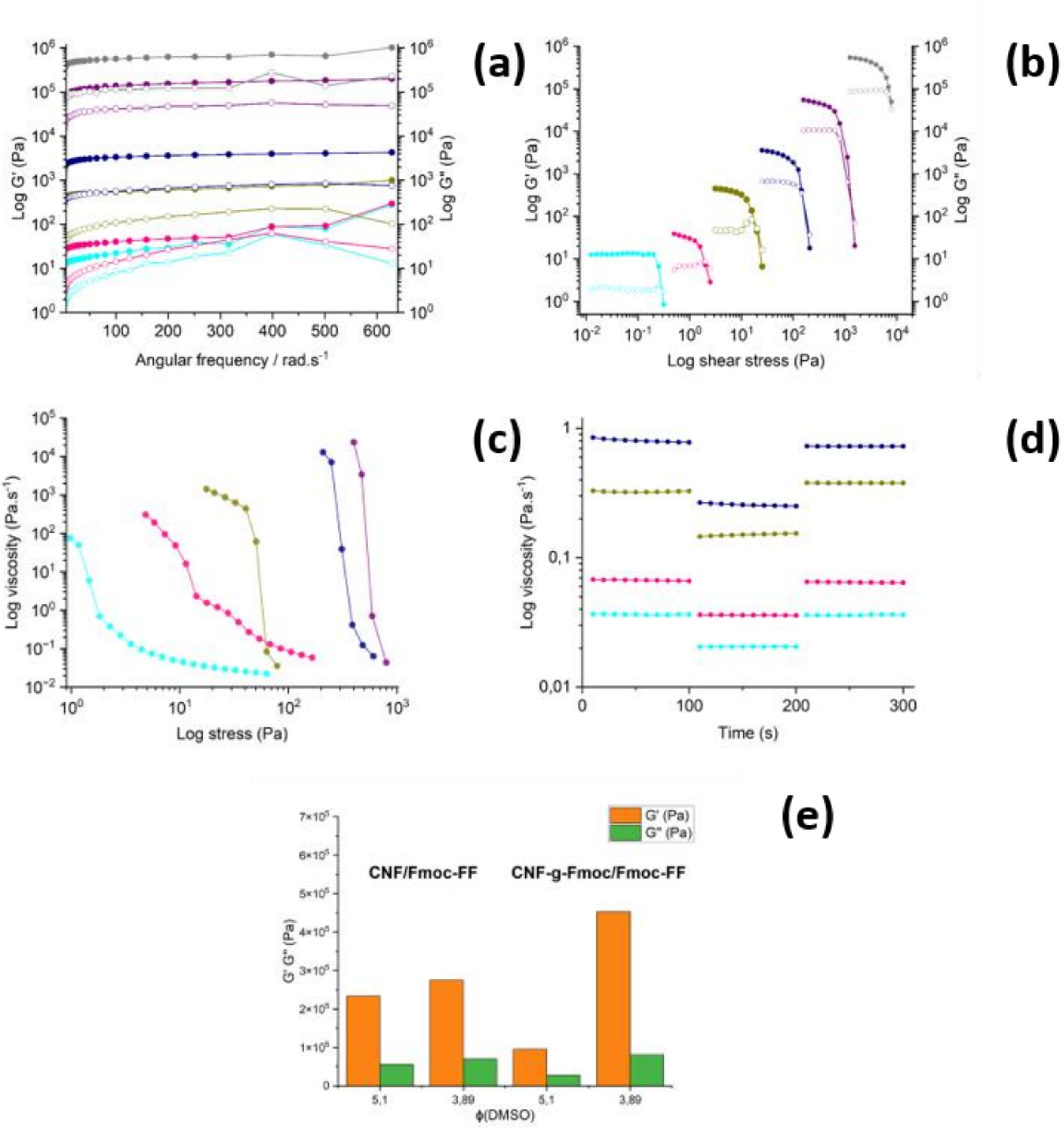

Figure 42: (a) frequency sweep plot; (b) oscillating stress sweep for yield stress measurement; (c) shear stress ramp data; (d) thixotropy tests with different shear rates (CNF-g-Fmoc/Fmoc-FF$_{3.89}$ data is not represented) (e) bar graph comparison of the viscoelastic properties of two composite gels at their higher dilutions. Colours code: CNF-g-Fmoc/Fmoc-FF$_{7.50}$: cyan, CNF-g-Fmoc/Fmoc-FF$_{6.40}$: pink, CNF-g-Fmoc/Fmoc-FF$_{6.20}$: dark yellow, CNF-g-Fmoc/Fmoc-FF$_{5.74}$: navy, CNF-g-Fmoc/Fmoc-FF$_{5.10}$: purple, CNF-g-Fmoc/Fmoc-FF$_{3.89}$: grey.

Field Emission Scanning Electron Microscopy (FESEM) was used to gain a more detailed insight into the fibril structure of Fmoc-FF and composites. An air-dried sample of Fmoc-FF with a ϕ(DMSO) of 0.66 and c of 3.89 wt.% was analysed and the results are shown in Figure 43a. This revealed a densely packed network of small rod-shaped and twisted nanowire structures with a mean fibril diameter of approximately 150 nm. These observed patterns and fibril diameters are in agreement with previous reports in the literature[209,238]. Figure 43b presents the obtained image of the CNF/Fmoc-FF$_{6.20}$ composite gel (ϕ(DMSO) of 0.83 and c of 6.40 wt.%), which was supercritical CO_2 dried to prevent the structure collapse. Two distinct network patterns were observed: one consisting of large, easily identifiable nanocellulose fibrils, and the smaller fibrils interspersed like a web. The dimensions and proportions suggested that the latter corresponds to Fmoc-FF. Then the CNF/Fmoc-FF$_{5.10}$ was dried in the same manner, resulting in a similar double network pattern (Figure 43c). However, the dispersion of the fibrils seemed significantly greater, and it was possible to identify each individually. Interestingly, CNF-g-Fmoc resulted in composites with a significantly different internal structure. The structure of CNF-g-Fmoc/Fmoc-FF$_{6.40}$ appeared to be more uniform, and it was not apparent which fibrils were present in each network (Figure 43d). The earlier rheological analysis revealed a slight delay in the gelation process, which may account for this result. However, at higher dilutions of the gel (CNF-g-Fmoc/Fmoc-FF$_{5.10}$) the structures of both networks become more distinct and similar to that shown above.

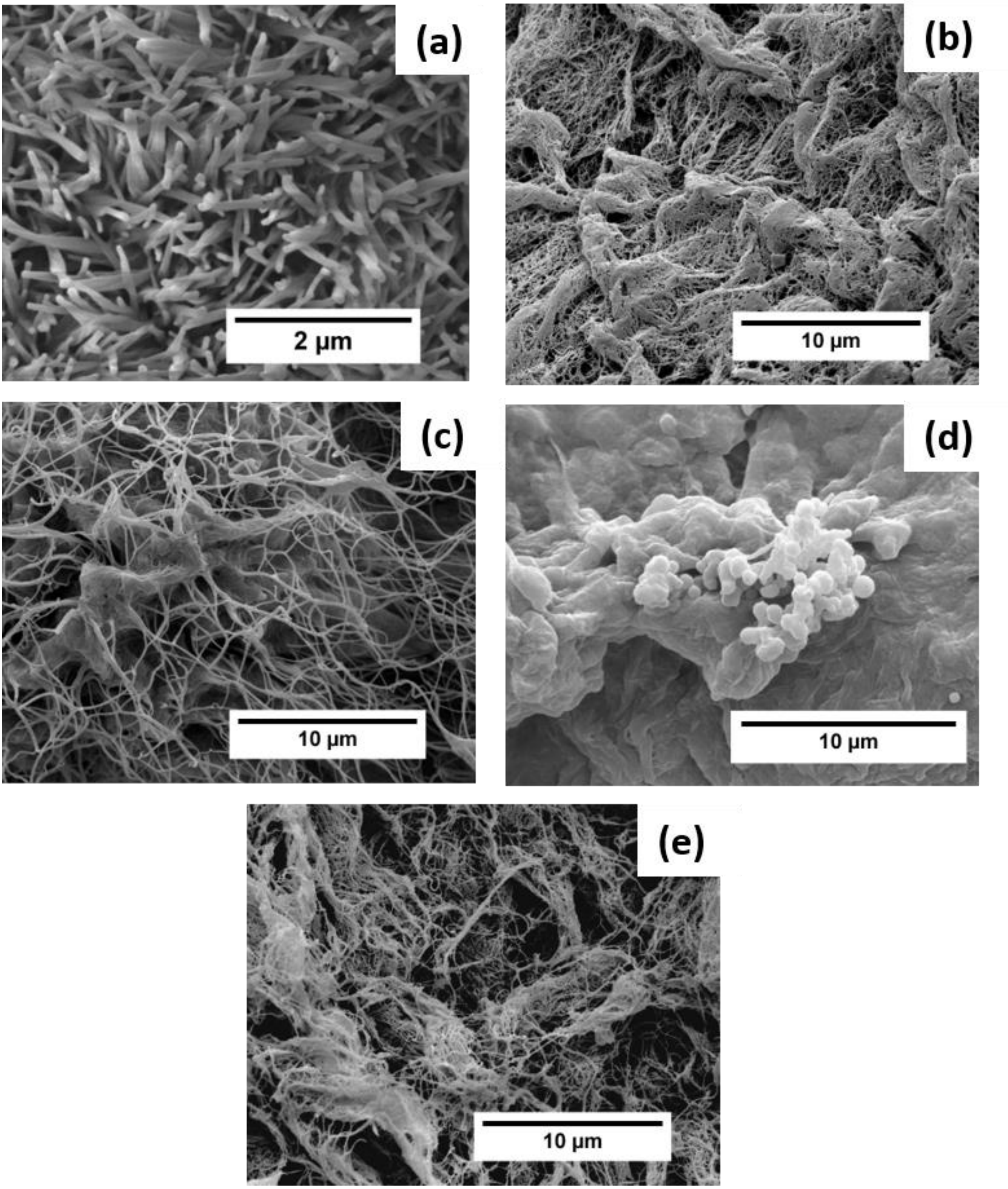

Figure 43: Field emission scanning electron microscopic (FESEM) images; *(a) Fmoc-FF sample, air dried; (b) CNF/Fmoc-FF*$_{6.40}$*, supercritical* CO_2 *dried; (c) CNF/Fmoc-FF*$_{5.10}$*, supercritical* CO_2 *dried; (d) CNF-g-Fmoc/Fmoc-FF*$_{6.40}$*, supercritical* CO_2 *dried; (e) CNF-g-Fmoc/Fmoc-FF*$_{5.10}$ *supercritical* CO_2 *dried.*

As strong evidence indicates that composites comprising Fmoc-FF and CNF, whether modified or not, exhibit superior, adjustable properties as measured by rheology, their potential as effective gel inks is significant, and preliminary tests on each gel were carried out. Each gel was used to print grid models, consisting of square models measuring 1.75 x 1.75 x 2 cm and containing four identical holes, allowing for the assessment of each gel's printing resolution. Photographs of the models can be found in Figure 44. It is worth noting that the gels were more translucent before the addition of water and became cloudy after the addition of water. This rise in absorbance was indicative of the peptide nucleation phase self-assembly[239]. No reduction in cloudiness was observed over time, which suggests that stable structures were formed that were of sufficient nanosize to scatter light[240,241]. The printing of the CNF/Fmoc-FF gels was initially carried out and all gels were printable. CNF/Fmoc-$FF_{7.50}$ gel, which was less diluted, showed rather poor print quality and the structure failed to be retained. The assumption that CNF/Fmoc-$FF_{6.40}$ hasn't reached its full gelation point as previously claimed can be confirmed as it remains translucent. Beyond this point, the compounds gradually turned increasingly white, suggesting the formation of structures large enough to scatter light. As the water content of the gel increased, the quality of grid printing improved. Compared to other gels, the CNF/Fmoc-$FF_{3.89}$ composite gel, which had the highest mechanical properties, displayed more solid-like behaviour. This made it difficult to extrude under the extrusion pressure of the gel 3D printer, resulting in poor shape uniformity during the first attempt. Studies have demonstrated that intense mixing alters the properties of the gel, improving the homogeneity of the hydrogel and the quality of the 3D printed structures[121,242]. Viscoelasticity and yield strength were measured both before and after 5 minutes of intensive mixing with a high-speed stirrer (ROTI®Speed). An associated reduction in mechanical properties was noted and can be particularly attributed to the decrease in particle size, facilitating printing (figure shown in *Appendix 3*). Nevertheless, due to its concentration, the material exhibited a degree of syneresis under extrusion pressure, rendering printing difficult. As a result, CNF/Fmoc-$FF_{5.10}$ was found to produce the most consistent and highest-quality print, thus making it an excellent candidate for further use. Furthermore, a printed sample of CNF/Fmoc-$FF_{6.40}$ is shown, which was left for two days in ambient conditions and proved to be solid enough to handle with tweezers, despite being in gel form. This illustrates the positive impact of ageing on the gel's properties. Printing was carried out using the CNF-g-Fmoc/Fmoc-FF composites. CNF-g-Fmoc/Fmoc-$FF_{7.50}$ and CNF-g-Fmoc/Fmoc-$FF_{6.40}$ were found unsuitable for printing due to their low viscosity. When compared to the analogous gels, the weaker properties reflected their reduced gelation and interaction between the components. CNF-g-Fmoc/Fmoc-$FF_{6.20}$ was used for printing, however, the quality of the print was poor due to a lack of definition. On the other hand, CNF-g-Fmoc/Fmoc-$FF_{5.74}$ produced satisfactory results. Increasing dilution resulted in significantly higher clumping and the formation of larger and more robust gel particles, which prevented CNF-g-Fmoc/Fmoc-$FF_{5.10}$ from being printable with intense stirring (used in CNF/Fmoc-FF). While this further mixing rendered the gel printable, it had a detrimental effect on the mechanical properties of the gel, resulting in reduced print quality. CNF-g-Fmoc/Fmoc-$FF_{3.89}$ failed to print due to pronounced, syneresis effects as seen with CNF/Fmoc-$FF_{3.89}$. As a result, CNF-g-Fmoc/Fmoc-$FF_{5.10}$ produced the most consistent and precise print quality and was therefore chosen as a suitable candidate for subsequent use.

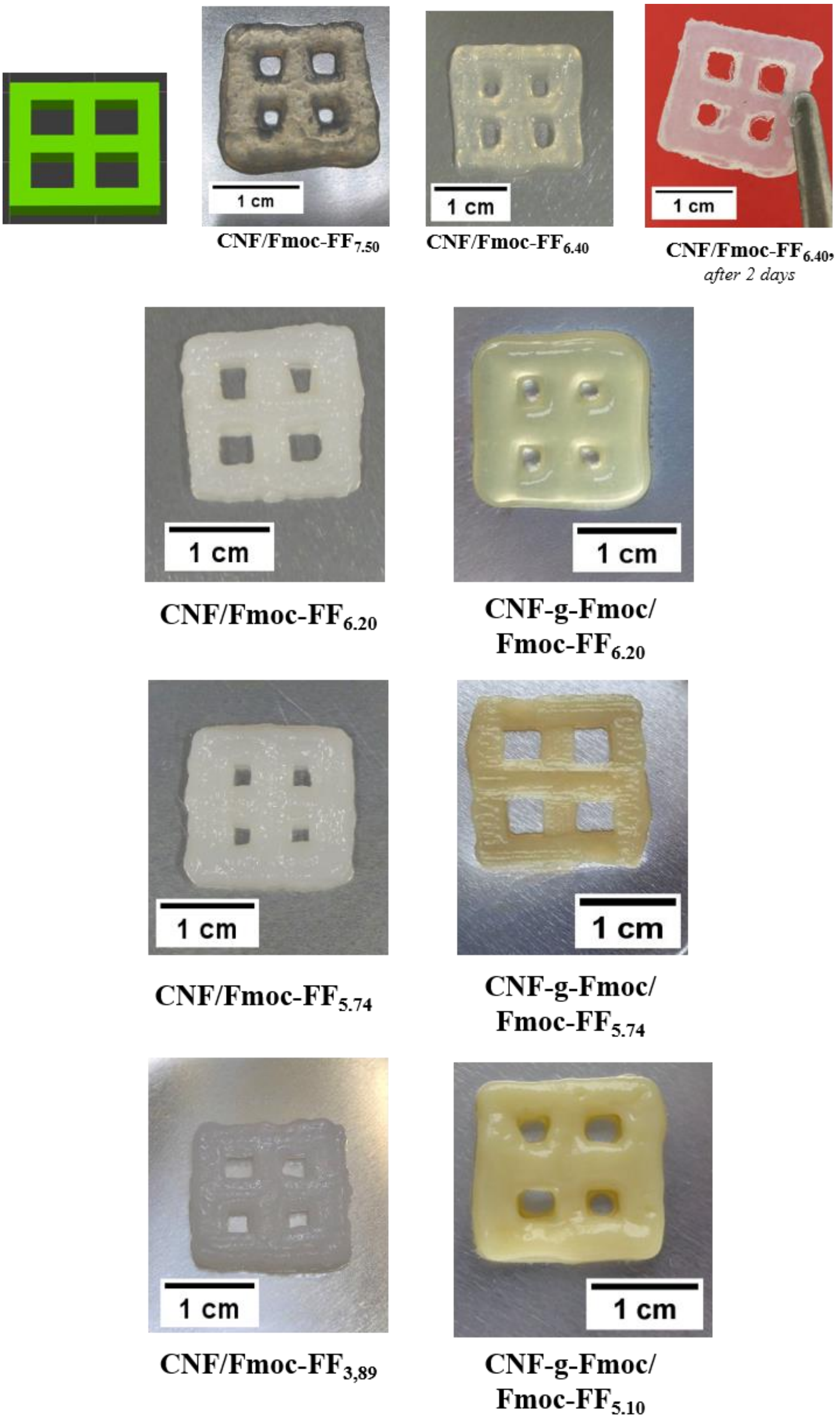

CNF/Fmoc-FF$_{7.50}$

CNF/Fmoc-FF$_{6.40}$

CNF/Fmoc-FF$_{6.40}$, *after 2 days*

CNF/Fmoc-FF$_{6.20}$

CNF-g-Fmoc/Fmoc-FF$_{6.20}$

CNF/Fmoc-FF$_{5.74}$

CNF-g-Fmoc/Fmoc-FF$_{5.74}$

CNF/Fmoc-FF$_{3,89}$

CNF-g-Fmoc/Fmoc-FF$_{5.10}$

Figure 44: Picture of the printed grids models using CNF/Fmoc-FF and CNF-g-Fmoc/Fmoc-FF composite gels.

The suitable gels from each set of composites were used to produce objects with varying levels of complexity. The fidelity to the original patterns, uniformity of extruded strains and the visual appearance were the evaluation factors for the quality of these models. The designs selected for this study consisted of a twelve-spoke wheel, a star and a bridge. Figure 45 presents these models alongside a screenshot of the 3D model and a photo of the printed results. To ensure uniformity and consistency in the preparation procedure, both products underwent rigorous mixing for five minutes with high intensity before printing. This ensures a higher level of control over the outcome of each print, as anomalies or variations in the extrusion could affect the quality and overall integrity of the finished product. While both gave satisfactory results with the wheel pattern, there was a noticeable lack of strain uniformity for CNF-g-Fmoc/Fmoc-$FF_{5.10}$. The star model showed also good printing properties for both composites. The superior mechanical properties of the gel were demonstrated by printing a bridge with several weak points. These weak points are essentially the central deck (or keystone), whose weight is supported by the two adjacent piers. The gel must be strong enough to support this and not collapse under gravity. Both products produced bridges capable of supporting the load of the deck, with CNF/Fmoc-$FF_{5.10}$ delivering more defined results. Prints displayed from CNF-g-Fmoc/Fmoc-$FF_{5.10}$ gel were obtained under optimal mixing and homogenization conditions. Various alternative techniques were tested, including slower mixing, drop-by-drop gelation, and heating cycles at 40 °C, but no significant improvement was achieved. These new composite gels were capable of excellent 3D printing quality with only one mixing step and no post-processing required.

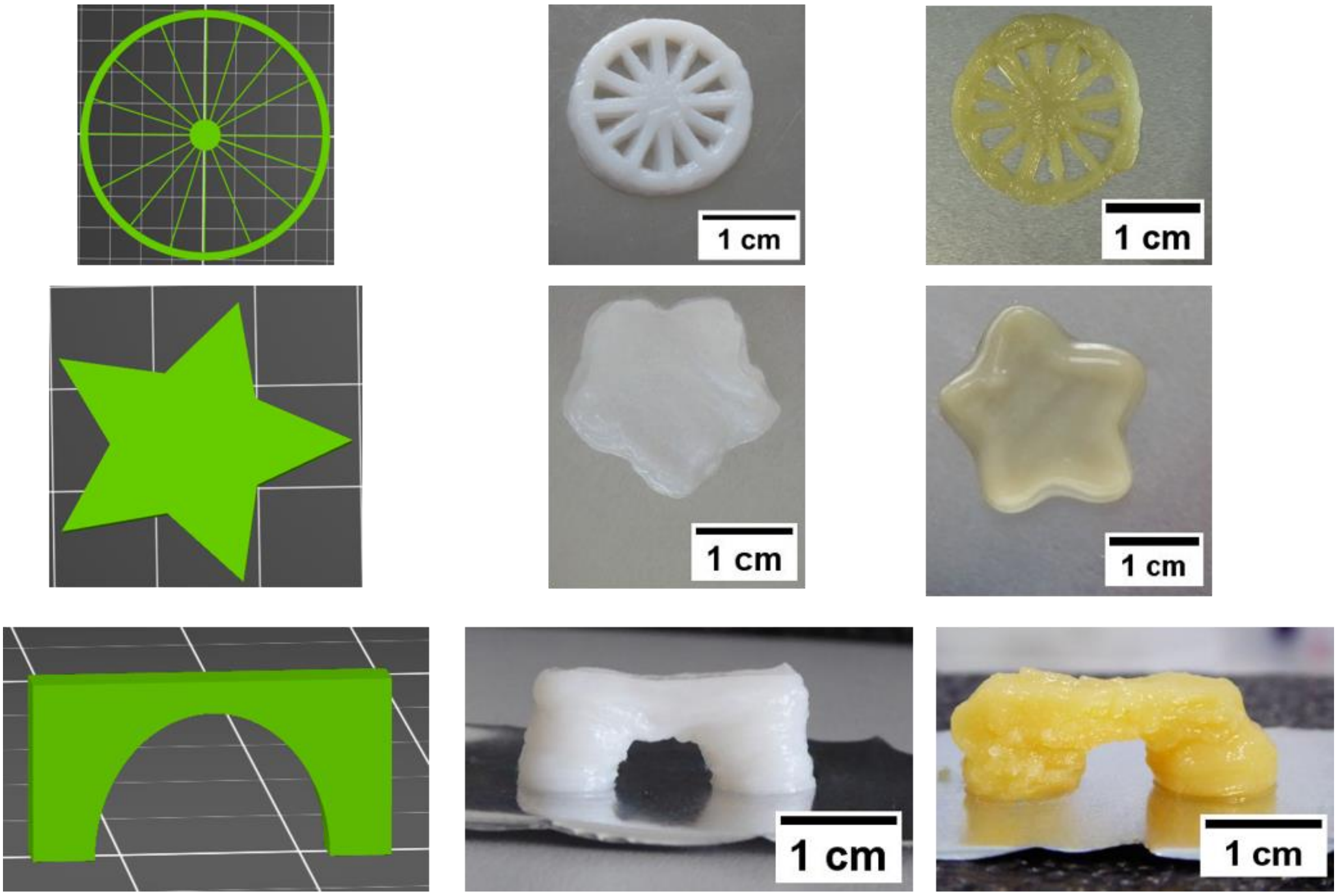

Figure 45: Screenshot from the slicer displaying the 3D model (wheel, star, circle and bridge); Photographs of the resulting prints; White gel: CNF/Fmoc-$FF_{5.10}$ & yellow gel: CNF-g-Fmoc/Fmoc-$FF_{5.10}$.

Supercritical drying was conducted on CNF/Fmoc-$FF_{5.10}$ and CNF-g-Fmoc/Fmoc-$FF_{5.10}$ grid models made from gels, which underwent sequential solvent exchange with ethanol beforehand. Photographs of the aerogels, specifically *SCD*:CNF/Fmoc-$FF_{5.10}$ and *SCD*:CNF-g-Fmoc/Fmoc-$FF_{5.10}$, are presented in Figure 46. The aerogels appeared to have retained their structural integrity with minimal deformation.

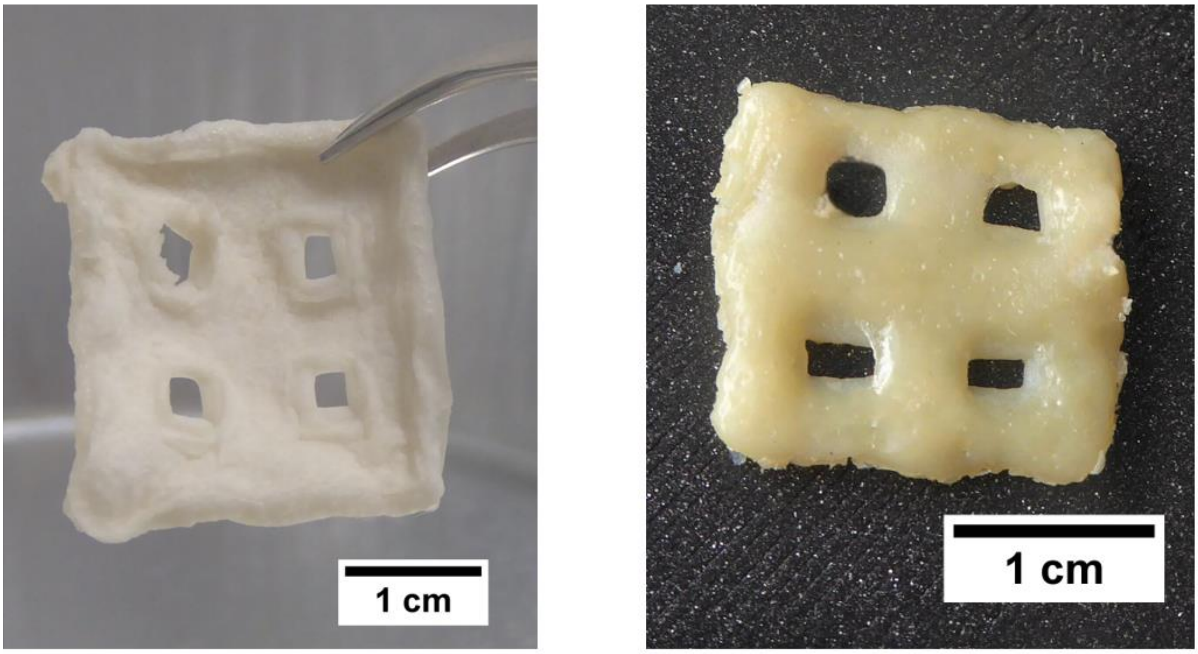

*SCD:*CNF/Fmoc-FF$_{5.10}$ *SCD:*CNF-g-Fmoc/Fmoc-FF$_{5.10}$

Figure 46: Photographs of the resulting supercritical CO_2-dried composite gels.

Portions of these gels were collected for measurement of specific surface area, shrinkage, pore volume and average pore diameter by Brunauer-Emmet-Teller (BET) and results are presented in Table 8. Using unmodified CNF as an additive, the results demonstrated a lower specific surface area. On the contrary, the pore volume and average pore diameter are much higher with the CNF-g-Fmoc composite. Reports[243] of cellulose nanofiber (CNF) aerogels obtained through supercritical CO_2 drying have shown a specific surface area of 296 – 330 $m^2 \cdot g^{-1}$ and a pore volume of 0.5 – 0.7 $cm^3 \cdot g^{-1}$. These results are similar to those of CNF/Fmoc-FF and CNF-g-Fmoc/Fmoc-FF, even though only one-quarter of the CNF was used. There are no reported data on Fmoc-FF aerogels alone, which may be due to the inability to switch solvents with ethanol, causing gelation disruption due to the fact that water is needed for the gelation. The gels exhibited minimal shrinkage in both instances.

Table 8: The shrinkage, specific surface area, pore volume, and average pore diameters of aerogels via the supercritical CO_2 drying method.

	Specific surface area, $m^2 \cdot g^{-1}$	**Pore volume, $cm^3 \cdot g^{-1}$**	**Average pore diameter, nm**	**Shrinkage (%)**

SCD:CNF/Fmoc-FF$_{5.10}$	212	0.92	17	4.7
SCD:CNF-g-Fmoc/Fmoc-FF$_{5.10}$	146	0.99	27	2.5

3 Conclusions and prospects

From lightweight composites to eco-friendly packaging solutions, CNF have been used as additives in a variety of applications to improve the mechanical and functional properties of materials. Although their use as reinforcing agents has been extensively researched, their potential as reinforcing agents in composite development, particularly for AM, remains relatively unexplored and should be further explored.

CNF were firstly successfully extracted from elemental chlorine-free (ECF) bleached softwood Kraft pulp through milling and microfluidisation. The process has successfully resulted in the production of a high amount of well-dispersed CNF. This was evidenced by a reduction in fibril size in the morphological state. The diameter of the obtained fibrils was in the range of 20 to 60 nm.

The synthesis of CNF-MI via an esterification reaction with 2-bromo-2-methylpropionic acid proved to be highly efficient, confirming its position as a robust and reproducible process. Although similar to native CNF, thr evidence of modification and emergence of ester function was demonstrated by ATR-FTIR on the resulting CNF-MI. This compound was ready to be used as an initiator in many radical polymerisation reactions, like Single Electron Transfer Living Radical Polymerisation (SET-LRP) reactions used in this work.

CNF was successfully hydrophobized by stearyl acrylate grafting via SI-SET-LRP, yielding stearyl acrylate-grafted cellulose nanofibrils (CNF-g-SA). To characterise the obtained compound, various analytical characterisations were carried out, including ATR-FTIR, solid-state ^{13}C NMR and FESEM. The initial hydrophilic properties of the CNF were successfully modified, as evidenced by an increase in the water contact angle from 36° to 105°. These changes were expected to improve the compatibility between the additive (CNF-g-SA) and the host material, HDPE, a semi-crystalline thermoplastic commonly known for its poor suitability for 3D printing (more precisely, fused deposition modelling). By extrusion in a twin-screw compounder at 150 °C, a composite consisting of 10 wt.% CNF-g-SA and HDPE were produced. Tensile testing revealed an increase in the overall mechanical properties, specifically an increase in Young's modulus (1094 MPa compared to 888 MPa) when compared to the HDPE as a starting material. The compatibility between the materials was found to be very high, and from a morphological point of view, no large gaps or irregularities were observed by FESEM, which supports the initial claim. Filaments of CNF-g-SA/HDPE were employed for

FDM 3D printing testing and various challenging objects were printed using HDPE, composite and a commercially available reference filament (Woodfill, PLA-based material). It was seen that warping was greatly reduced, with the composite experiencing much less deformation effects than HDPE. A difficult pawn model was also tested and while HDPE did not give satisfactory results, the composite on the other hand produced an excellent result.

To obtain a self-healing composite gel, a novel modification of the CNF was considered. The modification consisted of the grafting of UPy monomer onto the CNF using an SI-SET-LRP process, as has been described earlier. The monomer was synthesised in a one-step reaction and yielded a low solubility UPy monomer with a yield of 95 %. ATR-FTIR, solid-state ^{13}C NMR and FESEM were used to confirm the modification of cellulose nanofibrils (CNF-g-UPy) with UPy. CNF-g-UPy was incorporated at 20 wt.% as an additive for a random copolymer synthesised from UPy and DEGEEA (7:3) using SET-LRP with eBiB as initiator. The UPy-DEGEEA random copolymer was unsuitable for printing and, although it exhibited efficient self-healing, it underwent extreme structure alteration. To evaluate its suitability for gel printing, the mechanical properties of the composite (CNF-g-UPy/DEGEEA) were tested using rheology. Improved properties (*G’, G’’*, and yield stress) were obtained compared to the polymer and CNF-g-UPy, and even compared to a composite prepared with unmodified CNF (3.7-fold in *G'* and 2.8-fold in *G''*). These results confirmed the establishment of an ultra-reticulated 3D network due to the increase in dimerization units, resulting in enhanced cross-linking. CNF-UPy/UPy-DEGEEA was tested for extrusion gel printing and resulted in the successful printing of lattice models with minimal spacing strain and no fusing. Two half-arrows were then printed with high resolution and fused after heating at 60 °C, with little to no structural alteration, demonstrating the self-healing capacity of this gel. The mechanism of self-healing was elucidated by microscopic observation, which showed that heating increased mobility, as evidenced by a change in lower light scattering during heating.

It was then of interest to produce strong and higher resolution prints using a low molecular weight gelator (LWMG). The gelator used is a well-known self-supporting peptide called Fmoc-FF, but it has poor printability as a result of its lack of elastic behaviour. The incorporation of CNF to improve its properties was attempted to address this issue. The proportion chosen for CNF to Fmoc-FF was 25 wt.%. CNF-g-Fmoc was prepared using SI-SET-LRP in the same way as conducted for other grafting. Fmoc-AEEA, a synthetic Fmoc monomer with a yield of 82 %, was used to graft the Fmoc function onto CNF. Due to the limited information provided by the ATR-FTIR and NMR (solid state ^{13}CP-MAS and ^{1}H HRMAS) results, it was initially difficult to verify the successful synthesis of CNF-g-Fmoc. However, due to the grafting of the Fmoc-AEEA chromophore, CNF-g-Fmoc exhibited fluorescent behaviour. The amount of Fmoc-AEEA grafted onto the structure was measured using UV-Vis and was found to be 20 wt.% of the total structure, thus proving effective grafting. Two sets of composites were prepared using unmodified (CNF/Fmoc-FF) and (CNF-g-Fmoc/Fmoc-FF) with a range of DMSO volume content and concentration. Increasing the dilution resulted in an overall increase in mechanical properties for both samples. Unexpectedly, however, CNF-g-Fmoc gave poorer mechanical properties than CNF composites for most dilutions except the last, which showed a gel point shift. Morphology analysis revealed a double network, with a larger network representing CNF and a smaller web-like network representing Fmoc-FF. This demonstrates their compatibility and accounts for their strong mechanical properties. Printing tests were carried out on grids of both composites and both gave satisfactory resolution, with the unmodified CNF having higher resolution. More complex structures were then printed, including wheels, stars and vulnerable bridges. These were successfully printed using both inks, with satisfactory results and high fidelity. Samples of the grids were subjected to supercritical CO_2 drying with good results.

In conclusion, this research has demonstrated the effectiveness of the use of CNF for the optimisation of the mechanical and structural properties of composites for 3D printing. In addition, SI-SET-LRP demonstrated its versatility in successfully tailoring CNF properties to improve compatibility with different materials. The aim of future efforts could be to test CNF-g-SA on recycled HDPE and to investigate its compatibility with other thermoplastics such as LDPE and polypropylene (PP) to broaden the applicability of crystalline thermoplastics in FDM. This is expected to help expand the use of recycled platics for 3D printing. In the field of gel printing, this research provides a robust method for designing smart, high-resolution prints. Drying and using the gels as scaffolds for cell growth, taking advantage of their porous nanostructures, is a key step in exploiting these advances for biological applications. This would potentially lead to advances in tissue engineering and regenerative medicine, creating opportunities for bioengineering applications. This research provides a solid groundwork for future exploration of bio-based functional inks in 3D printing technology, opening up exciting possibilities for the development of bio-inspired, sustainable and functional 3D printable composite.

4 Materials and methods

4.1 Materials.

Di(ethylene glycol) ethyl ether acrylate (DEGEEA) (90 %), ethyl-2-bromo-2-methylpropionate (eBiB, 98 %), rhodamine B (>95 %), stearyl acrylate (SA, 97 %),and 2-amino-4-hydroxy-6-methylpyrimidine 98 % were purchased from Sigma-Aldrich. 1,1'-Carbonyldiimidazole (CDI, reagent grade), 2-bromo-2-methylpropionic acid 98 %, imidazole > 99 %, sodium bicarbonate (ACS reagent, > 99 %), sodium chloride (ACS reagent, > 99 %), 2-(2-aminoethoxy) ethanol (98 %), triethylamine (synthesis standard), dichloromethane, acryloyl chloride (97 %) and 2-isocyanatoethyl acrylate (> 98.0 %) was purchased from TCI Chemical. Dimethyl sulfoxide (DMSO, 99 %) was purchased from Merck KGaA. 9-flourenylmethoxycarbonyl chloride (Fmoc-Cl) was purchased by Carl Roth GmbH + Co. KG. Fmoc-Phe-Phe-OH (Fmoc-FF) was purchased of BLD Pharmatech (95 %). Carbon dioxide (99.5 %) was purchased from Linde AG (Pullach, Germany). Copper wire (diameter 1 mm) was purchased from Thermo Fisher Scientific. The source of the cellulose, elemental chlorine-free (ECF) bleached softwood kraft pulp, was supplied by MERCER Stendal GmbH, Germany. The Northern bleached softwood Kraft pulp was made from pine (30 - 60 %) and spruce (40 - 70 %).

4.2 Cellulose materials synthesis

4.2.1 Preparation of Cellulose Nanofibrils from Kraft Pulp

10g of dry cellulose pulp was shredded and then ground in a Herzog grinder with 200 ml of distilled water. A NORAM blender was then used to grind the mixture for 6 minutes at 1500 rpm. To determine the grinding rate, the suspension was diluted to 0.24 wt% with 4.2 litres of distilled water. 835 ml of fibre suspension was placed in the Schopper-Riegler and filled to 1000 ml. The suspension was then transferred to the Schopper Riegler for the measurement to be taken. The suspension was retained while the filtrate was drained off. The degree of refining was between 80° and 90°. The cellulose fibers were mechanically disintegrated into CNFs using the Microfluidizer (M-110EH-30 Microfluidics) from Indexcorp, under high pressure.

The fibre suspension was passed at pressures of 15,000 Psi and 25,000 Psi through four chambers with decreasing diameter widths (400 µm, 200 µm, 200 µm and 100 µm). The CNF suspension was concentrated by centrifugation at 5500 rpm for 45 minutes using a Thermo SCIENTIFIC Sorvall LYNX 6000 centrifuge.

4.2.2 Solvent exchange process

A defined amount of nanofibrillated cellulose (20.4 g, 2.36 wt%) was dispersed in 80 ml of distilled water in a glass flask and stirred at room temperature for 30 minutes. When the dispersion was complete, 150 ml of DMSO was added drop by drop while stirring. The resulting solution was then centrifuged at 10,000 rpm for 20 min, and the supernatant was discarded and replaced with fresh DMSO. This procedure was repeated for a total of four times.

4.2.3 Preparation of CNF macroinitiator (CNF-MI)

The CNF gel, which had been exchanged with solvent (12.35 g, 0.8 w.t% in DMSO), was suspended in DMSO (100 mL) and heated to 55 °C. Imidazole (3 g, 44 mmol) was subsequently dissolved in the CNF suspension. 2-bromo-2-methylpropionic acid (4 g, 24 mmol) was then dissolved in 80 ml of DMSO and 4 g of 1,1'-carbonyldiimidazol was added. Both flasks were stopped and nitrogen was added for degassing. The reaction was carried out at a temperature of 55 °C for 16 hours. The modified CNF was purified by centrifugation (5000 rpm for 15 minutes) and fresh DMSO was added to the gel. These purification steps were repeated eight times to ensure purity.

4.3 Monomers synthesis

4.3.1 Upy monomer synthesis

2-Amino-4-hydroxy-6-methylpyrimidine (10 g, 70.1 mmol) was dissolved in 150 ml DMSO at 130 °C. Once dissolved, 2-isocyanatoethyl acrylate was added to the flask and the reaction mixture was kept at 130 °C for 10 minutes. The reaction was then quenched using a cold water bath. The precipitate was filtered and washed with cold water under vacuum and then dried to obtain 2-(3-(6-methyl-4-oxo-1,4-dihydropyridine-2-yl)ureido)ethyl acrylate (UPy monomer) as a white solid with a yield of 95 %.

^{1}H NMR (400 MHz, DMSO-d_6, 60 °C): δ (ppm): 11.34 (1H, s), 9.88 (1H, s), 7.66 (1H, s), 6.38 − 6.34 (1H, d, *J* = 17.16 Hz), 6.21 − 6.14 (1H, dd, *J* = 17.17, 10.32 Hz), 5,96 (1H, d, *J* = 10.32 Hz), 5.78 (1H; s), 4,19 (2H, m), 3.47 (2H, m), 2,10 (s, 3H).

FTIR (attenuated total reflection (ATR), cm$^{-1)}$: ν = 3045 (R−CO−NH−C), 2935 (R−CH_2−R), 1732 (C=C−COOR), 1701 ((R)$_2$C=CHR), 1657 (R−CO−NH−), 1576 (C−NC), 1522 (R−CO−NH−), 1450 (R−CH_2−R), 1397 (RCHCH_2), 1327 (R−CO−NH−C), 1252 (C=C−COOR), 1180 (RCOOR), 1149 (R−NH−(C=O)−NH−R), 1053 (R−C=C−R), 968 (R_2C=CHR), 856 (−C=O−CH=CH2), 756 (broad, R_2C=CHR).

4.3.2 Fmoc-Monomer synthesis (Fmoc-AEEA)

Sodium hydrogen carbonate (974 mg, 11.6 mmol) and Fmoc-Cl (500 mg, 1.9 mmol) were added to dry dichloromethane (DCM) (6 mL) under nitrogen. 2-(2-aminoethoxy) ethanol (205 µL, 1.95 mmol) was then added dropwise. The reaction was stirred for 16 h. Sodium hydrogen carbonate was first filtered, and the solution was washed with distilled water, and brine and then dried with sodium sulfate. After solvent removal, the product (orange oil) was obtained with an 82 % yield.

^{1}H NMR (400 MHz, $CDCl_3$) δ 7.76 (d, *J* = 7.5 Hz, 7H), 7.59 (d, *J* = 7.4 Hz, 2H), 7.40 (t, *J* = 7.4 Hz, 2H), 7.31 (t, *J* = 7.4 Hz, 2H), 5.27 (s, 1H), 4.42 (d, *J* = 6.7 Hz, 2H), 4.22 (t, *J* = 6.6 Hz, 1H), 3.72 (m, 2H), 3.55 (m, 4H), 3.40 (m, 2H), 2.22 (s, 1H).

N-Fmoc-2-aminoethanol (599 mg, 1.86 mmol) was dissolved in dry DCM (20 ml) under nitrogen at 0 °C. Triethylamine (535 ml, 3.7 mmol) was then added to the solution. A solution of acryloyl chloride (270 µL, 3.4 mmol) in dry DCM (5 mL) was added dropwise to the mixture. After 2 hours, the reaction was warmed to room temperature, and the stirring continued for 16 hours. Finally, the reaction mixture was washed with saturated sodium bicarbonate (3x), and brine (3x) and dried with sodium sulphate. The solvent was removed to give an orange solid (yield 90 %).

^{1}H NMR (400 MHz, $CDCl_3$) δ 7.68 (d, *J* = 7.5 Hz, 2H), 7.52 (d, *J* = 7.5 Hz, 2H), 7.32 (t, *J* = 7.5 Hz, 2H), 7.23 (td, *J* = 7.5, 1.2 Hz, 2H), 6.34 (d, *J* = 1.4 Hz, 1H), 6.08 (d, *J* = 6.9 Hz, 1H), 5.75 (dd, *J* = 10.4, 1.4 Hz, 1H), 5.13 (t, *J* = 5.9 Hz, 1H), 4.32 (d, *J* = 7.0 Hz, 2H), 4.25 (t, *J* = 4.8 Hz, 2H), 4.14 (t, *J* = 7.0 Hz, 1H), 3.63 (m, 2H), 3.49 (m, 2H), 3.32 (m, 2H).

4.4 SI-SET-LRP grafting onto CNF-MI

4.4.1 SI-SET-LRP grafting of stearyl acrylate (SA) onto CNF-MI

The copper wire, 50 cm long, was activated by immersion in concentrated hydrochloric acid for approximately 10 minutes. Then it was rinsed with water, then with acetone and finally dried. In a three-neck flask, 15.3 g (2.1 wt.%) of the CNF macroinitiator was dispersed in 240 mL of DMSO. Meanwhile, dissolve 40 g of the monomer SA in 120 mL of toluene and pass it through an aluminium oxide plug (Al_2O_3 basic) to remove any inhibitor/stabiliser and then directly introduced it into the CNF suspension. The activated copper wire was then added to the mixture and the reaction flask was then degassed by nitrogen purging at 40 °C. The reaction mixture was prepared by adding the Me_6TREN ligand (2 wt.% in DMSO) and allowing the reaction to proceed for 16 hours at 40 °C under a nitrogen atmosphere. After cooling the suspension to room temperature, the CNF-g-SA precipitate was collected, suspended in toluene, and precipitated with isopropanol. The CNF-g-SA was purified by centrifugation (4000 rpm, 10 min), and this step was repeated five times. The gel was ultimately suspended in toluene and concentrated through centrifugation at 4000 rpm for 60 minutes. Subsequently, it was dried under a vacuum.

4.4.2 SI-SET-LRP grafting of UPy onto CNF-MI

UPy monomer (6.14 g) was dissolved in 85 ml DMSO at 110 °C and allowed to cool to 60 °C. Subsequently, 3.3 g (1.85 wt%) of the CNF macroinitiator was dispersed in 23 ml in DMSO. The monomer solution was gradually added to the CNF-MI solution at 60 °C. Prior to this, the copper wire (length = 9.32 cm) was activated by soaking it in concentrated hydrochloric acid for 10 minutes, followed by rinsing with acetone and drying. Finally, the activated copper wire was added to the flask containing the solution. The suspension was degassed by purging with nitrogen at 60 °C. Next, the Me_6TREN ligand (306 µl, 2 wt.%) was added and the reaction was allowed to proceed for 16 hours. The resulting CNF-g-UPy gel was collected by centrifugation at 4000 rpm for 20 minutes and washed four times with fresh DMSO.

4.4.3 SI-SET-LRP grafting of Fmoc-AEEA onto CNF-MI

A copper wire (diameter = 1 mm, length = 6.25 cm) was immersed in concentrated hydrochloric acid for 10 min, then rinsed first with distilled water, and acetone and finally dried with compressed air. Fmoc-AEEA (5 g, 13.11 mmol) was dissolved in 15 mL DMSO and added to a suspension of CNF-based macroinitiator (4 g, 1 wt.%) in DMSO (30 mL) containing the HCl-treated copper wire. The suspension was degassed via nitrogen purging for 10 min and the temperature was raised to 60 °C. The Me_6TREN ligand was added, and the reaction proceeded under a nitrogen atmosphere for 16 h. The resulting CNF-g-Fmoc gel was obtained through centrifugation (6000 rpm, 20 min). The supernatants were decanted and the rest was dispersed in fresh DMSO. This was repeated 5 times.

4.5 UPy-DEGEEA polymer synthesis

UPy monomer (3 g, 11.25 mmol) was initially dissolved in 60 mL of DMSO at 110 °C and then cooled to 60 °C. DEGEEA (0.7 g, 3.75 mmol) was added to the main flask after passing through the column of aluminium oxide. The polymerization reaction was carried out with a $[M]_0/[I]_0/[L]_0$ ratio of 100/1/0.2. Copper wire (length = 6 cm) was activated by soaking in concentrated hydrochloric acid for 10 minutes, rinsing with acetone and drying. The solution was purged with nitrogen for 10 minutes at 60°C before eBiB (0.3 g, 0.15 mmol) and the Me_6TREN ligand were added. The reaction was allowed to proceed for 16 hours. Subsequently, the gel was collected through centrifugation at 4000 rpm for 20 minutes and washed four times with fresh DMSO.

4.6 Composite preparation

4.6.1 CNF-g-SA/HDPE composite preparation

The composite material was prepared by combining HDPE with 10 wt% stearyl acrylate-grafted cellulose nanofibrils (CNF-g-SA). Prior to use, the CNF-g-SA was dried and cut into small pellets, and the HDPE was also dried. Mixing and extrusion were carried out in the HAAKE™ MiniLab 3 microcompounder with counter-rotating screws at 150 °C and 100 rpm for 5 minutes.

4.6.2 CNF-g-UPy/UPy-DEGEEA composite gel preparation

To prepare CNF-g-UPy/UPy-DEGEEA composite gel (2:8), 1.14 g of UPy-DEGEEA (7 wt.%) was first dispersed in 2 mL of DMSO. Then, 1.75 g of CNF-g-UPy (2.38 wt.%) was directly added to the polymer solution. The mixture was shaken vigorously for 10 minutes to ensure proper homogenisation. It was then concentrated through centrifugation (4000 rpm, 20 min) and the supernatant was discarded. This procedure was repeated twice. The resulting gel was used without further processing. Subsequently, an amount of DMSO was added to dilute to a final concentration of 4 wt%. To obtain a coloured gel, a solution of rhodamine B was prepared and added. The gel was gradually tinted until the desired shade was achieved.

4.6.3 CNF/Fmoc-FF and CNF-g-Fmoc/Fmoc-FF composite gel preparation

To produce a Fmoc-FF gel, a defined amount of Fmoc-FF was dissolved in 1 mL of DMSO. The following calculation based on Dudukovic and Zukoski[204] gives the amount of distilled water (DI) water that needs to be added to get a gel.

$$[x_{H_2O}]_g = 0{,}08 \frac{[x_{Fmoc-FF}]_g}{10}{}^{-0{,}285} \tag{10}$$

The volume fraction of DMSO, ϕ_{DMSO}, has been calculated using the formula shown in (2), with *v* for volume in millilitres.

$$\phi_{\mathrm{DMSO}} = \frac{v_{\mathrm{DMSO}}}{v_{\mathrm{total}}} \mathrm{x}\ 100 \tag{11}$$

10 µL DI water is added dropwise and the mixture is mixed for 20 seconds. After sitting for 10 minutes the gelation was tested by flipping the glass vile.

Fmoc-FF gel was made following this procedure: 50 mg Fmoc-FF dissolved in 1 mL DMSO. The gelation was started by adding 500 µL DI water, mixing for 10 seconds, and letting sit for 10 minutes after each addition.

"Gel mixing'' or "high-intensity mixing'' refers to the use of ROTI®Speed Agitators, purchased from Carl Roth GmbH + Co. KG, which operates at a speed of between 5,000 and 10,000 rpm. The agitator used is a Micropistil-type tool, made of stainless steel.

The composite gels were prepared using the same procedure. An example of a procedure used to make a gel: CNF/Fmoc-$FF_{3.89}$: 0.09 g of Fmoc-FF was taken and dissolved in 0.5 ml of DMSO, and then 1 g of CNF was added to it. This was mixed with a ROTI®Speed Agitator for 5 minutes. Afterwards, 1.5 ml of water was added and mixed again. The rest of the gels were made following the same pattern.

4.7 3D printing of composite materials

4.7.1 CNF-g-SA/HDPE composite material preparation

Filaments for 3D printing were produced using a HAAKE™ MiniLab 3 microcompounder. The components were loaded and compounded with counter-rotating screws at a screw speed of 35 rpm and a temperature of 150 °C. A caliper gauge was used to control filament size and the filament diameter was set at 1.75 mm to ensure compatibility with an original Prusa i3 MK3S+ printer. The 3D object STL file was downloaded from Thingiverse[244], created by SteedMaker and licensed under CC BY-NC 4.0. Printing parameters were modified using PrusaSlicer software (version 2.4.1). The temperature of the nozzle was set to 215 °C and the temperature of the bed was set to 60 °C. A nozzle diameter of 0.4 mm was used, and the printing speed was set to 20 $mm.s^{-1}$, with a layer height of 0.2 mm. The infill was a gyroïd pattern with a percentage of 15 %. Additionally, to improve adhesion, the object was printed on an LDPE sheet. The cooling fan was activated from the 4th layer onwards, operating at 50 % capacity.

4.7.2 CNF-g-UPy/UPy-DEGEEA composite gel printing

The models were created using Fusion360 and 3D gel printed using a CELLINK INKREDIBLE 3D Bioprinter via pneumatic extrusion. The gel, which has a high viscosity, was homogenised before printing using a screw-type mixer called 'HighVisc', which was developed by Dani and his team[245]. Printability was tuned by adjusting the flow rate through the fixed nozzle to achieve stable and consistent precision of filament printing. The gel was printed using a conical nozzle with a diameter of 0.59 mm and an applied pressure of 18 kPa.

4.7.3 CNF/Fmoc-FF and CNF-g-Fmoc/Fmoc-FF composite gel printing

A grid model has been designed using Fusion360 and 3D gel printed by pneumatic extrusion using a CELLINK INKREDIBLE 3D bioprinter. One disposable gel cartridge was charged and fitted into the print head. Printability was adjusted by setting the pneumatic pressure to achieve stable and consistent extrusion through the nozzle. The gel was printed with a 0.84 mm diameter conical nozzle with different applied pressure for each gel (18 – 50 kPa). The same procedure was used for the printing of the other models.

4.8 Material Characterization.

To determine the dry matter content of the CNF suspension, a certain mass of the suspension was dried under 60 °C overnight and weighed after drying. The calculation was done under this formula, with m_w for the weight of the gel in the wet state, and m_d when dry.

$$^{w}/_{w} = (1 - (\frac{m_w - m_d}{m_w})) \times 100 \qquad (12)$$

4.8.1 Attenuated Total Reflection Fourier-Transform Infrared Spectroscopy (ATR-FTIR)

ATR-FTIR analysis was performed using a Bruker Vector 33 FTIR Fourier-transform infrared spectrometer I18500 PS15. The spectra were recorded with 64 scans in the spectral region of 4000 – 500 cm^{-1} at a spectral resolution of 4 cm^{-1}.

4.8.2 Cross-Polarization Magic Angle Spinning (CPMAS)

The CP/MAS ^{13}C-NMR spectra for all samples were obtained using a Bruker 500 Avance III HD spectrometer at Larmor frequencies of 125 MHz and 500 MHz for ^{13}C and ^{1}H, respectively. The samples were placed in 4 mm zirconia rotors for magic angle spinning (MAS) at a rotation speed of 8 kHz. Creeping CP/MAS ^{13}C-NMR spectra were recorded using Fourier transforms of the FIDs with a ^{13}C mutation frequency of 50 kHz and a contact time of 1.5 ms. Chemical shifts were referenced to pure tetramethylsilane (TMS).

4.8.3 Water contact angle measurements

The contact angle measurements were conducted with a drop shape analyzer (DSA 100, Krüss, Hamburg, Germany) using the sessile drop method. 10 µL of Milli-Q water was automatically dispensed onto the surfaces and the static contact angle was measured using a Basler A6021-

2. Thin and flat films of CNF and modified CNF were prepared using vacuum filtration followed by air drying. Individual measurements were taken within 2 seconds of droplet deposition and averaged from ten measurements.

4.8.4 Tensile testing (special for CNF-g-SA/HDPE)

The nanocomposites were cut into pellets and then injection-molded using Haake Minijet II for tensile testing. The cylinder temperature was set to 160 °C, mold temperature to 80 °C, and pressure to 400 bars for 4 seconds. The dogbones used for the test had dimensions of 75 x 10 x 20 mm. The tensile test was performed in accordance with DIN EN ISO 527-1 using a Zwick-Roell universal testing machine with a 500 N load cell and a ZWICK videoXtens video extensometer. The crosshead speed was set to 20 mm.min^{-1} for plain matrix and 1 mm.min^{-1} for composites. An initial load of 1N was applied to determine the properties. Between 5 and 12 specimens were tested.

4.8.5 Warping measurements

To measure the warping effect of HDPE and composite, two 3D models were printed. The first model is a fully filled flat rectangle, while the second is a hollow flat rectangle. Both models were printed using the same parameters as previously described. Various configurations were used during the printing process, including with or without LDPE tape and with or without an enclosure. HDPE, composite, and WoodFill were printed, placed side by side, and photographed. The measurement of material warping utilises the circular arc method, as demonstrated in Scheme 14. Bent and warped materials are considered to be part of a circular arc. Both distances, a (the length between the two ends of the bent construction) and b (the height from the centre of a to the arc), were measured with ImageJ. The radius of the assumed circle, r, is calculated from these two values using the formula below. This is used for the quantification of the warping.

$$r = \frac{\sqrt{\left(\frac{a}{2}\right)^2 + c^2}}{2\cos(\tan^{-1}\left(\frac{a}{2c}\right))}$$

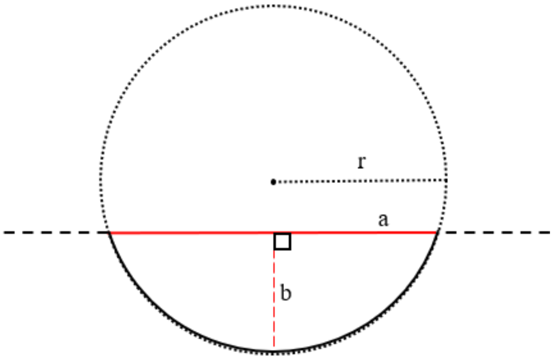

Scheme 14: Circular method: printed 3D models are represented as an arc.

4.8.6 UV-Vis spectroscopy

A calibration standard of varying concentrations of Fmoc-AEEA monomer was produced on a Lambda 65 UV-Vis spectrometer. This spectroscopy is performed in the ultraviolet-visual (UV-Vis) range from 380 to 900 nm. The absorption spectra were measured in DMSO as a standard solvent at a resolution of 1 nm in a quartz cuvette of 1 cm. The absorbance of the CNF-g-Fmoc sample used for quantitation purposes was recorded using the same concentration of CNF-MI as a blank.

4.8.7 Supercritical CO_2 drying

The excess DMSO and water were removed from the wet gel after printing by soaking it multiple times in ethanol. Once this was complete, the wet gel was transferred to a high-pressure vessel designed for supercritical CO_2 drying and extraction. CO_2 was introduced into the vessel at a temperature and pressure above its critical point (40 °C and 80 bar). The CO_2 supply was maintained for at least 30 minutes with a CO_2 flow of about 3 $g \cdot min^{-1}$ to replace and expel most of the solvent. Afterwards, the pressure was gradually released, causing the CO_2 to evaporate from the supercritical state, and leaving behind a solid aerogel structure.

The setup used here is illustrated in the Scheme 15. The first step is to use a CO_2 bottle with a dip tube (1) to reach the liquid phase. To generate the necessary pressure levels for the liquid carbon dioxide, a high-pressure pump with a Teflon diaphragm is used (2). Its adequate cooling is essential to counter the heat generated during compression, which may cause damage to the pump. The exact flow rate of carbon dioxide in grams per minute, regardless of its density, is determined by a mass flow controller (MFC, 3). The temperature is then raised (4) to reach the critical CO_2 state, while a back-pressure valve (5) maintains the desired pressure level. Pipe heating (6) guarantees uniform temperatures, especially at the separator's inlet. Samples are placed on a stainless-steel mesh (8) and a pressure gauge (7) measures pressure inside the chamber. A standard laboratory heater (10) is used. Finally, a crucial valve (9) is attached to the flow meter (12) to enable controlled depressurization, adjusting flow rates and controlling the rate of pressure decrease for system stabilisation and limiting the quick $scCO_2$ removal that can fracture the structure.

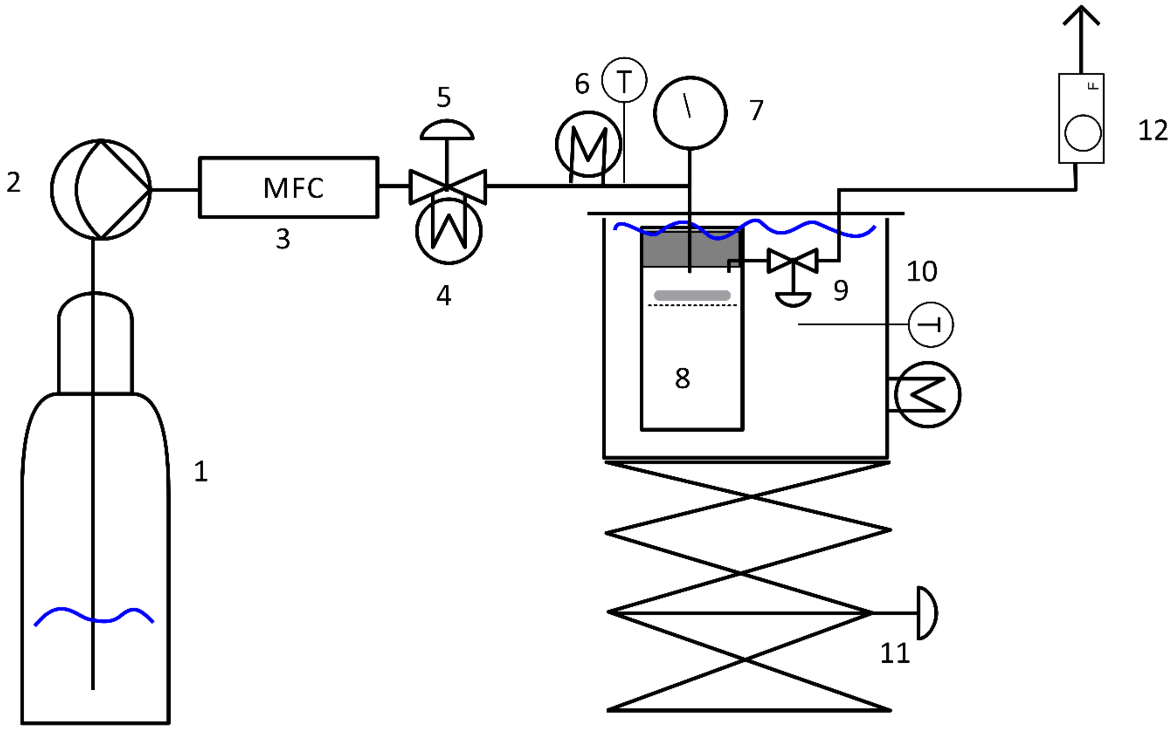

Scheme 15: Schematic representation of the experimental procedure for supercritical drying with CO_2. 1. CO_2 dip-tube bottle; 2. cooled high-pressure pump; 3. mass flow meter; 4. heater; 5. back pressure regulator; 6. pipe heating with thermocouple; 7. pressure gauge; 8. pressure separator with sample on stainless steel mesh; 9. proportional relief valve; 10. heating bath with thermocouples; 11. laboratory lift; 12. float-type flow meter.

4.8.8 Confocal Laser Scanning Microscopy

Confocal laser scanning microscopy imaging was performed with a Zeiss LSM900 microscope fitted with an Airyscan2 detector (Zeiss, Oberkochen, Germany), using a Plan-Apochromat 63x/1.4 NA oil immersion objective, a 488 nm solid-state laser diode, an MBS 405/488/561/640 as main beam splitter, 1 AU pinhole aperture and Nyquist sampling.

Fluorescent signals were collected by the Airyscan2 GaAsP detector, while transmitted light was collected by a Multi-Alkali PMT.

4.8.9 High-Resolution Magic Angle Spinning (HR-MAS) spectroscopy

High-Resolution Magic Angle Spinning (HR-MAS) spectroscopy was used to study the molecular composition of CNF-g-Fmoc. The experiments were performed using a Bruker Avance III HD spectrometer equipped with a high-speed magic angle spinning probe. The samples were prepared by placing them uniformly in a 4 mm zirconia rotor. For efficient spinning, the rotor was rotated at a speed of 8 kHz, ensuring efficient homogenization of the sample. For proton (^{1}H) spectra, a Larmor frequency of 500 MHz was used, while for carbon-13 (^{13}C) spectra, a Larmor frequency of 125 MHz was used. The acquisition parameters for HR-MAS included a 90° pulse length of 4 μs, a relaxation time of 2 s and a spectral width of 20 ppm. The spectra were processed using appropriate data analysis software, and the chemical shifts were referenced to an internal standard, such as tetramethylsilane (TMS).

4.8.10 Nuclear Magnetic Resonance (NMR) spectroscopy

The NMR spectra of each sample were acquired on a Bruker 500 Avance III HD spectrometer at 125 MHz and 500 MHz Larmor frequencies for ^{13}C and ^{1}H. The samples were placed in a 4 mm zirconium oxide rotor for magic angle spinning (MAS) at a rotational speed of 8 kHz. The creeping ^{13}C-MAS spectra were recorded with a ^{13}C mutation frequency of 50 kHz and a contact time of 1.5 ms. The spectra were obtained by Fourier transforming the FIDs and the chemical shifts were referenced to pure tetramethylsilane (TMS).

4.8.11 Field Emission Scanning Electron Microscopy (FE-SEM)

Ultra-high-resolution field emission scanning electron microscopy (FE-SEM) was used to observe the morphology of modified CNFs and composites. The modified CNFs were dispersed in polyvinyl alcohol, dried, and mounted on sample supports using carbon tape. A 5 nm layer of Pd/Pt was coated under an inert atmosphere. For the CNF-g-SA/HDPE composites, samples were cut at the fracture site from the mechanical test and then gold plated using the Biorad SC510 SEM coating system prior to analysis.

4.8.12 Differential Scanning Calorimeter (DSC)

The thermal behaviour of CNF, CNF-g-UPy, and UPy-DEGEEA polymer was analysed using a Mettler Toledo DSC 820 module differential scanning calorimeter (DSC). Each specimen, with an average mass of approximately 5 to 8 mg, was vacuum-dried beforehand and then encapsulated in a 40 μL aluminium cup before being placed in the measuring slot. The temperature program consisted of heating from 25 to 250 °C, followed by cooling to 25 °C and repeating the cycle once. The rate of heating and cooling was set at 10°C per minute under a nitrogen atmosphere with a flow rate of 50 mL.

4.8.13 Self-healing of UPy-DEGEEA and CNF-g-UPy/UPy-DEGEEA

A section of the composite is placed on a glass sheet. To initiate self-healing, a section was cut using a sharp blade. The fragmented portions were then set aside and heated to 80°C for 5 minutes. Photographs were taken before and after the process.

The self-healing process was then characterized by 3D printing two half-arrow patterns, each measuring 24x6 mm. Two differently colored gels were used to print the patterns for ease of observation. Once printed, both composites were frozen in liquid nitrogen and transferred onto a single plate. The plate was then heated to 80 °C for 2 minutes and subsequently cooled to room temperature.

4.8.14 Rheology

Rheology tests were conducted using a TA Instrument AR 2000ex and Advantage v5.8.2 software. A 40 mm parallel plate setup with a gap distance of 1000 μm was used, with the gel placed on the bottom plate. Sweep frequency was set between 0.1 and 100 rad·s^{-1} and strain sweep was performed at an angular frequency of 6.28 rad·s^{-1} to make sure that readings were taken in the linear viscoelastic region. Each material underwent a shear stress ramp, ranging from 0.01 to 100 Pa. The rotational shear viscosity measurements were carried out in the flow mode, with shear rates varying from 0.01 to 2000 s^{-1}. Rheological measurements were conducted at 25 °C to characterize the viscosity retrieval behaviour of the material after 3D printing. A low shear rate of 0.01 s was applied for 200 s, followed by a high shear rate at 895 s for 100 s, and finally a low shear rate of 0.01 s for 200 s.

5 References

(1) Costa, A. F. S.; Almeida, F. C. G.; Vinhas, G. M.; Sarubbo, L. A. Production of Bacterial Cellulose by Gluconacetobacter Hansenii Using Corn Steep Liquor As Nutrient Sources. *Front. Microbiol.* **2017**, *8*.

(2) Heinze, T.; El Seoud, O. A.; Koschella, A. *Cellulose Derivatives*; Springer Series on Polymer and Composite Materials; Springer International Publishing: Cham, 2018.

(3) Wahlström, N.; Edlund, U.; Pavia, H.; Toth, G.; Jaworski, A.; Pell, A. J.; Choong, F. X.; Shirani, H.; Nilsson, K. P. R.; Richter-Dahlfors, A. Cellulose from the Green Macroalgae Ulva Lactuca: Isolation, Characterization, Optotracing, and Production of Cellulose Nanofibrils. *Cellulose* **2020**, *27* (7), 3707–3725.

(4) Davison, B. H.; Parks, J.; Davis, M. F.; Donohoe, B. S. Plant Cell Walls: Basics of Structure, Chemistry, Accessibility and the Influence on Conversion. In *Aqueous Pretreatment of Plant Biomass for Biological and Chemical Conversion to Fuels and Chemicals*; Wiley, 2013; pp 23–38.

(5) Usov, I.; Nyström, G.; Adamcik, J.; Handschin, S.; Schütz, C.; Fall, A.; Bergström, L.; Mezzenga, R. Understanding Nanocellulose Chirality and Structure–Properties Relationship at the Single Fibril Level. *Nat. Commun.* **2015**, *6* (1), 7564.

(6) Statista Research Department. *Manmade cellulosic fibers worldwide production 2017-2021*. https://www.statista.com/statistics/1250891/global-production-manmade-cellulosic-fibers/#:~:text=Manmade cellulosic fibers worldwide production 2017-2021&text=The production of manmade cellulosic,comparison to the previous year.

(7) Brethauer, S.; Shahab, R. L.; Studer, M. H. Impacts of Biofilms on the Conversion of Cellulose. *Appl. Microbiol. Biotechnol.* **2020**, *104* (12), 5201–5212.

(8) Kroon-Batenburg, L. M. J.; Kroon, J.; Leeflang, B. R.; Vliegenthart, J. F. G. Conformational Analysis of Methyl β-Cellobioside by ROESY NMR Spectroscopy and MD Simulations in Combination with the CROSREL Method. *Carbohydr. Res.* **1993**, *245* (1), 21–42.

(9) Klemm, D.; Kramer, F.; Moritz, S.; Lindström, T.; Ankerfors, M.; Gray, D.; Dorris, A. Nanocelluloses: A New Family of Nature-Based Materials. *Angew. Chemie Int. Ed.* **2011**, *50* (24), 5438–5466.

(10) Zhao, Y.; Moser, C.; Lindström, M. E.; Henriksson, G.; Li, J. Cellulose Nanofibers from Softwood, Hardwood, and Tunicate: Preparation–Structure–Film Performance Interrelation. *ACS Appl. Mater. Interfaces* **2017**, *9* (15), 13508–13519.

(11) Gopi, S.; Balakrishnan, P.; Chandradhara, D.; Poovathankandy, D.; Thomas, S. General Scenarios of Cellulose and Its Use in the Biomedical Field. *Mater. Today Chem.* **2019**, *13*, 59–78.

(12) Seddiqi, H.; Oliaei, E.; Honarkar, H.; Jin, J.; Geonzon, L. C.; Bacabac, R. G.; Klein-Nulend, J. Cellulose and Its Derivatives: Towards Biomedical Applications. *Cellulose* **2021**, *28* (4), 1893–1931.

(13) Fernandes, A. N.; Thomas, L. H.; Altaner, C. M.; Callow, P.; Forsyth, V. T.; Apperley, D. C.; Kennedy, C. J.; Jarvis, M. C. Nanostructure of Cellulose Microfibrils in Spruce Wood. *Proc. Natl. Acad. Sci.* **2011**, *108* (47).

(14) Ding, S.-Y.; Zhao, S.; Zeng, Y. Size, Shape, and Arrangement of Native Cellulose Fibrils in Maize Cell Walls. *Cellulose* **2014**, *21* (2), 863–871.

(15) Moon, R. J.; Martini, A.; Nairn, J.; Simonsen, J.; Youngblood, J. Cellulose Nanomaterials Review: Structure, Properties and Nanocomposites. *Chem. Soc. Rev.* **2011**, *40* (7), 3941.

(16) Arthur, J. C. Chemical Modification of Cellulose and Its Derivatives. In *Comprehensive Polymer Science and Supplements*; Elsevier, 1989; pp 49–80.

(17) PÉrez, S.; Samain, D. Structure and Engineering of Celluloses; 2010; pp 25–116.

(18) Nunes, R. C. R. Rubber Nanocomposites with Nanocellulose. In *Progress in Rubber Nanocomposites*; Elsevier, 2017; pp 463–494.

(19) Rojas, J.; Bedoya, M.; Ciro, Y. Current Trends in the Production of Cellulose Nanoparticles and Nanocomposites for Biomedical Applications. In *Cellulose - Fundamental Aspects and Current Trends*; InTech, 2015.

(20) Mahmood, N.; Yuan, Z.; Schmidt, J.; Xu, C. (Charles). Depolymerization of Lignins and Their Applications for the Preparation of Polyols and Rigid Polyurethane Foams: A Review. *Renew. Sustain. Energy Rev.* **2016**, *60*, 317–329.

(21) Bouiri, B.; Amrani, M. Elemental Chlorine-Free Delignification of Kraft Pulp Produced from Halfa (Stipa Tenacissima). *Fibres Text. East. Eur.* **2011**, *87* (4), 142–147.

(22) Choi, K.; Gao, C.; Nam, J.; Choi, H. Cellulose-Based Smart Fluids under Applied Electric Fields. *Materials (Basel).* **2017**, *10* (9), 1060.

(23) Dufresne, A. *Nanocellulose*; DE GRUYTER, 2012.

(24) Daicho, K.; Kobayashi, K.; Fujisawa, S.; Saito, T. Crystallinity-Independent yet Modification-Dependent True Density of Nanocellulose. *Biomacromolecules* **2020**, *21* (2), 939–945.

(25) Dufresne, A. Nanocellulose: A New Ageless Bionanomaterial. *Mater. Today* **2013**, *16* (6), 220–227.

(26) Babaee, M.; Jonoobi, M.; Hamzeh, Y.; Ashori, A. Biodegradability and Mechanical Properties of Reinforced Starch Nanocomposites Using Cellulose Nanofibers. *Carbohydr. Polym.* **2015**, *132*, 1–8.

(27) Wang, B.; Sain, M.; Oksman, K. Study of Structural Morphology of Hemp Fiber from the Micro to the Nanoscale. *Appl. Compos. Mater.* **2007**, *14* (2), 89–103.

(28) Turbak, A. F., Snyder, F. W., & Sandberg, K. R. Microfibrillated Cellulose, a New Cellulose Product: Properties, Uses, and Commercial Potential. *J Appl Polym Sci Appl Polym Symp* **1983**, *37* (9), 815–827.

(29) Qing, Y.; Sabo, R.; Zhu, J. Y.; Agarwal, U.; Cai, Z.; Wu, Y. A Comparative Study of Cellulose Nanofibrils Disintegrated via Multiple Processing Approaches. *Carbohydr. Polym.* **2013**, *97* (1), 226–234.

(30) Nypelö, T., Österberg, M., & Laine, J. Nanostructured Coating for Improved Surface Characteristics of Paper. *7th Int. Pap. Coat. Chem. Symp.* **2009**, 29–32.

(31) Onyianta, A. J.; Dorris, M.; Williams, R. L. Aqueous Morpholine Pre-Treatment in Cellulose Nanofibril (CNF) Production: Comparison with Carboxymethylation and TEMPO Oxidisation Pre-Treatment Methods. *Cellulose* **2018**, *25* (2), 1047–1064.

(32) Tsalagkas, D.; Zhai, L.; Kafy, A.; Kim, J. W.; Kim, H. C.; Kim, J. Production of Micro- and Nanofibrillated Cellulose through an Aqueous Counter Collision System Followed by Ultrasound: Effect of Mechanical Pretreatments. *J. Nat. Fibers* **2020**, *17* (8), 1099–1110.

(33) Bastida, G. A.; Schnell, C. N.; Mocchiutti, P.; Solier, Y. N.; Inalbon, M. C.; Zanuttini, M. Á.; Galván, M. V. Effect of Oxalic Acid Concentration and Different Mechanical Pre-Treatments on the Production of Cellulose Micro/Nanofibers. *Nanomaterials* **2022**, *12* (17), 2908.

(34) Ribeiro, R. S. A.; Pohlmann, B. C.; Calado, V.; Bojorge, N.; Pereira, N. Production of Nanocellulose by Enzymatic Hydrolysis: Trends and Challenges. *Eng. Life Sci.* **2019**, *19* (4), 279–291.

(35) Lee, H.; Mani, S. Mechanical Pretreatment of Cellulose Pulp to Produce Cellulose Nanofibrils Using a Dry Grinding Method. *Ind. Crops Prod.* **2017**, *104*, 179–187.

(36) *No Title*. Webpage visited on 11.02.2024. https://www.celignis.com/enzymes.php.

(37) Doench, I.; Torres-Ramos, M.; Montembault, A.; Nunes de Oliveira, P.; Halimi, C.; Viguier, E.; Heux, L.; Siadous, R.; Thiré, R.; Osorio-Madrazo, A. Injectable and Gellable Chitosan Formulations Filled with Cellulose Nanofibers for Intervertebral Disc Tissue Engineering. *Polymers (Basel).* **2018**, *10* (11), 1202.

(38) Norrrahim, M. N. F.; Kasim, N. A. M.; Knight, V. F.; Halim, N. A.; Shah, N. A. A.; Noor, S. A. M.; Jamal, S. H.; Ong, K. K.; Wan Yunus, W. M. Z.; Farid, M. A. A.; Jenol, M. A.; Ahmad, I. R. Performance Evaluation of Cellulose Nanofiber Reinforced Polymer Composites. *Funct. Compos. Struct.* **2021**, *3* (2).

(39) Chen, J.-K.; Huang, H.-Y.; Tu, C.-W.; Lee, L.-T.; Jamnongkan, T.; Huang, C.-F. SI ATRP for the Surface Modifications of Optically Transparent Paper Films Made by TEMPO-Oxidized Cellulose Nanofibers. *Polymers (Basel).* **2022**, *14* (5), 946.

(40) Jamaluddin, N.; Hsu, Y.-I.; Asoh, T.-A.; Uyama, H. Effects of Acid-Anhydride-Modified Cellulose Nanofiber on Poly(Lactic Acid) Composite Films. *Nanomaterials* **2021**, *11* (3), 753.

(41) Sun, X.; Tyagi, P.; Agate, S.; McCord, M. G.; Lucia, L. A.; Pal, L. Highly Tunable Bioadhesion and Optics of 3D Printable PNIPAm/Cellulose Nanofibrils Hydrogels. *Carbohydr. Polym.* **2020**, *234* (November 2019), 115898.

(42) Ding, Z.; Liu, X.; Liu, Y.; Zhang, L. Enhancing the Compatibility, Hydrophilicity and

Mechanical Properties of Polysulfone Ultrafiltration Membranes with Lignocellulose Nanofibrils. *Polymers (Basel).* **2016**, *8* (10).

(43) Fernandes Diniz, J. M. B.; Gil, M. H.; Castro, J. A. A. M. Hornification?Its Origin and Interpretation in Wood Pulps. *Wood Sci. Technol.* **2004**, *37* (6), 489–494.

(44) Yildiz, S.; Gümüşkaya, E. The Effects of Thermal Modification on Crystalline Structure of Cellulose in Soft and Hardwood. *Build. Environ.* **2007**, *42* (1), 62–67.

(45) Lin, N.; Huang, J.; Dufresne, A. Preparation, Properties and Applications of Polysaccharide Nanocrystals in Advanced Functional Nanomaterials: A Review. *Nanoscale* **2012**, *4* (11), 3274.

(46) Heines, S. V. John Mercer and Mercerization, 1844. *J. Chem. Educ.* **1944**, *21* (9), 430.

(47) Roy Choudhury, A. K. Pre-Treatment and Preparation of Textile Materials Prior to Dyeing. In *Handbook of Textile and Industrial Dyeing*; Elsevier, 2011; pp 64–149.

(48) Seo, Y.-R.; Bae, S.-U.; Gwon, J.; Wu, Q.; Kim, B.-J. Effects of Methylenediphenyl 4,4’-Diisocyanate and Maleic Anhydride as Coupling Agents on the Properties of Polylactic Acid/Polybutylene Succinate/Wood Flour Biocomposites by Reactive Extrusion. *Materials (Basel).* **2020**, *13* (7), 1660.

(49) Isogai, A.; Zhou, Y. Diverse Nanocelluloses Prepared from TEMPO-Oxidized Wood Cellulose Fibers: Nanonetworks, Nanofibers, and Nanocrystals. *Curr. Opin. Solid State Mater. Sci.* **2019**, *23* (2), 101–106.

(50) Roy, D.; Semsarilar, M.; Guthrie, J. T.; Perrier, S. Cellulose Modification by Polymer Grafting: A Review. *Chem. Soc. Rev.* **2009**, *38* (7), 2046.

(51) Percec, V.; Popov, A. V.; Ramirez-Castillo, E.; Monteiro, M.; Barboiu, B.; Weichold, O.; Asandei, A. D.; Mitchell, C. M. Aqueous Room Temperature Metal-Catalyzed Living Radical Polymerization of Vinyl Chloride. *J. Am. Chem. Soc.* **2002**, *124* (18), 4940–4941.

(52) Rosen, B. M.; Percec, V. Single-Electron Transfer and Single-Electron Transfer Degenerative Chain Transfer Living Radical Polymerization. *Chem. Rev.* **2009**, *109* (11), 5069–5119.

(53) Anastasaki, A.; Nikolaou, V.; Nurumbetov, G.; Wilson, P.; Kempe, K.; Quinn, J. F.; Davis, T. P.; Whittaker, M. R.; Haddleton, D. M. Cu(0)-Mediated Living Radical Polymerization: A Versatile Tool for Materials Synthesis. *Chem. Rev.* **2016**, *116* (3), 835–877.

(54) Lligadas, G.; Grama, S.; Percec, V. Recent Developments in the Synthesis of Biomacromolecules and Their Conjugates by Single Electron Transfer–Living Radical Polymerization. *Biomacromolecules* **2017**, *18* (4), 1039–1063.

(55) Levere, M. E.; Nguyen, N. H.; Leng, X.; Percec, V. Visualization of the Crucial Step in SET-LRP. *Polym. Chem.* **2013**, *4* (5), 1635–1647.

(56) Alsubaie, F.; Anastasaki, A.; Wilson, P.; Haddleton, D. M. Sequence-Controlled Multi-Block Copolymerization of Acrylamides via Aqueous SET-LRP at 0 °C. *Polym.*

Chem. **2015**, *6* (3), 406–417.

(57) Nguyen, N. H.; Percec, V. Disproportionating versus Nondisproportionating Solvent Effect in the SET-LRP of Methyl Acrylate during Catalysis with Nonactivated and Activated Cu(0) Wire. *J. Polym. Sci. Part A Polym. Chem.* **2011**, *49* (19), 4227–4240.

(58) Percec, V.; Popov, A. V.; Ramirez-Castillo, E.; Weichold, O. Living Radical Polymerization of Vinyl Chloride Initiated with Iodoform and Catalyzed by Nascent Cu 0 /Tris(2-aminoethyl)Amine or Polyethyleneimine in Water at 25 °C Proceeds by a New Competing Pathways Mechanism. *J. Polym. Sci. Part A Polym. Chem.* **2003**, *41* (21), 3283–3299.

(59) Rosen, B. M.; Jiang, X.; Wilson, C. J.; Nguyen, N. H.; Monteiro, M. J.; Percec, V. The Disproportionation of Cu(I)X Mediated by Ligand and Solvent into Cu(0) and Cu(II)X 2 and Its Implications for SET-LRP. *J. Polym. Sci. Part A Polym. Chem.* **2009**, *47* (21), 5606–5628.

(60) Rosen, B. M.; Percec, V. Implications of Monomer and Initiator Structure on the Dissociative Electron-transfer Step of SET-LRP. *J. Polym. Sci. Part A Polym. Chem.* **2008**, *46* (16), 5663–5697.

(61) Guliashvili, T.; Percec, V. A Comparative Computational Study of the Homolytic and Heterolytic Bond Dissociation Energies Involved in the Activation Step of ATRP and SET-LRP of Vinyl Monomers. *J. Polym. Sci. Part A Polym. Chem.* **2007**, *45* (9), 1607–1618.

(62) Levere, M. E.; Willoughby, I.; O’Donohue, S.; De Cuendias, A.; Grice, A. J.; Fidge, C.; Becer, C. R.; Haddleton, D. M. Assessment of SET-LRP in DMSO Using Online Monitoring and Rapid GPC. *Polym. Chem.* **2010**, *1* (7), 1086–1094.

(63) Matyjaszewski, K.; Tsarevsky, N. V.; Braunecker, W. A.; Dong, H.; Huang, J.; Jakubowski, W.; Kwak, Y.; Nicolay, R.; Tang, W.; Yoon, J. A. Role of Cu 0 in Controlled/“Living” Radical Polymerization. *Macromolecules* **2007**, *40* (22), 7795–7806.

(64) Lligadas, G.; Percec, V. Ultrafast SET-LRP of Methyl Acrylate at 25 °C in Alcohols. *J. Polym. Sci. Part A Polym. Chem.* **2008**, *46* (8), 2745–2754.

(65) Lligadas, G.; Rosen, B. M.; Monteiro, M. J.; Percec, V. Solvent Choice Differentiates SET-LRP and Cu-Mediated Radical Polymerization with Non-First-Order Kinetics. *Macromolecules* **2008**, *41* (22), 8360–8364.

(66) Nguyen, N. H.; Rosen, B. M.; Jiang, X.; Fleischmann, S.; Percec, V. New Efficient Reaction Media for SET-LRP Produced from Binary Mixtures of Organic Solvents and H 2 O. *J. Polym. Sci. Part A Polym. Chem.* **2009**, *47* (21), 5577–5590.

(67) Hatano, T.; Rosen, B. M.; Percec, V. SET-LRP of Vinyl Chloride Initiated with CHBr 3 and Catalyzed by Cu(0)-wire/TREN in DMSO at 25 °C. *J. Polym. Sci. Part A Polym. Chem.* **2010**, *48* (1), 164–172.

(68) Nicol, E.; Derouineau, T.; Puaud, F.; Zaitsev, A. Synthesis of Double Hydrophilic Poly(Ethylene Oxide)- b -poly(2-hydroxyethyl Acrylate) by Single-electron Transfer–

Living Radical Polymerization. *J. Polym. Sci. Part A Polym. Chem.* **2012**, *50* (18), 3885–3894.

(69) Nguyen, N. H.; Percec, V. Acid Dissolution of Copper Oxides as a Method for the Activation of Cu(0) Wire Catalyst for SET-LRP. *J. Polym. Sci. Part A Polym. Chem.* **2011**, *49* (19), 4241–4252.

(70) Pei, X.; Zhai, K.; Wang, C.; Deng, Y.; Tan, Y.; Zhang, B.; Bai, Y.; Xu, K.; Wang, P. Polymer Brush Graft-Modified Starch-Based Nanoparticles as Pickering Emulsifiers. *Langmuir* **2019**, *35* (22), 7222–7230.

(71) Wen, N.; Lü, S.; Xu, X.; Ning, P.; Wang, Z.; Zhang, Z.; Gao, C.; Liu, Y.; Liu, M. A Polysaccharide-Based Micelle-Hydrogel Synergistic Therapy System for Diabetes and Vascular Diabetes Complications Treatment. *Mater. Sci. Eng. C* **2019**, *100*, 94–103.

(72) Wang, Y.; Li, S.; Ma, L.; Dong, S.; Liu, L. Corn Stalk as Starting Material to Prepare a Novel Adsorbent via SET-LRP and Its Adsorption Performance for Pb(II) and Cu(II). *R. Soc. Open Sci.* **2020**, *7* (3), 191811.

(73) Navarro, J. R. G.; Rostami, J.; Ahlinder, A.; Mietner, J. B.; Bernin, D.; Saake, B.; Edlund, U. Surface-Initiated Controlled Radical Polymerization Approach to in Situ Cross-Link Cellulose Nanofibrils with Inorganic Nanoparticles. *Biomacromolecules* **2020**, *21* (5), 1952–1961.

(74) Deng, Y.; Zhang, J. Z.; Li, Y.; Hu, J.; Yang, D.; Huang, X. Thermoresponsive Graphene Oxide-PNIPAM Nanocomposites with Controllable Grafting Polymer Chains via Moderate in Situ SET–LRP. *J. Polym. Sci. Part A Polym. Chem.* **2012**, *50* (21), 4451–4458.

(75) Ramesh, P.; Karla, S.; Alshehri, A.; Yu, M.; Kilduff, J.; Belfort, G. Stiffening Polymer Brush Membranes for Enhanced Organic Solvent Nanofiltration Selectivity. *ACS Appl. Mater. Interfaces* **2023**, *15* (26), 31966–31978.

(76) Gao, W.; Zhang, Y.; Ramanujan, D.; Ramani, K.; Chen, Y.; Williams, C. B.; Wang, C. C. L.; Shin, Y. C.; Zhang, S.; Zavattieri, P. D. The Status, Challenges, and Future of Additive Manufacturing in Engineering. *Comput. Des.* **2015**, *69*, 65–89.

(77) Motyl, B.; Filippi, S. Trends in Engineering Education for Additive Manufacturing in the Industry 4.0 Era: A Systematic Literature Review. *Int. J. Interact. Des. Manuf.* **2021**, *15* (1), 103–106.

(78) Goehrke, S. *Point of Pivot: 3D Printing vs. Injection Molding*. https://www.plasticstoday.com/3d-printing/point-pivot-3d-printing-vs-injection-molding.

(79) Kafle, A.; Luis, E.; Silwal, R.; Pan, H. M.; Shrestha, P. L.; Bastola, A. K. 3D/4D Printing of Polymers: Fused Deposition Modelling (FDM), Selective Laser Sintering (SLS), and Stereolithography (SLA). *Polymers (Basel).* **2021**, *13* (18), 3101.

(80) Mazzanti, V.; Malagutti, L.; Mollica, F. FDM 3D Printing of Polymers Containing Natural Fillers: A Review of Their Mechanical Properties. *Polymers (Basel).* **2019**, *11* (7).

(81) K-mac-plastics. *HDPE (High Density Polyethylene) Typical Properties*. retrieved on 01.09.2023. http://k-mac-plastics.com/data-sheets/hdpe.htm.

(82) Singh, N.; Hui, D.; Singh, R.; Ahuja, I. P. S.; Feo, L.; Fraternali, F. Recycling of Plastic Solid Waste: A State of Art Review and Future Applications. *Compos. Part B Eng.* **2017**, *115*, 409–422.

(83) Geyer, R.; Jambeck, J. R.; Law, K. L. Production, Use, and Fate of All Plastics Ever Made. *Sci. Adv.* **2017**, *3* (7).

(84) Jerry Fischer. *Handbook of Molded Part Shrinkage and Warpage*; Andrew, W., Ed.; 2013.

(85) *HDPE Filament - Natural - 1.75mm*. Available : https://filaments.ca/products/hdpe-filament-natural-1-75mm?variant=42590589320.

(86) Houshyar, S.; Shanks, R. A.; Hodzic, A. The Effect of Fiber Concentration on Mechanical and Thermal Properties of Fiber-Reinforced Polypropylene Composites. *J. Appl. Polym. Sci.* **2005**, *96* (6), 2260–2272.

(87) Erbetta, C. D. C.; Manoel, G. F.; Oliveira, A. P. L. R.; Silva, M. E. S. R. e; Freitas, R. F. S.; Sousa, R. G. Rheological and Thermal Behavior of High-Density Polyethylene (HDPE) at Different Temperatures. *Mater. Sci. Appl.* **2014**, *05* (13), 923–931.

(88) Schirmeister, C. G.; Hees, T.; Licht, E. H.; Mülhaupt, R. 3D Printing of High Density Polyethylene by Fused Filament Fabrication. *Addit. Manuf.* **2019**, *28* (April), 152–159.

(89) Mora, A.; Verma, P.; Kumar, S. Electrical Conductivity of CNT/Polymer Composites: 3D Printing, Measurements and Modeling. *Compos. Part B Eng.* **2020**, *183*, 107600.

(90) Spoerk, M.; Sapkota, J.; Weingrill, G.; Fischinger, T.; Arbeiter, F.; Holzer, C. Shrinkage and Warpage Optimization of Expanded-Perlite-Filled Polypropylene Composites in Extrusion-Based Additive Manufacturing. *Macromol. Mater. Eng.* **2017**, *302* (10), 1700143.

(91) Zander, N. E.; Park, J. H.; Boelter, Z. R.; Gillan, M. A. Recycled Cellulose Polypropylene Composite Feedstocks for Material Extrusion Additive Manufacturing. *ACS Omega* **2019**, *4* (9), 13879–13888.

(92) Rauwendaal, C. J. Analysis and Experimental Evaluation of Twin Screw Extruders. *Polym. Eng. Sci.* **1981**, *21* (16), 1092–1100.

(93) Ludvik, C. N.; Glenn, G. M.; Klamczynski, A. P.; Wood, D. F. Cellulose Fiber/Bentonite Clay/Biodegradable Thermoplastic Composites. *J. Polym. Environ.* **2007**, *15* (4), 251–257.

(94) Ponnamma, D.; Cabibihan, J.-J.; Rajan, M.; Pethaiah, S. S.; Deshmukh, K.; Gogoi, J. P.; Pasha, S. K. K.; Ahamed, M. B.; Krishnegowda, J.; Chandrashekar, B. N.; Polu, A. R.; Cheng, C. Synthesis, Optimization and Applications of ZnO/Polymer Nanocomposites. *Mater. Sci. Eng. C* **2019**, *98*, 1210–1240.

(95) Kerni, L.; Singh, S.; Patnaik, A.; Kumar, N. A Review on Natural Fiber Reinforced Composites. *Mater. Today Proc.* **2020**, *28*, 1616–1621.

(96) Gallos, A.; Paës, G.; Allais, F.; Beaugrand, J. Lignocellulosic Fibers: A Critical Review of the Extrusion Process for Enhancement of the Properties of Natural Fiber Composites. *RSC Adv.* **2017**, *7* (55), 34638–34654.

(97) Skeldon, G.; Lucendo-Villarin, B.; Shu, W. Three-Dimensional Bioprinting of Stem-Cell Derived Tissues for Human Regenerative Medicine. *Philos. Trans. R. Soc. B Biol. Sci.* **2018**, *373* (1750), 20170224.

(98) Kačarević, Ž.; Rider, P.; Alkildani, S.; Retnasingh, S.; Smeets, R.; Jung, O.; Ivanišević, Z.; Barbeck, M. An Introduction to 3D Bioprinting: Possibilities, Challenges and Future Aspects. *Materials (Basel).* **2018**, *11* (11), 2199.

(99) Zhou, M.; Lee, B. H.; Tan, L. P. A Dual Crosslinking Strategy to Tailor Rheological Properties of Gelatin Methacryloyl. *Int. J. Bioprinting* **2017**, *3* (2), 130.

(100) Xu, C.; Lee, W.; Dai, G.; Hong, Y. Highly Elastic Biodegradable Single-Network Hydrogel for Cell Printing. *ACS Appl. Mater. Interfaces* **2018**, *10* (12), 9969–9979.

(101) Ribeiro, A.; Blokzijl, M. M.; Levato, R.; Visser, C. W.; Castilho, M.; Hennink, W. E.; Vermonden, T.; Malda, J. Assessing Bioink Shape Fidelity to Aid Material Development in 3D Bioprinting. *Biofabrication* **2017**, *10* (1), 014102.

(102) Schwab, A.; Levato, R.; D'Este, M.; Piluso, S.; Eglin, D.; Malda, J. Printability and Shape Fidelity of Bioinks in 3D Bioprinting. *Chem. Rev.* **2020**, *120* (19), 11028–11055.

(103) Bian, L. Functional Hydrogel Bioink, a Key Challenge of 3D Cellular Bioprinting. *APL Bioeng.* **2020**, *4* (3), 030401.

(104) Khoeini, R.; Nosrati, H.; Akbarzadeh, A.; Eftekhari, A.; Kavetskyy, T.; Khalilov, R.; Ahmadian, E.; Nasibova, A.; Datta, P.; Roshangar, L.; Deluca, D. C.; Davaran, S.; Cucchiarini, M.; Ozbolat, I. T. Natural and Synthetic Bioinks for 3D Bioprinting. *Adv. NanoBiomed Res.* **2021**, *1* (8), 2000097.

(105) Skardal, A.; Zhang, J.; Prestwich, G. D. Bioprinting Vessel-like Constructs Using Hyaluronan Hydrogels Crosslinked with Tetrahedral Polyethylene Glycol Tetracrylates. *Biomaterials* **2010**, *31* (24), 6173–6181.

(106) Datta, S.; Das, A.; Chowdhury, A. R.; Datta, P. Bioink Formulations to Ameliorate Bioprinting-Induced Loss of Cellular Viability. *Biointerphases* **2019**, *14* (5).

(107) Blaeser, A.; Duarte Campos, D. F.; Puster, U.; Richtering, W.; Stevens, M. M.; Fischer, H. Controlling Shear Stress in 3D Bioprinting Is a Key Factor to Balance Printing Resolution and Stem Cell Integrity. *Adv. Healthc. Mater.* **2016**, *5* (3), 326–333.

(108) Cheng, Q.; Liu, Y.; Lyu, J.; Lu, Q.; Zhang, X.; Song, W. 3D Printing-Directed Auxetic Kevlar Aerogel Architectures with Multiple Functionalization Options. *J. Mater. Chem. A* **2020**, *8* (28), 14243–14253.

(109) Bohner, M.; Baroud, G. Injectability of Calcium Phosphate Pastes. *Biomaterials* **2005**, *26* (13), 1553–1563.

(110) Jiang, X.; Yang, X.; Yang, B.; Zhang, L.; Lu, A. Highly Self-Healable and Injectable Cellulose Hydrogels via Rapid Hydrazone Linkage for Drug Delivery and 3D Cell Culture. *Carbohydr. Polym.* **2021**, *273*, 118547.

(111) Abdulghani, S.; Morouço, P. G. Biofabrication for Osteochondral Tissue Regeneration: Bioink Printability Requirements. *J. Mater. Sci. Mater. Med.* **2019**, *30* (2), 20.

(112) Decante, G.; Costa, J. B.; Silva-Correia, J.; Collins, M. N.; Reis, R. L.; Oliveira, J. M. Engineering Bioinks for 3D Bioprinting. *Biofabrication* **2021**, *13* (3), 032001.

(113) *The IUPAC Compendium of Chemical Terminology*; Gold, V., Ed.; International Union of Pure and Applied Chemistry (IUPAC): Research Triangle Park, NC, 2019.

(114) Almdal, K.; Dyre, J.; Hvidt, S.; Kramer, O. Towards a Phenomenological Definition of the Term 'Gel.' *Polym. Gels Networks* **1993**, *1* (1), 5–17.

(115) Slomkowski, S.; Alemán, J. V.; Gilbert, R. G.; Hess, M.; Horie, K.; Jones, R. G.; Kubisa, P.; Meisel, I.; Mormann, W.; Penczek, S.; Stepto, R. F. T. Terminology of Polymers and Polymerization Processes in Dispersed Systems (IUPAC Recommendations 2011). *Pure Appl. Chem.* **2011**, *83* (12), 2229–2259.

(116) Fan, L.; He, Z.; Peng, X.; Xie, J.; Su, F.; Wei, D.-X.; Zheng, Y.; Yao, D. Injectable, Intrinsically Antibacterial Conductive Hydrogels with Self-Healing and PH Stimulus Responsiveness for Epidermal Sensors and Wound Healing. *ACS Appl. Mater. Interfaces* **2021**, *13* (45), 53541–53552.

(117) Dromel, P. C.; Singh, D.; Alexander-Katz, A.; Kurisawa, M.; Spector, M.; Young, M. Mechano-Chemical Effect of Gelatin- and HA-Based Hydrogels on Human Retinal Progenitor Cells. *Gels* **2023**, *9* (1), 58.

(118) Li, B.; Qin, H.; Ma, M.; Xu, X.; Zhou, M.; Hao, W.; Hu, Z. Preparation of Novel β-CD/P(AA- Co -AM) Hydrogels by Frontal Polymerization. *RSC Adv.* **2023**, *13* (9), 5667–5673.

(119) Bashir, S.; Hina, M.; Iqbal, J.; Rajpar, A. H.; Mujtaba, M. A.; Alghamdi, N. A.; Wageh, S.; Ramesh, K.; Ramesh, S. Fundamental Concepts of Hydrogels: Synthesis, Properties, and Their Applications. *Polymers (Basel).* **2020**, *12* (11), 2702.

(120) Madduma-Bandarage, U. S. K.; Madihally, S. V. Synthetic Hydrogels: Synthesis, Novel Trends, and Applications. *J. Appl. Polym. Sci.* **2021**, *138* (19).

(121) Panja, S.; Adams, D. J. Maintaining Homogeneity during a Sol–Gel Transition by an Autocatalytic Enzyme Reaction. *Chem. Commun.* **2019**, *55* (1), 47–50.

(122) Laurano, R.; Boffito, M.; Cassino, C.; Midei, L.; Pappalardo, R.; Chiono, V.; Ciardelli, G. Thiol-Ene Photo-Click Hydrogels with Tunable Mechanical Properties Resulting from the Exposure of Different -Ene Moieties through a Green Chemistry. *Materials (Basel).* **2023**, *16* (5), 2024.

(123) Engelberg, Y.; Ragonis-Bachar, P.; Landau, M. Rare by Natural Selection: Disulfide-Bonded Supramolecular Antimicrobial Peptides. *Biomacromolecules* **2022**, *23* (3), 926–936.

(124) Dong, H.; Wang, M.; Fan, S.; Wu, C.; Zhang, C.; Wu, X.; Xue, B.; Cao, Y.; Deng, J.; Yuan, D.; Shi, J. Redox-Regulated Conformational Change of Disulfide-Rich Assembling Peptides. *Angew. Chemie Int. Ed.* **2022**, *61* (44).

(125) He, L.; Fullenkamp, D. E.; Rivera, J. G.; Messersmith, P. B. PH Responsive Self-Healing Hydrogels Formed by Boronate–Catechol Complexation. *Chem. Commun.* **2011**, *47* (26), 7497.

(126) Yamauchi, K.; Lizotte, J. R.; Long, T. E. Thermoreversible Poly(Alkyl Acrylates) Consisting of Self-Complementary Multiple Hydrogen Bonding. *Macromolecules* **2003**, *36* (4), 1083–1088.

(127) Barbosa-Cánovas, G. V.; Kokini, J. L.; Ma, L.; Ibarz, A. The Rheology of Semiliquid Foods; 1996; pp 1–69.

(128) Dickinson, E. Structure, Stability and Rheology of Flocculated Emulsions. *Curr. Opin. Colloid Interface Sci.* **1998**, *3* (6), 633–638.

(129) Physics, I. *Types of Viscometer*. Cited on 28.09.2023. https://industrialphysics.com/knowledgebase/articles/types-of-viscometer/.

(130) Tschoegl, N. W. *The Phenomenological Theory of Linear Viscoelastic Behavior: An Introduction.*; Springer Science & Business Media, 2012.

(131) Cooke, M. E.; Rosenzweig, D. H. The Rheology of Direct and Suspended Extrusion Bioprinting. *APL Bioeng.* **2021**, *5* (1), 011502.

(132) Paxton, N.; Smolan, W.; Böck, T.; Melchels, F.; Groll, J.; Jungst, T. Proposal to Assess Printability of Bioinks for Extrusion-Based Bioprinting and Evaluation of Rheological Properties Governing Bioprintability. *Biofabrication* **2017**, *9* (4), 44107.

(133) Dinkgreve, M.; Paredes, J.; Denn, M. M.; Bonn, D. On Different Ways of Measuring "the" Yield Stress. *J. Nonnewton. Fluid Mech.* **2016**, *238*, 233–241.

(134) Sun, A.; Gunasekaran, S. Yield Stress in Foods: Measurements and Applications. *Int. J. Food Prop.* **2009**, *12* (1), 70–101.

(135) Gillispie, G.; Prim, P.; Copus, J.; Fisher, J.; Mikos, A. G.; Yoo, J. J.; Atala, A.; Lee, S. J. Assessment Methodologies for Extrusion-Based Bioink Printability. *Biofabrication* **2020**, *12* (2), 022003.

(136) Lee, W.-F.; Yen, S.-H. Thermoreversible Hydrogels. XII. Effect of the Polymerization Conditions on the Swelling Behavior of the N-Isopropylacrylamide Gel. *J. Appl. Polym. Sci.* **2000**, *78* (9), 1604–1611.

(137) Aerogel. In *The IUPAC Compendium of Chemical Terminology*; International Union of Pure and Applied Chemistry (IUPAC): Research Triangle Park, NC, 2014.

(138) Fricke, J. Aerogels and Their Applications. *J. Non. Cryst. Solids* **1992**, *147–148*, 356–362.

(139) C. Jeffrey Brinker, G. W. S. *Sol-Gel Science*; 1990.

(140) Sarkar, A.; Chaudhuri, S. R.; Wang, S.; Kirkbir, F.; Murata, H. Drying of Alkoxide

Gels?Observation of an Alternate Phenomenology. *J. Sol-Gel Sci. Technol.* **1994**, *2* (1–3), 865–870.

(141) Scherer, G. W.; Smith, D. M. Cavitation during Drying of a Gel. *J. Non. Cryst. Solids* **1995**, *189* (3), 197–211.

(142) Liang, X.-Y.; Wang, L.; Chang, Z.-Y.; Ding, L.-S.; Li, B.-J.; Zhang, S. Reusable Xerogel Containing Quantum Dots with High Fluorescence Retention. *Polymers (Basel).* **2018**, *10* (3), 310.

(143) Simón-Herrero, C.; Caminero-Huertas, S.; Romero, A.; Valverde, J. L.; Sánchez-Silva, L. Effects of Freeze-Drying Conditions on Aerogel Properties. *J. Mater. Sci.* **2016**, *51* (19), 8977–8985.

(144) Choi, M. J.; Briançon, S.; Andrieu, J.; Min, S. G.; Fessi, H. Effect of Freeze-Drying Process Conditions on the Stability of Nanoparticles. *Dry. Technol.* **2004**, *22* (1–2), 335–346.

(145) Tamon, H.; Ishizaka, H.; Yamamoto, T.; Suzuki, T. FREEZE DRYING FOR PREPARATION OF AEROGEL-LIKE CARBON. *Dry. Technol.* **2001**, *19* (2), 313–324.

(146) Krokida, M. K.; Karathanos, V. T.; Maroulis, Z. B. Effect of Freeze-Drying Conditions on Shrinkage and Porosity of Dehydrated Agricultural Products. *J. Food Eng.* **1998**, *35* (4), 369–380.

(147) Guastaferro, M.; Reverchon, E.; Baldino, L. Agarose, Alginate and Chitosan Nanostructured Aerogels for Pharmaceutical Applications: A Short Review. *Front. Bioeng. Biotechnol.* **2021**, *9*.

(148) Guastaferro, M.; Baldino, L.; Reverchon, E.; Cardea, S. Production of Porous Agarose-Based Structures: Freeze-Drying vs. Supercritical CO2 Drying. *Gels* **2021**, *7* (4), 198.

(149) Gurav, J. L.; Jung, I.-K.; Park, H.-H.; Kang, E. S.; Nadargi, D. Y. Silica Aerogel: Synthesis and Applications. *J. Nanomater.* **2010**, *2010*, 1–11.

(150) Gesser, H. D.; Goswami, P. C. Aerogels and Related Porous Materials. *Chem. Rev.* **1989**, *89* (4), 765–788.

(151) S. Thomas, L. A. Pothan, R. M.-S. *Biobased Aerogels*; Thomas, S., Pothan, L. A., Mavelil-Sam, R., Eds.; Green Chemistry Series; Royal Society of Chemistry: Cambridge, 2018.

(152) Meador, M. A. B.; Malow, E. J.; Silva, R.; Wright, S.; Quade, D.; Vivod, S. L.; Guo, H.; Guo, J.; Cakmak, M. Mechanically Strong, Flexible Polyimide Aerogels Cross-Linked with Aromatic Triamine. *ACS Appl. Mater. Interfaces* **2012**, *4* (2), 536–544.

(153) Maleki, H.; Durães, L.; Portugal, A. Synthesis of Lightweight Polymer-Reinforced Silica Aerogels with Improved Mechanical and Thermal Insulation Properties for Space Applications. *Microporous Mesoporous Mater.* **2014**, *197*, 116–129.

(154) Wang, J.; Petit, D.; Ren, S. Transparent Thermal Insulation Silica Aerogels. *Nanoscale*

Adv. **2020**, *2* (12), 5504–5515.

(155) Lu, T.; Li, Q.; Chen, W.; Yu, H. Composite Aerogels Based on Dialdehyde Nanocellulose and Collagen for Potential Applications as Wound Dressing and Tissue Engineering Scaffold. *Compos. Sci. Technol.* **2014**, *94*, 132–138.

(156) Hou, Y.; Zhong, X.; Ding, Y.; Zhang, S.; Shi, F.; Hu, J. Alginate-Based Aerogels with Double Catalytic Activity Sites and High Mechanical Strength. *Carbohydr. Polym.* **2020**, *245*, 116490.

(157) Yang, B.; Wang, L.; Zhao, J.; Pang, R.; Yuan, B.; Tan, J.; Song, S.; Nie, J.; Zhang, M. A Robust, Flexible, Hydrophobic, and Multifunctional Pressure Sensor Based on an MXene/Aramid Nanofiber (ANF) Aerogel Film. *ACS Appl. Mater. Interfaces* **2022**, *14* (41), 47075–47088.

(158) Wang, D.-C.; Yu, H.-Y.; Qi, D.; Ramasamy, M.; Yao, J.; Tang, F.; Tam, K. (Michael) C.; Ni, Q. Supramolecular Self-Assembly of 3D Conductive Cellulose Nanofiber Aerogels for Flexible Supercapacitors and Ultrasensitive Sensors. *ACS Appl. Mater. Interfaces* **2019**, *11* (27), 24435–24446.

(159) Daveiga, J. , Ferreira, P. *Smart and Nano Materials in Architecture.*; 2005.

(160) Funakubo Hiroyasu, J. B. Kennedy, G. & B. *Shape Memory Alloys*; New York: Gordon and Breach Science., 1987.

(161) Lagoudas, D. C. *Shape Memory Alloys*; Springer US: Boston, MA, 2008.

(162) Guo, M.; Pitet, L. M.; Wyss, H. M.; Vos, M.; Dankers, P. Y. W.; Meijer, E. W. Tough Stimuli-Responsive Supramolecular Hydrogels with Hydrogen-Bonding Network Junctions. *J. Am. Chem. Soc.* **2014**, *136* (19), 6969–6977.

(163) Ahn, S.; Kasi, R. M.; Kim, S.-C.; Sharma, N.; Zhou, Y. Stimuli-Responsive Polymer Gels. *Soft Matter* **2008**, *4* (6), 1151.

(164) Wei, J.; Chen, Y.; Liu, H.; Du, C.; Yu, H.; Zhou, Z. Thermo-Responsive and Compression Properties of TEMPO-Oxidized Cellulose Nanofiber-Modified PNIPAm Hydrogels. *Carbohydr. Polym.* **2016**, *147*, 201–207.

(165) Khan, S. A.; Azam, W.; Ashames, A.; Fahelelbom, K. M.; Ullah, K.; Mannan, A.; Murtaza, G. β-Cyclodextrin-Based (IA-Co-AMPS) Semi-IPNs as Smart Biomaterials for Oral Delivery of Hydrophilic Drugs: Synthesis, Characterization, in-Vitro and in-Vivo Evaluation. *J. Drug Deliv. Sci. Technol.* **2020**, *60*, 101970.

(166) Wang, X.; Schröder, H. C.; Müller, W. E. G. Amorphous Polyphosphate, a Smart Bioinspired Nano-/Bio-Material for Bone and Cartilage Regeneration: Towards a New Paradigm in Tissue Engineering. *J. Mater. Chem. B* **2018**, *6* (16), 2385–2412.

(167) Ziai, Y.; Rinoldi, C.; Nakielski, P.; De Sio, L.; Pierini, F. Smart Plasmonic Hydrogels Based on Gold and Silver Nanoparticles for Biosensing Application. *Curr. Opin. Biomed. Eng.* **2022**, *24*, 100413.

(168) Talon, I.; Schneider, A.; Ball, V.; Hemmerle, J. Polydopamine Functionalization: A Smart and Efficient Way to Improve Host Responses to e-PTFE Implants. *Front.*

Chem. **2019**, *7*.

(169) Van Gemert, G. M. L.; Peeters, J. W.; Söntjens, S. H. M.; Janssen, H. M.; Bosman, A. W. Self-Healing Supramolecular Polymers in Action. *Macromol. Chem. Phys.* **2012**, *213* (2), 234–242.

(170) Amaral, A. J. R.; Pasparakis, G. Stimuli Responsive Self-Healing Polymers: Gels, Elastomers and Membranes. *Polym. Chem.* **2017**, *8* (42), 6464–6484.

(171) Lan, Z.; Chen, X.; Zhang, X.; Zhu, C.; Yu, Y.; Wei, J. Transparent, High Glass-Transition Temperature, Shape Memory Hybrid Polyimides Based on Polyhedral Oligomeric Silsesquioxane. *Polymers (Basel).* **2019**, *11* (6), 1058.

(172) Wang, Y.; Pham, D. T.; Zhang, Z.; Li, J.; Ji, C.; Liu, Y.; Leng, J. Sustainable Self-Healing at Ultra-Low Temperatures in Structural Composites Incorporating Hollow Vessels and Heating Elements. *R. Soc. Open Sci.* **2016**, *3* (9), 160488.

(173) Utrera-Barrios, S.; Verdejo, R.; López-Manchado, M. A.; Hernández Santana, M. Evolution of Self-Healing Elastomers, from Extrinsic to Combined Intrinsic Mechanisms: A Review. *Mater. Horizons* **2020**, *7* (11), 2882–2902.

(174) Guo, H.; Han, Y.; Zhao, W.; Yang, J.; Zhang, L. Universally Autonomous Self-Healing Elastomer with High Stretchability. *Nat. Commun.* **2020**, *11* (1), 2037.

(175) Zhang, Y.; Khanbareh, H.; Roscow, J.; Pan, M.; Bowen, C.; Wan, C. Self-Healing of Materials under High Electrical Stress. *Matter* **2020**, *3* (4), 989–1008.

(176) Nakahata, M.; Takashima, Y.; Harada, A. Highly Flexible, Tough, and Self-Healing Supramolecular Polymeric Materials Using Host-Guest Interaction. *Macromol. Rapid Commun.* **2016**, *37* (1), 86–92.

(177) Fan, H.; Wang, J.; Jin, Z. Tough, Swelling-Resistant, Self-Healing, and Adhesive Dual-Cross-Linked Hydrogels Based on Polymer–Tannic Acid Multiple Hydrogen Bonds. *Macromolecules* **2018**, *51* (5), 1696–1705.

(178) Xing, R.; Li, S.; Zhang, N.; Shen, G.; Möhwald, H.; Yan, X. Self-Assembled Injectable Peptide Hydrogels Capable of Triggering Antitumor Immune Response. *Biomacromolecules* **2017**, *18* (11), 3514–3523.

(179) Zhang, K.; Liu, Y.; Wang, Z.; Song, C.; Gao, C.; Wu, Y. A Type of Self-Healable, Dissoluble and Stretchable Organosilicon Elastomer for Flexible Electronic Devices. *Eur. Polym. J.* **2020**, *134*, 109857.

(180) Canadell, J.; Goossens, H.; Klumperman, B. Self-Healing Materials Based on Disulfide Links. *Macromolecules* **2011**, *44* (8), 2536–2541.

(181) Pramanik, N. B.; Nando, G. B.; Singha, N. K. Self-Healing Polymeric Gel via RAFT Polymerization and Diels–Alder Click Chemistry. *Polymer (Guildf).* **2015**, *69*, 349–356.

(182) Feldblum, E. S.; Arkin, I. T. Strength of a Bifurcated H Bond. *Proc. Natl. Acad. Sci.* **2014**, *111* (11), 4085–4090.

(183) Eastmond, G. .; Smith, E. . Network Properties: 3. A Pulsed n.m.r. Study of Molecular

Motions in Some AB-Crosslinked Polymers. *Polymer (Guildf).* **1977**, *18* (3), 244–250.

(184) Hackelbusch, S.; Rossow, T.; van Assenbergh, P.; Seiffert, S. Chain Dynamics in Supramolecular Polymer Networks. *Macromolecules* **2013**, *46* (15), 6273–6286.

(185) Phadke, A.; Zhang, C.; Arman, B.; Hsu, C.-C.; Mashelkar, R. A.; Lele, A. K.; Tauber, M. J.; Arya, G.; Varghese, S. Rapid Self-Healing Hydrogels. *Proc. Natl. Acad. Sci.* **2012**, *109* (12), 4383–4388.

(186) Sijbesma, R. P.; Beijer, F. H.; Brunsveld, L.; Folmer, B. J. B.; Hirschberg, J. H. K. K.; Lange, R. F. M.; Lowe, J. K. L.; Meijer, E. W. Reversible Polymers Formed from Self-Complementary Monomers Using Quadruple Hydrogen Bonding. *Science (80-.).* **1997**, *278* (5343), 1601–1604.

(187) van Beek, D. J. M.; Spiering, A. J. H.; Peters, G. W. M.; te Nijenhuis, K.; Sijbesma, R. P. Unidirectional Dimerization and Stacking of Ureidopyrimidinone End Groups in Polycaprolactone Supramolecular Polymers. *Macromolecules* **2007**, *40* (23), 8464–8475.

(188) Suriano, R.; Brambilla, L.; Tommasini, M.; Turri, S. A Deep Insight into the Intrinsic Healing Mechanism in Ureido-Pyrimidinone Copolymers. *Polym. Adv. Technol.* **2018**, *29* (12), 2899–2908.

(189) Amaral, A. J. R.; Pasparakis, G. Stimuli Responsive Self-Healing Polymers: Gels, Elastomers and Membranes. *Polym. Chem.* **2017**, *8* (42), 6464–6484.

(190) Zhang, G.; Ngai, T.; Deng, Y.; Wang, C. An Injectable Hydrogel with Excellent Self-Healing Property Based on Quadruple Hydrogen Bonding. *Macromol. Chem. Phys.* **2016**, *217* (19), 2172–2181.

(191) Oya, N.; Ikezaki, T.; Yoshie, N. A Crystalline Supramolecular Polymer with Self-Healing Capability at Room Temperature. *Polym. J.* **2013**, *45* (9), 955–961.

(192) Zhu, D.; Ye, Q.; Lu, X.; Lu, Q. Self-Healing Polymers with PEG Oligomer Side Chains Based on Multiple H-Bonding and Adhesion Properties. *Polym. Chem.* **2015**, *6* (28), 5086–5092.

(193) Wang, Q.; Shi, Z.; Shou, Y.; Zhang, K.; Li, G.; Xia, P.; Yan, S.; Yin, J. Stack-Based Hydrogels with Mechanical Enhancement, High Stability, Self-Healing Property, and Thermoplasticity from Poly(<scp>l</Scp> -Glutamic Acid) and Ureido-Pyrimidinone. *ACS Biomater. Sci. Eng.* **2020**, *6* (3), 1715–1726.

(194) Biyani, M. V.; Foster, E. J.; Weder, C. Light-Healable Supramolecular Nanocomposites Based on Modified Cellulose Nanocrystals. *ACS Macro Lett.* **2013**, *2* (3), 236–240.

(195) Diaferia, C.; Sibillano, T.; Giannini, C.; Roviello, V.; Vitagliano, L.; Morelli, G.; Accardo, A. Photoluminescent Peptide-Based Nanostructures as FRET Donor for Fluorophore Dye. *Chem. – A Eur. J.* **2017**, *23* (36), 8741–8748.

(196) Li, L.; Charati, M. B.; Kiick, K. L. Elastomeric Polypeptide-Based Biomaterials. *Polym. Chem.* **2010**, *1* (8), 1160.

(197) Rubert Pérez, C. M.; Stephanopoulos, N.; Sur, S.; Lee, S. S.; Newcomb, C.; Stupp, S. I. The Powerful Functions of Peptide-Based Bioactive Matrices for Regenerative Medicine. *Ann. Biomed. Eng.* **2015**, *43* (3), 501–514.

(198) Sewald, N. / Jakubke, H.-D. *Peptides: Chemistry and Biology*; 2015.

(199) Gazit, E. Self-Assembled Peptide Nanostructures: The Design of Molecular Building Blocks and Their Technological Utilization. *Chem. Soc. Rev.* **2007**, *36* (8), 1263.

(200) Nolan, M. C.; Fuentes Caparrós, A. M.; Dietrich, B.; Barrow, M.; Cross, E. R.; Bleuel, M.; King, S. M.; Adams, D. J. Optimising Low Molecular Weight Hydrogels for Automated 3D Printing. *Soft Matter* **2017**, *13* (45), 8426–8432.

(201) Khalily, M. A.; Goktas, M.; Guler, M. O. Tuning Viscoelastic Properties of Supramolecular Peptide Gels via Dynamic Covalent Crosslinking. *Org. Biomol. Chem.* **2015**, *13* (7), 1983–1987.

(202) Choe, R.; Il Yun, S. Fmoc-Diphenylalanine-Based Hydrogels as a Potential Carrier for Drug Delivery. *e-Polymers* **2020**, *20* (1), 458–468.

(203) Xing, R.; Yuan, C.; Li, S.; Song, J.; Li, J.; Yan, X. Charge-Induced Secondary Structure Transformation of Amyloid-Derived Dipeptide Assemblies from B-Sheet to A-Helix. *Angew. Chemie Int. Ed.* **2018**, *57* (6), 1537–1542.

(204) Dudukovic, N. A.; Zukoski, C. F. Gelation of Fmoc-Diphenylalanine Is a First Order Phase Transition. *Soft Matter* **2015**, *11* (38), 7663–7673.

(205) Tang, C.; Smith, A. M.; Collins, R. F.; Ulijn, R. V.; Saiani, A. Fmoc-Diphenylalanine Self-ASsembly Mechanism Induces Apparent PK a Shifts. *Langmuir* **2009**, *25* (16), 9447–9453.

(206) Smith, A. M.; Williams, R. J.; Tang, C.; Coppo, P.; Collins, R. F.; Turner, M. L.; Saiani, A.; Ulijn, R. V. Fmoc-Diphenylalanine Self Assembles to a Hydrogel via a Novel Architecture Based on π–π Interlocked β-Sheets. *Adv. Mater.* **2008**, *20* (1), 37–41.

(207) Reches, M.; Gazit, E. Self-Assembly of Peptide Nanotubes and Amyloid-like Structures by Charged-Termini-Capped Diphenylalanine Peptide Analogues. *Isr. J. Chem.* **2005**, *45* (3), 363–371.

(208) Diaferia, C.; Morelli, G.; Accardo, A. Fmoc-Diphenylalanine as a Suitable Building Block for the Preparation of Hybrid Materials and Their Potential Applications. *J. Mater. Chem. B* **2019**, *7* (34), 5142–5155.

(209) Almohammed, S.; Alruwaili, M.; Reynaud, E. G.; Redmond, G.; Rice, J. H.; Rodriguez, B. J. 3D-Printed Peptide-Hydrogel Nanoparticle Composites for Surface-Enhanced Raman Spectroscopy Sensing. *ACS Appl. Nano Mater.* **2019**, *2* (8), 5029–5034.

(210) Gong, X.; Branford-White, C.; Tao, L.; Li, S.; Quan, J.; Nie, H.; Zhu, L. Preparation and Characterization of a Novel Sodium Alginate Incorporated Self-Assembled Fmoc-FF Composite Hydrogel. *Mater. Sci. Eng. C* **2016**, *58*, 478–486.

(211) Scott, G.; Roy, S.; Abul-Haija, Y. M.; Fleming, S.; Bai, S.; Ulijn, R. V. Pickering Stabilized Peptide Gel Particles as Tunable Microenvironments for Biocatalysis. *Langmuir* **2013**, *29* (46), 14321–14327.

(212) Diaferia, C.; Rosa, E.; Morelli, G.; Accardo, A. Fmoc-Diphenylalanine Hydrogels: Optimization of Preparation Methods and Structural Insights. *Pharmaceuticals* **2022**, *15* (9), 1048.

(213) Navarro, J. R. G.; Edlund, U. Surface-Initiated Controlled Radical Polymerization Approach To Enhance Nanocomposite Integration of Cellulose Nanofibrils. *Biomacromolecules* **2017**, *18* (6), 1947–1955.

(214) Wickholm, K.; Larsson, P. T.; Iversen, T. Assignment of Non-Crystalline Forms in Cellulose I by CP/MAS 13C NMR Spectroscopy. *Carbohydr. Res.* **1998**, *312* (3), 123–129.

(215) Johnson, R. L.; Schmidt-Rohr, K. Quantitative Solid-State 13C NMR with Signal Enhancement by Multiple Cross Polarization. *J. Magn. Reson.* **2014**, *239*, 44–49.

(216) Falourd, X.; Rondeau-Mouro, C.; Cambert, M.; Lahaye, M.; Chabbert, B.; Aguié-Béghin, V. Assessing the Complementarity of Time Domain NMR, Solid-State NMR and Dynamic Vapor Sorption in the Characterization of Polysaccharide-Water Interactions. *Carbohydr. Polym.* **2024**, *326*, 121579.

(217) Wu, Y.; Wang, L.; Zhao, X.; Hou, S.; Guo, B.; Ma, P. X. Self-Healing Supramolecular Bioelastomers with Shape Memory Property as a Multifunctional Platform for Biomedical Applications via Modular Assembly. *Biomaterials* **2016**, *104*, 18–31.

(218) Yan, J.; Li, M.; Wang, Z.; Chen, C.; Ma, C.; Yang, G. Highly Tough, Multi-Stimuli-Responsive, and Fast Self-Healing Supramolecular Networks toward Strain Sensor Application. *Chem. Eng. J.* **2020**, *389*, 123468.

(219) Tao, K.; Levin, A.; Adler-Abramovich, L.; Gazit, E. Fmoc-Modified Amino Acids and Short Peptides: Simple Bio-Inspired Building Blocks for the Fabrication of Functional Materials. *Chem. Soc. Rev.* **2016**, *45* (14), 3935–3953.

(220) Avitabile, C.; Diaferia, C.; Della Ventura, B.; Mercurio, F. A.; Leone, M.; Roviello, V.; Saviano, M.; Velotta, R.; Morelli, G.; Accardo, A.; Romanelli, A. Self-Assembling of Fmoc-GC Peptide Nucleic Acid Dimers into Highly Fluorescent Aggregates. *Chem. – A Eur. J.* **2018**, *24* (18), 4729–4735.

(221) Gawande, M. B.; Branco, P. S. An Efficient and Expeditious Fmoc Protection of Amines and Amino Acids in Aqueous Media. *Green Chem.* **2011**, *13* (12), 3355.

(222) Courtier-Murias, D.; Farooq, H.; Masoom, H.; Botana, A.; Soong, R.; Longstaffe, J. G.; Simpson, M. J.; Maas, W. E.; Fey, M.; Andrew, B.; Struppe, J.; Hutchins, H.; Krishnamurthy, S.; Kumar, R.; Monette, M.; Stronks, H. J.; Hume, A.; Simpson, A. J. Comprehensive Multiphase NMR Spectroscopy: Basic Experimental Approaches to Differentiate Phases in Heterogeneous Samples. *J. Magn. Reson.* **2012**, *217*, 61–76.

(223) Dong, X. M.; Gray, D. G. Effect of Counterions on Ordered Phase Formation in Suspensions of Charged Rodlike Cellulose Crystallites. *Langmuir* **1997**, *13* (8), 2404–

2409.

(224) Beck, S.; Bouchard, J.; Berry, R. Dispersibility in Water of Dried Nanocrystalline Cellulose. *Biomacromolecules* **2012**, *13* (5), 1486–1494.

(225) Catrinck, T. C. P. G.; Dias, A.; Aguiar, M. C. S.; Silvério, F. O.; Fidêncio, P. H.; Pinho, G. P. A Simple and Efficient Method for Derivatization of Glyphosate and AMPA Using 9-Fluorenylmethyl Chloroformate and Spectrophotometric Analysis. *J. Braz. Chem. Soc.* **2014**.

(226) Tao, K.; Yoskovitz, E.; Adler-Abramovich, L.; Gazit, E. Optical Property Modulation of Fmoc Group by PH-Dependent Self-Assembly. *RSC Adv.* **2015**, *5* (90), 73914–73918.

(227) Gulmine, J. .; Janissek, P. .; Heise, H. .; Akcelrud, L. Polyethylene Characterization by FTIR. *Polym. Test.* **2002**, *21* (5), 557–563.

(228) Ding, W.; Kuboki, T.; Wong, A.; Park, C. B.; Sain, M. Rheology, Thermal Properties, and Foaming Behavior of High <scp>d</Scp> -Content Polylactic Acid/Cellulose Nanofiber Composites. *RSC Adv.* **2015**, *5* (111), 91544–91557.

(229) Liang, J.-Z. Effects of Tension Rates and Filler Size on Tensile Properties of Polypropylene/Graphene Nano-Platelets Composites. *Compos. Part B Eng.* **2019**, *167*, 241–249.

(230) Stinchcomb, W.; Reifsnider, K. Fatigue Damage Mechanisms in Composite Materials: A Review. In *Fatigue Mechanisms*; ASTM International: 100 Barr Harbor Drive, PO Box C700, West Conshohocken, PA 19428-2959; pp 762-762–26.

(231) Zhu, D.; Ye, Q.; Lu, X.; Lu, Q. Self-Healing Polymers with PEG Oligomer Side Chains Based on Multiple H-Bonding and Adhesion Properties. *Polym. Chem.* **2015**, *6* (28), 5086–5092.

(232) Mouser, V. H. M.; Abbadessa, A.; Levato, R.; Hennink, W. E.; Vermonden, T.; Gawlitta, D.; Malda, J. Development of a Thermosensitive HAMA-Containing Bio-Ink for the Fabrication of Composite Cartilage Repair Constructs. *Biofabrication* **2017**, *9* (1), 015026.

(233) Santoni, S.; Sponchioni, M.; Gugliandolo, S. G.; Colosimo, B. M.; Moscatelli, D. Preliminary Tests on PEG-Based Thermoresponsive Polymers for the Production of 3D Bioprinted Constructs. *Procedia CIRP* **2022**, *110* (C), 348–353.

(234) Song, G.; Zhao, Z.; Peng, X.; He, C.; Weiss, R. A.; Wang, H. Rheological Behavior of Tough PVP- in Situ -PAAm Hydrogels Physically Cross-Linked by Cooperative Hydrogen Bonding. *Macromolecules* **2016**, *49* (21), 8265–8273.

(235) Boztepe, S.; Gilblas, R.; de Almeida, O.; Gerlach, C.; Le Maoult, Y.; Schmidt, F. The Role of Microcrystalline Structure on Optical Scattering Characteristics of Semi-Crystalline Thermoplastics and the Accuracy of Numerical Input for IR-Heating Modeling. *Int. J. Mater. Form.* **2018**, *11* (5), 717–727.

(236) Dudukovic, N. A.; Zukoski, C. F. Evidence for Equilibrium Gels of Valence-Limited Particles. *Soft Matter* **2014**, *10* (39), 7849–7856.

(237) Dudukovic, N. A.; Zukoski, C. F. Mechanical Properties of Self-Assembled Fmoc-Diphenylalanine Molecular Gels. *Langmuir* **2014**, *30* (15), 4493–4500.

(238) Jian, H.; Wang, M.; Dong, Q.; Li, J.; Wang, A.; Li, X.; Ren, P.; Bai, S. Dipeptide Self-Assembled Hydrogels with Tunable Mechanical Properties and Degradability for 3D Bioprinting. *ACS Appl. Mater. Interfaces* **2019**, *11* (50), 46419–46426.

(239) Raeburn, J.; Pont, G.; Chen, L.; Cesbron, Y.; Lévy, R.; Adams, D. J. Fmoc-Diphenylalanine Hydrogels: Understanding the Variability in Reported Mechanical Properties. *Soft Matter* **2012**, *8* (4), 1168–1174.

(240) Collings, P. J.; Gibbs, E. J.; Starr, T. E.; Vafek, O.; Yee, C.; Pomerance, L. A.; Pasternack, R. F. Resonance Light Scattering and Its Application in Determining the Size, Shape, and Aggregation Number for Supramolecular Assemblies of Chromophores. *J. Phys. Chem. B* **1999**, *103* (40), 8474–8481.

(241) Yu, G.; Yan, X.; Han, C.; Huang, F. Characterization of Supramolecular Gels. *Chem. Soc. Rev.* **2013**, *42* (16), 6697.

(242) Cohen, D. L.; Lo, W.; Tsavaris, A.; Peng, D.; Lipson, H.; Bonassar, L. J. Increased Mixing Improves Hydrogel Homogeneity and Quality of Three-Dimensional Printed Constructs. *Tissue Eng. Part C Methods* **2011**, *17* (2), 239–248.

(243) Wang, Z.; Zhu, W.; Huang, R.; Zhang, Y.; Jia, C.; Zhao, H.; Chen, W.; Xue, Y. Fabrication and Characterization of Cellulose Nanofiber Aerogels Prepared via Two Different Drying Techniques. *Polymers (Basel).* **2020**, *12* (11), 1–13.

(244) Stl file from the author: SteedMaker; file used on the 04/04/2022. *SteedMaker;*. https://www.thingiverse.com/thing:34017; Licence: CC BY-NC 4.0.

(245) Dani, S.; Ahlfeld, T.; Albrecht, F.; Duin, S.; Kluger, P.; Lode, A.; Gelinsky, M. Homogeneous and Reproducible Mixing of Highly Viscous Biomaterial Inks and Cell Suspensions to Create Bioinks. *Gels* **2021**, *7* (4), 1–17.

Appendix

Publications included in the thesis in their published format:

- Appendix 1 -

Production and 3D Printing of a Nanocellulose-Based Composite Filament Composed of Polymer-Modified Cellulose Nanofibrils and High-Density Polyethylene (HDPE) for the Fabrication of 3D Complex Shapes

- Appendix 2 -

Three-Dimensional Printing of a Tough Polymer Composite Gel Ink Reinforced with Chemically Modified Cellulose Nanofibrils Showing Self-Healing Behavior

Figures not shown in the manuscript, which is currently being revised, are shown in Appendix 3.

- Appendix 3 -

Development of a bio-based composite for 3D printing from diphenylalanine peptide (Fmoc-FF) nanowires with unmodified or polymer-grafted cellulose nanofibrils: from an unprintable material to a strong and reliable printable gel

Appendix 1:

Production and 3D Printing of a Nanocellulose-Based Composite Filament Composed of Polymer-Modified Cellulose Nanofibrils and High-Density Polyethylene (HDPE) for the Fabrication of 3D Complex Shapes

Feras Dalloul, Jakob Benedikt Mietner and Julien R. G. Navarro

Fibers 2022, 10, 91

https://doi.org/10.3390/fib10100091

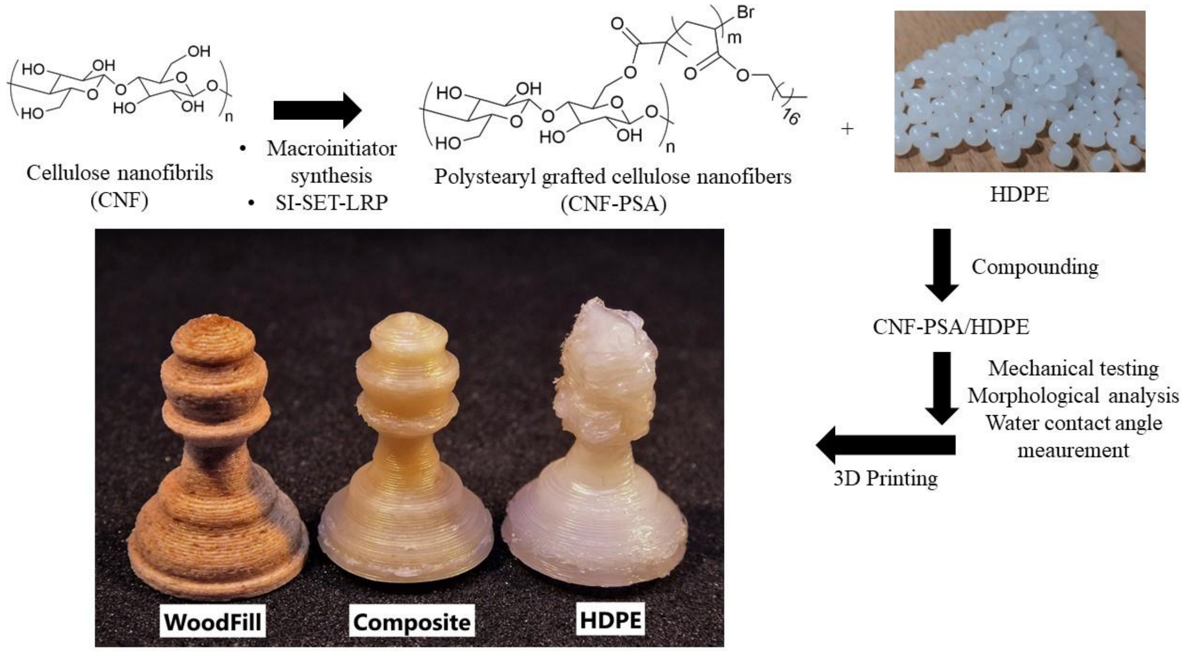

fibers

Article

Production and 3D Printing of a Nanocellulose-Based Composite Filament Composed of Polymer-Modified Cellulose Nanofibrils and High-Density Polyethylene (HDPE) for the Fabrication of 3D Complex Shapes

Feras Dalloul, Jakob Benedikt Mietner and Julien R. G. Navarro *

Institute of Wood Science, Universität Hamburg, 21031 Hamburg, Germany
* Correspondence: julien.navarro@uni-hamburg.de

Abstract: This work aims to produce a 3D-printable bio-based filament composed of high-density polyethylene (HDPE) and chemically modified cellulose nanofibrils. Printing using HDPE as a raw material is challenging due to its massive shrinkage and warping problems. This paper presents a new method to overcome those difficulties by enhancing the mechanical properties and achieving better print quality. This was achieved using modified cellulose nanofibrils (CNFs) as fillers. Firstly, CNF was converted to a CNF-based macroinitiator through an esterification reaction, followed by a surface-initiated single-electron transfer living radical polymerization (SI-SET-LRP) of the hydrophobic monomer stearyl acrylate. Poly stearyl acrylate-grafted cellulose nanofibrils, CNF-PSAs, were synthesized, purified and characterized with ATR-FTIR, ^{13}C CP-MAS NMR, FE-SEM and water contact angle measurements. A composite was successfully produced using a twin-screw extruder with a CNF-PSA content of 10 wt.%. Mechanical tests were carried out with tensile testing. An increase in the mechanical properties, up to 23% for the Young's modulus, was observed. A morphologic analysis also revealed the good matrix/CNF compatibility, as no CNF aggregates could be observed. A reduction in the warping behavior for the composite filament compared to HDPE was assessed using a circular arc method. The 3D printing of complex objects using the CNF-PSA/HDPE filament resulted in better print quality when compared to the object printed with neat HDPE. Therefore, it could be concluded that CNF-PSA was a suitable filler for the reinforcement of HDPE, thus, rendering it suitable for 3D printing.

Keywords: cellulose nanofibrils (CNFs); single-electron transfer living radical polymerization (SET-LRP); 3D printing; bio-based nanocomposite

check for updates

Citation: Dalloul, F.; Mietner, J.B.; Navarro, J.R.G. Production and 3D Printing of a Nanocellulose-Based Composite Filament Composed of Polymer-Modified Cellulose Nanofibrils and High-Density Polyethylene (HDPE) for the Fabrication of 3D Complex Shapes. *Fibers* **2022**, *10*, 91. https://doi.org/10.3390/fib10100091

Academic Editor: Alain Dufresne

Received: 26 September 2022
Accepted: 18 October 2022
Published: 21 October 2022

1. Introduction

Academic and public interest in additive manufacturing (AM), also known as 3D printing, has been growing rapidly during the last decade [1–3]. Fused-filament fabrication or fused deposition modeling (FDM) is a 3D-printing technology, which uses a continuous filament as the starting 3D ink material. The FDM process and the construction/building-up of complex 3D-printed objects are based on the layer-by-layer deposition process of a thermoplastic material (filament) extruded through a heated nozzle [4,5]. FDM is an efficient approach for the production of components and objects with complex geometries that are hardly achievable with traditional subtractive machining methods. As a result, 3D objects can be produced relatively rapidly and at a lower cost while using less material, thus, minimizing industrial waste [6–9].

Nowadays, numerous 3D-printable filaments, mainly composed of amorphous polymers, are commercially available. The most commonly used filaments are acrylonitrile butadiene styrene (ABS) [10], polylactic acid (PLA) [11], high-impact polystyrene (HIPS) [12] and polycarbonate (PC) [13]. This popularity can be explained by the fact that they are nontoxic, exhibit good printability and are available in a wide range of colors with good durability of the printed object.

In contrast, 3D filaments composed of semicrystallized polymers are harder to process due to shrinkage and warpage of the final 3D-printed object after cooling [14], which leads to unsuccessful prints or poorer quality products. A good example of these polymers' kind is high-density polyethylene (HDPE). HDPE is a semicrystalline polymer and one of the most widely manufactured polymers worldwide. Its potential conversion (or waste reconversion) into a 3D-printable material is crucial for the environment as it would improve significantly its recycling availability, and lower the carbon footprint [15,16]. However, HDPE is a challenging material to print as it crystallizes rapidly upon cooling, leading to a decrease in the object dimension, e.g., shrinkage [17]. Moreover, the low surface energy often results in poor layer–layer adhesion, e.g., layer separation, which when combined with the first layer–print bed (e.g., build surface) adhesion difficulty, automatically leads to warping out of the printing plane [18]. Gudadhe et al. [19] successfully 3D printed numerous objects composed of recycled HDPE through the incorporation of additives in the HDPE formulation. The use of dimethyl dibenzylidene sorbitol (DMDBS) and linear low-density polyethylene (LDPE) as additives allowed to improve the layer adhesion but also avoid warpage-related issues.

Mora et al. [20] reported that the incorporation of carbon nanotubes (CNTs) in the HDPE formulation provided considerable improvements in the printing process while also increasing the final mechanical properties. It can be noted that the mechanical properties of the composite can be improved by adding a filler, a reinforcing agent, to reduce those undesired and unwanted effects (shrinkage and warpage). These modifications lead to better object printability and shape fidelity as already reported elsewhere [21,22]. In contrast to those synthetic fillers, numerous efforts have been made to use natural fibers as reinforcing agents for polymers to address the environmental challenges and offer a greener alternative. Cellulose nanofibrils (CNFs) are among the candidates extensively used to produce lightweight composites with excellent mechanical properties [23–27]. CNF is attractive for its nontoxicity, biodegradability, biological availability and rigidity [28,29].

The main challenge to overcome with a bio-based (nano)composite is the correct adhesion between the filler/reinforcing agent and the host matrix [30]. CNF has an abundant number of hydroxyl groups on its surface, conferring its hydrophilic character, while most thermoplastic polymers are nonpolar and have a hydrophobic matrix. This ultimately results in poor interfacial compatibility between the two components, with a large aggregation of the fibers in the host matrix. To overcome this issue, it is mandatory to decrease the fibril hydrophilicity through chemical surface modification of the nanocellulose [31–36].

This work aimed to investigate the potential ability of a polymer-modified CNF to drastically increase the 3D printability of a HDPE bio-based composite through fused deposition modeling (FDM). After careful extraction and a solvent exchange to dimethyl sulfoxide (DMSO), the CNF was converted into a CNF-based macroinitiator, followed by a surface-initiated single-electron transfer living radical polymerization (SI-SET-LRP) of the stearyl acrylate monomer. The purpose of this polymerization reaction was to modify the overall surface polarity and, therefore, improve the compatibility with the hydrophobic HDPE. All these reactions were characterized with ATR-FTIR, CP/MAS ^{13}C-NMR spectroscopy, ultra-high-resolution field emission scanning electron microscopy (FE-SEM) and contact angle measurements. Finally, the poly(stearyl acrylate)-grafted CNF was compounded with HDPE and extruded to produce a 3D-printable filament. This extruded filament was also used to produce standard specimens for mechanical testing through injection molding; therefore, the mechanical properties were evaluated. The effectiveness and compatibility of the composite could also be monitored with scanning electron microscopy (SEM) and analysis of the broken specimen. Finally, its suitability as a 3D-printing filament, its deformation/warping reduction and the shape fidelity of the printed object were studied and compared to pure HDPE and Woodfill (PLA/PHA fine pinewood fibers).

2. Materials and Methods

2.1. Materials

Imidazole (≥99%), dimethyl sulfoxide (DMSO, ≥99%), tris[2-(dimethylamino)ethyl] amine (Me_6TREN, 97%), isopropanol, toluene and Cu wire (diameter 1 mm) were purchased from Alfa Aesar. 2-bromo-2-methylpropionate (98%), ethyl 2-bromo-2-methylpropionate (98%) and stearyl acrylate (SA, 97%) were purchased from Sigma-Aldrich. High-density polyethylene was obtained from SABIC (HDPE CC3054). For cellulose nanofibril (CNF) production, a dried elemental chlorine-free (ECF) bleached softwood kraft pulp was obtained from MERCER Stendal GmbH, Germany. The kraft pulp was composed from pine (30–60%) and spruce (40–70%), PFI-milled at 23 °C and 50% of relative humidity. Ultrapure Milli-Q water was used for the solvent exchange procedure. Woodfill (PLA/PHA + fine pinewood fibers) filament was obtained from ColorFabb, Belfeld, The Netherlands.

2.2. Materials Synthesis

2.2.1. Preparation of Cellulose Nanofibrils from Kraft Pulp

An amount of 10 g of dry pulp was shredded and ground using a Herzog grinding machine to achieve a high degree of grinding. The milling vessel was set in the vibrating mill and ground with a certain amount of 215 mL of distilled water for 6 min at 6000 rpm. To determine the grinding rate, the suspension was diluted to 0.24 wt.% and measured using a Schopper–Riegler measuring vessel. The degree of grinding was 92° SR. Then, the suspension was passed through a microfluidizer (Microfluidics^{TM} M-100EH-30). This process was completed in two steps, firstly the suspension was passed twice through two thin chambers with orifice widths of 400 μm and 200 μm under 15,000 Psi, and then six times through two thinner chambers of 200 μm and 100 μm under 25,000 Psi. The CNF suspension was then concentrated through centrifugation (Sorvall^{TM} LYNX^{TM} 6000 Superspeed centrifuge, Thermo Scientific, Shanghai, China) at 5500 rpm for 45 min.

2.2.2. Solvent Exchange Process

The gel-like CNF (20.4 g, 2.36 wt.%) was firstly mixed with 80 mL of distilled water and stirred for 30 min. DMSO (150 mL) was then added dropwise while maintaining vigorous stirring of the suspension. The obtained CNF/H_2O/DMSO suspension was concentrated using centrifugation (12,000 rpm, 20 min). The supernatant was discarded and replaced with fresh DMSO. This process was repeated four times and resulted in a 1.8 wt.% DMSO-based gel.

2.2.3. Preparation of CNF Macroinitiators by Esterification

The macroinitiator was prepared following the same procedure previously reported [37]. From this procedure, a total of 16.7 g of gel (2.1 wt.%) was obtained.

2.2.4. Grafting of Stearyl Acrylate onto CNF (CNF-PSA) Using SET-LRP

A copper wire (length = 50 cm) was first activated by soaking it in concentrated hydrochloric acid for approximately 10 min. After that, the wire was rinsed with water then acetone and finally dried. In a three-neck flask, 15.3 g (2.1 wt.%) of the CNF macroinitiator was dispersed in 240 mL of DMSO. In the meantime, the monomer SA (40 g) dissolved in toluene (120 mL) was passed through an aluminum oxide plug (Al_2O_3 basic) to remove the inhibitor/stabilizer, and then immediately injected in the CNF suspension. The activated copper wire was then added to the mixture and the reaction flask was then degassed by nitrogen purging at 40 °C. Me_6TREN (2 wt.% in DMSO) ligand was finally added and the reaction was allowed to proceed for 16 h at 40 °C under a nitrogen atmosphere. The suspension was then cooled down to room temperature. The CNF-PSA precipitate was collected, suspended in toluene and precipitated with isopropanol. The CNF-PSA was collected through centrifugation (4000 rpm, 10 min). This step was repeated 5 times. Finally, the CNF-PSA was suspended in toluene and the gel was concentrated through centrifugation (4000 rpm, 60 min). The resulting gel was finally dried under vacuum.

2.2.5. CNF Nanocomposite Preparation

A composite of HDPE with 10 wt.% poly(stearyl acrylate)-grafted cellulose nanofibrils (CNF-PSAs) was prepared. CNF-PSA was dried beforehand and chopped into small pellets. HDPE was also dried. Then, both components were mixed in the HAAKE™ MiniLab 3 microcompounder with counter-rotating screws at 150 °C and 100 rpm for 5 min for the first batch.

2.2.6. Filament Extrusion and 3D Printing

Filaments for 3D printing were produced using a HAAKE™ MiniLab 3 microcompounder. The components were loaded and compounded with counter-rotating screws, with a screw speed of 35 rpm at 150 °C. A caliper was used for controlling the filament size (1.75 mm) to ensure that the filament could be used on an Original Prusa i3 MK3S+ printer. The 3D-object STL file was obtained from Thingiverse [38] (creator: SteedMaker, license: CC BY-NC 4.0). The printing parameters were adjusted within the PrusaSlicer software (version 2.4.1). The nozzle temperature was set to 215 °C and the bed temperature to 60 °C. The nozzle diameter used was 0.4 mm and the printing speed was set to 20 mm/s, with a layer height of 0.2 mm. For the infill, a gyroïd pattern was chosen, with an infill percentage of 15%. In addition, for better adhesion, the object was printed on a HDPE sheet. The cooling fan was used starting from the 4th layer, at 50% of its capacity.

2.3. Material Characterization

ATR-FTIR (attenuated total reflection Fourier-transform infrared spectroscopy) was performed using a Bruker Vector 33 FTIR Fourier-transform infrared spectrometer I18500 PS15. Spectra were recorded with 64 scans in the spectral region of 4000–500 cm^{-1}. The spectral resolution was 4 cm^{-1}.

All samples' CP/MAS ^{13}C-NMR spectra were acquired on a Bruker 500 Avance III HD spectrometer at Larmor frequencies of 125 MHz and 500 MHz for ^{13}C and ^{1}H, respectively. These samples were placed into 4 mm zirconia rotors for magic angle spinning (MAS) at a rotation speed of 8 kHz. Creeping CP/MAS ^{13}C-NMR spectra were recorded with a ^{13}C mutation frequency of 50 kHz and a contact time of 1.5 ms. These spectra were acquired using Fourier transforms of the FIDs, and chemical shifts were referenced to pure tetramethylsilane (TMS).

For tensile testing, the nanocomposite was chopped into pellets and injection molded using a HAAKE™ Minijet II into test specimens for tensile testing with the cylinder temperature at 150 °C, mold temperature at 80 °C and pressure at 400 bar for 4 s. Specimens for tensile testing dimensions were 75 × 10 × 20 mm (according to the DIN EN ISO 527). In accordance with DIN EN ISO 527, the tensile test was performed using a Zwick-Roell universal testing machine with a load cell of 500 N and a ZWICK videoXtens video extensometer. The crosshead speed was 20 mm/min for the plain matrix and 1 mm/min for the composite. An initial load of 1 N was utilized to determine the properties. At minimum 5 and up to 12 specimens were tested, and the average values were obtained.

To measure the warping effect of HDPE and the composite, two 3D models were printed, both of which were flat rectangles. The first was fully filled and the second was hollow. The 3D patterns are presented in Scheme 1. Both models were printed using the same parameters described previously. The 3D prints were composed with various configurations, such as with/without LDPE tape and with/without enclosure. HDPE, composite and Woodfill were printed, placed side-by-side and pictured (Scheme 2). The warping of materials was measured using a circular arc method as illustrated in Scheme 1. Warped and bent materials were assumed to be part of a circular arc.

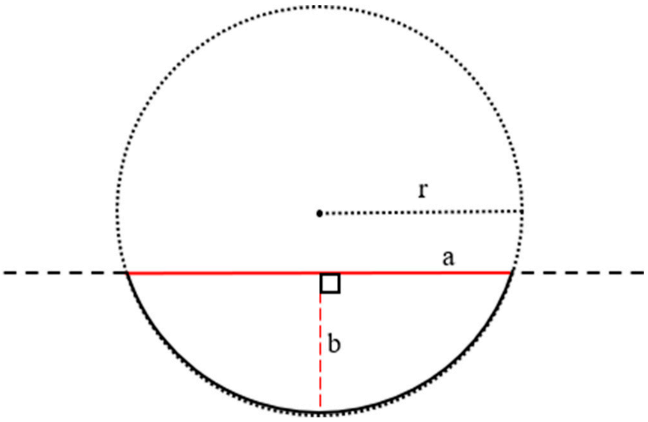

Scheme 1. Circular method: printed 3D models are represented as an arc.

Both distances, *a*: which was the length between the two extremities of the bent structure and *b*: the height from the middle of *a* to the arc, were measured using ImageJ. The radius of the assumed circle, *r*, was calculated using the formula below based on these two values. This was used for the quantification of the warping.

$$r = \frac{\sqrt{\left(\frac{a}{2}\right)^2 + c^2}}{2\ \cos\left(\ \tan^{-1}\left(\frac{a}{2c}\right)\right)} \tag{1}$$

Measurements of the contact angle were carried out using a drop shape analyzer (DSA 100, Krüss, Hamburg, Germany). Using the sessile drop method, automatic dispensers dropped 10 µL of Milli-Q water on the surfaces and the angle of static contact was measured using a Basler A6021-2. Both thin and flat films of the CNF and modified CNF were prepared using vacuum filtration followed by air drying. Single measurements were performed within 2 s of droplet deposition and averaged from ten measurements.

The morphologies of the modified CNF and composite were observed via ultra-high-resolution field emission scanning electron microscopy (FE-SEM) with a Hitachi S-800. Modified CNF was dispersed in polyvinyl alcohol, dried and then mounted on sample supports using carbon tape and coated with a 5 nm layer of Pd/Pt under an inert atmosphere. For the composite, samples from mechanical testing were cut at the fracture site and then gold plated with the Biorad SC510 SEM coating system prior to analysis.

3. Results and Discussion

3.1. Chemical Surface Modification of Cellulose Nanofibrils

Several chemical surface modifications of the cellulose nanofibrils (CNFs) were required to ensure better compatibility between the nanocellulose filler and the high-density polyethylene matrix. This surface modification of the nanocellulose through surface-initiated single-electron transfer living radical polymerization (SI-SET-LRP) was previously used and detailed by Navarro et al. [37], and the strategy was applied here as outlined. By grafting stearyl acrylate chains in the fibrils, this process aimed to decrease their hydrophilic character, thus, limiting their aggregation due to fibril–fibril interactions [39,40]. Grafted cellulose could be completely suspended in toluene, which was not possible for pristine nanocellulose [41], providing evidence that chemical properties were effectively altered. Through using this strategy, a better compatibility between the CNF and the HDPE host matrix could be achieved, making CNF a potential candidate as a reinforcing agent for the HDPE composite, enhancing the 3D printability of the HDPE composite.

Following the nanocellulose production with the microfluidizer, it was necessary to perform a solvent exchange from water to DMSO. The surface chemical modification occurred on the hydroxyl groups contained within the cellulose structure through esterification with 2-bromoisobutyric acid (Scheme 2a). This reaction yielded a CNF-based macroinitiator (CNF-MI) suitable for the SET-LRP reaction.

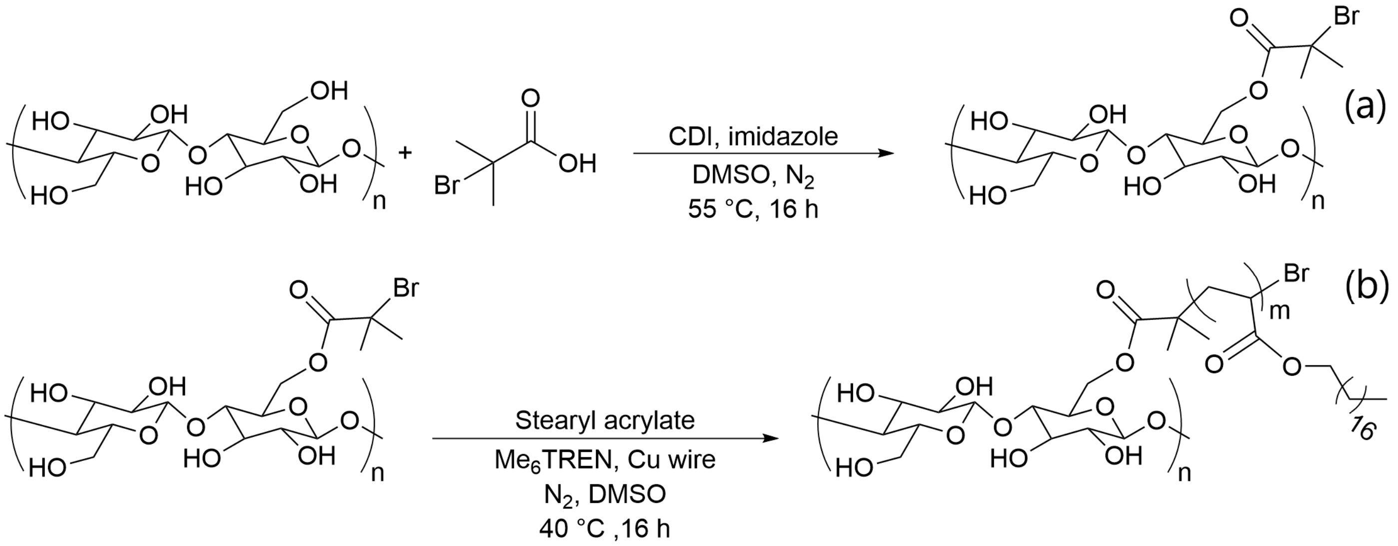

Scheme 2. (**a**) Synthetic process of the CNF-based macroinitiator (CNF-MI) and (**b**) polymerization onto CNF-based macroinitiator with the SA monomer through SET-LRP, yielding CNF-PSA.

An easy and robust way of grafting polymer chains onto the surface of the CNF-based macroinitiator was the use of surface-initiated polymerization SI-SET-LRP [42–45]. The CNF-based macroinitiator could initiate the polymerization reaction of the monomer stearyl acrylate in the presence of copper and a tetradentate tertiary amine ligand (Me_6TREN), as shown in Scheme 2b. This resulted in the incorporation of a saturated hydrocarbon chain, which dramatically increased the hydrophobicity of the CNF.

After polymerization, the PSA-grafted CNF was obtained as a translucid gel, and suspended in a nonpolar solvent such as toluene.

The chemical modifications of CNF were evaluated using ATR-FTIR (Figure 1). Pristine nanocellulose characteristic (Figure 1a) bands could be easily identified with bands located at 3320 cm^{-1} (O-H), 2950 and 2895 cm^{-1} (C-H), 1430 cm^{-1} (C-H) and 1161 cm^{-1} (C-O-C). The CNF-MI was successfully synthesized, and in comparison to the pristine CNF, its spectra (Figure 1b) revealed the presence of an additional absorption band localized at 1733 cm^{-1}, attributed to the ester groups (C=O).

Following the SET-LRP reaction, the spectrum of CNF-PSA (Figure 1c) exhibited a significant increase in the number of bands. The key characteristic absorption bands were localized at 2916 and 2848 cm^{-1} (C-H), 1736 cm^{-1} (C=O), 1470 cm^{-1} (C-H), 1159 cm^{-1} (C-O-C) and 721 cm^{-1} ($-CH_2-$).

Unmodified CNF and CNF-PSA were also studied using CP/MAS ^{13}C-NMR, and their spectra are presented in Figure 2 with their respective peak assignments. Typical unmodified CNF peaks (shown in red) were found at 105 ppm for C1, with duplicated contributions for C4 and C6 signals, due to crystalline (89 ppm and 65 ppm) and amorphous (84 ppm and 62 ppm) regions, with the remaining carbon signal (C2, C3 and C5) clustered in the 72–75 ppm region [46]. After the addition of stearyl acrylate, an increase in peak density was observed. There was a peak at 175 ppm corresponding to the carbonyl bonds (C12), and intense peaks in the 40–20 ppm were observed for long alkyl chains grafted onto the CNF (C14 to C20). These results demonstrated the introduction of new esters and abundant methylene groups throughout the overall structure; therefore, successful chemical modification of the CNF could be deduced.

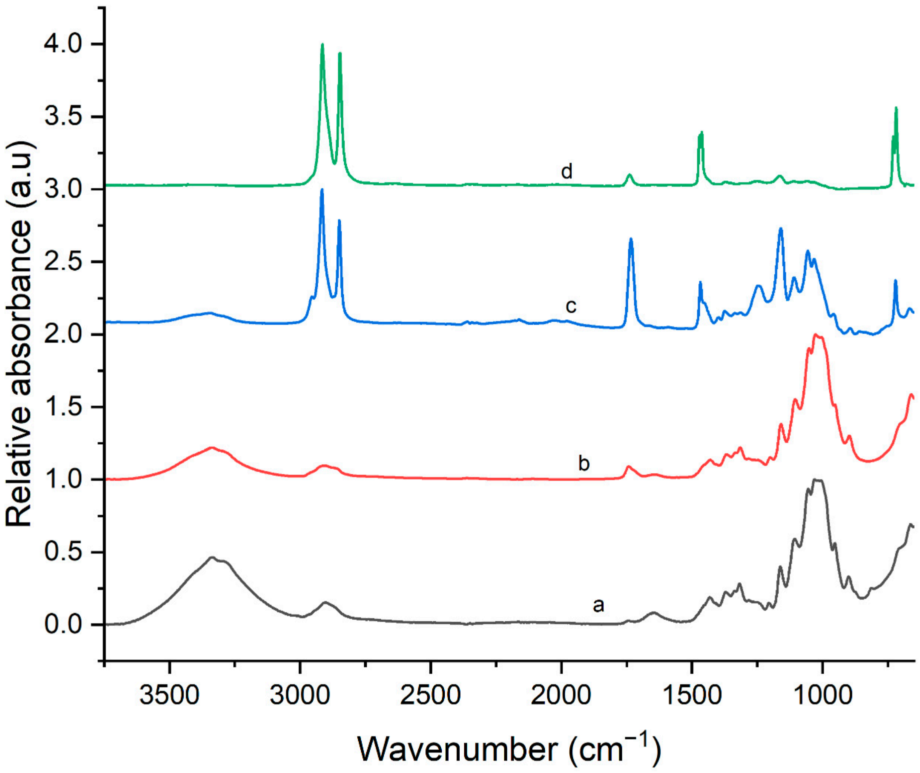

Figure 1. ATR-FTIR spectra of pristine CNF (a), CNF-MI (b), CNF-PSA (c) and CNF-PSA/HDPE composite (d).

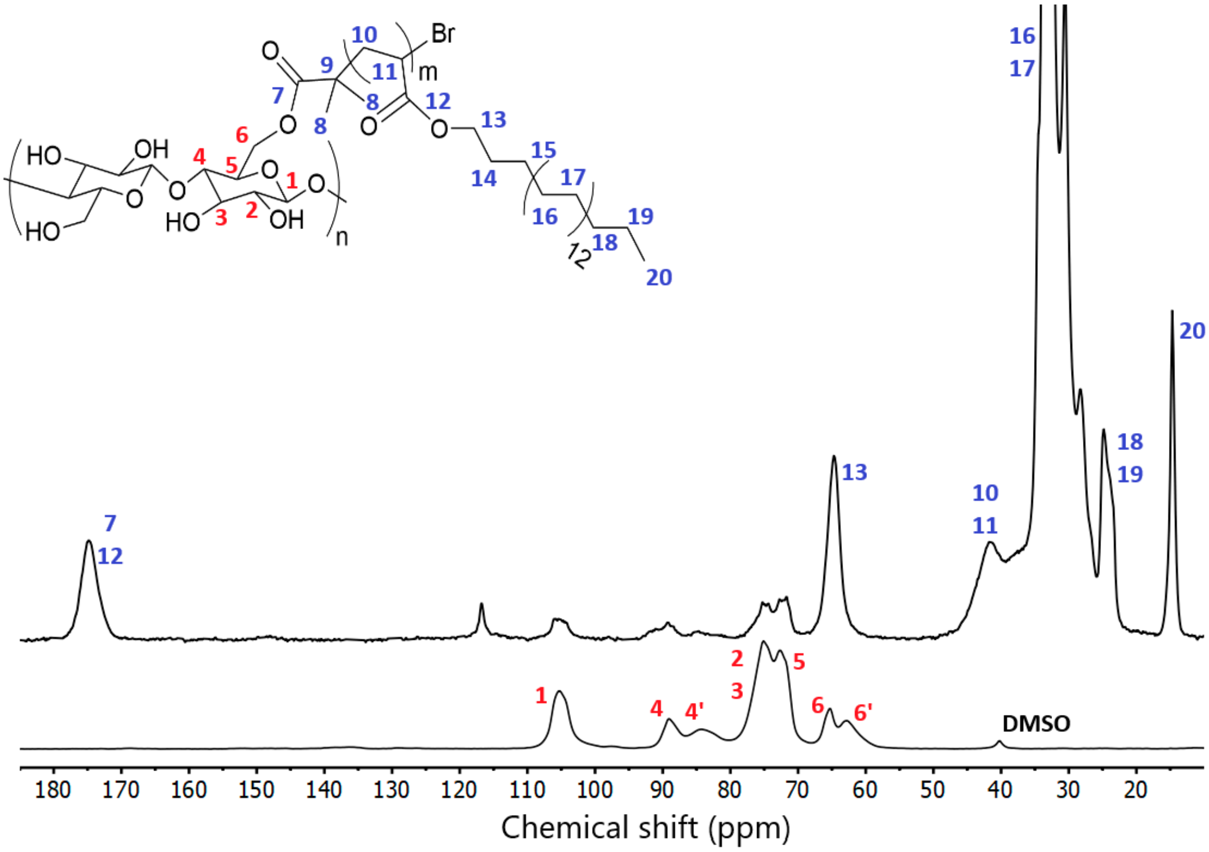

Figure 2. CP/MAS ^{13}C-NMR spectra of unmodified CNF on the lower part and CNF-PSA on the upper part.

3.2. Surface Wetting Analysis

The modification of the cellulose nanofibrils led to the incorporation of multiple stearyl acrylate chains. The physical characteristics were expected to be altered, with a marked increase in hydrophobicity. To confirm this, the water contact angle of each specimen was measured. Therefore, CNF and CNF-PSA films were prepared for testing. A significant increase in the water contact angle on the films is shown in Figure 3 (from 36° to 105°). This phenomenon proved the high degree of hydrophobicity of CNF-PSA and, hence, the successful chemical modification.

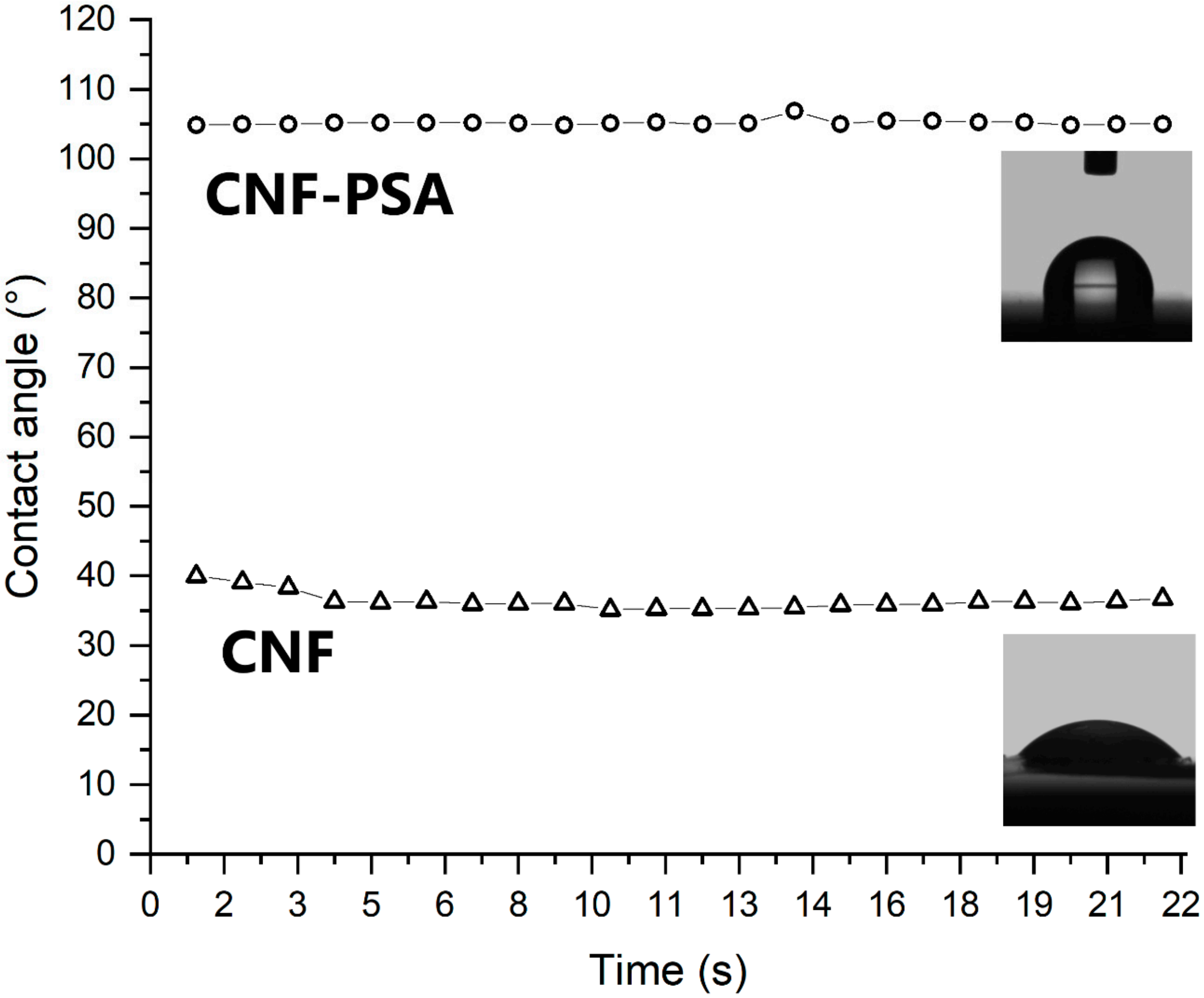

Figure 3. Photographs of the static contact angle measurements of water on unmodified CNF and CNF-PSA films, and the evolution of the contact angle against time. The CNF-PSA film has a contact angle of 105°, while unmodified film has a 36° contact angle.

3.3. Composite Production and Characterization

The nanocomposite formulation was composed of HDPE and the modified CNF-PSA, which were both completely dried before compounding. The compounding was carried out using a twin-screw extruder at 150 °C with a filler CNF-PSA content of 10 wt.%. ATR-FTIR was carried out on the extruded CNF-PSA/HDPE nanocomposite at 150 °C, and its spectrum is shown in Figure 1d. The distinctive high-density polyethylene bands [47,48] were easily recognizable, such as at 2912 and 2846 cm^{-1} (C-H) and the rocking peak near 719 cm^{-1} (-CH$_2$). However, additional adsorption bands were located at 1741 cm^{-1} (C=O) and 1165 cm^{-1} (C-O-C), which proved that ester groups were contained in the extruded filament and, thus, ensured proper integration of the CNF-PSA into the HDPE.

3.4. Mechanical Properties

Depending on the filler's size, shape, dispersion and interaction/adhesion with the matrix and the inherent properties of the matrix, the composite could have distinct and different mechanical properties [49–53]. Figure 4 shows typical stress–strain curves of neat HDPE and HDPE/CNF-PSA composite. The recorded data after HDPE necking were removed for better observation. The table shows the mechanical properties of the composite and neat HDPE, i.e., the Young's modulus, tensile strength and strain at the break of each material. A minimum of five samples were run for each case and the values shown, in Table 1, are the averages of these results.

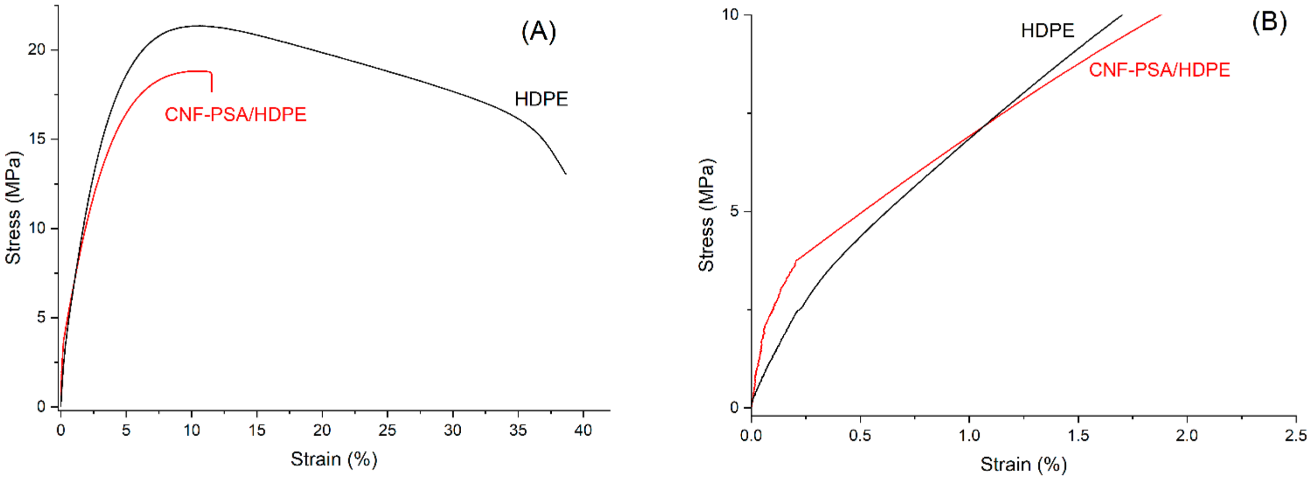

Figure 4. Experimental stress–strain curves of CNF-PSA/HDPE with neat HDPE; HDPE is represented by the black curve and red for the composite. Stress–strain curves (**B**) are zoomed versions of (**A**).

Table 1. Summary of the tensile properties of the HDPE and composite of 10 wt.% of CNF-PSA/HDPE.

CNF Content in HDPE (%)	Extrusion Temperature (°C)	Young's Modulus (MPa)	Yield Strength (MPa)	Strain at Break (%)
0	150	888 ± 135	21.4 ± 0.3	38.6 ± 1.4
10	150	1094 ± 77	18.8 ± 0.1	11.6 ± 1.3

A general improvement in the overall mechanical properties was observed upon the addition of CNF-PSA. The greatest Young's modulus recorded was 1094 MPa with an improvement of approximately 23% for the composite. However, a slight decrease in tensile strength and a considerable drop in elongation at break were observed. This phenomenon was caused by the increasing stiffness due to the filler possessing this characteristic. This has been reported in other research papers as well [54–56]. The fracture of material was driven mainly through crack initiation and propagation, which in turn, with increasing filler content, led to an increase in graininess and agglomeration, resulting in areas requiring lower energy for fracture initiation or propagation [57]. This was supported by the lack of necking elongation of the composite samples under tensile stress as opposed to neat HDPE.

3.5. Morphological Analysis

In order to verify the nanofibrous morphology after the chemical modification, cellulose, CNF-based macroinitiator and CNF-PSA adducts were characterized by field emission scanning electron microscopy (FE-SEM). Images of the cellulose and CNF macroinitiator (Figure 5A,B) revealed a dense network of aggregated fibrils, with very few differences following the initial chemical modification. In contrast, the CNF-PSA images (Figure 5C) contained no discernable fibers, indicating that they were fully embedded in the grafted polymer matrix. This result confirmed that a modification of the properties of the cellulose nanofibrils took place. Successful grafting of poly stearyl acrylate, therefore, led to better compatibility with the hydrophobic polymer.

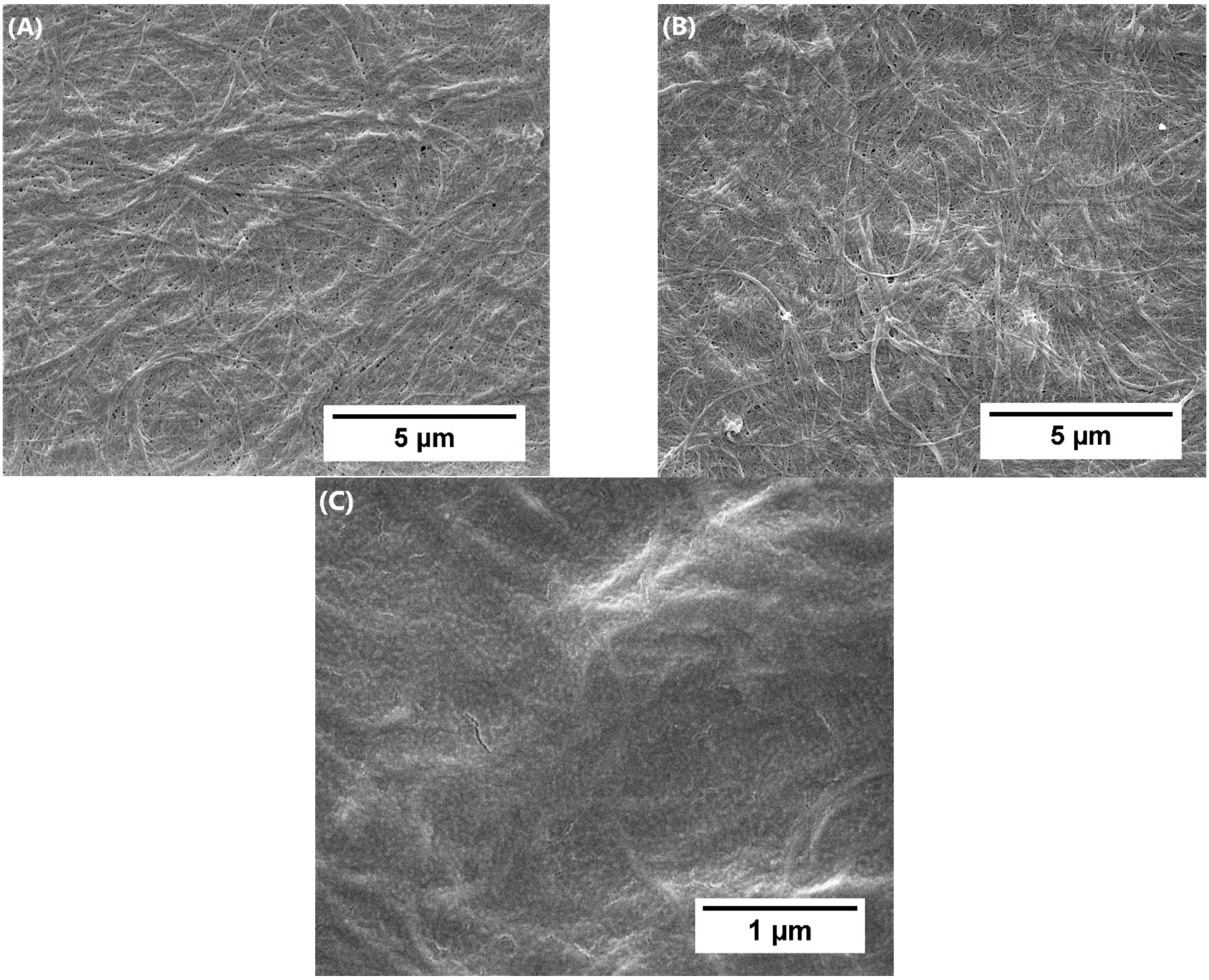

Figure 5. FE-SEM images of (**A**) CNF, (**B**) CNF-based macroinitiator and (**C**) CNF-PSA.

Figure 6 displays a cross-section of the composite mechanical testing specimen before fracture and extrusion at 150 °C. It could be seen that the surface smoothness was slightly reduced by the occurrence of a few tiny aggregates. Nevertheless, as a whole, we concluded that the surface was clear, without voids or large fiber aggregates. The broken surface was homogeneous, indicating the good adhesion between the CNF-PSA and the HDPE matrix. This demonstrated the CNF strengthening effect on the matrix polymer. Figure 7 shows the fractured cross-section surface of a tested specimen. The absence of cavities and irregularities confirmed that there was good interfacial bonding of the filler and matrix polymer. For comparison, attempts were made to produce composites of unmodified CNF with the HDPE matrix. Unfortunately, this was not possible, mainly due to the large macroscopic aggregation of CNF. The reason for poor dispensability was the hydrophilic properties that were not compatible with the hydrophobic polymer. These data indicated the necessity of having the chemical modification to render the initially hydrophilic CNF into the much more compatible CNF-PSA.

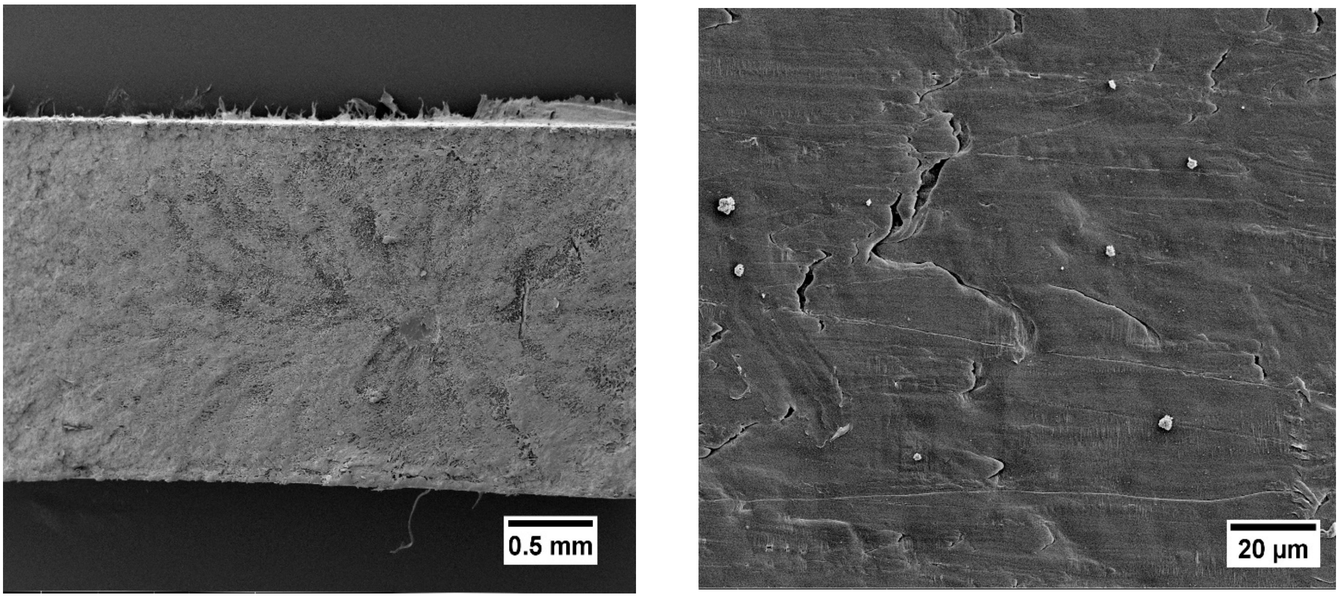

Figure 6. SEM images showing the cross-section of a broken mechanical test specimen composed with CNF-PSA/HDPE.

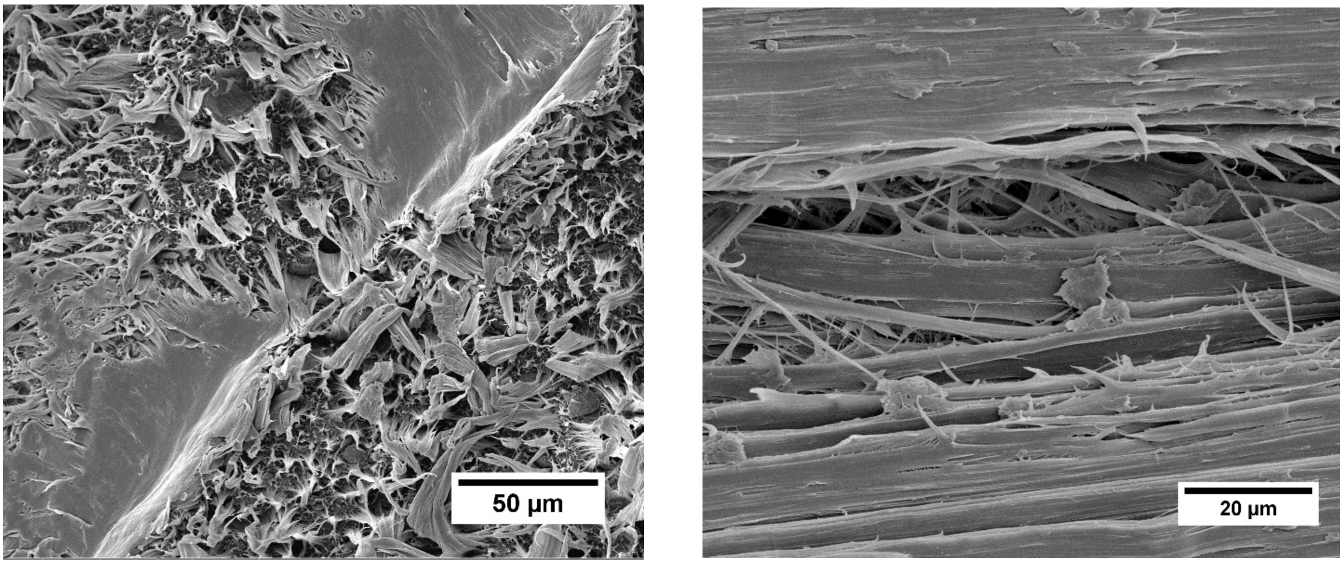

Figure 7. SEM images of a broken mechanical test specimen composed with CNF-PSA/HDPE at fracture point.

3.6. *Printability of Neat HDPE and HDPE Composites*

High-density polyethylene has hardly ever been suggested as a filament for fused deposition modeling. Where it is being sold as a 3D-printing filament, it is stated by the manufacturer that no reliable method of printing is available [58]. This is because HDPE is prone to shrinkage, bending and deformation as its temperature cools down [59], which significantly hinders its printing. However, it has been found that composites with improved mechanical properties show better printability [60–62]. It was then expected that the composite HDPE/CNF-PSA would have better printability compared to the neat HDPE. Schirmeister and his teammates [63] managed to 3D print complex designs with commercial HDPE while preventing shrinkage, warping and voiding. The surface quality of the printed HDPE was improved by adjusting the printing parameters. The printing parameters employed were: a nozzle temperature of 215 °C and bed temperature of 60 °C.

Designs which were difficult for a semicrystalline polymer to print were chosen to demonstrate the improvement in 3D-printing quality. Two cuboid designs were created, each 60 mm long, 10 mm wide and 3 mm high, one being solid and the second hollow, as shown in Figure 8. The hollow model was expected to undergo less deformation than the solid model. This was due to the fact that the full design contained a greater number of layers that could contribute to the overall deformation. Such models were subject to post-printing deformation problems, such as not adhering to the 3D printer's surface and warping. These items tended not to remain flat but rather to bend. Thus, to quantify their deformation, the distorted specimens were assumed to belong to an arc of a circle, and the radius was calculated. With less deformation of the cuboid, the size of the circle was larger; hence, the radius was larger. Several parameters affecting print quality were investigated in this experiment, including printing on an LDPE-based tape, which is known to improve the adhesion of HDPE and closure for temperature stabilization [63]. Results are shown in Tables 2 and 3.

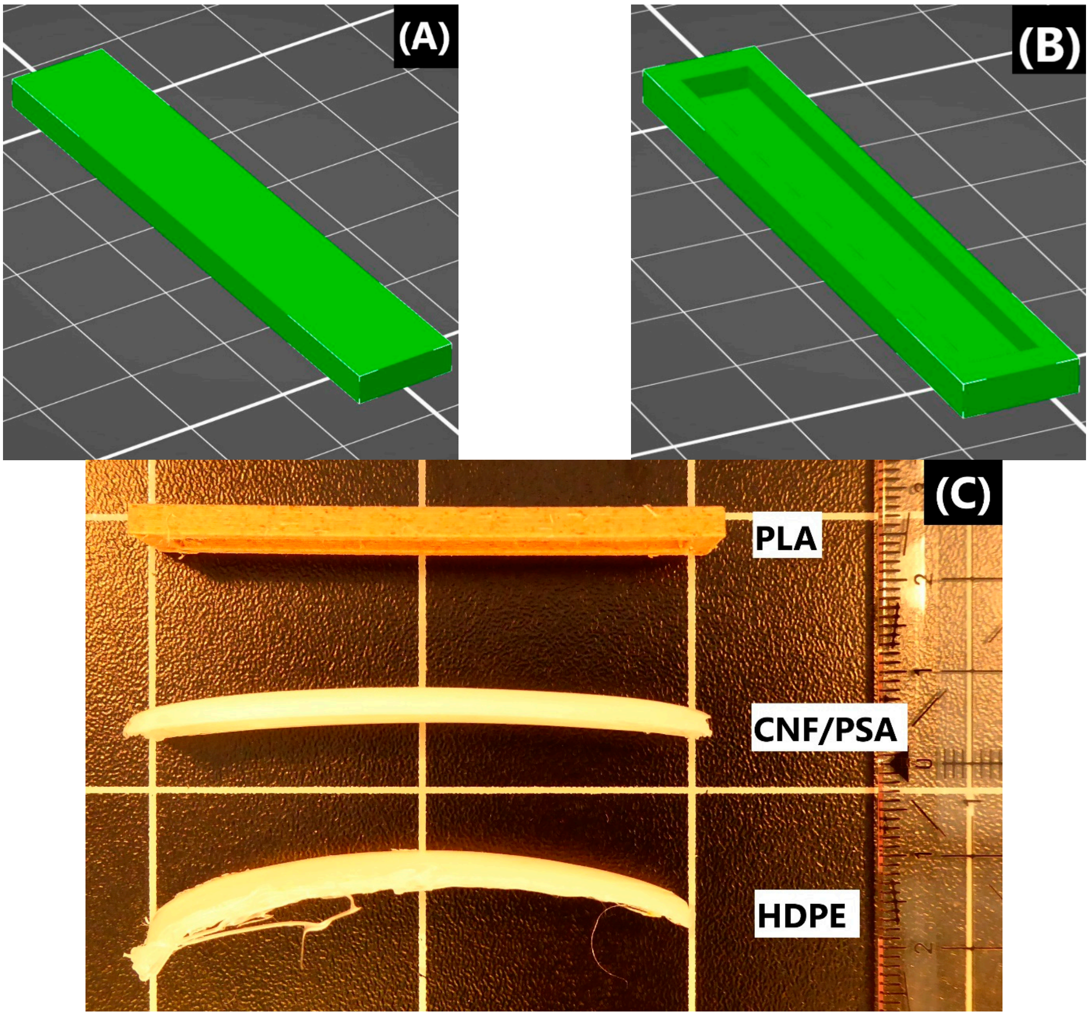

Figure 8. Three-dimensional models of full (**A**) and notched (**B**) designs; (**C**) is a representative photo of printed notched models.

In both models, the HDPE and composite failed to give satisfactory results without the addition of LDPE tape or closure (samples 1–2 and 7–8), reflecting the poor suitability of HDPE for printing. In contrast, improved performance was observed when the LDPE tape was applied to the printer bed. For samples 3 and 4, the composite was able to produce prints, whereas the HDPE was unable to do so. Lastly, for samples 5–6 and 9–12, an increase in radius ranging from 58% (samples 5–6) to 222% (samples 11–12) was observed for the designs produced using the composite filament versus the one produced using HDPE. The increase in radius indicated that there was less deformation. Cuboids printed with CNF-PSA-reinforced composite filament showed significantly less warpage than those printed with HDPE, proving the strengthening and enhancing effect of the filler and, thus, its relevance in allowing HDPE to be 3D printed with a higher definition.

Table 2. Summary of warping measurements of HDPE and composite of 10 wt.% of CNF PSA/HDPE in the full model.

Sample	Material Used	LDPE Tape	Closure	Radius (cm)
1	HDPE	No	No	-
2	CNF-PSA/HDPE	No	No	-
3	HDPE	Yes	No	-
4	CNF-PSA/HDPE	Yes	No	11.62
5	HDPE	Yes	Yes	7.80
6	CNF-PSA/HDPE	Yes	Yes	12.30

Table 3. Summary of warping measurements of HDPE and composite of 10 wt.% of CNF PSA/HDPE in the notched model.

Sample	Material Used	LDPE Tape	Closure	Radius (cm)
7	HDPE	No	No	-
8	CNF-PSA/HDPE	No	No	-
9	HDPE	Yes	No	9.67
10	CNF-PSA/HDPE	Yes	No	23.57
11	HDPE	Yes	Yes	7.15
12	CNF-PSA/HDPE	Yes	Yes	23.05

Then, a chess pawn was printed using filaments composed from HDPE, CNF-PSA/HDPE and Woodfill for reference. The production of this pattern was challenging because of some difficulties, such as overhangs, that could hinder the printing process. Figure 9 is a representative picture of the pawns produced using the same printing parameters.

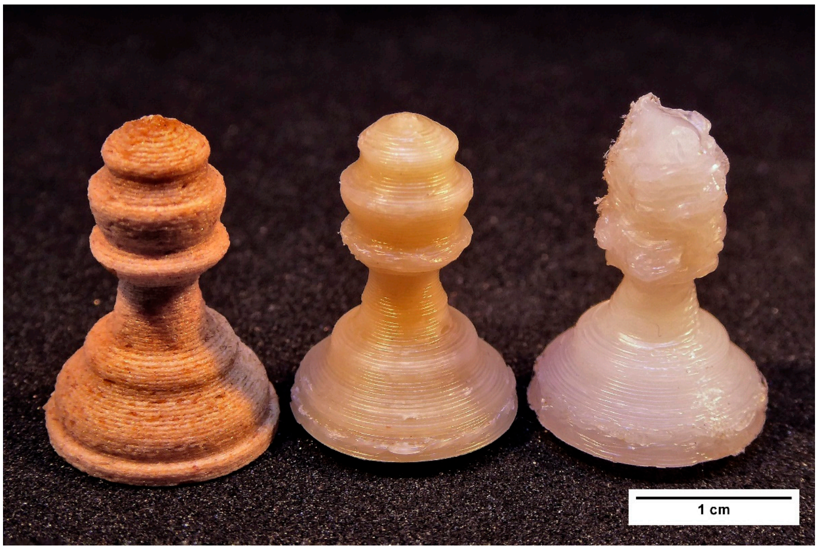

Figure 9. Three-dimensional printed models: filament used on the left pawn is Woodfill, HDPE for the middle and CNF-PSA/HDPE composite for the right one.

As expected, there were no issues with printing the pawn using Woodfill filament, which was used as a standard. However, the printing using HDPE filament proved to be less successful, because the upper part of the pawn failed to print the set structure and rather collapsed. The pawn produced using CNF-PSA/HDPE filament exhibited significant resolution and overall print quality improvements. Smoother lines, reduced warpage and better layer definition with good dimensional accuracy were achieved.

4. Conclusions

In summary, it can be stated that CNF grafted with poly stearyl acrylate proved to be an efficient filler for producing a new HDPE-based filament suitable for 3D printing. First of all, we converted CNF to a CNF-based macroinitiator through an esterification reaction. Then, the cellulosic fiber surface was hydrophobized through surface-induced radical graft polymerization, SET-LRP, and stearyl acrylate groups were incorporated. A nanocomposite of HDPE with 10% CNF-PSA filler was produced with twin-screw extrusion at 150 °C. Tensile testing of the HDPE and composite demonstrated an increase of 23% in the Young’s modulus (888 MPa to 1094 MPa). The compatibility was confirmed with a morphological analysis (SEM). An improvement in the printing quality was demonstrated with the printing of two models and measurements of their deformation. The warping was quantified with the measurement of the radius corresponding to each specimen, and an increase of 58 to 222% in the radius was noted. The composite was found to exhibit much less warpage compared to neat HDPE. Finally, pawns of chess using Woodfill, composite and pure HDPE filaments were printed. These prints demonstrated that HDPE/CNF-PSA filament had good printability and higher resolution than HDPE neat. The conclusion could be drawn that the CNF-PSA filler exhibited thermoplastic behavior and a high compatibility with HDPE.

Author Contributions: All authors: F.D., J.B.M. and J.R.G.N. contributed to the study, conception and design of the experiments. The synthesis and material preparations were performed by F.D. The data collection and analyses were performed by F.D., J.B.M. and J.R.G.N. All authors: F.D., J.B.M. and J.R.G.N. contributed to writing the submitted version of the manuscript. All authors have read and agreed to the published version of the manuscript.

Funding: J. Navarro and all authors would like to express our thanks to the Fachagentur Nachwachsende Rohstoffe e.V. (FNR/BMEL, HolzMat3D project, number 2220HV024X) for their financial support.

Institutional Review Board Statement: Not applicable.

Informed Consent Statement: Not applicable.

Data Availability Statement: Not applicable.

Acknowledgments: We would like to thank T. Potsch for the FE-SEM imaging. We are also grateful to J. Beruda for the tensile test measurements.

Conflicts of Interest: The authors declare no competing financial interests.

References

1. Gao, W.; Zhang, Y.; Ramanujan, D.; Ramani, K.; Chen, Y.; Williams, C.B.; Wang, C.C.L.; Shin, Y.C.; Zhang, S.; Zavattieri, P.D. The Status, Challenges, and Future of Additive Manufacturing in Engineering. *Comput. Des.* **2015**, *69*, 65–89. [CrossRef]
2. Motyl, B.; Filippi, S. Trends in Engineering Education for Additive Manufacturing in the Industry 4.0 Era: A Systematic Literature Review. *Int. J. Interact. Des. Manuf.* **2021**, *15*, 103–106. [CrossRef]
3. Patel, D.K.; Dutta, S.D.; Shin, W.-C.; Ganguly, K.; Lim, K.-T. Fabrication and Characterization of 3D Printable Nanocellulose-Based Hydrogels for Tissue Engineering. *RSC Adv.* **2021**, *11*, 7466–7478. [CrossRef]
4. Mohamed, O.A.; Masood, S.H.; Bhowmik, J.L. Optimization of Fused Deposition Modeling Process Parameters: A Review of Current Research and Future Prospects. *Adv. Manuf.* **2015**, *3*, 42–53. [CrossRef]
5. Picard, M.; Mohanty, A.K.; Misra, M. Recent Advances in Additive Manufacturing of Engineering Thermoplastics: Challenges and Opportunities. *RSC Adv.* **2020**, *10*, 36058–36089. [CrossRef] [PubMed]

6. Bandyopadhyay, A.; Bose, S.; Das, S. 3D Printing of Biomaterials. *MRS Bull.* **2015**, *40*, 108–115. [CrossRef]
7. Wu, G.-H.; Hsu, S. Review: Polymeric-Based 3D Printing for Tissue Engineering. *J. Med. Biol. Eng.* **2015**, *35*, 285–292. [CrossRef]
8. Chen, C.; Mehl, B.T.; Munshi, A.S.; Townsend, A.D.; Spence, D.M.; Martin, R.S. 3D-Printed Microfluidic Devices: Fabrication, Advantages and Limitations—A Mini Review. *Anal. Methods* **2016**, *8*, 6005–6012. [CrossRef]
9. Attaran, M. The Rise of 3-D Printing: The Advantages of Additive Manufacturing over Traditional Manufacturing. *Bus. Horiz.* **2017**, *60*, 677–688. [CrossRef]
10. Bartolomé, E.; Bozzo, B.; Sevilla, P.; Martínez-Pasarell, O.; Puig, T.; Granados, X. ABS 3D Printed Solutions for Cryogenic Applications. *Cryogenics* **2017**, *82*, 30–37. [CrossRef]
11. Rojas-Martínez, L.E.; Flores-Hernandez, C.G.; López-Marín, L.M.; Martinez-Hernandez, A.L.; Thorat, S.B.; Reyes Vasquez, C.D.; Del Rio-Castillo, A.E.; Velasco-Santos, C. 3D Printing of PLA Composites Scaffolds Reinforced with Keratin and Chitosan: Effect of Geometry and Structure. *Eur. Polym. J.* **2020**, *141*, 110088. [CrossRef]
12. Sieradzka, M.; Fabia, J.; Biniaś, D.; Graczyk, T.; Fryczkowski, R. High-Impact Polystyrene Reinforced with Reduced Graphene Oxide as a Filament for Fused Filament Fabrication 3D Printing. *Materials* **2021**, *14*, 7008. [CrossRef]
13. Liu, F.; Vyas, C.; Poologasundarampillai, G.; Pape, I.; Hinduja, S.; Mirihanage, W.; Bartolo, P. Structural Evolution of PCL during Melt Extrusion 3D Printing. *Macromol. Mater. Eng.* **2018**, *303*, 1700494. [CrossRef]
14. Li, J.; Yuan, S.; Zhu, J.; Li, S.; Zhang, W. Numerical Model and Experimental Validation for Laser Sinterable Semi-Crystalline Polymer: Shrinkage and Warping. *Polymers* **2020**, *12*, 1373. [CrossRef]
15. Cruz Sanchez, F.A.; Boudaoud, H.; Camargo, M.; Pearce, J.M. Plastic Recycling in Additive Manufacturing: A Systematic Literature Review and Opportunities for the Circular Economy. *J. Clean. Prod.* **2020**, *264*, 121602. [CrossRef]
16. Vidakis, N.; Petousis, M.; Maniadi, A. Sustainable Additive Manufacturing: Mechanical Response of High-Density Polyethylene over Multiple Recycling Processes. *Recycling* **2021**, *6*, 4. [CrossRef]
17. Fu, J.; Ma, Y. Mold Modification Methods to Fix Warpage Problems for Plastic Molding Products. *Comput. Aided. Des. Appl.* **2016**, *13*, 138–151. [CrossRef]
18. Fischer, J. *Handbook of Molded Part Shrinkage and Warpage*; William Andrew: Norwish, NY, USA, 2013.
19. Gudadhe, A.; Bachhar, N.; Kumar, A.; Andrade, P.; Kumaraswamy, G. Three-Dimensional Printing with Waste High-Density Polyethylene. *ACS Appl. Polym. Mater.* **2019**, *1*, 3157–3164. [CrossRef]
20. Mora, A.; Verma, P.; Kumar, S. Electrical Conductivity of CNT/Polymer Composites: 3D Printing, Measurements and Modeling. *Compos. Part B Eng.* **2020**, *183*, 107600. [CrossRef]
21. Spoerk, M.; Sapkota, J.; Weingrill, G.; Fischinger, T.; Arbeiter, F.; Holzer, C. Shrinkage and Warpage Optimization of Expanded-Perlite-Filled Polypropylene Composites in Extrusion-Based Additive Manufacturing. *Macromol. Mater. Eng.* **2017**, *302*, 1700143. [CrossRef]
22. Zander, N.E.; Park, J.H.; Boelter, Z.R.; Gillan, M.A. Recycled Cellulose Polypropylene Composite Feedstocks for Material Extrusion Additive Manufacturing. *ACS Omega* **2019**, *4*, 13879–13888. [CrossRef] [PubMed]
23. Jonoobi, M.; Harun, J.; Mathew, A.P.; Oksman, K. Mechanical Properties of Cellulose Nanofiber (CNF) Reinforced Polylactic Acid (PLA) Prepared by Twin Screw Extrusion. *Compos. Sci. Technol.* **2010**, *70*, 1742–1747. [CrossRef]
24. Babaee, M.; Jonoobi, M.; Hamzeh, Y.; Ashori, A. Biodegradability and Mechanical Properties of Reinforced Starch Nanocomposites Using Cellulose Nanofibers. *Carbohydr. Polym.* **2015**, *132*, 1–8. [CrossRef] [PubMed]
25. Saba, N.; Safwan, A.; Sanyang, M.L.; Mohammad, F.; Pervaiz, M.; Jawaid, M.; Alothman, O.Y.; Sain, M. Thermal and Dynamic Mechanical Properties of Cellulose Nanofibers Reinforced Epoxy Composites. *Int. J. Biol. Macromol.* **2017**, *102*, 822–828. [CrossRef] [PubMed]
26. Vidakis, N.; Petousis, M.; Velidakis, E.; Spiridaki, M.; Kechagias, J.D. Mechanical Performance of Fused Filament Fabricated and 3D-Printed Polycarbonate Polymer and Polycarbonate/Cellulose Nanofiber Nanocomposites. *Fibers* **2021**, *9*, 74. [CrossRef]
27. Lesovik, V.; Fediuk, R.; Amran, M.; Alaskhanov, A.; Volodchenko, A.; Murali, G.; Uvarov, V.; Elistratkin, M. 3D-Printed Mortars with Combined Steel and Polypropylene Fibers. *Fibers* **2021**, *9*, 79. [CrossRef]
28. Eichhorn, S.J.; Dufresne, A.; Aranguren, M.; Marcovich, N.E.; Capadona, J.R.; Rowan, S.J.; Weder, C.; Thielemans, W.; Roman, M.; Renneckar, S.; et al. Review: Current International Research into Cellulose Nanofibres and Nanocomposites. *J. Mater. Sci.* **2010**, *45*, 1–33. [CrossRef]
29. Kafy, A.; Kim, H.C.; Zhai, L.; Kim, J.W.; Van Hai, L.; Kang, T.J.; Kim, J. Cellulose Long Fibers Fabricated from Cellulose Nanofibers and Its Strong and Tough Characteristics. *Sci. Rep.* **2017**, *7*, 17683. [CrossRef]
30. Lewandowska, A.E.; Inai, N.H.; Ghita, O.R.; Eichhorn, S.J. Quantitative Analysis of the Distribution and Mixing of Cellulose Nanocrystals in Thermoplastic Composites Using Raman Chemical Imaging. *RSC Adv.* **2018**, *8*, 35831–35839. [CrossRef]
31. Jonoobi, M.; Harun, J.; Mathew, A.P.; Hussein, M.Z.B.; Oksman, K. Preparation of Cellulose Nanofibers with Hydrophobic Surface Characteristics. *Cellulose* **2010**, *17*, 299–307. [CrossRef]
32. Ashori, A.; Babaee, M.; Jonoobi, M.; Hamzeh, Y. Solvent-Free Acetylation of Cellulose Nanofibers for Improving Compatibility and Dispersion. *Carbohydr. Polym.* **2014**, *102*, 369–375. [CrossRef] [PubMed]

33. Sato, A.; Kabusaki, D.; Okumura, H.; Nakatani, T.; Nakatsubo, F.; Yano, H. Surface Modification of Cellulose Nanofibers with Alkenyl Succinic Anhydride for High-Density Polyethylene Reinforcement. *Compos. Part A Appl. Sci. Manuf.* **2016**, *83*, 72–79. [CrossRef]
34. Cichosz, S.; Masek, A.; Rylski, A. Cellulose Modification for Improved Compatibility with the Polymer Matrix: Mechanical Characterization of the Composite Material. *Materials* **2020**, *13*, 5519. [CrossRef]
35. Li, J.; Zhai, S.; Wu, W.; Xu, Z. Hydrophobic Nanocellulose Aerogels with High Loading of Metal-Organic Framework Particles as Floating and Reusable Oil Absorbents. *Front. Chem. Sci. Eng.* **2021**, *15*, 1158–1168. [CrossRef]
36. Zhai, S.; Chen, H.; Zhang, Y.; Li, P.; Wu, W. Nanocellulose: A Promising Nanomaterial for Fabricating Fluorescent Composites. *Cellulose* **2022**, *29*, 7011–7035. [CrossRef]
37. Navarro, J.R.G.; Edlund, U. Surface-Initiated Controlled Radical Polymerization Approach To Enhance Nanocomposite Integration of Cellulose Nanofibrils. *Biomacromolecules* **2017**, *18*, 1947–1955. [CrossRef]
38. Thingiverse. Available online: https://www.thingiverse.com/thing:34017/files (accessed on 4 April 2022).
39. Wang, L.; Ando, M.; Kubota, M.; Ishihara, S.; Hikima, Y.; Ohshima, M.; Sekiguchi, T.; Sato, A.; Yano, H. Effects of Hydrophobic-Modified Cellulose Nanofibers (CNFs) on Cell Morphology and Mechanical Properties of High Void Fraction Polypropylene Nanocomposite Foams. *Compos. Part A Appl. Sci. Manuf.* **2017**, *98*, 166–173. [CrossRef]
40. Sharma, A.; Mandal, T.; Goswami, S. Dispersibility and Stability Studies of Cellulose Nanofibers: Implications for Nanocomposite Preparation. *J. Polym. Environ.* **2021**, *29*, 1516–1525. [CrossRef]
41. Chu, Y.; Sun, Y.; Wu, W.; Xiao, H. Dispersion Properties of Nanocellulose: A Review. *Carbohydr. Polym.* **2020**, *250*, 116892. [CrossRef]
42. Worthley, C.H.; Constantopoulos, K.T.; Ginic-Markovic, M.; Pillar, R.J.; Matisons, J.G.; Clarke, S. Surface Modification of Commercial Cellulose Acetate Membranes Using Surface-Initiated Polymerization of 2-Hydroxyethyl Methacrylate to Improve Membrane Surface Biofouling Resistance. *J. Memb. Sci.* **2011**, *385–386*, 30–39. [CrossRef]
43. Morandi, G.; Heath, L.; Thielemans, W. Cellulose Nanocrystals Grafted with Polystyrene Chains through Surface-Initiated Atom Transfer Radical Polymerization (SI-ATRP). *Langmuir* **2009**, *25*, 8280–8286. [CrossRef] [PubMed]
44. Zhang, Z.; Sèbe, G.; Hou, Y.; Wang, J.; Huang, J.; Zhou, G. Grafting Polymers from Cellulose Nanocrystals via Surface-initiated Atom Transfer Radical Polymerization. *J. Appl. Polym. Sci.* **2021**, *138*, 51458. [CrossRef]
45. Bansal, A.; Singhal, N.; Panwar, V.; Kumar, A.; Kumar, U.; Ray, S.S. Ex Situ Cu(0) Nanoparticle Mediated SET-LRP of Methyl Methacrylate/Styrene-Methyl Methacrylate in a Biphasic Toluene–Water System. *RSC Adv.* **2017**, *7*, 11191–11197. [CrossRef]
46. Mariño, M.A.; Rezende, C.A.; Tasic, L. A Multistep Mild Process for Preparation of Nanocellulose from Orange Bagasse. *Cellulose* **2018**, *25*, 5739–5750. [CrossRef]
47. Gulmine, J.; Janissek, P.; Heise, H.; Akcelrud, L. Polyethylene Characterization by FTIR. *Polym. Test.* **2002**, *21*, 557–563. [CrossRef]
48. Erbetta, C.D.C.; Manoel, G.F.; Oliveira, A.P.L.R.; Silva, M.E.S.R.E.; Freitas, R.F.S.; Sousa, R.G. Rheological and Thermal Behavior of High-Density Polyethylene (HDPE) at Different Temperatures. *Mater. Sci. Appl.* **2014**, *5*, 923–931. [CrossRef]
49. Ponnamma, D.; Cabibihan, J.-J.; Rajan, M.; Pethaiah, S.S.; Deshmukh, K.; Gogoi, J.P.; Pasha, S.K.K.; Ahamed, M.B.; Krishnegowda, J.; Chandrashekar, B.N.; et al. Synthesis, Optimization and Applications of ZnO/Polymer Nanocomposites. *Mater. Sci. Eng. C* **2019**, *98*, 1210–1240. [CrossRef] [PubMed]
50. Kerni, L.; Singh, S.; Patnaik, A.; Kumar, N. A Review on Natural Fiber Reinforced Composites. *Mater. Today Proc.* **2020**, *28*, 1616–1621. [CrossRef]
51. Móczó, J.; Pukánszky, B. Polymer Micro and Nanocomposites: Structure, Interactions, Properties. *J. Ind. Eng. Chem.* **2008**, *14*, 535–563. [CrossRef]
52. Gallos, A.; Paës, G.; Allais, F.; Beaugrand, J. Lignocellulosic Fibers: A Critical Review of the Extrusion Process for Enhancement of the Properties of Natural Fiber Composites. *RSC Adv.* **2017**, *7*, 34638–34654. [CrossRef]
53. Qiu, K.; Netravali, A. In Situ Produced Bacterial Cellulose Nanofiber-Based Hybrids for Nanocomposites. *Fibers* **2017**, *5*, 31. [CrossRef]
54. Houshyar, S.; Shanks, R.A.; Hodzic, A. The Effect of Fiber Concentration on Mechanical and Thermal Properties of Fiber-Reinforced Polypropylene Composites. *J. Appl. Polym. Sci.* **2005**, *96*, 2260–2272. [CrossRef]
55. Liang, J.-Z. Effects of Tension Rates and Filler Size on Tensile Properties of Polypropylene/Graphene Nano-Platelets Composites. *Compos. Part B Eng.* **2019**, *167*, 241–249. [CrossRef]
56. Ding, W.; Kuboki, T.; Wong, A.; Park, C.B.; Sain, M. Rheology, Thermal Properties, and Foaming Behavior of High D-Content Polylactic Acid/Cellulose Nanofiber Composites. *RSC Adv.* **2015**, *5*, 91544–91557. [CrossRef]
57. Stinchcomb, W.; Reifsnider, K. Fatigue Damage Mechanisms in Composite Materials: A Review. In *Fatigue Mechanisms*; ASTM International: West Conshohocken, PA, USA; pp. 762–787.
58. HDPE Filament—Natural—1.75 mm. Available online: https://filaments.ca/products/hdpe-filament-natural-1-75mm?variant=42590589320 (accessed on 30 April 2022).
59. Pešić, N.; Živanović, S.; Garcia, R.; Papastergiou, P. Mechanical Properties of Concrete Reinforced with Recycled HDPE Plastic Fibres. *Constr. Build. Mater.* **2016**, *115*, 362–370. [CrossRef]
60. Peng, F.; Jiang, H.; Woods, A.; Joo, P.; Amis, E.J.; Zacharia, N.S.; Vogt, B.D. 3D Printing with Core–Shell Filaments Containing High or Low Density Polyethylene Shells. *ACS Appl. Polym. Mater.* **2019**, *1*, 275–285. [CrossRef]

61. Koffi, A.; Toubal, L.; Jin, M.; Koffi, D.; Döpper, F.; Schmidt, H.; Neuber, C. Extrusion-based 3D Printing with High-density Polyethylene Birch-fiber Composites. *J. Appl. Polym. Sci.* **2022**, *139*, 51937. [CrossRef]
62. Ji, A.; Zhang, S.; Bhagia, S.; Yoo, C.G.; Ragauskas, A.J. 3D Printing of Biomass-Derived Composites: Application and Characterization Approaches. *RSC Adv.* **2020**, *10*, 21698–21723. [CrossRef]
63. Schirmeister, C.G.; Hees, T.; Licht, E.H.; Mülhaupt, R. 3D Printing of High Density Polyethylene by Fused Filament Fabrication. *Addit. Manuf.* **2019**, *28*, 152–159. [CrossRef]

Appendix 2

Three-Dimensional Printing of a Tough Polymer Composite Gel Ink Reinforced with Chemically Modified Cellulose Nanofibrils Showing Self-Healing Behavior

Feras Dalloul, Jakob Benedikt Mietner and Julien R. G. Navarro

ACS Appl. Polym. Mater. 2023, 5, 5, 3256–3269

https://doi.org/10.1021/acsapm.2c02065

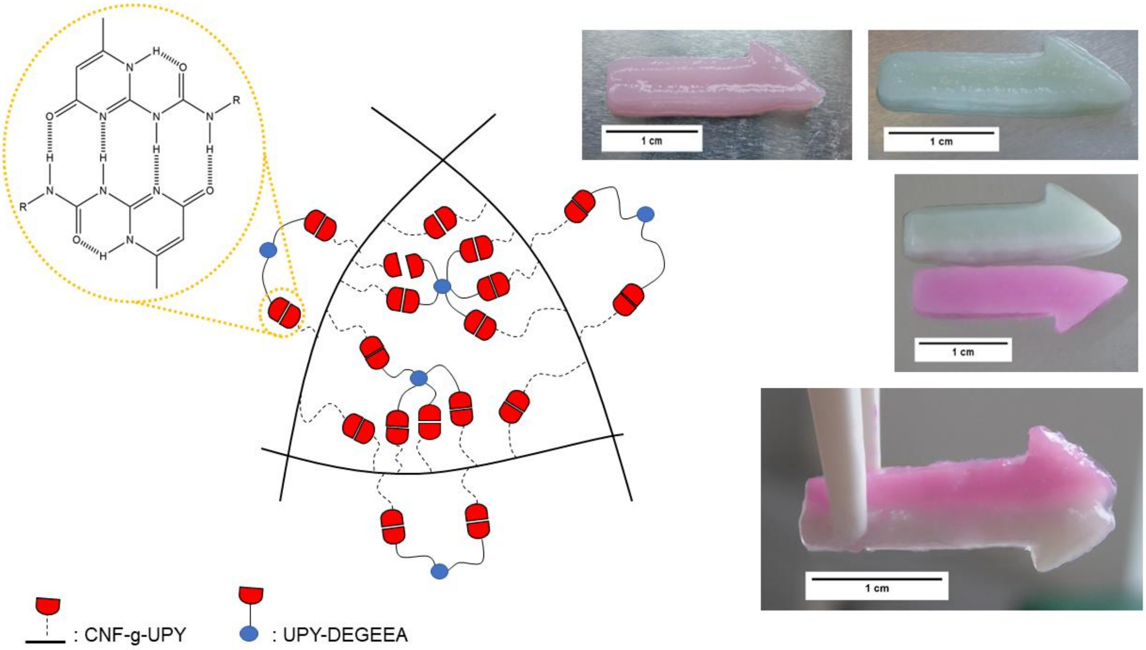

Reprinted with permission from ”Dalloul, F.; Mietner, J. B.; Navarro, J. R. G. Three-Dimensional Printing of a Tough Polymer Composite Gel Ink Reinforced with Chemically Modified Cellulose Nanofibrils Showing Self-Healing Behavior. ACS Appl. Polym. Mater. 2023’. Copyright 2023. American Chemical Society

ACS APPLIED POLYMER MATERIALS

pubs.acs.org/acsapm Article

Three-Dimensional Printing of a Tough Polymer Composite Gel Ink Reinforced with Chemically Modified Cellulose Nanofibrils Showing Self-Healing Behavior

Feras Dalloul, J. Benedikt Mietner, and Julien R. G. Navarro*

Cite This: *ACS Appl. Polym. Mater.* 2023, 5, 3256−3269 Read Online

ACCESS | Metrics & More | Article Recommendations | Supporting Information

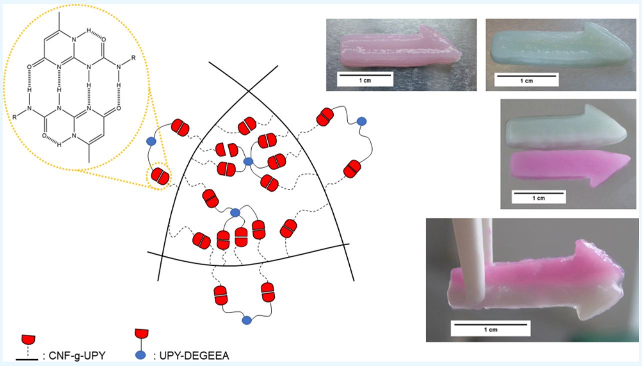

ABSTRACT: Three-dimensional (3D) gel printing has significant potential for producing structurally accurate biomaterials based on complex biological tissues for use in regenerative biotechnology. The efficiency depends on the chosen gel printing device and the parameters used but also primarily on the selection of the gel ink. In the present study, the dimerizing functions in ureidopyrimidinone (UPy) were exploited to develop a gel ink. A composite gel ink was developed made out of a polymer consisting of UPy and di(ethylene glycol) ethyl ether (DEGEEA) functions and modified cellulose nanofibril-containing UPy groups (CNF-*g*-UPy) as print performance-enhancing additives. This resulted in a hyper-cross-linked network with superior mechanical strength compared to the matrix itself, with an increase of 3.7× in storage modulus and 2.8× in loss modulus. The CNF-*g*-UPy/UPy-DEGEEA gel ink exhibited shear-thinning properties and could therefore be extruded to form uniform strands with no merging and retain a relatively stable structure. The self-healing ability was demonstrated by the adhesion of two printed patterns after 2 min at 80 °C. The multiple cross-linkages and self-healing ability of the filaments, therefore, allow for stable printed structures. All of these findings point out the promising potential of such gel ink for many biotechnological applications.

KEYWORDS: *cellulose nanofibrils (CNF), nanocellulose, gel ink, self-healing, single-electron transfer living radical polymerization (SET-LRP), 3D gel printing, direct ink writing*

■ INTRODUCTION

Three-dimensional (3D) gel printing, also known as direct ink writing or robocasting, is a fast-growing technology field that allows complex, multilayered structures to be created with a high degree of precision and accuracy.[1] Printing hydrogels have been widely tested for their potential use in tissue engineering or organ bioprinting.[2−5] For the production of these human body imprints, it is essential that the properties of the gel are not impaired and that cell viability is preserved.[6] Although the reliability of printing devices and the control of resolution are greatly improving, the selection of the right gel ink remains essential. The gels must have specific physicomechanical and rheological properties for them to exhibit structural stability and retention after extrusion.[7,8] Numerous natural biomaterial-based inks have recently been reported in the literature.[9,10] Kesti et al.[11] developed a bioink using a mixture of a hyaluronan-grafted heat-sensitive poly(*N*-isopropylacrylamide) polymer (HA-pNIPAAM) and a photo-cross-linkable biopolymer (methacrylated hyaluronan (HA-MA)) with improved mechanical properties and a great cellular viability performance. Although biocompatible and highly similar to extracellular matrices, gel inks suffer from numerous problematic attributes, such as batch-to-batch variation and a restricted range of properties (structure, solubility, and viscosity).[12,13] Such problems can be prevented by using synthetic polymers, which are fully customizable. For example, by changing the monomers, the functional properties can be adjusted, and the amount of cross-linking is controlled.[14]

Self-healing materials may be divided into two classes, intrinsic and extrinsic. For extrinsic polymers, a chemical agent is preincorporated in the matrix and released into the fracture once the polymer is damaged.[15] Intrinsic self-healing materials, however, are based on reversible bonds that are inherently within the polymer matrix's structure.[16] They can be subdivided into two categories—autonomous,[17] in which repair occurs without an external stimulus, and nonautono-

Received: November 29, 2022
Accepted: March 27, 2023
Published: April 6, 2023

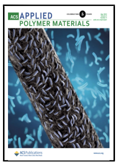

https://doi.org/10.1021/acsapm.2c02065

mous materials, in which repair is triggered through an external stimulus.

Self-healing gels can be produced by either covalent or noncovalent cross-linking chemistry.[18] Examples of noncovalent bonds include imine bonds, disulfide bonds, and diels alder click chemistry.[19] In contrast, many noncovalent self-healing gels rely on weak reversible bonds, including ionic interactions, hydrogen bonds, host-guest, and hydrophobic bonds.[20] The principal benefit of physically cross-linked gels is the absence of functional reactive groups necessary for cross-linking and establishing the network. 2-Ureido-4[1*H*]-pyrimidone (UPy) units, strongly dimerizing moieties, have been extensively researched and documented in the literature.[21−23] Its self-healing properties are based on dynamic noncovalent bonds, which can be disrupted by external stimuli such as heat, mechanical force, and UV light.[24] As a result of this, the gels are capable of reforming after the removal of the stimulus, rendering them suitable for injection.[25]

So far, few studies have been reported to develop highly cross-linked gels with self-healing ability, exhibiting good mechanical and shear-thinning properties. To address this, the production of a supramolecular gel consisting mainly of UPy units to produce tissue regeneration solutions were considered. In order to synthesize the polymer, it was decided to add di(ethylene glycol) ethyl ether (DEGEEA) functions to confer thermo-responsive properties, improved solubility in dimethyl sulfoxide (DMSO), and reduced aggregation of the UPy functions, all without reducing the number of hydrogen bonds.[26,27] UPy-grafted cellulose nanofibrils (CNF) were also incorporated as a reinforcing agent in order to enhance the polymer's mechanical properties and resulted in improved post-printing behavior of the nanocomposite. Pitton and his research team succeeded in developing a gel ink based on a combination of pectin and nanocellulose fibrils. The viscosity of pectin restricts its suitability for gel printing, but by adding 1% w/v 2,2,6,6-tetramethylpiperidine-1-oxyl (TEMPO)-oxidized cellulose nanofibrils, precise 3D structures were printed.[28] Therefore, the supramolecular nanocomposites would offer significantly better mechanical properties than just the matrix.

The synthesis of the UPy monomer suitable for the polymerization reaction is first described. Then, the synthetic processes of macroinitiator (MI)-based nanocellulose fibrils (CNF-MI), as well as the single-electron transfer living radical polymerization (SET-LRP) reaction to obtain UPy-grafted cellulose nanofibrils (CNF-*g*-UPy), are described. The supramolecular polymer is also produced by a SET-LRP reaction, with a ratio of one-third UPy monomer and the remaining DEGEEA monomer. This reaction yields the UPY-DEGEEA polymer. The products were analyzed by ^{1}H NMR, solid-state cross polarization/magic angle spinning (CP/MAS) ^{13}C NMR, Fourier transform infrared (FTIR) spectrometry, and differential scanning calorimetry (DSC). The composites were made with a proportion of 20% CNF-*g*-UPy and were analyzed by rheological measurements, in addition to the methods mentioned above. Finally, the gel was used for 3D gel printing to print complex models, and the self-healing behavior was investigated under visual and microscopic observation.

■ MATERIALS AND METHODS

Materials. Imidazole (≥99%), dimethyl sulfoxide (DMSO, ≥99%), tris[2-(dimethylamino)ethyl]amine (Me$_6$TREN, 97%), isopropanol, toluene, and Cu wire (diameter 0.812 mm) were purchased from Alfa-Aesar. 2-Bromo-2-methylpropionate (98%), 1,1′-carbonyldiimidazole (CDI) (reagent grade), di(ethylene glycol) ethyl ether acrylate (DEGEEA) (90%), ethyl-2-bromo-2-methylpropionate (ebib, 98%), rhodamine B (>95%), 1,1′-carbonyldiimidazole (CDI), and 2-amino-4-hydroxy-6-methylpyrimidine 98% were purchased from Sigma-Aldrich. For cellulose nanofibrils (CNF) production, dried elemental chlorine-free (ECF) bleached softwood kraft pulp was obtained from MERCER Stendal GmbH, Germany. The kraft pulp is made from pine (30−60%) and spruce (40−70%) and PFI-milled at 23 °C and 50% of relative humidity. Ultrapure Milli-Q water was used for the solvent exchange procedure.

Materials Synthesis. *Extraction of Cellulose Nanofibrils from Kraft Pulp and Solvent Exchange.* CNF was produced from a procedure reported previously.[29] Dry pulp was cut and ground to a high degree using a mill. To measure the degree of milling, the suspension was diluted to 0.24 wt % and then measured with the Schopper−Riegler measuring vessel. The degree of grinding was 92° SR. The suspension was then passed through a microfluidiser (Microfluidics M-100EH-30) with two fine chambers with orifice widths of 400 and 200 μm at 15,000 Psi and two finer chambers of 200 and 100 μm at 25,000 Psi. Afterward, the CNF was concentrated by centrifugation to yield an aqueous CNF gel (2 wt %).

10 g of the gel was dispersed in 80 mL of water and then 150 mL of DMSO was added dropwise. This procedure has also been described previously.[30] The resulting suspension was then concentrated to yield a 1.5 wt % CNF gel.

Preparation of the CNF Macroinitiator by Esterification. The solvent-exchanged CNFs were processed through an esterification reaction to yield a CNF-based macroinitiator (CNF-MI). The procedure used here is the same as that reported previously.[30] Accordingly, an amount of 10 g of CNF-MI was obtained at a concentration of 3.4 wt %.

UPy Monomer Synthesis. 2-Amino-4-hydroxy-6-methylpyrimidine (10 g, 70.1 mmol) was dissolved in 150 mL of DMSO at 130 °C using an oil bath. Upon dissolution, 2-isocyanatoethyl acrylate was added to the main flask. The flask was kept at 130 °C for 10 min. Then, the reaction was quenched using a cold water bath. The precipitate was filtrated and washed under vacuum with cold water and dried to give 2-(3-(6-methyl-4-oxo-1,4-dihydropyridine-2-yl)ureido)ethyl acrylate (UPy monomer), a white solid (95% yield).

^{1}H NMR (400 MHz, DMSO-d_6, 60 °C): δ (ppm): 11.34 (1H, s), 9.88 (1H, s), 7.66 (1H, s), 6.38−6.34 (1H, d, J = 17.16 Hz), 6.21−6.14 (1H, dd, J = 17.17, 10.32 Hz), 5,96 (1H, d, J = 10.32 Hz), 5.78 (1H; s), 4,19 (2H, m), 3.47 (2H, m), 2,10 (s, 3H). FTIR (attenuated total reflection (ATR), cm^{-1}): ν = 3045 (R−CO−NH−C), 2935 (R−CH2−R), 1732 (C═C−COOR), 1701 ((R)2C═CHR), 1657 (R−CO−NH−), 1576 (C−N═C), 1522 (R−CO−NH−), 1450 (R−CH2−R), 1397 (RCH═CH2), 1327 (R−CO−NH−C), 1252 (C═C−COOR), 1180 (RCOOR), 1149 (R−NH−(C═O)−NH−R), 1053 (R−C═C−R), 968 (R2C═CHR), 856 (−C═O−CH═CH2), 756 (broad, R2C═CHR).

Grafting of the UPy Monomer onto the CNF by SET-LRP. The UPy monomer (6 g, 22.5 mmol) was first dissolved in DMSO at 110 °C and then the flask was allowed to cool to 60 °C. In a three-neck flask, 7.42 g (0.8 wt %) of the CNF macroinitiator was dispersed in 25 mL of DMSO at 60 °C, and then the monomer solution was gradually added. The copper wire (length = 9.14 cm) was activated by soaking it in concentrated hydrochloric acid for 10 min, followed by rinsing with acetone and drying. It was then added to the flask and the whole suspension was degassed by nitrogen purging while maintaining an overall temperature of 60 °C. The Me$_6$TREN ligand was finally added and the reaction was allowed to proceed for 16 h. Afterward, the resulting CNF-*g*-UPy gel was collected through centrifugation (4000 rpm, 20 min) and repeatedly washed (4×) with new DMSO.

UPy-DEGEEA Polymer Synthesis. The same starting procedure for the CNF-*g*-UPy synthesis was used. The UPy monomer solution (3 g, 11.25 mmol), initially dissolved in 60 mL of DMSO at 110 °C and cooled to 60 °C, was passed through an aluminum oxide column. DEGEEA (0.7 g, 3.75 mmol) was also run through the column of aluminum oxide and then added to the principal flask. The ratio of polymerization $[M]_0/[I]_0/[L]_0$ is 100/1/0.2. The copper wire (length = 6 cm) was activated by soaking it in concentrated hydrochloric acid for 10 min, followed by rinsing with acetone and drying. It was eventually added while the solution was degassed by nitrogen purging for 10 min at 60 °C. Ethyl-2-isobutyrate (0.3 g, 0.15 mmol) was then added to the solution. The Me_6TREN ligand was finally added and the reaction was allowed to proceed for 16 h. Afterward, the gel was collected by centrifugation (4000 rpm, 20 min) and repeatedly washed (4×) with new DMSO.

Preparation of the Cross-Linked Gel (CNF-g-UPy/UPy-DEGEEA, 2:8). 1.14 g of the polymer gel (7 wt %) was first dispersed in 2 mL of DMSO. Afterward, 1.75 g of CNF-*g*-UPy (2.38 wt %) was directly added to the solution of the polymer. The mixture was then shaken vigorously for 10 min to ensure proper homogenization. This was concentrated by centrifugation (4000 rpm, 20 min) and the supernatant was discarded. This procedure was repeated twice, resulting in a white gel that was used without further processing. After that, an amount of DMSO was added to swell the solid gel to 4 wt %.

To obtain a colored gel, a rhodamine B solution was prepared and added to the gel slowly until the desired color was obtained.

Three-Dimensional Gel Printing. The models were designed using Fusion360 and 3D gel-printed by pneumatic extrusion using a CELLINK INKREDIBLE 3D bioprinter. Before printing, the gel, which has a high viscosity, was homogenized using a screw-shaped mixing unit called "HighVisc," developed by Dani and his teammates.[31] A disposable syringe was loaded and inserted into the printing cartridge. Printability was tuned by adjusting the inflow rate through the fixed nozzle to achieve stable and consistent precision of filament printing. The gel was printed using a 0.59 mm diameter conical nozzle with an applied pressure of 18 kPa.

Material Characterization. Attenuated total reflection Fourier transform infrared spectroscopy (ATR-FTIR) was conducted using a Bruker Vector 33 FTIR I18500 PS15 infrared spectrometer. The spectra were recorded with 64 scans across the 4000−500 cm^{-1} spectral region. The spectral resolution is 4 cm^{-1}.

A nuclear magnetic resonance (NMR) spectrometer (Bruker-AVANCE III HD 400) operating at 400 MHz was also used to analyze the structure of the compounds. Nuclear magnetic resonance in the solution state with DMSO-d_6 as a solvent was performed at 60 °C and transferred to NMR tubes with a 5 mm outer diameter.

The copolymer composition has been determined by ^1H NMR measurements as well. Since there are distinguishable peaks arising from one of the repeating units of the monomer, the integration of each peak is done and the monomer ratio of one monomer can be calculated using the formula below

$$\text{proportion of monomer (\%)} = \frac{\frac{I(A)}{x}}{\left(\frac{I(A)}{x}\right) + \left(\frac{I(B)}{x}\right)} \qquad (1)$$

where *A* and *B* are considered as the integral of the chosen peak in each monomer and the *x* and *y* are the number of hydrogens associated with it.

All ^{13}C NMR spectra were acquired on a Bruker 500 Avance III HD spectrometer at Larmor frequencies of 125 and 500 MHz for ^{13}C and ^1H, respectively. These samples were put into 4 mm zirconia rotors for magic angle spinning (MAS) at a rotation speed of 8 kHz. Creeping ^{13}C MAS NMR spectra were recorded with a ^{13}C mutation frequency of 50 kHz and a contact time of 1.5 ms. These spectra were acquired by the Fourier transform of the FIDs, and chemical shifts were referenced to pure tetramethylsilane (TMS).

Size exclusion chromatography, multidetector system (UV−vis, RI, MALLS), size exclusion chromatography (MALLS, RI), and triple-detection size exclusion chromatography (Triple-SEC) measurements were conducted on the SEC system equipped with a Waters 515 pump, an autosampler, and two MZ gel columns (103 and 104 Å) with a flow rate of 0.5 mL/min in tetrahydrofuran (THF) (high-performance liquid chromatography (HPLC) grade) at 25 °C. Detectors included a differential refractometer (Optilab rEX,Wyatt), a multiangle light scattering (MALS) detector equipped with a 632.8 nm He−Ne laser (DAWN EOS, Wyatt), and a Viscometer (ViscoStar, Wyatt). The MALS detector was used to determine the molecular weight, whereas the viscometer provided Mark−Houwink−Sakurada relationships. The refractive index increments of polymers in THF were measured at 25 °C using an Optilab rEX differential refractometer. ASTRA software (version 5.1.3.0) was utilized for the acquisition and analysis of data.

The rheology tests were carried out with a TA Instrument AR 2000ex and Advantage v5.8.2 software. Rheological tests were performed using a 40 mm parallel plate setup and a gap distance of 1000 μm. All rheological measurements were made at 25 °C. Each sample was placed on the bottom plate. Each measurement was made following these parameters:

- The shear stress ramp was measured with a 4-min-long continuous ramp testing method, with the shear stress ranging from 0.01 to 1000 Pa.
- The shear rate sweep was recorded with a shear rate between 0.01 and 2200 s^{-1} in the continuous ramp mode.
- Rotational recovery measurements were performed to characterize the viscosity retrieval behavior of the material after 3D printing by applying a shear rate of 200 s^{-1} for 200 s, then a shear rate at 895 s^{-1} for 100 s, and finally returning to a shear rate of 200 s^{-1} for 200 s. An acquisition was made every 10 s.
- For the oscillation measurement, a frequency sweep with an angular frequency ranging from 0.1 to 628.3 rad s^{-1} was measured in the logarithmic modus.
- The strain sweep was performed with a fixed angular frequency of 6.28 rad s^{-1} to ensure that measurements were made in the linear viscoelastic region. This was done with an oscillating stress ranging from 1 to 1000 Pa.

The thermal behavior of CNF, CNF-*g*-UPy, and UPy-DEGEEA polymer was monitored using a differential scanning calorimeter (DSC) Mettler Toledo DSC 820 module equipment. Each specimen was vacuum dried in advance. For each sample, the average mass was approximately 5−8 mg. Encapsulated in a 40 μL aluminum cup, it was placed in the measuring slot. The temperature program consisted of first heating from 25 to 250 °C, followed by cooling to 25 °C, and the same cycle was repeated once. The heating/cooling rate was set at 10 °C/min under an atmosphere of nitrogen at a flow rate of 50 mL/min.

The morphology of modified CNFs and composites was observed via ultrahigh-resolution field emission scanning electron microscopy (FE-SEM) with a Hitachi S-800. Modified CNFs were dried and then mounted on sample supports using carbon tape and coated with a 5 nm layer of Pd/Pt under an inert atmosphere.

The printability characterization was done by printing two separate patterns. The first design was made using a Fusion360 with a 15 × 15 × 0.5 mm^3 partial grid and nine junction points between two strands. An additional test was carried out by printing an 18 × 30 × 0.5 mm^3 model consisting of strands separated by distances of 0.5 and 1 mm. The color of the gel differed due to the use of dyed and undyed gels.

A fragment of the composite is placed on a glass sheet. The self-healing of the composite was first performed by making a section with a sharp blade. Fragmented portions were set aside and heated to 80 °C for 5 min. Photographs were taken before and after the process.

The self-healing was characterized by printing two half-arrow patterns of 24 × 6 mm^2 in size. These models were printed using two differently colored gels for ease of observation. Once printed, both were frozen in liquid nitrogen and transferred onto a single plate. Then, placed side by side, the plate was heated to 80 °C for 2 min. Afterward, it was removed and the temperature was brought back to room temperature.

Two strands of each composite gel were extruded, one on top of the other. The same process as described above was used for self-healing. The extruded strips were then placed under an optical microscope and a camera was used to record the process. The temperature was then raised to 80 °C and lowered to room temperature.

Scheme 1. Synthetic Scheme for the UPy Monomer

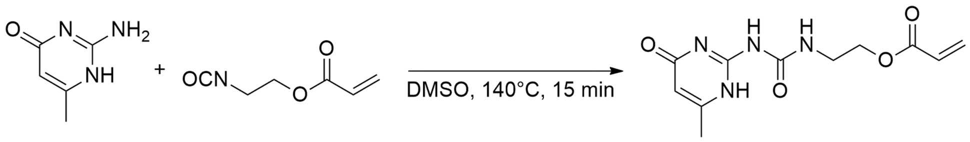

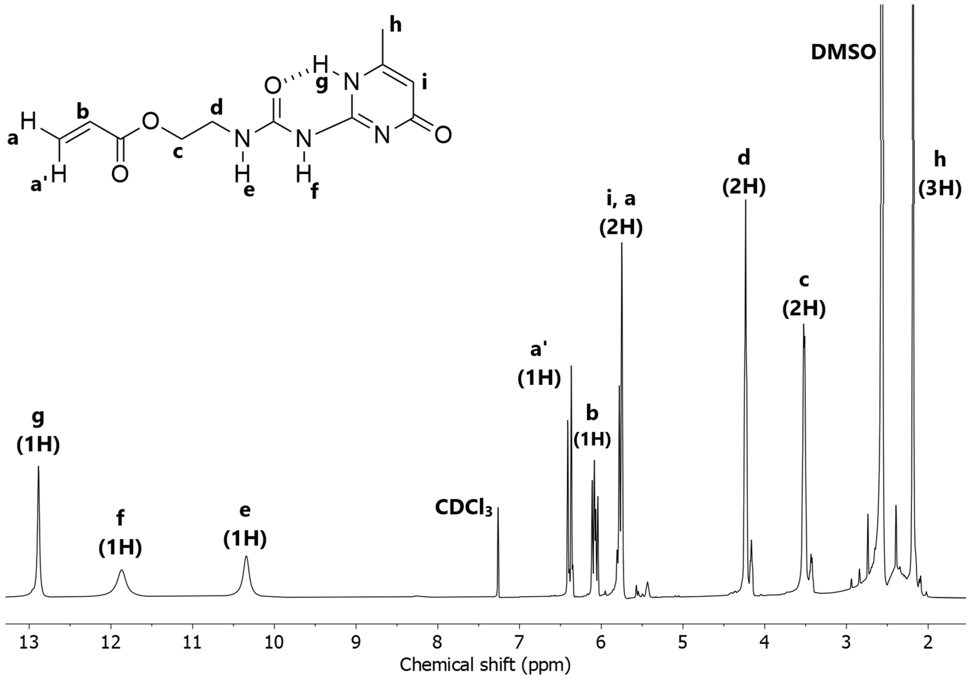

Figure 1. ^{1}H NMR spectrum of the UPy monomer.

Scheme 2. (a) Synthetic Process of the CNF-Based Macroinitiator (CNF-MI) and (b) Graft Polymerization of CNF-Based Macroinitiators with the UPy Monomer via SET-LRP, Yielding CNF-*g*-UPy

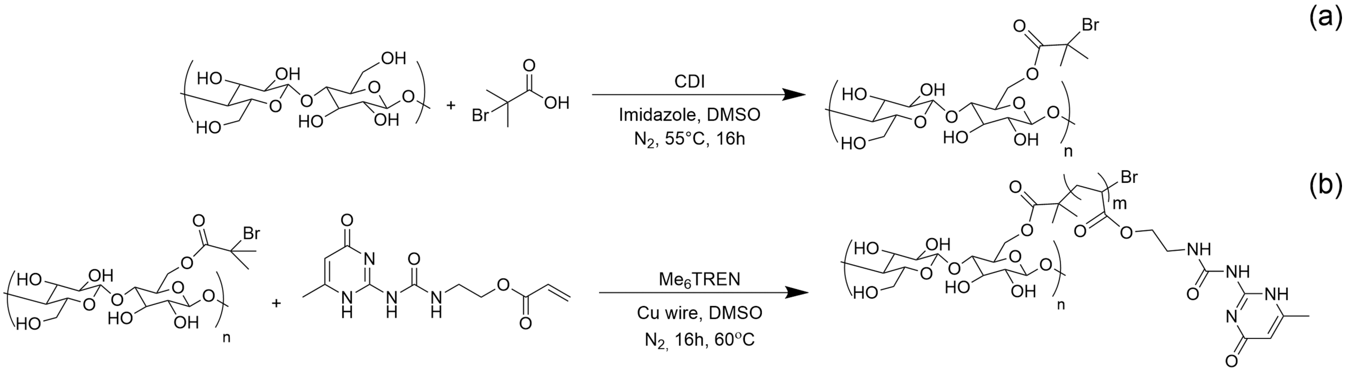

RESULTS AND DISCUSSION

UPy Monomer Synthesis. The hydrogen bonding dimerization properties of UPy monomers were first studied by Meijer.[32] The dimerization constant reaches 10^6 M^{-1} in chloroform and can be attributed to four hydrogen bonds arranged in a donor−donor−acceptor−acceptor pattern.[33] These supramolecular properties have been extensively exploited to produce self-healing materials.[34,35]

The first step required in our procedure to introduce this self-dimerization unit into the cellulose nanofibrils is to produce the corresponding monomer with a function capable of engaging in a radical polymerization reaction. The corresponding UPy monomer was achieved through the reaction of the amine of 2-amino-4-hydroxy-6-methylpyrimidine with the corresponding isocyanate from 6-methylisocytosine (Scheme 1).

This reaction was performed in DMSO at 140 °C to ensure complete solubilization, and it was complete after 15 min. Then, after cooling to room temperature, a white solid precipitated and it was washed with an excess of cold distilled water and dried under vacuum. The desired compound was obtained with a yield of 92%.

The compound was then analyzed by ^{1}H NMR in DMSO-d_6 at 60 °C (Figure 1). Integrations of the peaks were in good accordance with the suggested structure; therefore, the monomer composition was confirmed.

Chemical Surface Modification of Cellulose Nanofibrils. Cellulose nanofibrils (CNF) have been extensively researched to develop innovative and versatile gels for a wide range of applications.[36] In order to achieve the desired material properties, it is often necessary to chemically modify the surface of the cellulose nanofibrils.[37,38] To introduce the dimerizing function into cellulose fibrils, CNF must first be chemically modified. First, a solvent exchange procedure is required from water to DMSO. Next, an esterification reaction was performed to convert the CNFs into nanocellulose-based macroinitiators (CNF-MI). This is achieved through a reaction between the hydroxyl groups present on the surface of CNF with 2-bromoisobutyric acid in a basic medium promoted by CDI at 55 °C (Scheme 2a). The grafting of the UPy moiety by surface-initiated single-electron transfer living radical polymerization (SI-SET-LRP)[39] is now achievable. Monomer solubility at room temperature is poor, so the polymerization reaction has to be carried out in DMSO at a higher temperature than at room temperature. Murali's team[40] was able to synthesize bromide-functionalized graphene polymer nanocomposites using the single-electron transfer living radical polymerization (SET-LRP) at 60 °C. Therefore, the macroinitiator from the esterification can trigger the controlled polymerization of the UPy monomer, which has to be first solubilized at 120 °C and then cooled to 60 °C. The SET-LRP was finally performed in the presence of Cu(0) and the tetradentate tertiary amine ligand (Me_6TREN) in DMSO (at 60 °C), as shown in Scheme 2b. UPy-grafted CNF (CNF-*g*-UPy) is finally obtained as a translucid gel after purification by centrifugation with a concentration of 4−5 wt %.

The resulting product was first characterized by FTIR spectroscopy (Figure 2). The characteristic peaks of non-modified nanocellulose are identifiable with localized peaks at 3320 cm^{-1} (O−H), 2950 cm^{-1} and 2895 cm^{-1} (C−H), 1430 cm^{-1} (C−H), and 1161 cm^{-1} (C−O−C). CNF-MI was confirmed by the emergence of the peak at 1733 cm^{-1}, representing the ester groups (C═O in COOR) introduced following this reaction. Finally, the successful grafting of the UPy monomer was confirmed by the occurrence of broad peaks around 1500−1700 cm^{-1}, with characteristic peaks such as 1657 cm^{-1} (R−CO−NH) and 1576 cm^{-1} (R−NH−C═C) corresponding to amide and urea peaks.

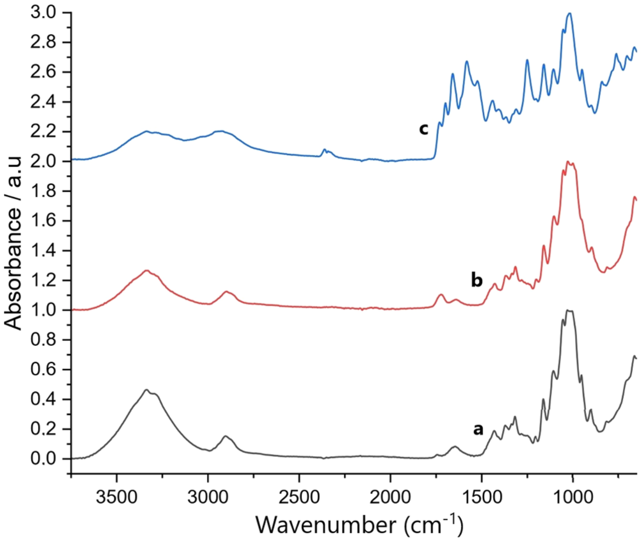

Figure 2. IR spectra of pristine (a) CNF, (b) CNF-based macroinitiator, and (c) CNF-*g*-UPy.

Similarly, the chemical modification of CNF was monitored by solid-state CP-MAS ^{13}C NMR. The resulting spectra of the modified and unmodified CNFs are shown in Figure 3 with the corresponding peak assignment.

In accordance with Kono's research work,[41] characteristic bands of the CNF have been assigned. An increase in peak density is noted as a result of the increased number of carbons undergoing different shielding. These can be grouped between, with the least shielded around 20−40 ppm corresponding to non-heteroatom neighboring carbons. Other peaks are found around 63 ppm (C13) and 105 ppm (C18) for carbons next to one single oxygen or involved in a double bond. Lastly, the heavily shielded region at the chemical shift above 140 ppm and below 180 ppm corresponds to diagonal carbons (sp carbons) adjacent to two or more heteroatoms. The combination of FTIR analysis and solid-state NMR confirms the successful grafting of the monomer and the obtention of UPy-grafted CNF (CNF-*g*-UPy).

UPy-DEGEEA Polymer Synthesis. Achieving 3D-printable self-healing gels containing CNF requires the formation of a 3D cross-linked network formed through either irreversible covalent bonds[42] or dynamic bonds.[43] 2-Ureido-4[1*H*]-pyrimidinone units (UPy) have been extensively used in research for the formation of gels.[44,45] Zhu and his research team[46] were able to obtain a self-healing polymer based on low cross-linking materials. This material was prepared using hydroxyethyl acrylate (HEA) and poly(ethylene glycol) methacrylate (PEGMA) with UPy moieties. Therefore, we decided to synthesize a similar polymer consisting of UPy and di(ethylene glycol) ethyl ether acrylate (DEGEEA) repeating units. The resultant product would then be used as a matrix for the target composite gel.

The process was done under SI-SET-LRP conditions similar to those described above (Scheme 3). Reaction conditions were similar to grafting UPy to CNF, except that instead of the CNF macroinitiator, the molecular initiator ethyl-2-bromo-2-methylpropionate was used with a ratio of polymerization $[M]_0/[I]_0/[L]_0$ of 100/1/0.2. (Scheme 3). The end product would be a copolymer with a UPy/DEGEEA ratio of 3/1. The reaction was left at 60 °C for 16 h, followed by purification by centrifugation with water and DMSO. This resulted in a white gel, which was investigated by IR, NMR, SEM, and DSC.

Prior to FTIR analysis, the product was dried under vacuum. The spectrum is presented in Figure S1 and is plotted versus the monomer. The two spectra are quite similar since the DEGEEA monomer is not providing an additional chemical function for the overall structure. However, the decrease of the peak at 860 cm^{-1} corresponding to the double bond (CH_2═CH−), representing the acrylate function of the monomer, is observed. In addition, there is a significant increase in the peak at 1016 cm^{-1}, typical of the aliphatic C−O stretching. For further structural analysis, ^{1}H NMR was conducted in DMSO-d_6 at 60 °C, and the obtained spectrum is displayed in Figure 4. For comparison purposes, the monomer spectrum is also presented. The peaks related to the UPy monomer are well identified, such as the peak at 5.78 ppm, hydrogen 13, corresponding to the unshielded C−H in the heterocyclic ring. The absence of the peaks at 5.91 and 6.40 ppm, which belong to the acrylate function of the monomer, indicates that the polymerization has been completed. Furthermore, new peaks such as 1.05 and 2.26 ppm and an increase in the 3.43 and 4.08

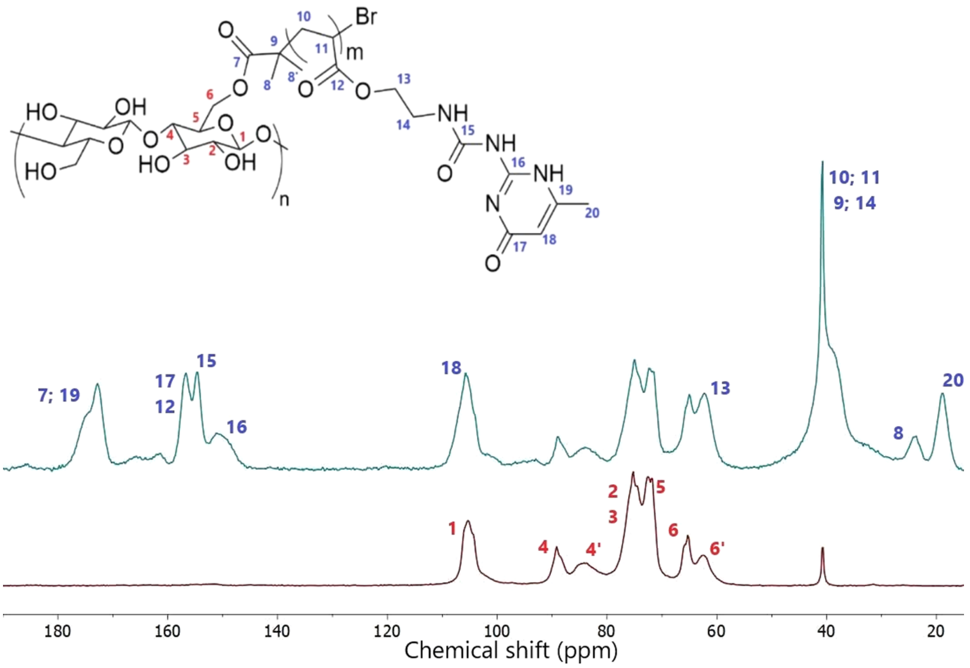

Figure 3. Solid-state CP-MAS ^{13}C NMR spectra of unmodified CNF on the lower part and CNF-*g*-UPy on the upper part.

Scheme 3. Synthetic Scheme of UPy-DEGEEA

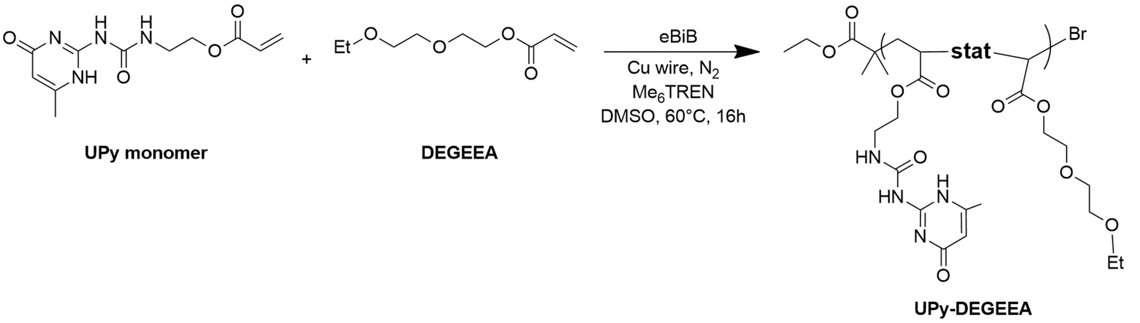

ppm peaks were observed, representing the addition of hydrogens derived from the DEGEEA monomer.

NMR spectroscopy was also used to accurately determine the ratios of each of the monomers within the polymer. The peak number 13, located at 5.78 ppm, is representative of the UPy monomer and has been integrated ($I = 1$) for reference. Although the peak at 1.05 ppm corresponds to hydrogen 1 and 16, there is a minimal number of hydrogens originating from the initiator, so it can be overlooked. Therefore, it was chosen to represent the DEGEEA monomer and was integrated with a value of 1.86. Based on this data, the ratio of monomers can be obtained, which consists of 59% UPy and 39% DEGEEA which is in good accordance with the theoretical ratio UPy/DEGEEA of 3/1, which would lead to 67% UPy and 33% DEGEEA.

Gel Preparation and Rheology. Polymer gels are semisolid materials whose properties range from soft and weak to firm and tough.[47,48] They are formed by three-dimensional networks of solvent-swollen cross-linked macromolecular chains. Depending on the type of cross-links, they can have varying characteristics, such as thermo-responsive, pH-responsive, or photoinduced gelating.[49] In this case, the aim is to produce a polymer gel, achieved by combining the matrix (UPy-DEGEEA polymer) and the modified cellulose nanofibrils (CNF-*g*-UPy) that is adapted to gel printing by pneumatic extrusion. Upon mixing, an exponential increase in hydrogen bonding occurs, increasing the degree of association between the supramolecular building blocks to form a cross-linked structure (Scheme 4). For a printable gel ink, there are certain minimum requirements[8,50] that must be met. The gel needs to have supramolecular interactions, which can be disrupted by an external stimulus and re-established once standard conditions are restored. This feature gives rise to the property of shear thinning and thus allows the printability of a gel.[51] Compounds with UPy moieties fulfill these criteria and have proven to have robust mechanical properties[52] and injectability.[53]

Rheological characteristics are commonly used to predict gel ink printability and shape fidelity.[54−58] The rheology measurements were performed on the matrix (UPy-DEGEEA), CNF-*g*-UPy, and the composite gel. The first test was carried out with increasing shear stress to assess the sample's viscosity behavior, and the results are presented in Figure 5a. These compounds exhibited a shear-thinning effect, manifested by a decrease in viscosity with increasing shear stress, which is typical of a non-Newtonian material. Modified CNF has a resting viscosity 20 times higher (9854 to 492 Pa s) than the polymer. With the incorporation of 20% CNF-*g*-UPy, the composite exhibits a 5-fold increase in viscosity over the matrix. It proves that the

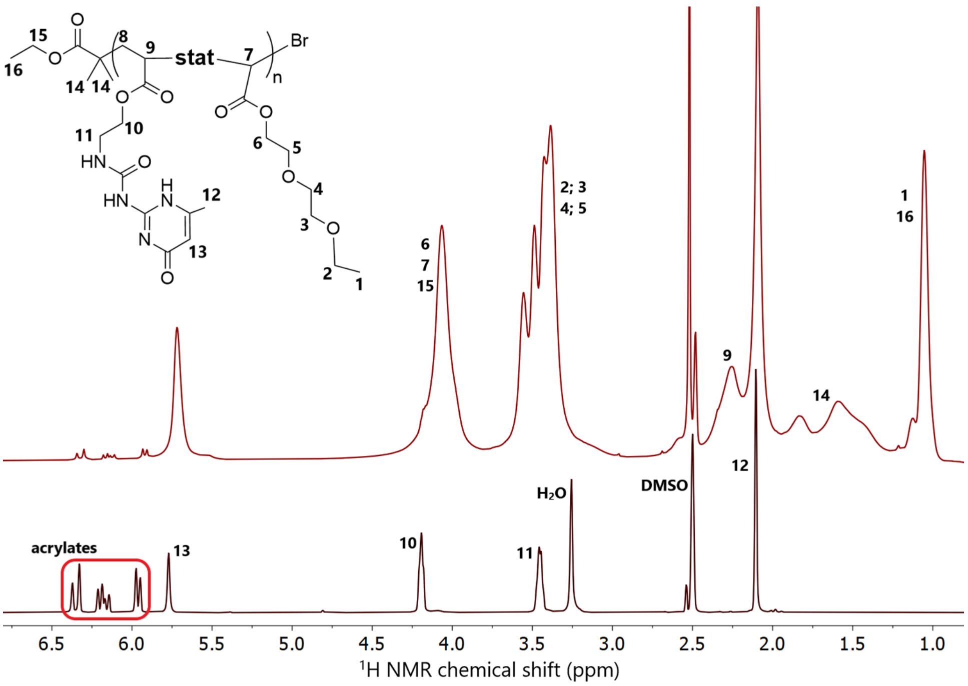

Figure 4. ^{1}H NMR spectrum of UPy-DEGEEA. The UPy monomer is represented on the lower part and UPy-DEGEEA on the upper part.

Scheme 4. Schematic Presentation of the Gelation Procedure Resulting in the Mixing of CNF-*g*-UPy and the UPy-DEGEEA Polymer

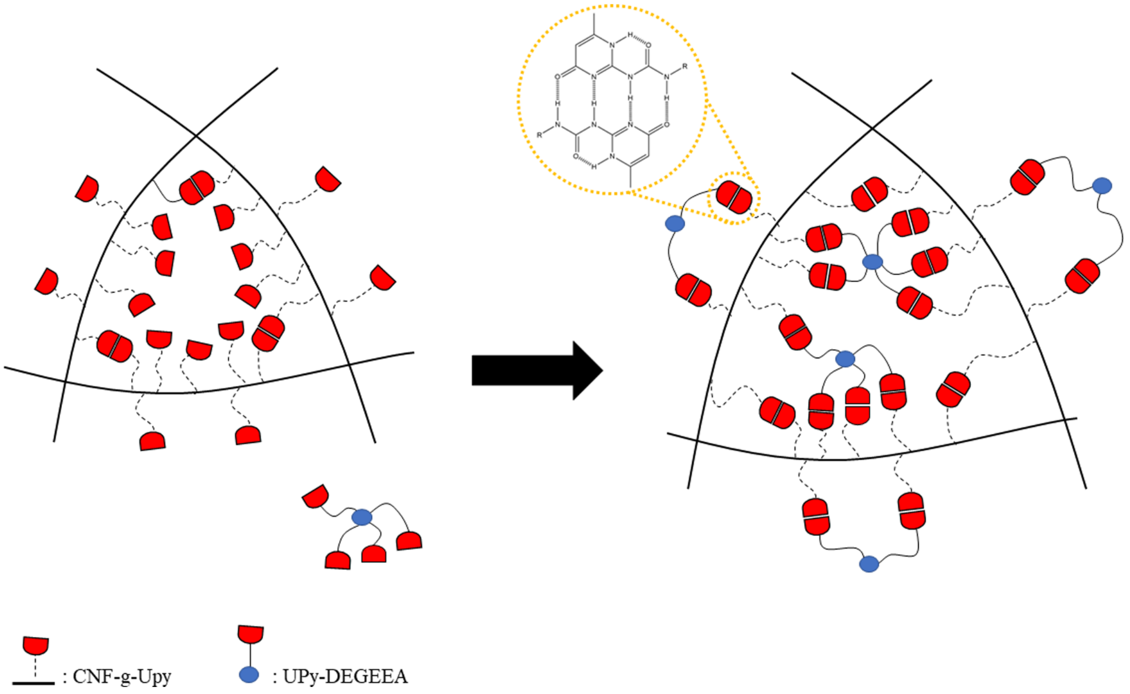

matrix and the nanocellulose are well-compatible and that hydrogen bond density is increased. Next, a shear rate sweep measurement was performed, and the flow curve of shear stress versus shear rate is displayed in Figure 5b. This measurement was able to confirm that these materials are yielding fluids and exhibit pseudo-plastic flow behavior since the stress axis is intersected at a non-zero value, thereby demonstrating that a shear rate is only induced when the yield point has been exceeded. In contrast to UPY-DEGEEA, CNF-*g*-UPY and CNF-*g*-UPy/UPy-DEGEEA exhibit quite similar behavior, confirming their high compatibility. Then, the pre- and post-printing behavior of the gels was evaluated, and the results are shown in Figure 5c. To obtain an accurate simulation of extrusion, each material was subjected to a low shear rate of 0.01, mimicking the resting state before printing, followed by a high shear rate for 200 s, mimicking the extrusion process. Finally, the minimum shear rate was restored to evaluate the recovery of the initial viscosity of the materials after extrusion. The materials show suitable behavior for printing, with an

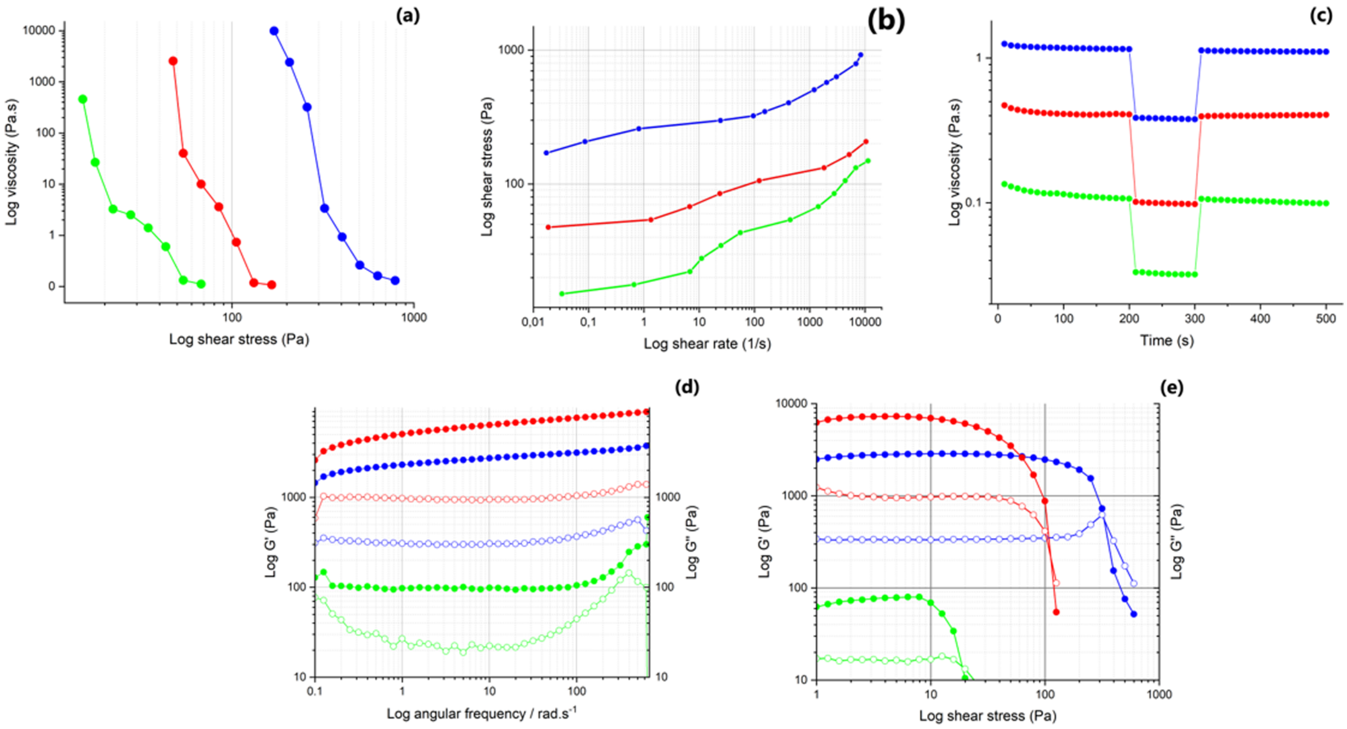

Figure 5. (a) Shear stress ramp data; (b) flow curves (shear stress versus shear rate); (c) recovery tests demonstrate the ability of materials to quickly recover their initial viscosity from high shear rates to near zero shear to simulate conditions experienced during extrusion printing; (d) frequency spectra of dynamic modules with a steady increase of the angular frequency applied; and (e) dynamic modulus under increasing stress to determine yield stress. Sample color codes: red: CNF-*g*-UPy/UPy-DEGEEA; blue: CNF-*g*-UPy; and green: UPy-DEGEEA. For viscoelastic properties, G' values are represented with full symbols and G'' with open symbols.

instant return to the original viscosity after removing the excessive shear rate.

The viscoelastic properties, storage modulus (G') and loss modulus (G'') against the angular frequency of the compounds were measured and are presented in Figure 5d. The data was recorded using a dynamic frequency sweep ranging between 0.1 and 100 rad/s. The storage moduli are all higher than the loss modulus over the entire frequency range, typical of a gel-like behavior. The composite has the highest modulus of elasticity relative to the matrix and nanocellulose, with very low variation across the range of defined angular frequencies.[59,60] Finally, in an attempt to simulate where the static gel undergoes injectability, the samples were subjected to increasing shear stress with a constant angular frequency,[61,62] and the dynamic moduli are measured. Upon reaching the critical shear stress level, all gels were disrupted and experienced a loss in mechanical strength, in which the storage modulus (G') decreased below the loss modulus (G'') (Figure 5e). As there is a correlation between viscoelastic properties and the number of cross-links,[63] these outcomes are due to the high density of reversible supramolecular bonds in the composite as a result of the dimerization functions of UPy.

For an additional rheological study, a second composite was produced using the same proportions of the CNF-*g*-UPy/UPy-DEGEEA composite but substituting the modified CNF with an unmodified CNF. The shear stress sweep, stress ramp, and rotational thixotropy have been measured and the results are shown in Figure S2. Unexpectedly, the viscosity of the gel is increased in comparison to the composite with CNF-*g*-UPy. Afterward, a measurement of the oscillating stress ramp was performed (Figure S2d). Both the storage modulus and the loss modulus of CNF-*g*-UPy/UPy-DEGEEA were increased. A 3.7-fold increase in G' and a 2.8-fold increase in G'' were measured. These results are in agreement with the previous results and demonstrate the enhanced mechanical properties of the composite caused by the high amount of cross-linking.

Differential Scanning Calorimetry (DSC). By successfully integrating several side chains of the UPy group into the composite structure, the number of hydrogen bonds present is expected to increase significantly. Hydrogen bonding is a noncovalent, reversible bond, which is dissociable by an external stimulus (force, heat, etc.).[64] Molecular chain motility is induced by increasing temperature, and the extent of movement is limited due to quadruple hydrogen bonds. As a result, UPy-grafted materials would be expected to have increased resistance to movement compared to nongrafted products. Therefore, thermal characterization of CNF, CNF-*g*-UPy, and UPy-DEGEEA was performed by DSC and the results are shown in Figure S3. This thermogram represents only the initial heating cycle from 25 to 250 °C. Following this initial run, all of the peaks present in the samples are no longer present (Figure S4). The presence of these peaks can be assigned to moisture and the occurrence of impurities, which is likely to correspond to the observed peak for the unmodified CNF. The decrease in melting enthalpy during subsequent heating cycles is most likely due to structural degradation. This effect has also been identified in several other studies.[65] Armstrong and his team performed IR analysis of the *N*-[(butylamino)carbonyl]-6-methylisocytosine samples after DSC analysis and noticed additional peaks, which correlate with the presence of ammonium ions indicative of degradation occurring during heating and cooling cycles.[66] Unmodified CNF shows no evidence of thermal transitions in the measured temperature range. The UPy function is present through the

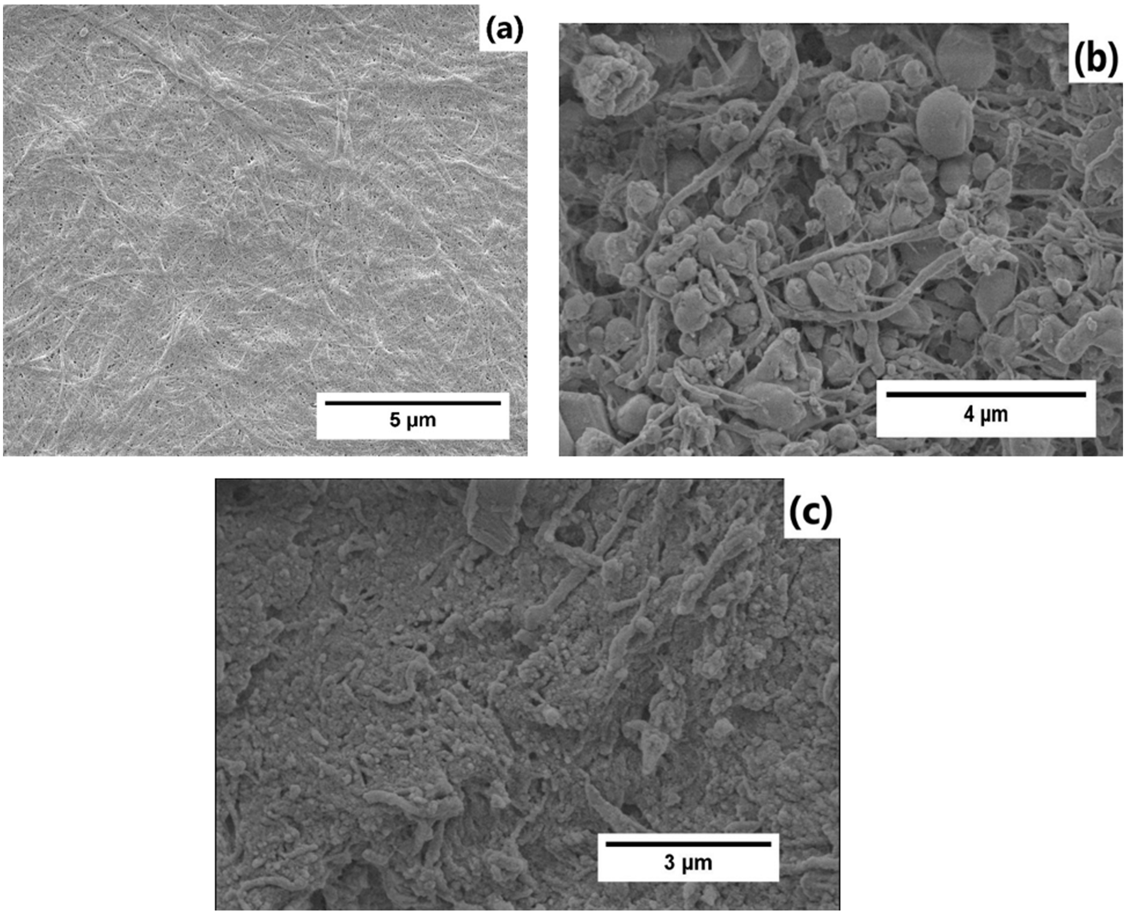

Figure 6. FE-SEM images of (a) CNF; (b) CNF-*g*-UPy; and (c) CNF-*g*-UPy/UPy-DEGEEA.

exothermic peak at 225 °C; this peak is present in the polymer as well as in the grafted CNF, which demonstrates its successful insertion. The 83 °C endothermic peak of the polymer surely corresponds to that of the ethylene glycol ethyl ether functions. Taken together, these transitions are indicative of the presence of polymeric species on the CNF surface since the CNF on its own does not exhibit any significant transition by DSC.

Morphological Analysis. To investigate the nanofibrillar morphology following chemical modification, each of the cellulose, CNF-*g*-UPy, and CNF-*g*-UPy/UPy-DEGEEA adducts have been characterized by field emission scanning electron microscopy (FE-SEM). An unmodified cellulose image (Figure 6a) reveals a dense network of aggregated fibrils. Multiple measurements of the size of the CNF diameter have been made, and the width range is between 20 and 60 nm. In Figure 6b, it is possible to observe a spacing between the nanocellulose fibers. Therefore, the presence of spherical shapes can be observed, likely caused by the aggregation of the UPy moiety. These patterns seem to be quite dispersed and cover most of the discernible fibers. In contrast, images of CNF-*g*-UPy/UPy-DEGEEA (Figure 6c) have significantly less distinguishable fiber structures, which suggests that they were successfully integrated into the polymer matrix. A few patterns from the previous observation are discernible but are not as prevalent. This is expected due to the proportion of CNF-*g*-UPy within the UPy-DEGEEA polymer. This result confirms that a change in the properties of the cellulose nanofibrils has occurred.

Printability of UPy-DEGEEA and CNF-*g*-UPy/UPy-DEGEEA. The main considerations for extrusion gel printing include the ability to print the gel and the structure's stability following the process of printing. Some gel inks necessitate additional secondary cross-linking following the impression.[67] In contrast, the CNF-*g*-UPy/UPy-DEGEEA gel requires no post-printing treatment. To characterize the print quality, two patterns have been designed. One consists of a part of a grid, while the second consists of a pattern with gradually increasing distances between each strand, ranging from 0.5 and 1 mm, to assess the merging of individual strands and the minimum interstrand distance (Figure S5a,c). The UPy-DEGEEA polymer was first tested for printing the models to assess its suitability for printing. However, the printing was not successful because of nozzle clogging even after dilutions, homogenization, and varying nozzle sizes. This can be explained by the formation of aggregates in the gel, rendering it nonprintable. Next, the CNF-*g*-Upy/Upy-DEGEEA composite has been printed with a 0.59 mm nozzle and the results are shown in Figure S5b,d. The partial grid was printed, showing defined strands without any structural collapse. This result is attributed to the improved rheological characteristics observed previously. In addition, fewer clogging events occurred, proving reduced clustering as a result of the better spacing of individual dimerizing moieties from the addition of CNF-*g*-Upy. Then, Figure S5d shows a zoomed photograph of the design printed using rhodamine B-stained CNF-*g*-Upy/Upy-DEGEEA (original photograph in Figure S6). No significant strand fusion has been observed in the 0.5 mm-separated

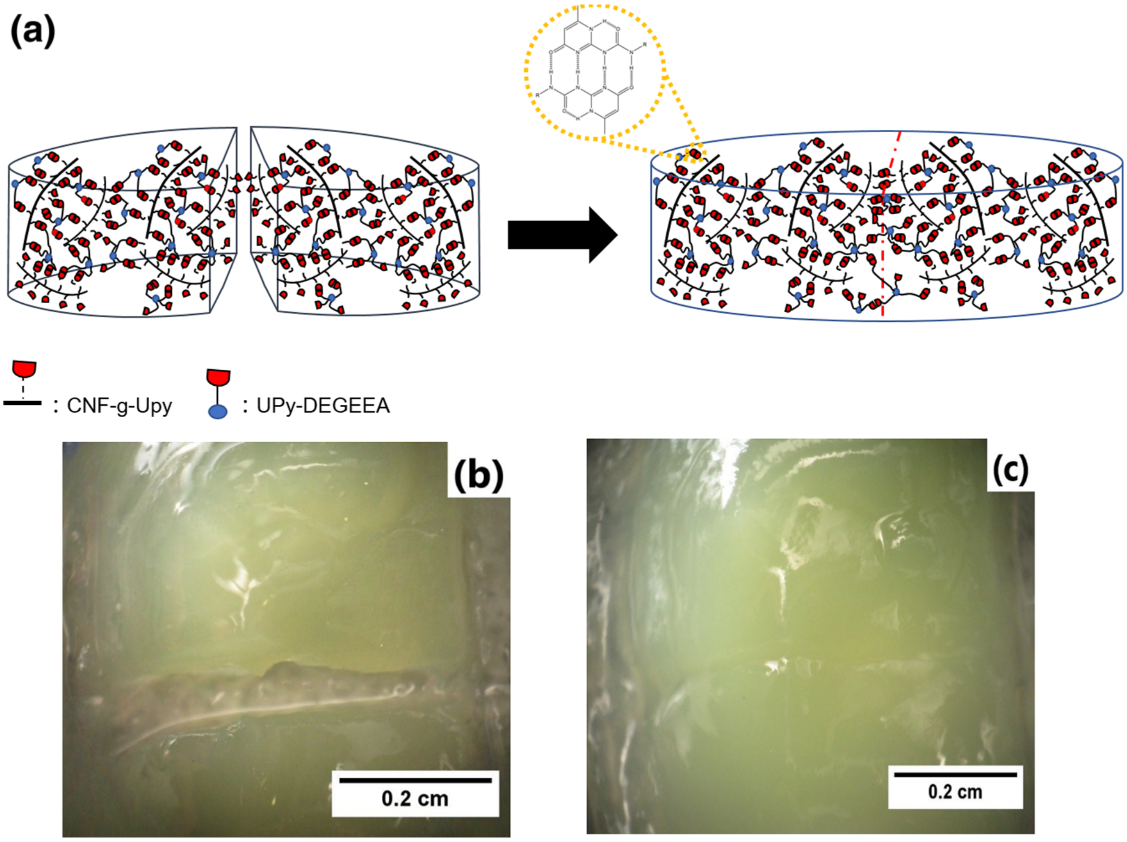

Figure 7. (a) Schematic presentation of the self-healing trial using the CNF-*g*-UPy/UPy-DEGEEA composite; (b) photograph of the gel ink CNF-*g*-UPy/UPy-DEGEEA that was cut prior to the self-healing process at room temperature; and (c) photograph of the gel after being heated to 80 °C for 5 min.

strands. These findings confirm the print capability of this composite and its suitability for pneumatic gel printing.

Characterization of the Self-Healing Property. Now that composite gels are proven to be suitable for printing, the self-healing character may be demonstrated. Preliminary studies were carried out on the UPy-DEGEEA polymer's self-healing capabilities, and the results are shown in Figure S7. A sample of the polymer was placed on an aluminum plate, split in two, and resealed after heating to 80 °C for about 2 min. The self-healing process can be seen to have occurred, but the whole of the structure has been altered. This is likely due to the poor structural properties of the gel which the addition of the modified cellulose is intended to remedy. This outcome is expected given the superior viscoelastic performance of the composite compared to the matrix. The gel "repair" mechanism is illustrated in Figure 7a. Before printing the models, it was necessary to conduct an experiment in order to verify the self-healing properties of the composite. For this purpose, a portion of the gel was deposited on a glass sheet and sectioned into two pieces. The composite was placed on a heated plate at 80 °C for 5 min, and the pre- and post-experiment photographs are shown in Figure 7b,c. As a result of the heating, it can be seen that the two portions have been merged without fluidization and that the cut has been restored, even though the cut is still visible. Now that the self-healing character has been demonstrated, we can print both models and put them back together.

To have a more meaningful and visible result, it was decided that two identical half-arrows be printed, which, after self-healing, would make a complete arrow. Both patterns were designed, and they were gel-printed (Figure 8a,b). One of the gels was dyed with rhodamine B for better observation. From this, the gel's good printing and superior quality of impression can be assessed. Afterward, the resulting gels were flash-frozen for transport and laid side by side, ready for self-healing (Figure 8c). These were then brought together and placed on a heating plate at 80 °C for 2 min, and the result is shown in Figure 8d. The self-healing was successful, and the arrow structure was not affected by the heating.

For closer observation of the self-healing mechanism, two strands of each composite gel were deposited on a glass plate, with the undyed gel on top of the stained gel, to be observed under an optical microscope. The microscope slide was placed on a heating bed, heated from 25 to 80 °C, and then cooled to 40 °C. The whole experiment has been recorded and the time-lapse video is available in the Supporting Information. Photographs that were captured during the experiment at different moments are presented in Figure S8. The first notable feature is the change in transparency with heating, where the gels become translucent in comparison to their initial opaque appearance. This shift takes place at a temperature around 80 °C, and it goes back to opaque after decreasing the temperature. The decrease in supramolecular interaction, therefore, leads to a greater degree of molecular mobility, which is associated with a change in the material's optical properties and light transmittance.[68] This high mobility also allows for new molecular rearrangement among different moieties upon recovery to room temperature. This is supported by the opaque reappearance after cooling. This shows the expected increase in molecular mobility. The

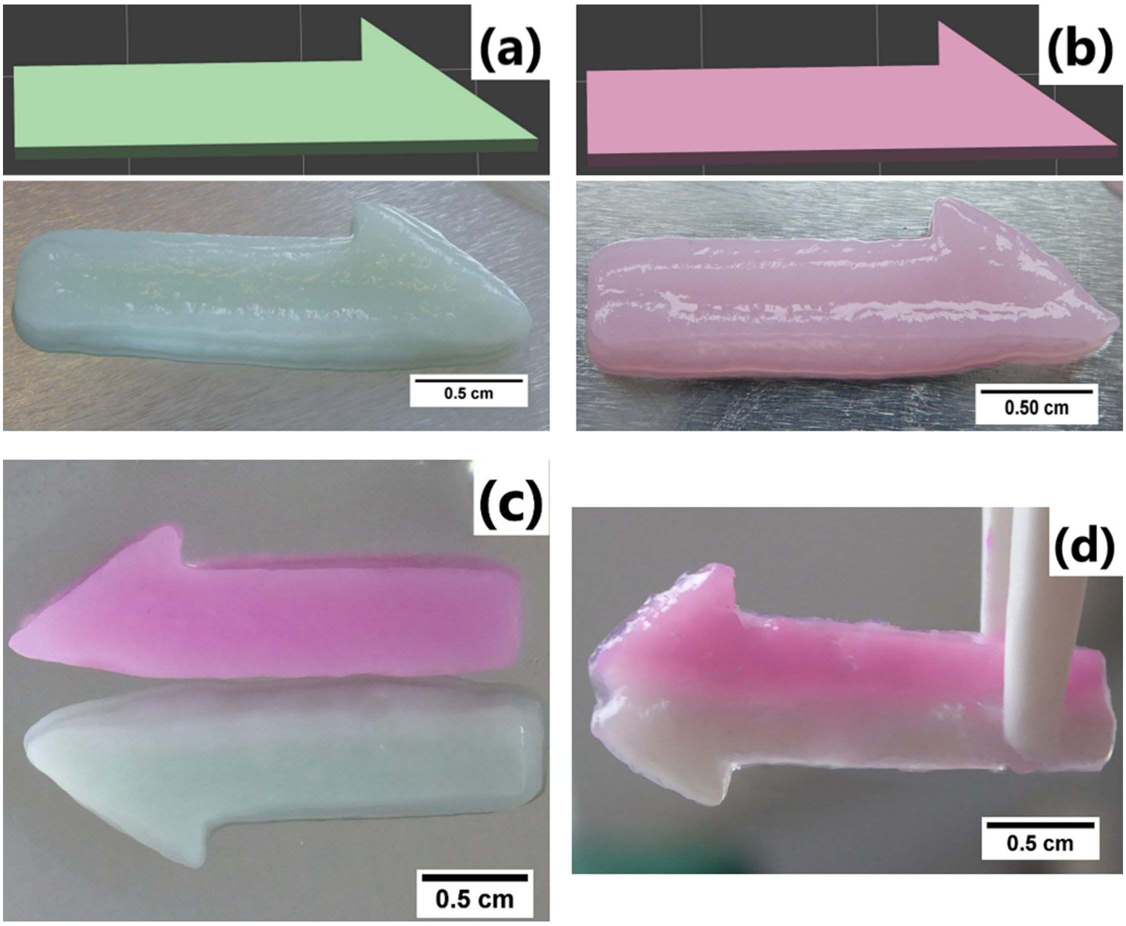

Figure 8. Templates of half-arrows at the top and pictures of the printed templates at the bottom; the greenish gel corresponds to the unstained gel and pink is the rhodamine B-stained gel (a, b); pictures of the two half-arrows frozen and laid side by side (c); the picture of the resulting arrow formed after the joined half-arrows were heated to 80 °C for 2 min. After completing the self-healing process, the new reformed arrow was frozen for better handling with a tweezer (d).

extremities of the two bands are less pronounced. Furthermore, the coloration is no longer as strong as at the beginning, indicating diffusion of the dye (rhodamine B) between the two gels.

CONCLUSIONS

In summary, CNF grafted with ureidopyrimidinone moieties (CNF-*g*-UPy) was found to be an effective print performance-enhancing additive to produce a hyper-cross-linked, injectable, and heat-induced self-healing gel based on a ureidopyrimidinone (UPy) and di(ethylene glycol) ethyl ether (DEGEEA) supramolecular copolymer. The gel is suitable for 3D gel printing with no additional cross-linking post-printing or reinforcing and provides a targeted application for self-healing. First, the monomer was successfully obtained after one synthesis step with a 92% yield. Surface modification of cellulose nanofibrils was carried out efficiently by first achieving the nanocellulose-based macroinitiator (CNF-MI) and then the grafted cellulose with the UPy (CNF-*g*-UPy) units. A matrix copolymer was successfully produced by UPy with DEGEEA moieties. Successful grafting was demonstrated through DSC analysis. The enhancement of the mechanical properties has been demonstrated by rheological measurements. Successful modification of the CNF was well observed by SEM, along with the effective incorporation into the polymer. The printability of the composite was assessed by printing specific models. These trials proved the superior capability of the composite and its suitability for gel 3D printing. Ultimately, the self-healing properties were confirmed by bonding two preprinted half-arrows together after about 2 min at 80 °C with no additional treatment. An experiment with an optical microscope was done for a better observation of self-healing.

ASSOCIATED CONTENT

Supporting Information

The Supporting Information is available free of charge at https://pubs.acs.org/doi/10.1021/acsapm.2c02065.

ATR-FTIR spectrum of the pristine UPY monomer and UPY-DEGEEA polymer; rheology measurement comparison of pristine CNF in UPy-DEGEEA and CNF-*g*-UPy/UPy-DEGEEA; DSC measurement; pictures of the gel ink shape fidelity test; and self-healing test of the DEGEEA-UPY polymer (PDF)

Time-lapse video (MP4)

AUTHOR INFORMATION

Corresponding Author

Julien R. G. Navarro − *Institute of Wood Science, University Hamburg, 21031 Hamburg, Germany;* orcid.org/0000-0001-8791-6190; Email: Julien.navarro@uni-hamburg.de

Authors

Feras Dalloul − *Institute of Wood Science, University Hamburg, 21031 Hamburg, Germany*

J. Benedikt Mietner − *Institute of Wood Science, University Hamburg, 21031 Hamburg, Germany*

Complete contact information is available at: https://pubs.acs.org/10.1021/acsapm.2c02065

Funding

We would like to express our thanks to the Fachagentur Nachwachsende Rohstoffe e.V. (FNR/BMEL, HolzMat3D project, number 2220HV024X) for their financial support.

Notes

The authors declare no competing financial interest.

■ ACKNOWLEDGMENTS

We would like to thank the Thünen-Institut für Holzforschung for enabling us to make the rheology and differential scanning calorimetry measurements. We would like to thank MSE Supplies for the SEM images.

■ REFERENCES

(1) Kačarević, Ž.; Rider, P.; Alkildani, S.; Retnasingh, S.; Smeets, R.; Jung, O.; Ivanišević, Z.; Barbeck, M. An Introduction to 3D Bioprinting: Possibilities, Challenges and Future Aspects. *Materials* **2018**, *11*, No. 2199.

(2) Hoch, E.; Tovar, G. E. M.; Borchers, K. Bioprinting of Artificial Blood Vessels: Current Approaches towards a Demanding Goal. *Eur. J. Cardio-Thoracic Surg.* **2014**, *46*, 767−778.

(3) Ong, C. S.; Fukunishi, T.; Zhang, H.; Huang, C. Y.; Nashed, A.; Blazeski, A.; DiSilvestre, D.; Vricella, L.; Conte, J.; Tung, L.; Tomaselli, G. F.; Hibino, N. Biomaterial-Free Three-Dimensional Bioprinting of Cardiac Tissue Using Human Induced Pluripotent Stem Cell Derived Cardiomyocytes. *Sci. Rep.* **2017**, *7*, No. 4566.

(4) Chimene, D.; Miller, L.; Cross, L. M.; Jaiswal, M. K.; Singh, I.; Gaharwar, A. K. Nanoengineered Osteoinductive Bioink for 3D Bioprinting Bone Tissue. *ACS Appl. Mater. Interfaces* **2020**, *12*, 15976−15988.

(5) Augustine, R. Skin Bioprinting: A Novel Approach for Creating Artificial Skin from Synthetic and Natural Building Blocks. *Prog. Biomater.* **2018**, *7*, 77−92.

(6) Malekpour, A.; Chen, X. Printability and Cell Viability in Extrusion-Based Bioprinting from Experimental, Computational, and Machine Learning Views. *J. Funct. Biomater.* **2022**, *13*, No. 40.

(7) Gillispie, G.; Prim, P.; Copus, J.; Fisher, J.; Mikos, A. G.; Yoo, J. J.; Atala, A.; Lee, S. J. Assessment Methodologies for Extrusion-Based Bioink Printability. *Biofabrication* **2020**, *12*, No. 022003.

(8) Theus, A. S.; Ning, L.; Hwang, B.; Gil, C.; Chen, S.; Wombwell, A.; Mehta, R.; Serpooshan, V. Bioprintability: Physiomechanical and Biological Requirements of Materials for 3D Bioprinting Processes. *Polymers* **2020**, *12*, No. 2262.

(9) Stichler, S.; Bertlein, S.; Tessmar, J.; Jüngst, T.; Groll, J. Thiol-Ene Cross-Linkable Hydrogels as Bioinks for Biofabrication. *Macromol. Symp.* **2017**, *372*, 102−107.

(10) Le Thi, P.; Son, J. Y.; Lee, Y.; Ryu, S. B.; Park, K. M.; Park, K. D. Enzymatically Crosslinkable Hyaluronic Acid-Gelatin Hybrid Hydrogels as Potential Bioinks for Tissue Regeneration. *Macromol. Res.* **2020**, *28*, 400−406.

(11) Kesti, M.; Müller, M.; Becher, J.; Schnabelrauch, M.; D'Este, M.; Eglin, D.; Zenobi-Wong, M. A Versatile Bioink for Three-Dimensional Printing of Cellular Scaffolds Based on Thermally and Photo-Triggered Tandem Gelation. *Acta Biomater.* **2015**, *11*, 162−172.

(12) Bian, L. Functional Hydrogel Bioink, a Key Challenge of 3D Cellular Bioprinting. *APL Bioeng.* **2020**, *4*, No. 030401.

(13) Khoeini, R.; Nosrati, H.; Akbarzadeh, A.; Eftekhari, A.; Kavetskyy, T.; Khalilov, R.; Ahmadian, E.; Nasibova, A.; Datta, P.; Roshangar, L.; Deluca, D. C.; Davaran, S.; Cucchiarini, M.; Ozbolat, I. T. Natural and Synthetic Bioinks for 3D Bioprinting. *Adv. NanoBiomed Res.* **2021**, *1*, No. 2000097.

(14) Skardal, A.; Zhang, J.; Prestwich, G. D. Bioprinting Vessel-like Constructs Using Hyaluronan Hydrogels Crosslinked with Tetrahedral Polyethylene Glycol Tetracrylates. *Biomaterials* **2010**, *31*, 6173−6181.

(15) Utrera-Barrios, S.; Verdejo, R.; López-Manchado, M. A.; Hernández Santana, M. Evolution of Self-Healing Elastomers, from Extrinsic to Combined Intrinsic Mechanisms: A Review. *Mater. Horiz.* **2020**, *7*, 2882−2902.

(16) Zhong, N.; Post, W. Self-Repair of Structural and Functional Composites with Intrinsically Self-Healing Polymer Matrices: A Review. *Composites, Part A* **2015**, *69*, 226−239.

(17) Guo, H.; Han, Y.; Zhao, W.; Yang, J.; Zhang, L. Universally Autonomous Self-Healing Elastomer with High Stretchability. *Nat. Commun.* **2020**, *11*, No. 2037.

(18) Almutairi, M. D.; Aria, A. I.; Thakur, V. K.; Khan, M. A. Self-Healing Mechanisms for 3D-Printed Polymeric Structures: From Lab to Reality. *Polymers* **2020**, *12*, No. 1534.

(19) Billiet, S.; Hillewaere, X. K. D.; Teixeira, R. F. A.; Du Prez, F. E. Chemistry of Crosslinking Processes for Self-Healing Polymers. *Macromol. Rapid Commun.* **2013**, *34*, 290−309.

(20) Syrett, J. A.; Becer, C. R.; Haddleton, D. M. Self-Healing and Self-Mendable Polymers. *Polym. Chem.* **2010**, *1*, 978−987.

(21) Chirila, T. V.; Lee, H. H.; Oddon, M.; Nieuwenhuizen, M. M. L.; Blakey, I.; Nicholson, T. M. Hydrogen-Bonded Supramolecular Polymers as Self-Healing Hydrogels: Effect of a Bulky Adamantyl Substituent in the Ureido-Pyrimidinone Monomer. *J. Appl. Polym. Sci.* **2014**, *131*, No. 39932.

(22) Biyani, M. V.; Foster, E. J.; Weder, C. Light-Healable Supramolecular Nanocomposites Based on Modified Cellulose Nanocrystals. *ACS Macro Lett.* **2013**, *2*, 236−240.

(23) Zhu, B.; Merindol, R.; Benitez, A. J.; Wang, B.; Walther, A. Supramolecular Engineering of Hierarchically Self-Assembled, Bioinspired, Cholesteric Nanocomposites Formed by Cellulose Nanocrystals and Polymers. *ACS Appl. Mater. Interfaces* **2016**, *8*, 11031−11040.

(24) Amaral, A. J. R.; Pasparakis, G. Stimuli Responsive Self-Healing Polymers: Gels, Elastomers and Membranes. *Polym. Chem.* **2017**, *8*, 6464−6484.

(25) Zhang, G.; Ngai, T.; Deng, Y.; Wang, C. An Injectable Hydrogel with Excellent Self-Healing Property Based on Quadruple Hydrogen Bonding. *Macromol. Chem. Phys.* **2016**, *217*, 2172−2181.

(26) Mouser, V. H. M.; Abbadessa, A.; Levato, R.; Hennink, W. E.; Vermonden, T.; Gawlitta, D.; Malda, J. Development of a Thermosensitive HAMA-Containing Bio-Ink for the Fabrication of Composite Cartilage Repair Constructs. *Biofabrication* **2017**, *9*, No. 015026.

(27) Santoni, S.; Sponchioni, M.; Gugliandolo, S. G.; Colosimo, B. M.; Moscatelli, D. Preliminary Tests on PEG-Based Thermoresponsive Polymers for the Production of 3D Bioprinted Constructs. *Procedia CIRP* **2022**, *110*, 348−353.

(28) Pitton, M.; Fiorati, A.; Buscemi, S.; Melone, L.; Farè, S.; Contessi Negrini, N. 3D Bioprinting of Pectin-Cellulose Nanofibers Multicomponent Bioinks. *Front. Bioeng. Biotechnol.* **2021**, *9*, No. 732689.

(29) Navarro, J. R. G.; Rostami, J.; Ahlinder, A.; Mietner, J. B.; Bernin, D.; Saake, B.; Edlund, U. Surface-Initiated Controlled Radical Polymerization Approach to in Situ Cross-Link Cellulose Nanofibrils with Inorganic Nanoparticles. *Biomacromolecules* **2020**, *21*, 1952−1961.

(30) Navarro, J. R. G.; Edlund, U. Surface-Initiated Controlled Radical Polymerization Approach To Enhance Nanocomposite Integration of Cellulose Nanofibrils. *Biomacromolecules* **2017**, *18*, 1947−1955.

(31) Dani, S.; Ahlfeld, T.; Albrecht, F.; Duin, S.; Kluger, P.; Lode, A.; Gelinsky, M. Homogeneous and Reproducible Mixing of Highly Viscous Biomaterial Inks and Cell Suspensions to Create Bioinks. *Gels* **2021**, *7*, No. 227.

(32) Sijbesma, R. P.; Beijer, F. H.; Brunsveld, L.; Folmer, B. J. B.; Hirschberg, J. H. K. K.; Lange, R. F. M.; Lowe, J. K. L.; Meijer, E. W. Reversible Polymers Formed from Self-Complementary Monomers Using Quadruple Hydrogen Bonding. *Science* **1997**, *278*, 1601−1604.

(33) Beijer, F. H.; Sijbesma, R. P.; Kooijman, H.; Spek, A. L.; Meijer, E. W. Strong Dimerization of Ureidopyrimidones via Quadruple Hydrogen Bonding. *J. Am. Chem. Soc.* **1998**, *120*, 6761−6769.

(34) Wu, Y.; Wang, L.; Zhao, X.; Hou, S.; Guo, B.; Ma, P. X. Self-Healing Supramolecular Bioelastomers with Shape Memory Property as a Multifunctional Platform for Biomedical Applications via Modular Assembly. *Biomaterials* **2016**, *104*, 18−31.

(35) Yan, J.; Li, M.; Wang, Z.; Chen, C.; Ma, C.; Yang, G. Highly Tough, Multi-Stimuli-Responsive, and Fast Self-Healing Supramolecular Networks toward Strain Sensor Application. *Chem. Eng. J.* **2020**, *389*, No. 123468.

(36) Doench, I.; Torres-Ramos, M.; Montembault, A.; Nunes de Oliveira, P.; Halimi, C.; Viguier, E.; Heux, L.; Siadous, R.; Thiré, R.; Osorio-Madrazo, A. Injectable and Gellable Chitosan Formulations Filled with Cellulose Nanofibers for Intervertebral Disc Tissue Engineering. *Polymers* **2018**, *10*, No. 1202.

(37) Kobe, R.; Yoshitani, K.; Teramoto, Y. Fabrication of Elastic Composite Hydrogels Using Surface-Modified Cellulose Nanofiber as a Multifunctional Crosslinker. *J. Appl. Polym. Sci.* **2016**, *133*, No. 42906.

(38) Li, N.; Chen, W.; Chen, G.; Tian, J. Rapid Shape Memory TEMPO-Oxidized Cellulose Nanofibers/Polyacrylamide/Gelatin Hydrogels with Enhanced Mechanical Strength. *Carbohydr. Polym.* **2017**, *171*, 77−84.

(39) Bensabeh, N.; Ronda, J. C.; Galià, M.; Cádiz, V.; Lligadas, G.; Percec, V. SET-LRP of the Hydrophobic Biobased Menthyl Acrylate. *Biomacromolecules* **2018**, *19*, 1256−1268.

(40) Murali, A.; Sampath, S.; Appukutti Achuthan, B.; Sakar, M.; Chandrasekaran, S.; Suthanthira Vanitha, N.; Joseph Bensingh, R.; Abdul Kader, M.; Jaisankar, S. N. Copper (0) Mediated Single Electron Transfer-Living Radical Polymerization of Methyl Methacrylate: Functionalized Graphene as a Convenient Tool for Radical Initiator. *Polymers* **2020**, *12*, No. 874.

(41) Kono, H.; Yunoki, S.; Shikano, T.; Fujiwara, M.; Erata, T.; Takai, M. CP/MAS 13C NMR Study of Cellulose and Cellulose Derivatives. 1. Complete Assignment of the CP/MAS 13C NMR Spectrum of the Native Cellulose. *J. Am. Chem. Soc.* **2002**, *124*, 7506−7511.

(42) Syverud, K.; Pettersen, S. R.; Draget, K.; Chinga-Carrasco, G. Controlling the Elastic Modulus of Cellulose Nanofibril Hydrogels—Scaffolds with Potential in Tissue Engineering. *Cellulose* **2015**, *22*, 473−481.

(43) Mietner, J. B.; Jiang, X.; Edlund, U.; Saake, B.; Navarro, J. R. G. 3D Printing of a Bio-Based Ink Made of Cross-Linked Cellulose Nanofibrils with Various Metal Cations. *Sci. Rep.* **2021**, *11*, No. 6461.

(44) Guo, M.; Pitet, L. M.; Wyss, H. M.; Vos, M.; Dankers, P. Y. W.; Meijer, E. W. Tough Stimuli-Responsive Supramolecular Hydrogels with Hydrogen-Bonding Network Junctions. *J. Am. Chem. Soc.* **2014**, *136*, 6969−6977.

(45) You, Y.; Yang, J.; Zheng, Q.; Wu, N.; Lv, Z.; Jiang, Z. Ultra-Stretchable Hydrogels with Hierarchical Hydrogen Bonds. *Sci. Rep.* **2020**, *10*, No. 11727.

(46) Zhu, D.; Ye, Q.; Lu, X.; Lu, Q. Self-Healing Polymers with PEG Oligomer Side Chains Based on Multiple H-Bonding and Adhesion Properties. *Polym. Chem.* **2015**, *6*, 5086−5092.

(47) Noro, A.; Hayashi, M.; Matsushita, Y. Design and Properties of Supramolecular Polymer Gels. *Soft Matter* **2012**, *8*, 6416.

(48) Seiffert, S. *Supramolecular Polymer Networks and Gels*; Springer, 2015.

(49) Ahn, S.-k.; Kasi, R. M.; Kim, S.-C.; Sharma, N.; Zhou, Y. Stimuli-Responsive Polymer Gels. *Soft Matter* **2008**, *4*, 1151.

(50) Kesti, M.; Fisch, P.; Pensalfini, M.; Mazza, E.; Zenobi-Wong, M. Guidelines for Standardization of Bioprinting: A Systematic Study of Process Parameters and Their Effect on Bioprinted Structures. *BioNanoMaterials* **2016**, *17*, 193.

(51) Loebel, C.; Rodell, C. B.; Chen, M. H.; Burdick, J. A. Shear-Thinning and Self-Healing Hydrogels as Injectable Therapeutics and for 3D-Printing. *Nat. Protoc.* **2017**, *12*, 1521−1541.

(52) Zhang, G.; Lv, L.; Deng, Y.; Wang, C. Self-Healing Gelatin Hydrogels Cross-Linked by Combining Multiple Hydrogen Bonding and Ionic Coordination. *Macromol. Rapid Commun.* **2017**, *38*, No. 1700018.

(53) Mol, E. A.; Lei, Z.; Roefs, M. T.; Bakker, M. H.; Goumans, M.; Doevendans, P. A.; Dankers, P. Y. W.; Vader, P.; Sluijter, J. P. G. Injectable Supramolecular Ureidopyrimidinone Hydrogels Provide Sustained Release of Extracellular Vesicle Therapeutics. *Adv. Healthcare Mater.* **2019**, *8*, No. 1900847.

(54) Hou, S.; Wang, X.; Park, S.; Jin, X.; Ma, P. X. Rapid Self-Integrating, Injectable Hydrogel for Tissue Complex Regeneration. *Adv. Healthcare Mater.* **2015**, *4*, 1491−1495.

(55) Paxton, N.; Smolan, W.; Böck, T.; Melchels, F.; Groll, J.; Jungst, T. Proposal to Assess Printability of Bioinks for Extrusion-Based Bioprinting and Evaluation of Rheological Properties Governing Bioprintability. *Biofabrication* **2017**, *9*, No. 044107.

(56) Schwab, A.; Levato, R.; D'Este, M.; Piluso, S.; Eglin, D.; Malda, J. Printability and Shape Fidelity of Bioinks in 3D Bioprinting. *Chem. Rev.* **2020**, *120*, 11028−11055.

(57) Haider, M. S.; Ahmad, T.; Yang, M.; Hu, C.; Hahn, L.; Stahlhut, P.; Groll, J.; Luxenhofer, R. Tuning the Thermogelation and Rheology of Poly(2-Oxazoline)/Poly(2-Oxazine)s Based Thermosensitive Hydrogels for 3D Bioprinting. *Gels* **2021**, *7*, No. 78.

(58) Martorana, A.; Pitarresi, G.; Palumbo, F. S.; Barberi, G.; Fiorica, C.; Giammona, G. Correlating Rheological Properties of a Gellan Gum-Based Bioink: A Study of the Impact of Cell Density. *Polymers* **2022**, *14*, No. 1844.

(59) Siqueira, G.; Kokkinis, D.; Libanori, R.; Hausmann, M. K.; Gladman, A. S.; Neels, A.; Tingaut, P.; Zimmermann, T.; Lewis, J. A.; Studart, A. R. Cellulose Nanocrystal Inks for 3D Printing of Textured Cellular Architectures. *Adv. Funct. Mater.* **2017**, *27*, No. 1604619.

(60) Jiang, J.; Oguzlu, H.; Jiang, F. 3D Printing of Lightweight, Super-Strong yet Flexible All-Cellulose Structure. *Chem. Eng. J.* **2021**, *405*, No. 126668.

(61) Donley, G. J.; Singh, P. K.; Shetty, A.; Rogers, S. A. Elucidating the G″ Overshoot in Soft Materials with a Yield Transition via a Time-Resolved Experimental Strain Decomposition. *Proc. Natl. Acad. Sci. U.S.A.* **2020**, *117*, 21945−21952.

(62) Dinkgreve, M.; Paredes, J.; Denn, M. M.; Bonn, D. On Different Ways of Measuring "the" Yield Stress. *J. Non-Newtonian Fluid Mech.* **2016**, *238*, 233−241.

(63) Song, G.; Zhao, Z.; Peng, X.; He, C.; Weiss, R. A.; Wang, H. Rheological Behavior of Tough PVP- in Situ -PAAm Hydrogels Physically Cross-Linked by Cooperative Hydrogen Bonding. *Macromolecules* **2016**, *49*, 8265−8273.

(64) Tang, X. C.; Pikal, M. J.; Taylor, L. S. The Effect of Temperature on Hydrogen Bonding in Crystalline and Amorphous Phases in Dihydropyrine Calcium Channel Blockers. *Pharm. Res.* **2002**, *19*, 484−490.

(65) van Beek, D. J. M.; Spiering, A. J. H.; Peters, G. W. M.; te Nijenhuis, K.; Sijbesma, R. P. Unidirectional Dimerization and Stacking of Ureidopyrimidinone End Groups in Polycaprolactone Supramolecular Polymers. *Macromolecules* **2007**, *40*, 8464−8475.

(66) Armstrong, G.; Buggy, M. Thermal Stability of a Ureidopyrimidinone Model Compound. *Mater. Sci. Eng., C* **2001**, *18*, 45−49.

(67) Ouyang, L.; Highley, C. B.; Rodell, C. B.; Sun, W.; Burdick, J. A. 3D Printing of Shear-Thinning Hyaluronic Acid Hydrogels with Secondary Cross-Linking. *ACS Biomater. Sci. Eng.* **2016**, *2*, 1743−1751.

(68) Boztepe, S.; Gilblas, R.; de Almeida, O.; Gerlach, C.; Le Maoult, Y.; Schmidt, F. The Role of Microcrystalline Structure on Optical Scattering Characteristics of Semi-Crystalline Thermoplastics

and the Accuracy of Numerical Input for IR-Heating Modeling. *Int. J. Mater. Form.* **2018**, *11*, 717−727.

Supporting Information

3D printing of a tough polymer composite gel Ink reinforced with chemically modified cellulose nanofibrils showing self-healing behaviour.

Feras Dalloul, J. Benedikt Mietner and Julien R. G. Navarro*

Institute of Wood Science, University Hamburg, Leuschnerstraße 91, 21031 Hamburg, Germany

* Correspondence: julien.navarro@uni-hamburg.de

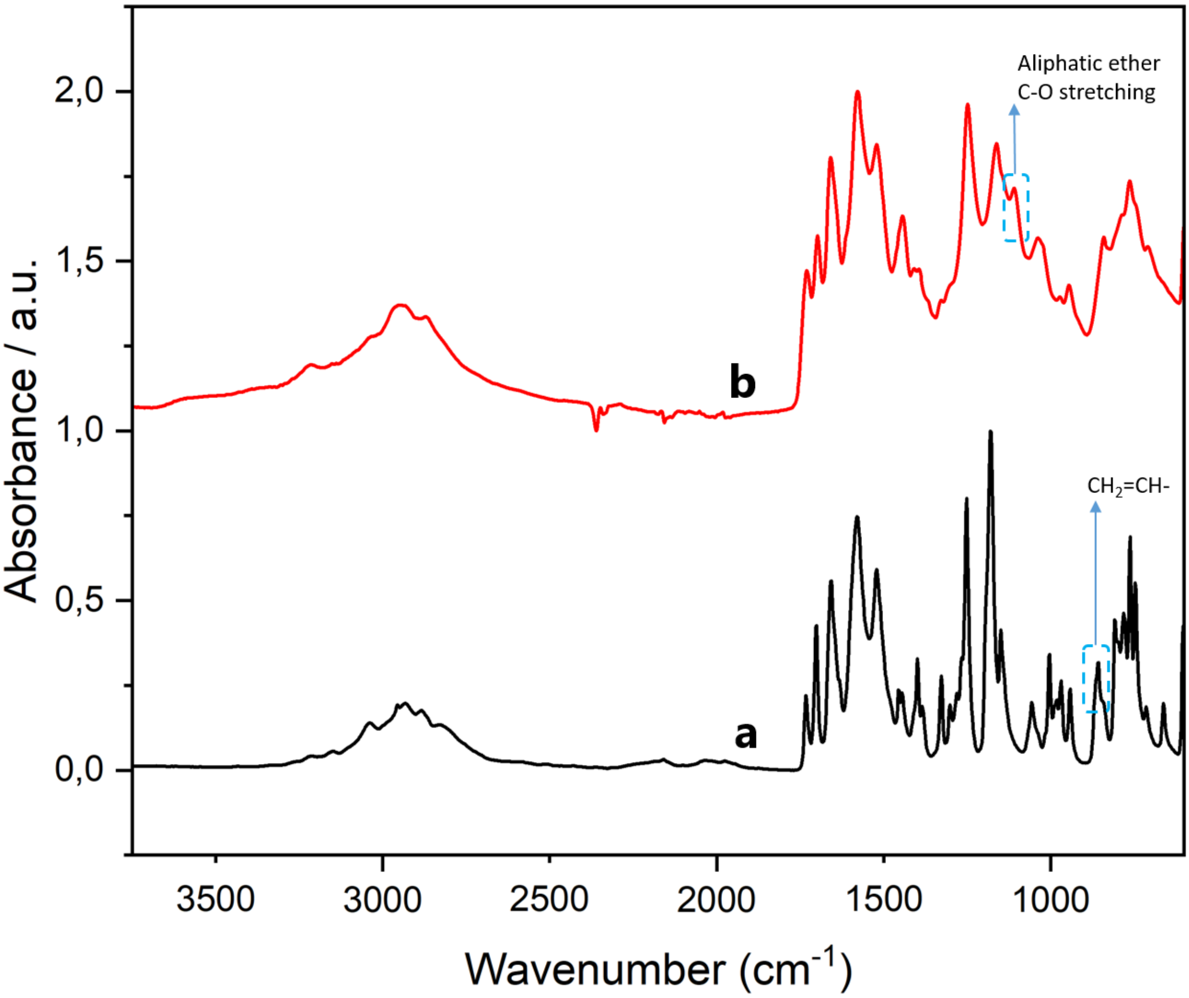

Figure S1: ATR-FTIR spectrum of pristine (a) UPY monomer and (b) UPY-DEGEEA polymer

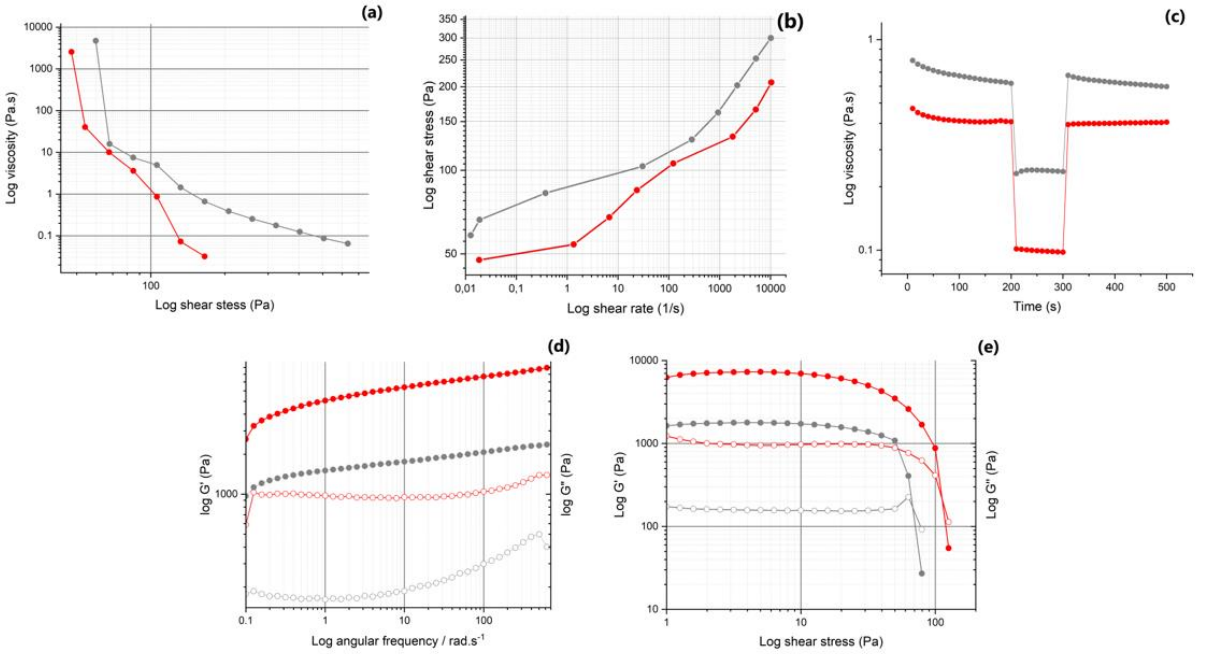

Figure S2: (a) Shear stress ramp data; (b) Flow curves (shear stress vs shear rate); (c) Recovery tests demonstrate the ability of materials to quickly recover their initial viscosity from high shear rates to near zero shear to simulate conditions experienced during extrusion printing; (d) Frequency spectra of dynamic modules with a steady increase of the angular frequency applied; (e) Dynamic modulus under increasing stress to determine yield stress; Samples colours code: red: CNF-g-UPy/UPy-DEGEEA; grey: CNF/UPy-DEGEEA. For viscoelastic properties, G' values are represented with full symbols and G'' with open symbols

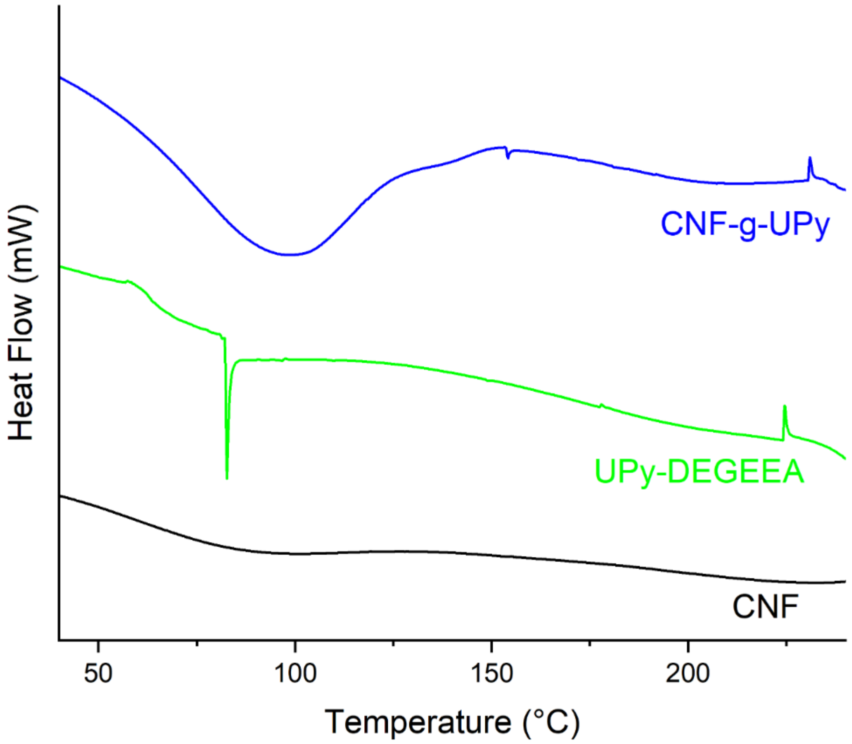

Figure S3: DSC thermograms recorded during heating of unmodified CNF, CNF-g-UPy, UPy-DEGEEA polymer

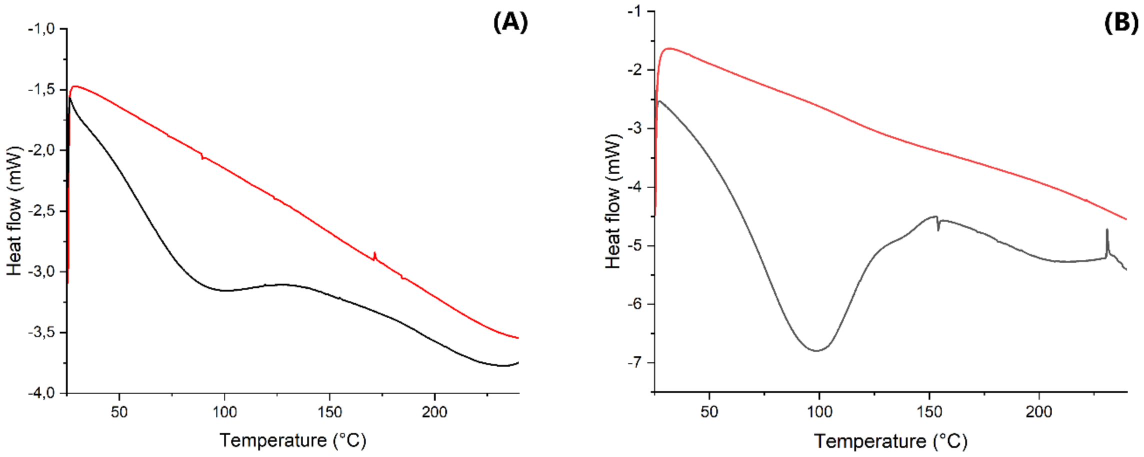

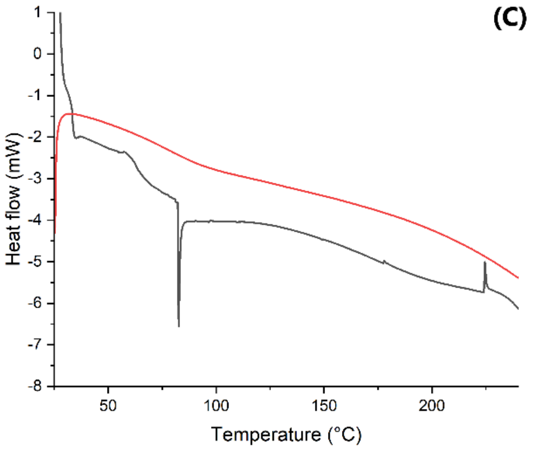

Figure S4. DSC thermograms were recorded during the first (in black) and second heating (in red) of unmodified CNF (a), CNF-g-UPY (b), and UPY-DEGEEA polymer (c).

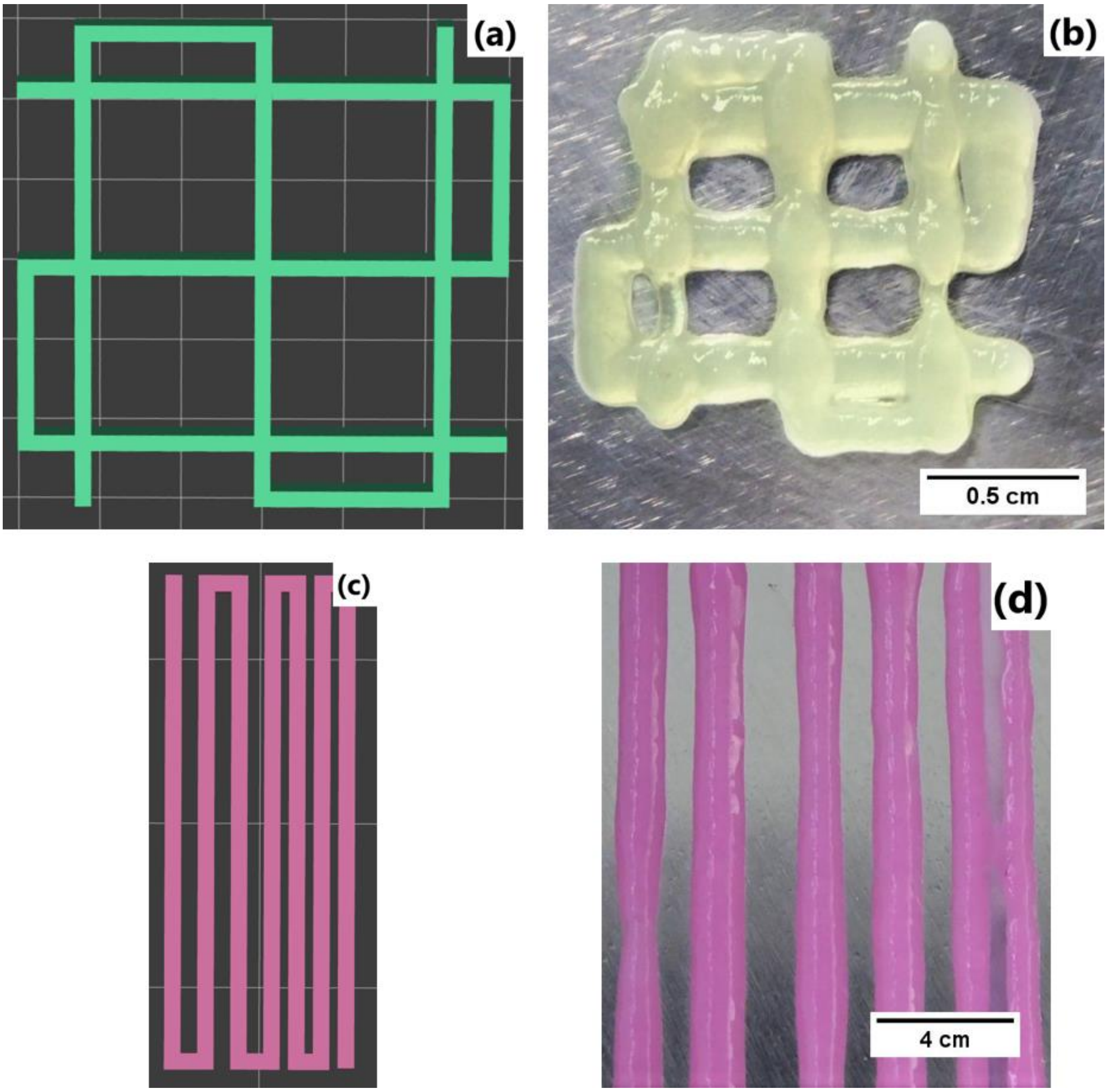

Figure S5: (a) 3D grid model composed of one layer of 15 x 15 mm with orthogonal strands; (b) Picture of the printed model using CNF-g-UPy/UPy-DEGEEA composite; (c) 3D models of a 12 x 30 mm layer, to evaluate minimal distance between the strands and gel-ink shape fidelity; (d) Zoomed picture of the printed model using CNF-g-UPy/UPy-DEGEEA composite

Figure S6. Picture of the printed model of a pattern with gradually increasing distances (0,5 and 1 mm between strands) using CNF-g-UPY/UPY-DEGEEA composite

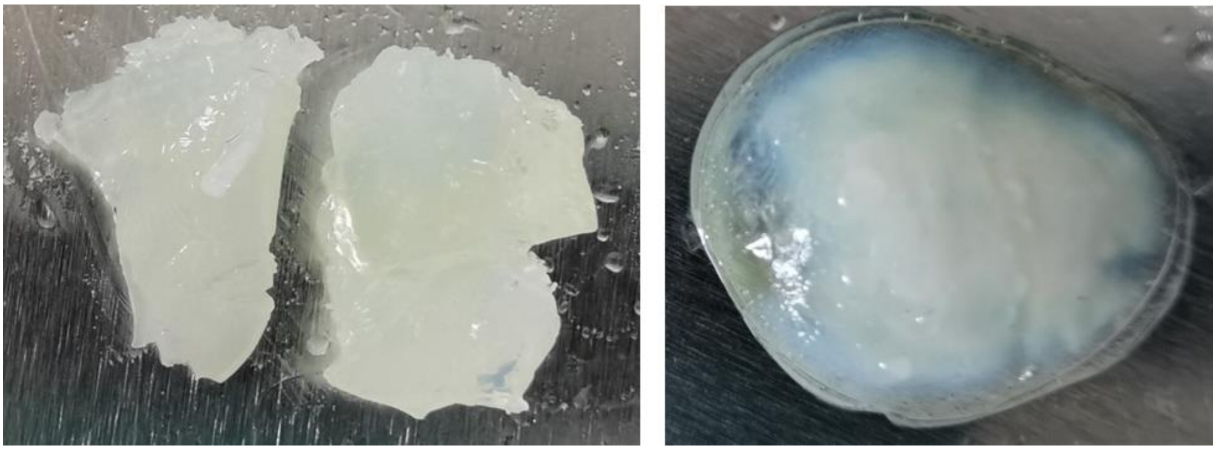

Figure S7. Picture of DEGEEA-UPY sample before heating at 80°C for 2 minutes (left), and after the heating (right)

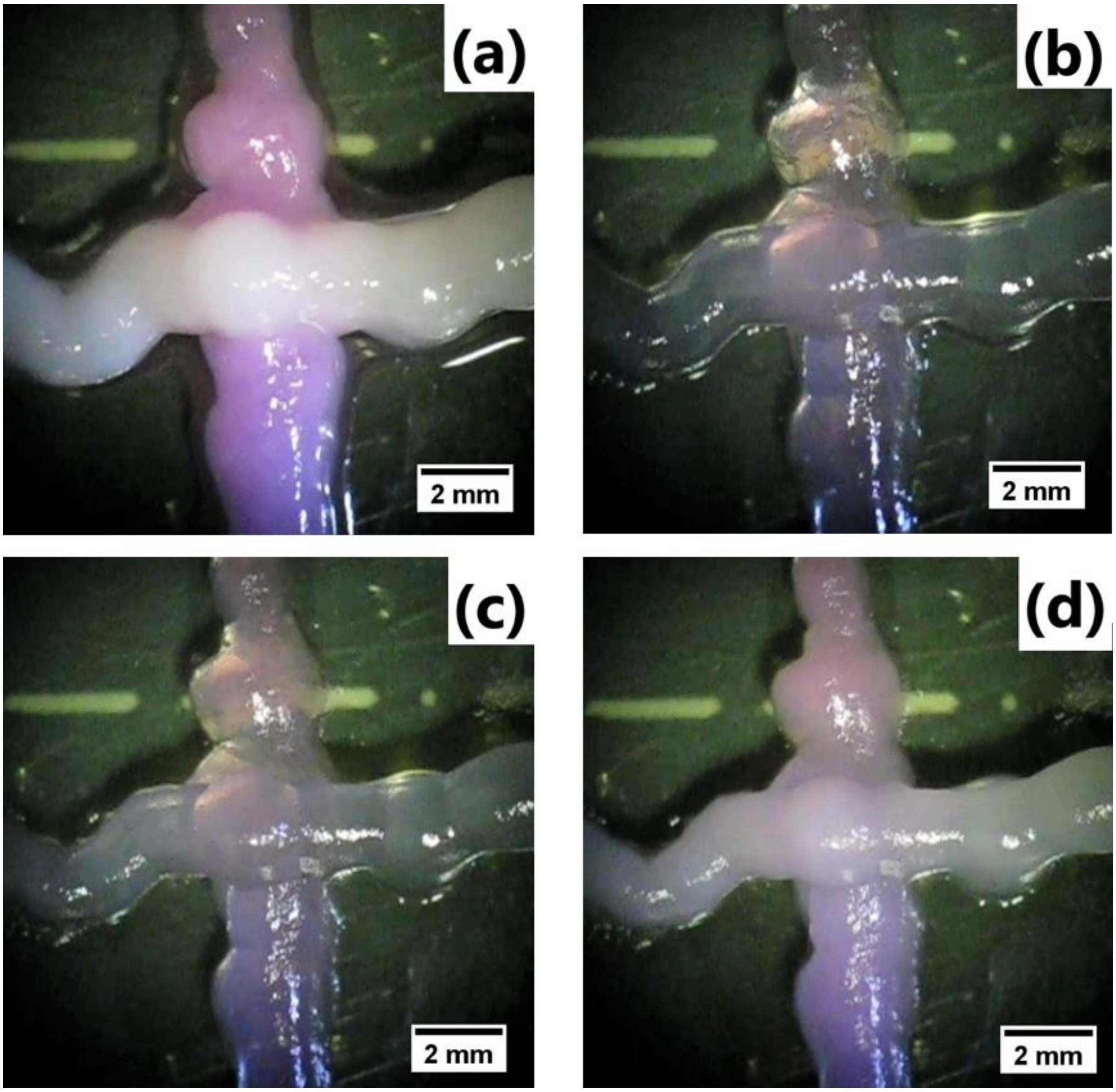

Figure S8: Microscopy of self-healing from two different stained strands of CNF-g-UPy/UPy-DEGEEA gel (a) t = 0s; (b) t = 6 min 30s; (c) t = 11 min 58s; (d) t = 17 min 20s

Appendix 3:

Development of a bio-based composite for 3D printing from diphenylalanine peptide (Fmoc-FF) nanowires with unmodified or polymer-grafted cellulose nanofibrils: from an unprintable material to a strong and reliable printable gel

Feras Dalloul, J. Benedikt Mietner, Dhanya Raveendran, Fabio Hubel, Dennis M. J. Möck, Jörn Appelt and Julien R. G. Navarro

Under revision in RSC Nanoscale

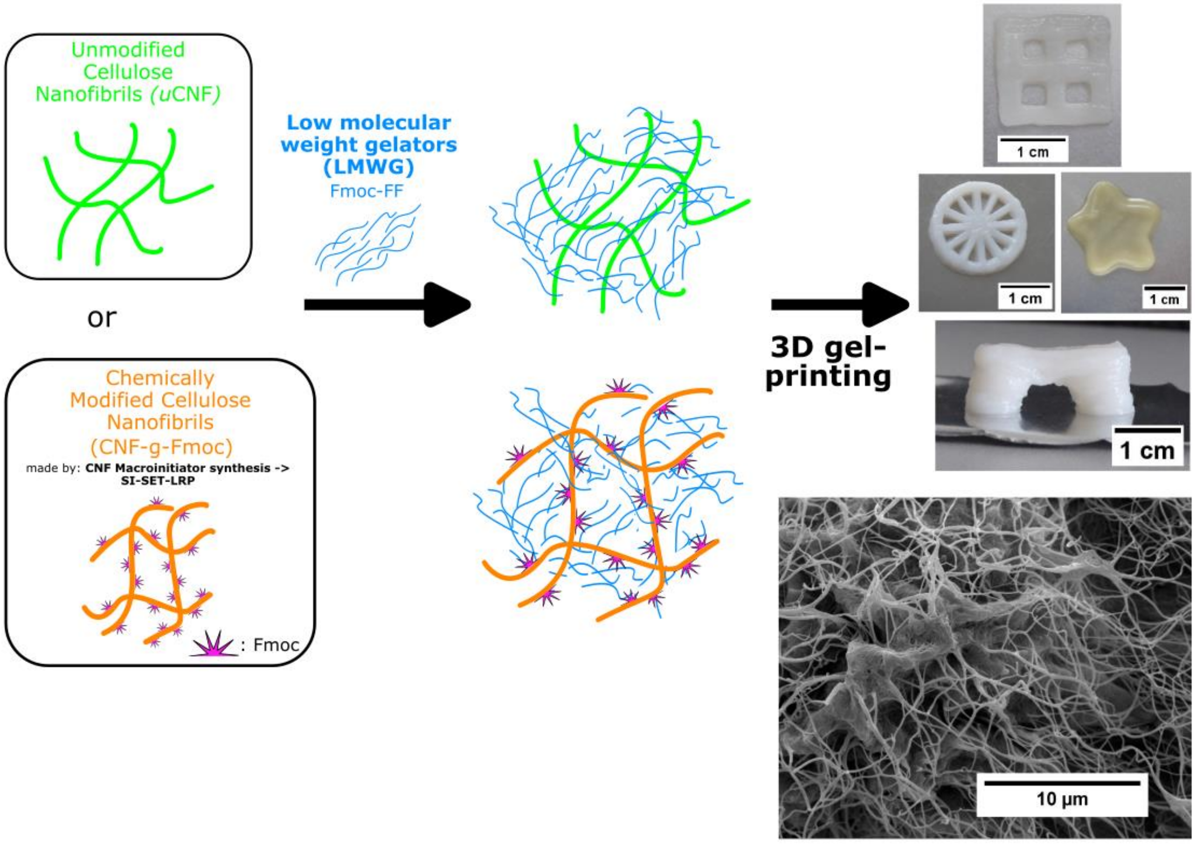

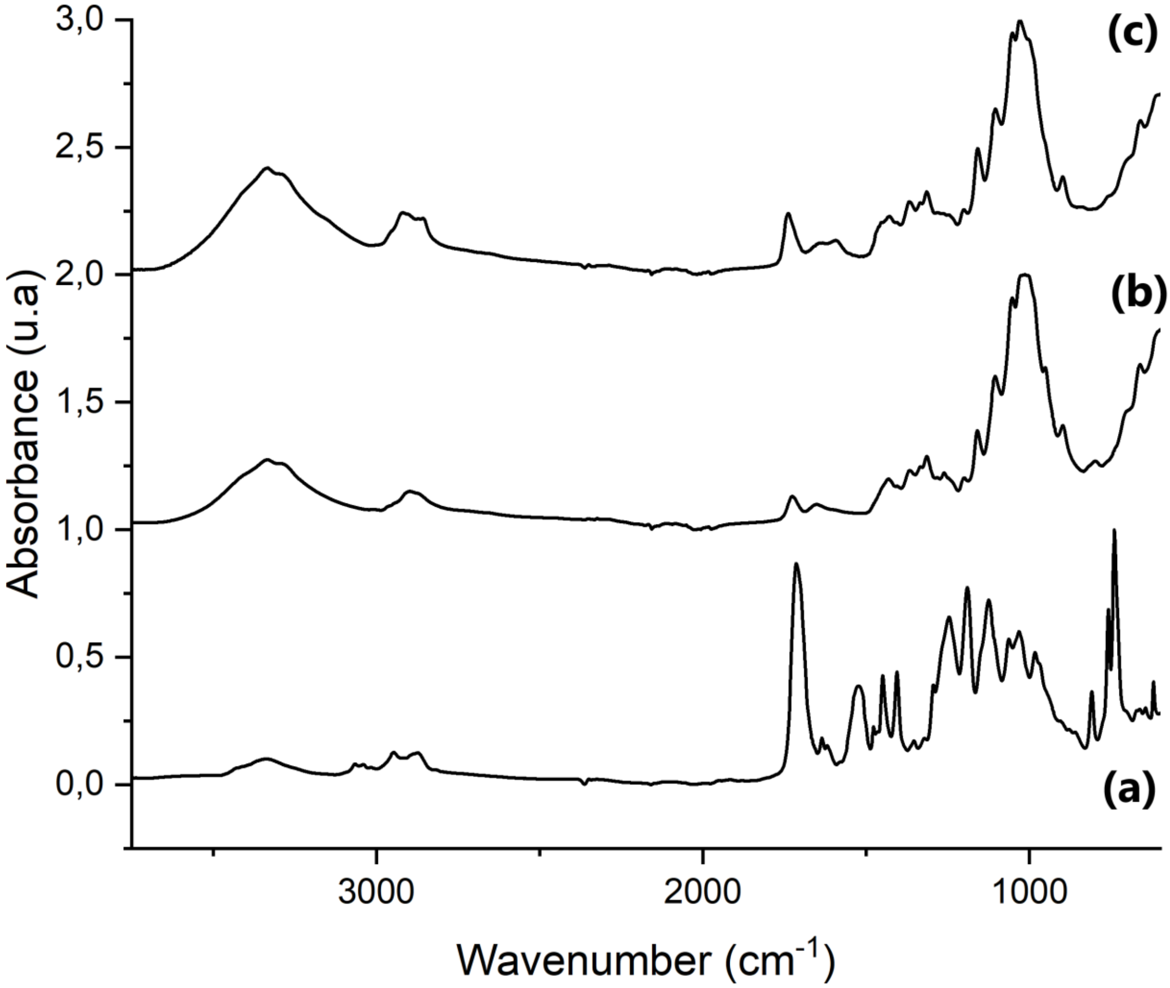

Figure 1: ATR-FTIR spectrum of pristine (a) Fmoc-AEEA, (b) CNF-MI, and (c) CNF-g-Fmoc

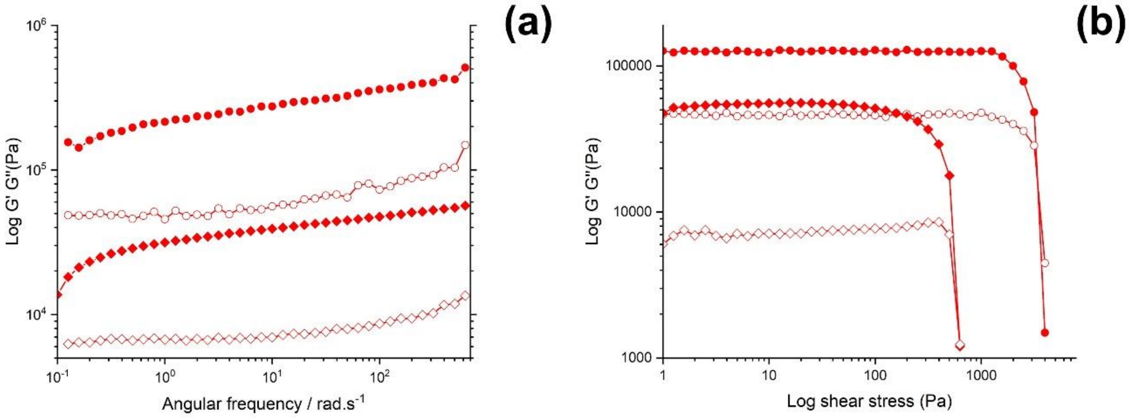

Figure 2: (a) Viscoelastic properties data and ddynamic modulus under increasing stress to determine yield stress (b) of *u*CNF/Fmoc-FF$_{3.89}$ before (○) and after mixing (◊); Full symbols for G’ and hallow ones for G”.